![University of Glasgow logo]

Patterson, Courtenay (2023) *The electrofabrication of di- and tripeptide hydrogels and their subsequent material properties.* PhD thesis.

https://theses.gla.ac.uk/83597/

The Electrofabrication of Di- and Tripeptide Hydrogels and their Subsequent Material Properties

Courtenay Patterson

Submitted in fulfilment of the requirements for the Degree of Doctor of Philosophy

School of Chemistry

College of Science and Engineering

University of Glasgow

April 2023

Abstract

In this thesis, we report the ability to fabricate hydrogels using low molecular weight gelators (LMWGs) and the subsequent characterisation of their mechanical properties over a variety of different length scales. These materials have been investigated due to their potential use in a wide range of biomedical applications including drug delivery, tissue engineering, cell culture and wound healing.

We describe the localised gelation of LMWGs on electrode surfaces via electrochemically generated pH gradients. The electrofabrication of hydrogels on electrode surfaces has shown great potential in the field of biomedicine, with applications ranging from antimicrobial wound dressings, tissue engineering scaffolds and biomimetic materials.

First, we describe the largest reported di- and tri-peptide-based hydrogels on electrode surfaces via the electrochemical oxidation of hydroquinone. Expanding upon previous work which focuses on the fabrication of hydrogels on the nanometre to millimetre scale, we deposit hydrogels around 3 cm^3 in size. Furthermore, we demonstrate that there is an upper limit to how large the hydrogels can grow which is determined by the size of the pH gradient from the electrode surface. To grow hydrogels of this size, much longer deposition times of two to five hours are required than in previous reports. When the gelator/hydroquinone solution is left exposed to the open atmosphere for this amount of time, the hydroquinone in solution oxidises to benzoquinone/quinhydrone before it can be consumed electrochemically. This inhibits the electrochemical reaction and reduces gelation efficiency. To prevent this, we build a system that can perform the fabrication process under an inert nitrogen atmosphere. Using this system, we show how the choice of gelator affects the mechanical properties of the hydrogel and the resulting material phenomena that cause these changes. As well as this, we show how this approach can be used to grow multi-layered hydrogels, with each layer presenting different chemical and mechanical properties.

Secondly, we report the first known example of electrodeposition for a LMWG molecule using an electrochemically generated basic pH gradient at electrode surfaces. This approach has previously been used to fabricate hydrogels of the biopolymer chitosan using the galvanostatic reduction of hydrogen peroxide. During the electrochemical reduction of hydrogen peroxide, hydroxide ions are produced. As a result, a basic pH zone is generated at the electrode, triggering solutions of chitosan to form immobilised hydrogels on the electrode surface. Using this approach, we show how electrodeposition at high pH can be applied to our LMWG system.

We then show that we can electrochemically form hydrogels at high pH, with the gel properties being greatly improved by the addition and increased concentration of hydrogen peroxide. Following from this, we then show the simultaneous formation of two low molecular weight hydrogels at acidic and basic pH extremes. To achieve this, we couple the electrochemical reduction of hydrogen peroxide and the electrochemical oxidation of hydroquinone described in the previous chapter.

Finally, we report the electrodeposition of five carbazole-protected amino acid hydrogels on electrode surfaces via the electrochemical oxidation of hydroquinone. As well as this, we report the full to partial electropolymerisation of the pre-assembled hydrogels in perchloric acid. For the less bulky carbazole-protected amino acids, the full collapse of the hydrogel to form electrochromic polymers on the electrode surface is achieved. However, for the bulkier gelators, little to no evidence of polymerisation occurs. We believe this is due to the bulky side chain on the gelator backbone preventing the molecular reorganization required for polymerization to occur. To probe the primary self-assembled structures of the carbazole-based hydrogels growing in-situ and their full to partial electropolymerisation in perchloric acid, a first-of-its-kind experiment was performed using small-angle X-ray scattering (SAXS) at Diamond Light Source (I22 beamline, Oxfordshire, UK). We present the novel SAXS set-up discussed as a tool to open up new opportunities to probe and analyse soft materials in real-time.

Acknowledgements

First and foremost, I would like to say a massive thank you to my supervisor Prof. Dave Adams. If I hadn't ended up in your research group for my undergraduate dissertation project, I would never have known that the possibility of a PhD was open to me. I'm so very grateful that you encouraged me to put one foot in front of the other when the bigger picture seemed overwhelming. Thank you for the support, guidance, and mentorship over the past three and half years. I'll miss walking into your office every week to the deafening sound of rock music blasting from your Mac.

Thank you to the School of Chemistry and all the staff that have supported and inspired me over the past eight years.

Thank you to Dr Spence, my school chemistry teacher, for making a daunting and difficult subject so fun and accessible. Thank you for the laughs, the patience (much needed) and your continued support from across the water.

I'd like to give a special thanks to Libby Marshall, for being by my side for the entirety of this PhD. Thank you for your endless help, your generosity and your ability to see the best in any given situation. I know my experience would have been a whole lot different without you and I couldn't have asked for a better person to do this with.

Thank you to all the past and present Adams and Draper group members that I've had the pleasure to work with and learn from. To Chloe Wallace, my fellow Irish companion and the little sister I never had, thank you for making every day at work better. To Simona Bianco, thank you for all the help with the cursed SAXS files and for being the best Diamond partner imaginable. Here's to learning choreographed dances in the early hours of the morning! To Rebecca Ginesi, thank you for your friendship and help over the past few years, you are the smartest and kindest soul I've ever met. To Jakki, thank you for always bringing the good Canadian snacks, even if I did eat the majority. It was a bumpy road but we made it! To Nick, if sunshine was a person, thank you for never failing to make me laugh. To Max Hill, thank you for always checking in on me in those final months. To Bart Dietrich, thank you for all your synthesis help and for making the impossible possible with your trusty 3D-printer. To Alex Loch, a late but wonderful addition to the group, thank you for all the help with my final chapter. Your future group doesn't know how lucky they are!

List of publications arising from this thesis

Patterson, C., Dietrich, B., Wilson, C., Mount, A. R., & Adams, D. J. (2022). Electrofabrication of large volume di-and tripeptide hydrogels via hydroquinone oxidation. Soft Matter, 18 (5), 1064-1070.

Patterson, C., Panjaa, S., Liu, W., Mount, A., Squires, A., Adams, D. J. (2023). Electrofabrication of a Low Molecular Weight Hydrogel at High pH. Materials Chemistry Frontiers.

List of abbreviations

1D: One-dimensional

2D: Two-dimensional

3D: Three-dimensional

AAP: Arylazopyrazole

AFM: Atomic force microscopy

Ala: Alanine

APTES: (3-aminopropyl)triethoxysilane

BFEE: Boron trifluoride diethyl etherate

BQ: Benzoquinone

BSE detectors: Backscattered electron detectors

C: Cylinder

Carb: Carbazole

CNT: Carbon nanotubes

CV: Cyclic voltammetry

DBS: 1,3:2,4-dibenzylidenesorbitol

ddH2O: double-distilled water

DEP: Dielectrophoresis

DMF-d_7: Deuterated DMF

DMF: Dimethylformamide

DMSO-d^6: Deuterated DMSO

DMSO: Dimethyl sulfoxide

DNA: Deoxyribonucleic acid

E-gels: Electrochemical gels

EC: Elliptical cylinder

Echem cell: Electrochemical cell

ECM: Extracellular matrix

ECOM: Electrocompacted

FEC: Flexible elliptical cylinder

FTIR: Fourier transform infrared

FTO: Fluorene-doped tin oxide

G′: Shear storage modulus

G″: Shear loss modulus

GdL: Glucono delta-lactone

Gel-to-sol: Gel to solution

GelMA: Gelatin methacryol

Gly: Glycine

GPC: Gel permeation chromatography

Hap: Hydroxyl apatite

HQ: Hydroquinone

HRMS: High resolution mass spectrometry

I: Intensity

Ile: Isoleucine

ITO: Indium tin oxide

KGM: Konjac glucomannan

Leu: Leucine

LHS: Left hand side

LMWG: Low Molecular Weight Gelator

NBD: 7-nitrobenzo-2-oxa-1,3-diazole

NMR: Nuclear magnetic resonance

PBS: Phosphate-buffered saline

PDMS: Polymethylsiloxane

PEGDA: Polyethylene glycol diacrylate

Phe: Phenylalanine

pI: Isoelectric point

PL: Power law

pXRD: powder X-ray diffraction

Q: Scattering vector

qNMR: Quantitative nuclear magnetic resonance

RHS: Right hand side

SAXS: Small angle X-ray scattering

SDS: Sodium dodecyl sulfate

SE detectors: Secondary electron detectors

SEM: Single electron microscope

SPPS: Solid phase peptide synthesis

TEM: Transmission electron microscope

T_{gel}: Gelling temperature

TLC: Thin layer chromatography

UV: Ultraviolet

Val: Valine

Table of contents

Declaration of authorship

I declare that, except where explicit reference is made to the contribution of others, that this thesis is the result of my own work and has not been submitted for any other degree at the University of Glasgow or any other institution.

Courtenay Patterson

CHAPTER 1

Introduction

Chapter 1

1.1 Gels

Gels are viscoelastic materials that can be characterized by the duality of their liquid (elastic) and solid (viscous) properties.[1] The two components that make up the gel include the solid crosslinked network and the solvent component, with the latter, often accounting for >99% of the weight of the gel (Figure 1.1a). To confer the material with viscoelastic properties, the three-dimensional network entraps the solvent component, reducing the surface tension and preventing flow.[2] As a result, elastic-like properties arise from the solid network and the liquid-like properties derive from the solvent component trapped within it. Depending on the solvent phase, gels can be grouped into categories, including hydrogels, organogels, aerogels and xerogels.[3-6] Consequently, there is an infinite number of solvent and synthetic/natural network combinations. This results in a plethora of soft materials with unique mechanical and chemical properties, deeming them suitable for applications across an extensive range of fields such as electronics, cosmetics, medicine, agriculture and many more.[7-10]
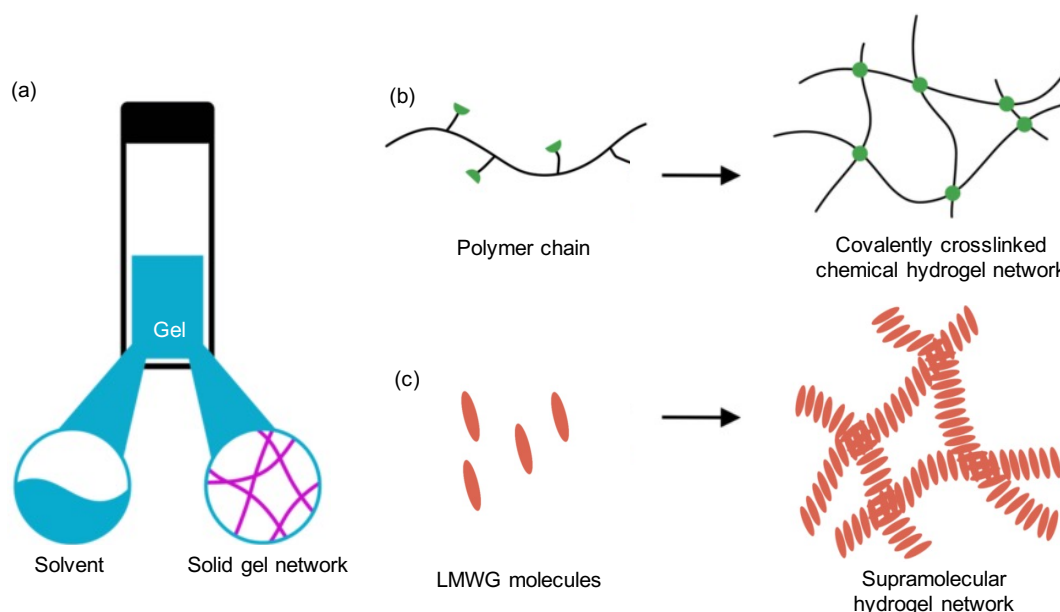
Figure 1.1 (a) Schematic showing the two components that make a gel: the solvent component and the solid gel network. Cartoon showing the different hydrogel networks underpinning (b) chemical hydrogels and (c) supramolecular hydrogels.

1.2 Hydrogels

When the solvent component of the gel is water, the material is called a hydrogel.[11] Due to their high-water content, hydrogels are prevalent materials in biomedical science, with applications ranging from wound dressings, tissue engineering scaffolds, drug-delivery

agents, animal-on-a-chip applications and regenerative medicine.[12-16] Based on the nature of their constituent polymers or molecules, hydrogels can also be characterized as either synthetic, natural or hybrid.[17] Hydrogels can then be further subcategorized into chemical or physical hydrogels, depending on the interactions of the solid gel network.[18] Hydrogel networks held together by covalent crosslinks are deemed chemical hydrogels, often displaying structural stability, high mechanical strength and irreversible properties (Figure 1.1b).[19] Silicone-based hydrogels, which are used to make soft contact lenses, are a common example of chemical hydrogels.[20] In contrast, physical hydrogels, also known as supramolecular hydrogels, have networks held together by weaker non-covalent interactions such as π-π stacking, hydrogen bonding and van der Waals interactions.[21] This property often means the gel network is easily perturbed or broken, showing inferior mechanical properties in comparison to chemical hydrogels. Examples of physical hydrogels include polynucleotide (RNA and DNA) and poly (lactic-co-glycolic acid (PLGA) based hydrogels.[22-24] Despite this disadvantage, physical hydrogels have many attractive mechanical properties; as the supramolecular interactions are easily perturbed/broken, the networks formed are often reversible and can be disassembled/reassembled by applying various external stimuli.[25]

1.3 Low Molecular Weight Hydrogels

Low molecular weight gelators (LMWGs) are the monomeric sub-units that form gels by supramolecular self-assembly, driven by weak yet numerous attractive secondary or non-covalent interactions (Figure 1.1c).[26] When the self-assembly is initiated using an appropriate gelation trigger, the molecules self-assemble in a hierarchal fashion to form long one-dimensional structures that can immobilize the solvent, forming a physical gel. The number of reported LMWG molecules is vast, including peptide amphiphiles[27], Fmoc-protected amines[28], functionalized sugars[29], nucleobases[30], surfactants and many more.[31] LMWG can be distinguished from polymer-based gels as they are held together by non-covalent bonds, unlike polymer gels which are formed via permanent covalent crosslinks.[32] This property endows LMWG with several advantages over chemical-based hydrogels, including commercially available starting materials, simple synthesis, and the ability to tailor the structure and function through chemical functionalization of the molecule's backbone. As the supramolecular interactions that hold the gel network together are easily perturbed, the final hydrogel often exhibits reversible stimulus-responsive properties, meaning they are promising candidates for designing 'smart' materials.[33] Due to their low molecular weight

(typically 300-1000 Da), they do not suffer from the slow aggregation times and diffusion-limited issues seen in high molecular weight structures or polymer-based gelators.[31]

1.3.1 LMWG self-assembly

The supramolecular self-assembly of LMWG occurs in a hierarchal fashion and is understood across three levels of assembly; the molecular level, the fibre level and the network level (Figure 1.2).[26, 34, 35] Whitesides et al.[36] defined molecular self-assembly as the process in which disordered molecules or systems spontaneously associate under equilibrium conditions to form more defined structures as a result of molecular non-covalent interactions. To initiate the self-assembly of LMWG, a gelation trigger is applied to significantly decrease the solubility of the molecule within the solvent. The LMWG molecules respond to this reduction in solubility by self-assembling via non-covalent forces, forming long one-dimensional structures such as tapes, fibres or other helical structures.[37] Once this is complete, the one-dimensional fibres cross-link and entangle by lateral association to form the three-dimensional gel network, entrapping the water component and preventing flow. As the LMWG molecules often include large aromatic groups or alkyl chains, the hydrophobic effect is also an important consideration in the self-assembly process.[38, 39]
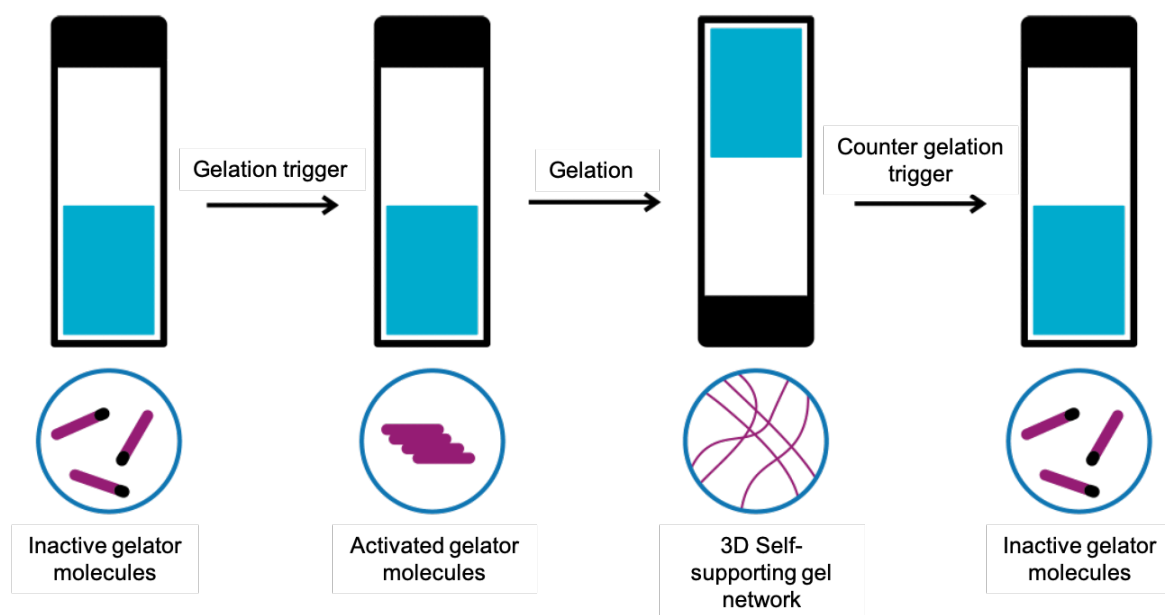
Figure 1.2 Schematic showing the hierarchal self-assembly of LMWGs. To activate the gelator molecules to self-assemble, a gelation trigger is applied, reducing their solubility in the solvent. This initiates the gelator molecules to self-assemble into long one-dimensional fibres which then entangle to form the self-supporting three-dimensional hydrogel network. As the supramolecular network is stimuli responsive, counter gelation triggers can be applied to initiate the disassembly and collapse of the gel network.

1.4 The *N*-protected peptide

An interesting subclass of LMWG is the *N*-protected peptide.[40-42] The architecture of these gelators (Figure 1.3) includes a large aromatic capping group on the *N*-terminus of the molecule such as Fmoc, carbazole and naphthalene.[43] On the opposing end of the molecule, a pH-sensitive group is incorporated such as an amine or carboxylic acid to give an amphiphilic chemical structure. The backbone of the *N*-protected peptide consists of 2-3 amino acids which can be modified using identical or different amino acid side chains. As each amino acid and aromatic group have unique hydrophilic and hydrophobic properties, careful gelator design can be used to generate materials with unique chemical and physical properties.[41] This class of material is frequently used to form synthetic hydrogels, with the chemical composition and physical properties of various hydrogels reported extensively within literature.[34, 44, 45] Some of the main advantages of this class of gelator include controllable mechanical properties, low batch-to-batch variation, biodegradability, commercially available starting materials and simple synthesis methods. However, some *N*-capping aromatic groups such as Fmoc have been reported as toxic.[46] This poses potential limitations to these materials in biomedical applications.
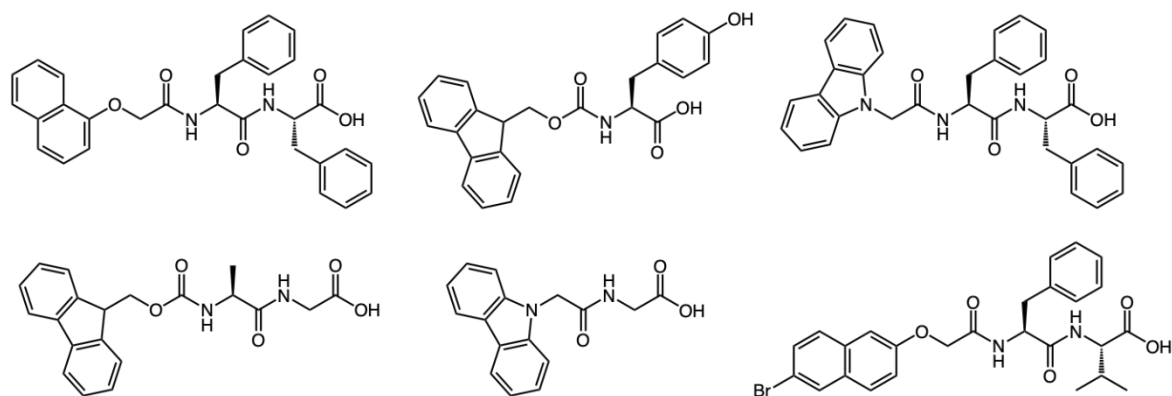
Figure 1.3 Various example known *N*-protected LMWG. Right to left: 1NapFF, FmocY, CarbFF, FmocAG, CarbG, 6Br2NapFV (single letter code used to represent amino acids).

Due to the architecture of *N*-protected peptide gelator molecules, they are usually amphiphilic in nature, meaning their solubility can be altered by varying the reaction conditions. For example, it is common for these molecules to present a free carboxylic acid group on the *C*-terminus of the gelator structure. As a result, their solubility in water can be adjusted by exploiting the pK_a of the terminal carboxylic acid. For these gelator molecules, the pK_a of the carboxylic acid is that of the aggregate and is often higher than the reported value of the free *N*-protected peptide gelator molecule.[47, 48] Certain studies claim this change in pK_a value is entropically controlled, caused by the reordering of the solvent molecules during gelator aggregation.[49] The apparent pK_a value also increases with the hydrophobicity (clogP) of the molecule and is highly dependent on gelator concentration.[41] As a result, these gelator molecules can be dispersed in high pH to form gelator solutions, deprotonating the terminal carboxylic acid and rendering them soluble in aqueous solutions. Research has shown that these gelator molecules are not uniformly dissolved in high pH solutions but are dispersed as surfactant-like aggregates depending on the hydrophobicity and concentration of the gelator molecule in the solution.[41, 50] More hydrophobic gelator molecules tend to form highly viscous solutions, attributed to preexisting structures referred to as worm-like micelles.[51, 52] Less hydrophobic gelator molecules form less viscous solutions as gelator molecules tend to aggregate less strongly to form spherical-like aggregates.[53] For certain *N*-protected peptide gelators, higher concentrations can also see the formation of liquid crystals in solution.[50]

1.5 Gelation triggers

To control the mechanical properties of LMWG, the self-assembly kinetics can be modified by changing the gelator molecule, gelator concentration, temperature, solvent and external gelation trigger.[54] LMWGs form supramolecular hydrogels using a wide variety of physical and chemical gelation triggers.[42] Commonly used triggers include pH changes,[55] solvent switches,[56] use of enzymes,[57] temperature changes,[58] UV irradiation,[59] and electrical signals.[60] Research has shown that sample history and the method of self-assembly have a profound effect on the mechanical properties of the final gel.[61] This is because the method of gelation is one of the parameters that alter the kinetics of the self-assembly process, changing the structures formed and as a result, changing the mechanical properties of the bulk material.[62] Depending on the application, hydrogels must usually meet very specific material requirements. Consequently, the type of gelation trigger used is of the utmost importance.

Despite the differences between the gelation triggers used, the effect on the LMWGs to induce gelation is the same. For all the LMWGs mentioned in this thesis, gelation is triggered by changing the solubility of the LMWG molecules. Once the gelation trigger is applied, the solubility of the LMWG in the solvent is significantly decreased, initiating the aggregation and self-assembly of the LMWGs in the solution to form a hydrogel.

1.5.1 Temperature change (Heat/Cool)

One of the most established and simple gelation triggers is the use of temperature to change the solubility of the LMWGs in water. To use this method, the LMWG and solvent are heated until the LMWGs dissolve to form a solution. As the solution is left to cool, the LMWGs become insoluble in the solution. Ultimately, this change in solubility triggers the self-assembly and gelation of the LMWGs. Work within this area has shown that the final gel properties are highly dependent on the rate of cooling. Smith and co-workers[63] have recently used this method to combine two supramolecular LMWG which are derivatives of the molecule 1,3:2,4-dibenzylidenesorbitol (DBS). In their work, the properties of each LMWG are utilised to create mechanically enhanced hydrogels with controlled release of the pharmaceutically active ingredient Naproxen. They also showed that the T_{gel} (gelling temperature) could be finely tuned by varying the concentration of each respective LMWG.[63]

1.5.2 UV irradiation

The presence of a chromophore can often result in the formation of a photoresponsive gelator, with the absorption of light inducing either photoisomerisation, photocleavage or photodimerisation.[64] Examples of chromophores that have resulted in the successful formation of photoresponsive LMWGs include spiropyran, stilbene, diarylethene and azobenzene.[64] One of the most common methods of inducing gel-to-sol transition by photo irradiation is the attachment of azobenzene derivatives that can undergo *trans*-to-*cis* isomerisation when exposed to light of the appropriate wavelength.[65] This absorption can convert the gelator into the non-gelating isomer which ultimately results in the gel-to-sol transition phase.[66] Another photo-induced reaction is the formation and breakage of covalent bonds during photoirradiation. This can be seen during photodimerisation and photocleavage reactions, which are particularly prevalent in conjugated molecules due to the π-π stacking interactions and the driving force of regained aromaticity. Chromophores can also undergo photocleavage reactions of ring opening and closing through the breakage and formation of covalent bonds. The absorption of UV light provides the system with enough energy to promote bond formation and the closure of the ring, which forms the less strained 'open' ring when the light source is removed.

In 2020, Ravoo and co-workers[67] reported an example of a photoresponsive hybrid hydrogel consisting of two networks: the photoresponsive LMWG (AAP-FGDS) network and the non-responsive polymeric network of agarose (Figure 1.4a). Ravoo and co-workers employed this hybrid strategy to combine the dynamic and phototunable properties of the LMWG (AAP-FGDS) with the superior mechanical properties of agarose. Thus, forming the first reported hybrid hydrogel capable of light induced supramolecular assembly and disassembly.[67] It is important to note that due to the high pH used, a 'true' self-supporting hydrogel network of AAP-FGDS is not formed within the hybrid material but rather a very viscous solution of assembled worm-like micelles/highly aggregated structures.

The reversible photoresponsive properties of the AAP-FGDS network arise due to the incorporation of the photoswitchable arylazopyrazole (AAP) moiety into the gelator structure (Figure 1.4b). Upon irradiation of the hybrid material with UV-light ($\lambda = 365$ nm), the assembled AAP-FGDS network disassembles as the AAP unit isomerises from the planar E-isomer to the sterically hindering Z-isomer. This gives rise to a material in which the AAP-FGDS network is disrupted while the agarose network remains unaffected. Despite the

disassembly of the AAP-FGDS network, the agarose network which is unaffected by the irradiation process, maintains the self-supporting hydrogel structure throughout. It was also shown that this process is highly reversible, recovering the AAP-FGDS network within the agarose hydrogel by exposing the material to visible light. Upon irradiation of the hybrid material, no macroscopic change was observed. However, photo-rheological measurements revealed a drop of the storage modulus for the hybrid material by over an order of magnitude after UV irradiation. The original storage modulus could then be restored upon exposure to visible light, showing this process was highly reversible over at least three irradiation cycles.
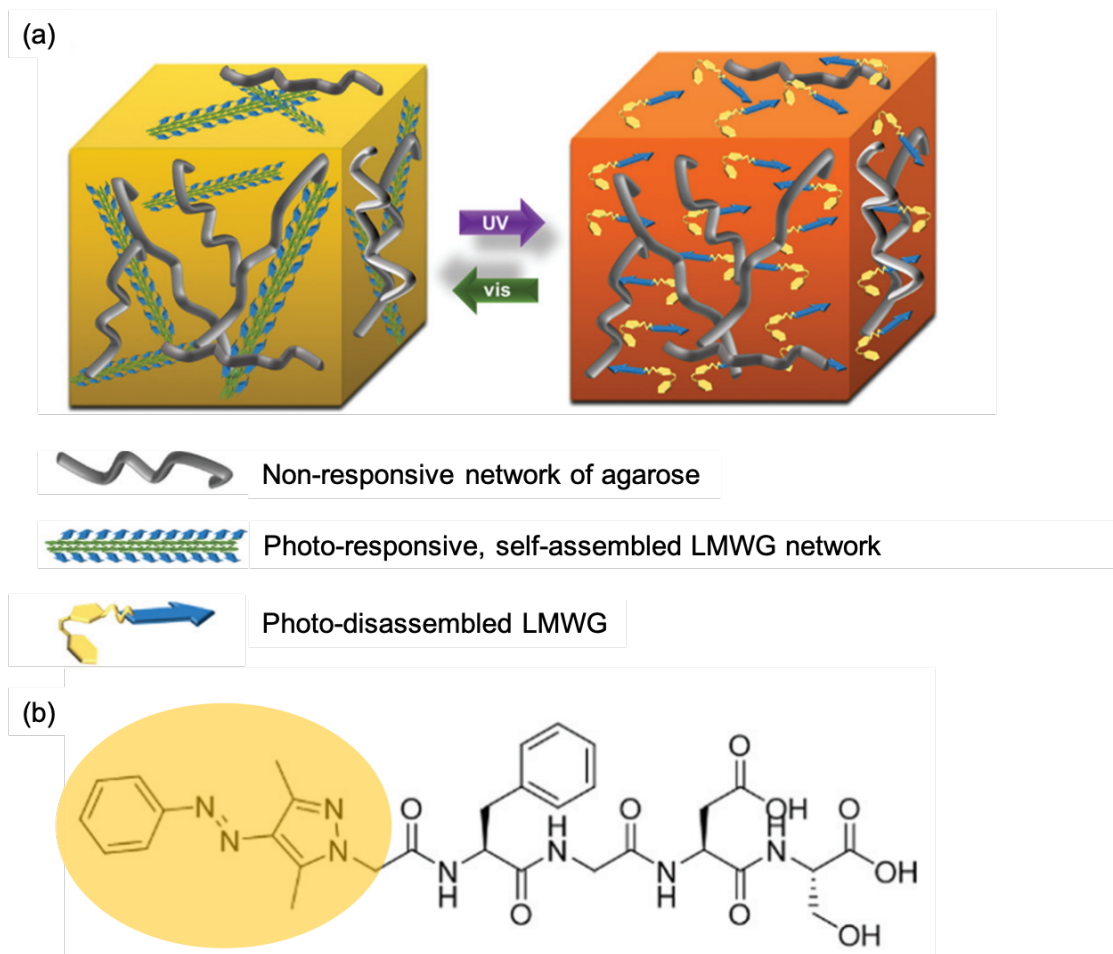
Figure 1.4 (a) Schematic representation of a hybrid hydrogel consisting of the photoresponsive LMWG (AAP-FGDS) network and the non-responsive polymeric network of agarose. Upon irradiation with UV-light, the supramolecular network of AAP-FGDS disassembles while the agarose network is unaffected. The network of AAP-FGDS can be restored by exposing the irradiated hybrid material to visible light (b) Chemical structure of the novel gelator AAP-FGDS. The photoswitchable arylazopyrazole (AAP) moiety has been highlighted. Structures and images reproduced from *Soft Matter*. 2020, **16**, 7300 with permission from the Royal Society of Chemistry.[67]

1.5.3 Divalent Salts

N-Protected dipeptide gelators with a free terminal carboxylic acid on the *C*-terminus can be dissolved at high pH to form gelator solutions. However, research has shown that these gelator molecules are not uniformly dissolved in high pH solutions but dispersed as surfactant-like aggregates depending on the hydrophobicity of the gelator molecule. In 2011, Chen et al.[52] first showed that adding divalent cations such as calcium to the solution resulted in the cross-linking of the neighbouring carboxylate groups, reducing the solubility of the *N*-protected dipeptide to form a gel.[52] BrNapAV and 1NapFF are *N*-protected dipeptide gelators that self-assemble to form self-supporting hydrogels at low pH. The apparent pK_a of BrNapAV and 1NapFF have been reported within literature[41] and are shown to directly correlate to the type of aggregate that the gelator molecules occupy in solution (Figure 1.5) Due to its more hydrophobic structure, 1NapFF has a higher apparent pK_a than BrNapAV and has been shown to form worm-like micelles in an aqueous solution at high pH.[51] As these structures result in the close proximity of the carboxylate groups, calcium can be added as a gelation trigger to crosslink the 1NapFF molecules, forming a gel. BrNapAV gelator molecules behave much differently in aqueous solutions at high pH, forming spherical aggregates with no preferential alignment.[53] This means, unlike 1NapFF gelator molecules, they do not entangle or form large aggregated structures such as worm-like micelles. As a result, divalent cations such as calcium cannot effectively crosslink the BrNapAV molecules, meaning gelation cannot be triggered using this method for this material.
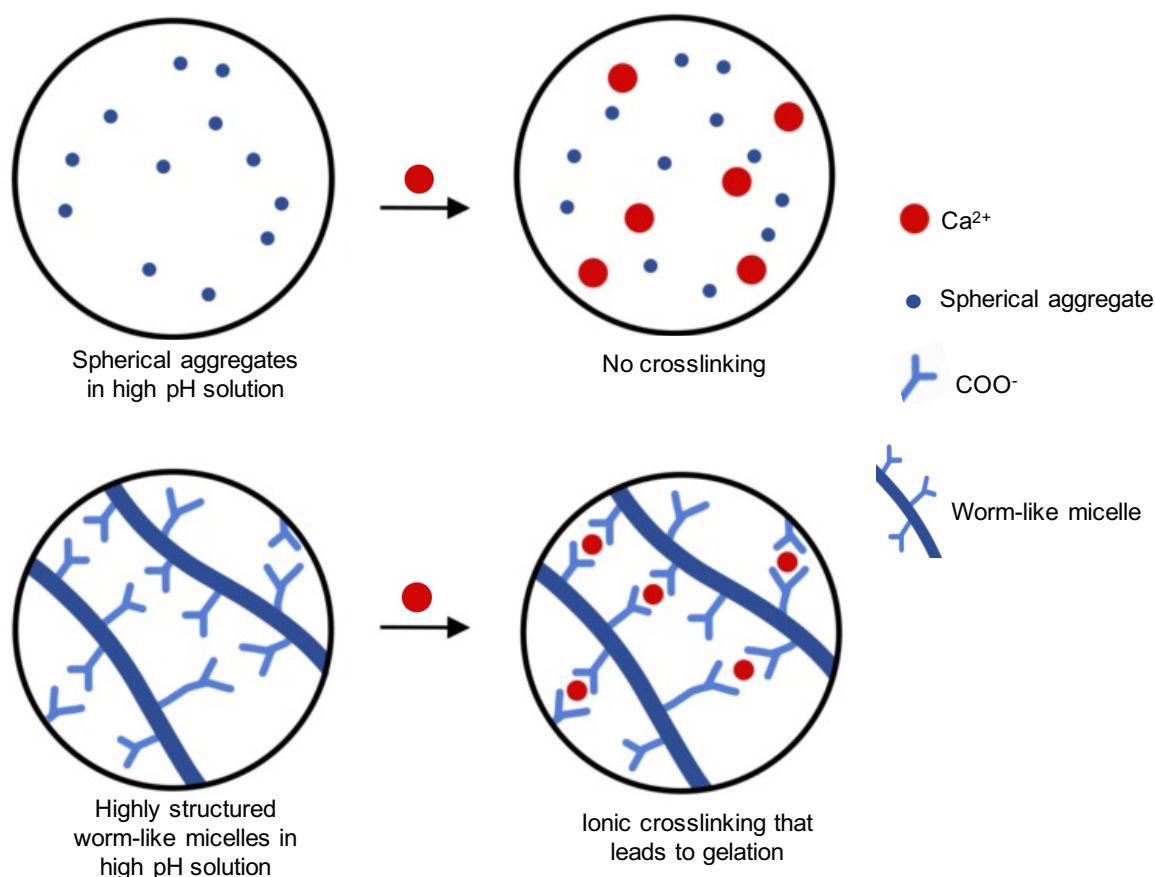
Figure 1.5 Schematic showing the effect of divalent metal ions (e.g., Ca^{2+}) on the pre-assembled structures of LMWG in high pH solutions. When the LMWG are dispersed as spherical aggregates, the addition of divalent metal ions to the solution does not result in hydrogel formation, as the carboxylate groups of the LMWG are not in close enough proximity to each other. When the LMWG are dispersed as highly aggregated worm like-micelles, the LMWG can crosslink the divalent metal ions to form the hydrogel network.

1.5.4 Solvent switches

To drive the self-assembly of LMWG, a variety of aromatic groups are incorporated into the gelator structure. As a result, the molecule is rendered soluble in organic solvents and insoluble in water. Consequently, a solvent switch can be used to trigger the gelation of LMWGs.[56, 68] First, the LMWG is dissolved in a water-miscible organic solvent such as dimethyl sulfoxide (DMSO), methanol or acetone.[69] The solvent-switch approach can then be carried out by diluting the solution with water. As the LMWG molecules are insoluble in water, the gelator molecules begin to aggregate to form self-supporting hydrogels with time. Using this solvent-switch approach, Huang et al.[70] triggered the gelation of hybrid hydrogels composed of the LMWG Fmoc-diphenylalanine (Fmoc-FF) peptide and konjac glucomannan (KGM). To prepare the hydrogels, KGM was dispersed in double-distilled

H$_2$O (ddH$_2$O) and stirred for 24 hours. Separately, the LMWG Fmoc-FF was dissolved in DMSO. The hydrogels could then be formed via a solvent switch gelation trigger by diluting the organic solutions of Fmoc-FF with the solution of KGM in ddH$_2$O. For these systems, the mechanical properties of final hydrogels are highly dependent on the ratio of the water and the organic solvent used, making them suitable for multiple applications with specific material requirements.[56, 69] This, alongside the ease of preparation and quick gelation times, makes the solvent switch a common choice of gelation trigger.

1.5.5 Enzymes

Enzymes are considered as one of the most useful gelation triggers for *off-on* switching of gelation (or vice versa) because of their high substrate specificity and catalytic efficiency.[71] One of the main benefits of using an enzymatic gelation trigger is that they can be used in both intracellular and extracellular environments. As a result, these systems are highly sensitive to environmental conditions such as temperature and pH, which must be kept constant during the gelation process. In natural systems, most of the chemical reactions are driven by enzymes, of which the self-assembly reactions within biological systems are kept away from equilibrium.[72] Enzymes allow such unfavourable reactions to occur by lowering the activation barrier needed for the reaction to occur. Thus, enzymatic reactions have gained tremendous attention as gelation triggers for LMWG.[28, 73] To initiate gelation of LMWGs, enzymes are mostly used to interact with LMWG to induce specific chemical changes on the gelator backbone. This may either trigger gelation by activating the pro-gelator molecule or it may cause the gel-to-sol transition through hydrolysis/condensation of the assembled gel network.[74] Examples of enzymatic reactions used to activate the pro-gelator molecule of LMWGs include the phosphatase-catalysed dephosphorylation of Fmoc-Tyr phosphate and the subtilisin-catalysed cleavage of the ester group from various Fmoc-protected dipeptide gelators (Figure 1.6).[75, 76] Likewise, enzyme triggered gel-to-sol transformations have also been studied for LMWG. John and co-workers[77] use the lipase-induced ester hydrolysis reaction for gel-to-sol conversion. In their study, they showed that the delivery of hydrophobic drugs like curcumin is possible by encapsulation of the drug within the gel media, followed by degradation of the gel with time. Following the same strategy, they later construct an enzyme-catalysed drug delivery system where they synthesise a gelator by direct coupling with a drug. This synthesised gelator can behave as a pro-drug which upon treatment with the lipase enzyme (esterase), undergoes an ester hydrolysis reaction. As a result, the transient gel network slowly disintegrates accompanied by the release of the desired drug.[77]
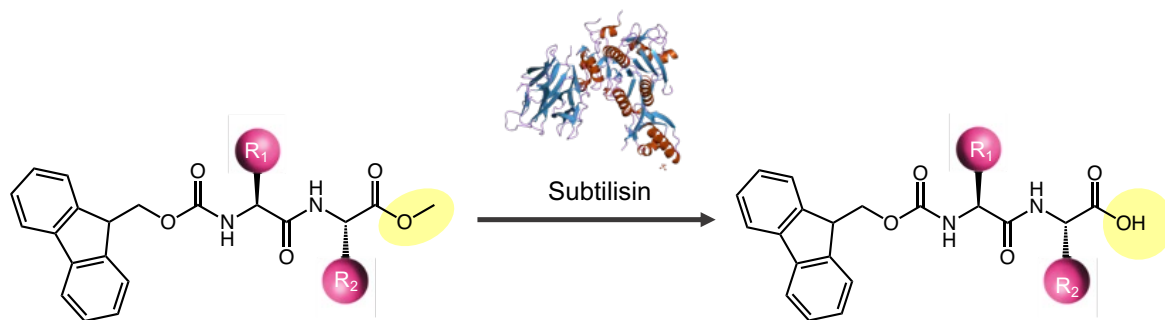
Figure 1.6 Scheme showing the general structure of Fmoc-protected dipeptide esters which upon addition of the enzyme subtilisin hydrolyse, converting the terminal ester group to a carboxylic acid. This conversion results in the generation of the gelating molecule which self-assembles to form hydrogels. Redrawn with permission from Hirst, A., Roy, S., Arora, M. *et al.* Biocatalytic induction of supramolecular order. *Nature Chem* **2**, 1089–1094 (2010).[75]

1.5.6 pH

The use of pH triggers on LMWG systems is one of the most established gelation triggers in literature due to the multitude of different methods. This includes photoacids[78], electrochemical signals[79], direct addition of mineral acid/base,[80] hydrolysis of anhydrides[81], hydrolysis of lactones[82] and enzymatic triggers.[83] Although the methods used to alter the pH of the system are different, the mechanism of action is the same. Many LMWGs are amphiphilic in nature, due to the combination of hydrophobic aromatic groups and charged side or head groups on the molecule. This allows their solubility in water to be adjusted by exploiting the pK_a of the charged groups, which will be highly pH dependent. In 2022, Ravoo and coworkers[84] successfully gelled the LMWG 2NapFF via the oxidation of thioethers using triiodide (a highly soluble iodine source), a process which generates a stochiometric number of protons (Figure 1.7). The production of protons decreases the pH of the 2NapFF solution below the terminal carboxylic acids pKa, protonating the carboxylate group to form the neutral, gelling molecule.
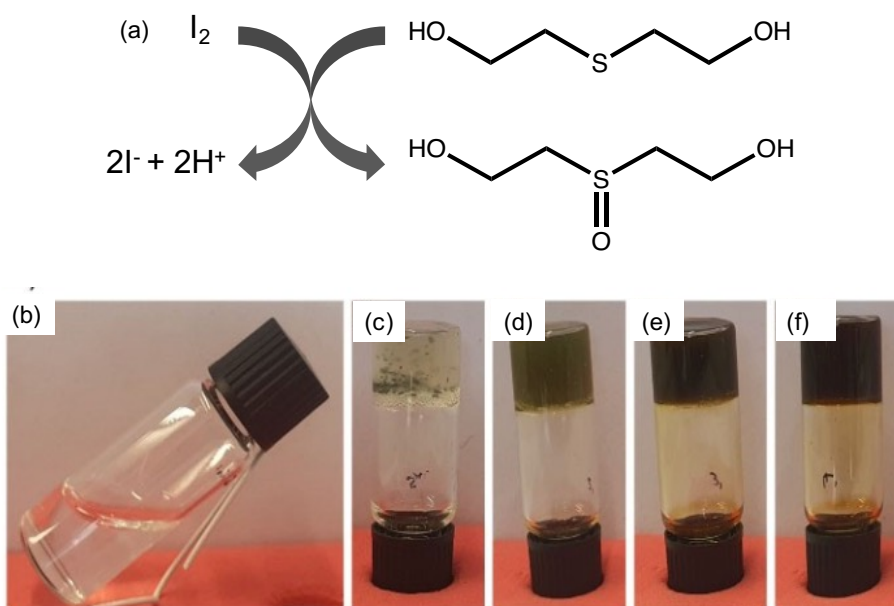
Figure 1.7 (a) Scheme showing the oxidation of the thioether thiodiglycol to the corresponding sulfoxide using molecular iodine. This process generates two molar equivalents of hydrogen iodide (HI) which subsequently decreases the pH of the solution (b) Images of 0.5 wt% 2NapFF and 1% vol% thiodiglycol gelator solutions triggered using (b) 2.5 mM (c) 5 mM (d) 15 mM (e) 30 mM and (f) 50 mM triiodide solution. Self-supporting hydrogels were formed in cases were the concentration of triiodide ≥5 mM. Images were taken with permission from *Angew. Chem. Int. Ed*. 2022, **61**, e2022017.[84] © 2022 The Authors. Angewandte Chemie International Edition published by Wiley-VCH GmbH.

1.6 Electrofabrication

Electrofabrication is a blanket term that covers a range of methods that impose electrical signals to solutions of biologically derived macromolecules/gelator molecules to form soft materials for practical applications.[15, 85, 86] Biofabrication aims to create 2D and 3D tissues, organs and scaffolds from biomaterials. This has been carried out using sophisticated photolithographic techniques,[87, 88] 3D bioprinting[89] and other established additive manufacturing procedures. Electrofabrication is an electrochemical approach to biofabrication. Conventional biofabrication methods are much more advanced in comparison to electrofabrication techniques. However, with significant funding and research, the benefits afforded to electrofabrication present significant potential within the field.

The use of electrofabrication methods to construct hydrogels opens a promising approach to creating bioactive and organic materials and has several advantages over other established biofabrication techniques. For example, electrofabrication methods are not limited by the long fabrication times seen in stereolithography or the clogging in layer-by-layer printing. The setup is simple and cost-efficient and does not require the use of external photomasks, polymethylsiloxane (PDMS) moulds or laser sources to achieve patterning on the surface/bulk of the gel. The use of potentially cytotoxic and non-biocompatible photoinitiators and photoacids is often avoided.

Electrofabrication techniques can be split into two categories; indirect electrochemical approach and direct electrochemical approach.[90] An indirect electrochemical approach sees the production of target molecules at the electrode surface that are responsible for the fabrication of soft materials. This technique is highly advantageous as it affords excellent spatiotemporal control, with fabrication limited exclusively to the electrode surface. The most common biomaterials within literature fabricated using this indirect approach include chitosan[91], silk[92], and alginate[93].

These materials have terminal pH-sensitive groups such as -COOH and -NH$_2$ which can be protonated/deprotonated by controlling the pH at the electrode-solution interface as well as electrostatically interacting with electrochemically generated metal ions and reactive species. The generation of a pH gradient at the electrode-solution interface is a common approach used to induce the self-assembly and formation of hydrogels and bio constructs. One way this can be achieved is by exploiting the electrolytic reactions of water at the electrode surface. Chitosan self-assembles at high pH which can be induced locally by the electrochemical reduction of water at the cathode surface to form hydroxide ions and hydrogen gas.[94] This local increase in pH results in the neutralisation of chitosan's terminal -NH$_3^+$ group to form a supramolecular hydrogel at the cathode surface.[95]

Other indirect approaches include the generation of reactive oxidising agents (e.g., HBrO and HClO) and metal ions (e.g., Cu^{2+}, Fe^{2+}, Fe^{3+}) at the electrode surface. Alginate forms hydrogels by chelating free Cu^{2+} and Fe^{3+} ions, which can be generated electrochemically at the anode surface.[86] Adding ferrous ions to an alginate solution allows for the electrodeposition of Fe^{3+}-Alginate hydrogels at the anode surface through the oxidation of ferrous ions to ferric ions, which then go onto chelate with alginate's terminal COO$^-$ group (Figure 1.8).[96] The addition of NaCl to a solution of chitosan means the -OH groups present on chitosan's backbone can be oxidised by the electrochemical generation of reactive

chlorine species (HClO) at the anode surface to form aldehyde groups.[12] These aldehyde groups can then crosslink with chitosan's terminal -NH$_2$ groups through Schiff base linkages to form chemical hydrogels.
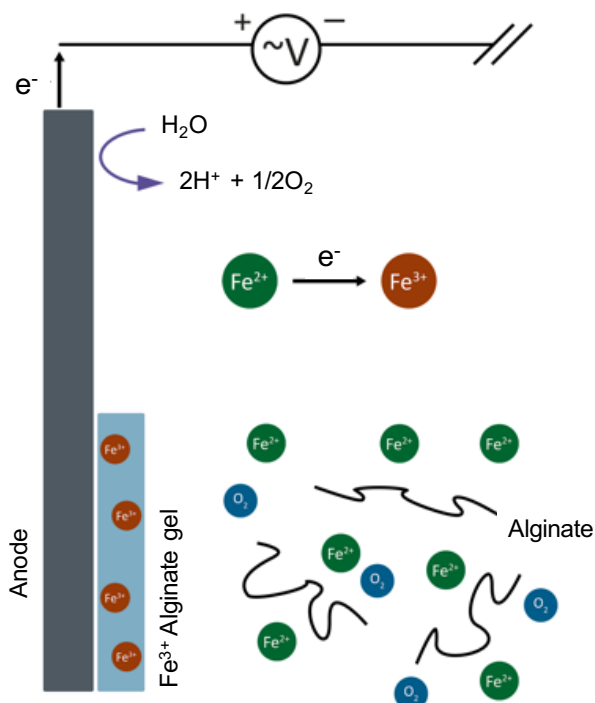
Figure 1.8 Schematic showing the formation of Fe^{3+}-Alginate hydrogel films on electrode surfaces via the electrochemical oxidation of ferrous (Fe^{2+}) to ferric (Fe^{3+}) ions.

A direct electrochemical approach to fabricating biomaterials commonly employs an induced electric field, allowing biomaterials to be formed far from the electrode surface as well as controlling the movement, morphology and direction of cells within the material. Such techniques include electrophoresis, dielectrophoresis (DEP) and electrotaxis.[90] DEP is one of the most common direct electrochemical approaches to assembling biomaterials. Matsue and co-workers[97] used this technique to align carbon nanotubes (CNT) in gelatin methacrylol (GelMA) hydrogels to form CNT-hydrogel scaffolds. This resulted in the enhanced differentiation of mouse embryoid bodies compared to non-aligned CNT-hydrogels and pure GelMA.[97] Direct approaches that do not employ an electric field include electropolymerisation and the direct formation/detachment of biomolecules from the electrode surface.

1.6.1 Specific biomaterials used in electrofabrication

1.6.1.1 Chitosan

One of the most established hydrogels fabricated using this technique is chitosan, an amino-polysaccharide that self-assembles at high pH (Figure 1.9a).[94] The amino groups become deprotonated at high pH, resulting in the polymer becoming insoluble in an aqueous solution. This induces the self-assembly of the chitosan molecules to form a hydrogel. A low cathodic voltage of around 1.2 V is applied to a chitosan solution of low pH.[12, 98] This reduces the water molecules at the electrode surface to produce hydroxide ions and hydrogen gas, locally increasing the pH at the electrode surface. However, the electrolytic reactions of water produce bubbles of hydrogen gas meaning the reaction must be carefully controlled and undertaken slowly to prevent bubbles from forming in the chitosan material films, as this can be detrimental to the films' mechanical strength.[99] To overcome this, hydrogen peroxide is now commonly used, which can be electrochemically reduced to generate hydroxide ions without the formation of hydrogen gas (Figure 1.9b).[95]

Dual responsive or binary blend hydrogels containing chitosan can be fabricated to create materials with a higher degree of functionality and sophistication.[86] This can be seen by blending an acidic solution of chitosan with a warm agarose solution.[91] When the agarose-chitosan solution was cooled to room temperature, the agarose component forms a hydrogel, entrapping the chitosan solution within the gel network. Localised gelation of the chitosan within the agarose hydrogel could then be achieved by moving a 'cathodic pen' (various shaped electrodes) across the surface of the gel to create specific regions of high pH. This induced the chitosan within the agarose hydrogels to self-assemble and form precisely shaped hydrogels (Figure 1.9f-g). To remove the agarose component, the material was heated which caused the disassembly of the agarose hydrogel, leaving the chitosan hydrogel pattern intact.
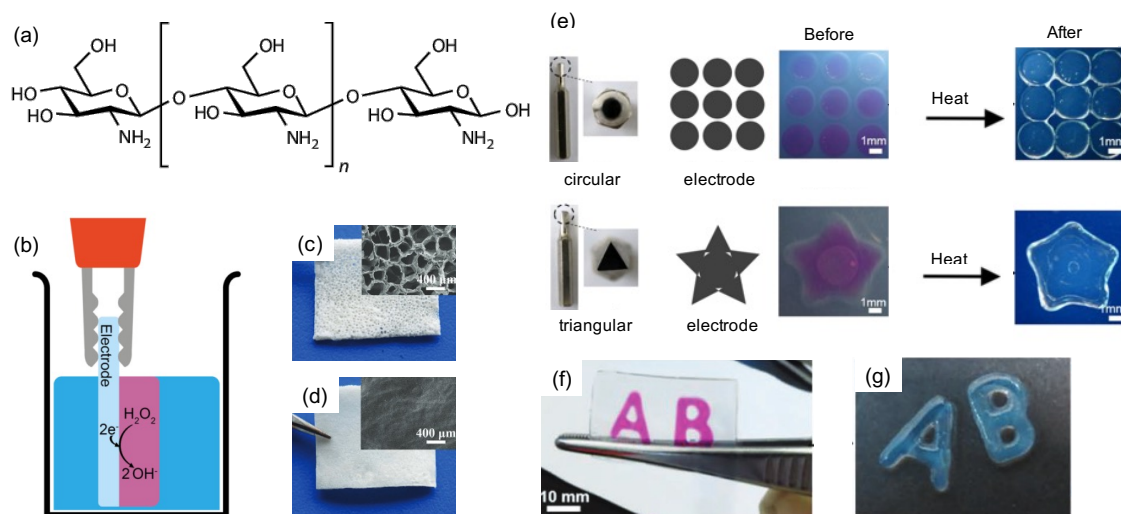
Figure 1.9 (a) Chemical structure of the amino polysaccharide chitosan (b) Schematic showing the electrofabrication of chitosan films on electrode surfaces via hydrogen peroxide reduction. The localised increase in pH at the electrode surface deprotonates chitosan's charged amino groups, reducing its solubility in solution to initiate gelation. No gelation is observed in the bulk solution as the pH remains unaffected (c-d) To fabricate asymmetric 'Janus' films of chitosan hydrogels, a thin dense layer of chitosan is formed on the electrode surface via hydrogen peroxide reduction. The second chitosan layer is then deposited on top of this dense layer by adding the soluble salt NaH_2PO_4 to the gelator solution. (c) shows films formed using higher concentrations of NaH_2PO_4 in comparison to (d) where lower concentrations of are used. As the concentration of NaH_2PO_4 increases, so does the degree of porosity within the chitosan films. Images taken with permission from *Adv. Funct. Mater.* 2019, 29, 1900065.[95] © 2019 WILEY-VCH Verlag GmbH & Co. KGaA, Weinheim (e) Images showing how complex patterns of chitosan hydrogels be formed within agarose hydrogels using triangular and circular electrodes. As the chitosan network is more stable to temperature treatment than the agarose network, heat can be used to dissolve the agarose hydrogel, leaving the chitosan hydrogel pattern intact. (f) Using a cathodic pen (acupuncture needle) the letters 'A' and 'B' were written in the chitosan/agarose blend hydrogels. The pink colour arises from the indicator phenolphthalein which was added to the chitosan/agarose solution to show high pH regions (g) Heat treatment was used to dissolve the agarose hydrogel and leave the chitosan 'A' and 'B' hydrogels. For e-g, images were taken with permission from *Adv. Funct. Mater.* 2018, **28**, 1803139. [91] © 2018 WILEY-VCH Verlag GmbH & Co. KGaA, Weinheim.

The cathodic deposition of chitosan can also be coupled with other biofabrication technologies such as printing. An example of this shows the electrodeposition of chitosan followed by printing the chitosan hydrogel film with 'ink' containing acidic sodium dodecyl sulfate (SDS) micelles.[100] The acidic nature of the ink protonates the chitosan film, inducing disassembly of the chitosan chains followed by the SDS micelles physically crosslinking the cationic chitosan molecules through electrostatic interactions. The combination of these two techniques created patterned films exhibiting anisotropic mechanical properties.

Using a two-step method electrofabrication method, Qu and co-workers created an antimicrobial chlorinated chitosan film by incorporating NaCl into chitosan solutions. Firstly, the chitosan hydrogel was electrodeposited on the cathode surface via hydrogen peroxide reduction. The chlorination of the chitosan was then achieved by biasing the electrode to an anodic voltage, which saw the oxidation of the chloride ions in solution to HClO. The reactive mediator HClO can then react covalently with chitosan's amine groups to form chloramine residues.[12] The chitosan films formed by this method showed a significant increase in mechanical strength in comparison to those created by cathodic deposition alone and could be peeled from the electrode surface. This alongside chitosan's antimicrobial properties meant this material met the criteria for a potential wound dressing. The films formed also showed much higher stability to acidic conditions which can be attributed to the strong covalent crosslinks present in the hydrogel film.

In 2019, Lei and co-workers[95] created asymmetric 'Janus' films using chitosan, with a dense bottom layer of chitosan and a top porous layer of chitosan and hydroxyl apatite (Hap) (Figure 1.9c-d). The top porous composite layer of chitosan and Hap provided a microenvironment to enhance osteogenic differentiation. To create these novel asymmetric films, a dense layer of chitosan was first deposited on the cathode surface using the electrochemical reduction of hydrogen peroxide, producing hydroxide ions at the electrode surface to neutralise the cationic amine groups present on the chitosan backbone, forming a dense hydrogel. On top of these dense chitosan films, a porous chitosan-Hap layer was fabricated by the addition of the soluble salt NaH_2PO_4 to the deposition solution. The addition of NaH_2PO_4 to the deposition solution resulted in the formation of an interconnected porous top layer, as the salt screens the interchain electrostatic repulsions of the protonated chitosan chains and the imposed electric field. The properties of the porous layer such as pore distribution and pore size could be precisely controlled by varying the salt concentration. To study the osteogenesis capacity of the Janus films, the films were implanted into the skulls of mice with two calvarial defects. In comparison to the other three

control groups, the Janus composite films showed the most effective new bone formation, promoting prolonged and earlier osteogenesis.

1.6.1.2 Collagen

Collagen is the main structural protein in the ECM (extracellular matrix).[101] Like chitosan, collagen-based materials are non-toxic, biocompatible and biodegradable.[102] Collagen is capable of becoming anionic or cationic (i.e., it is ampholytic) depending on the pH of its environment, whereas chitosan is neutral at one extreme and charged at the other. The fabrication of collagen materials is different from chitosan as it employs an electric field to drive the migration/alignment of collagen molecules instead of applying an electrical current and forming a material solely at the electrode surface.[102]

Typically, collagen gels are fabricated by adding phosphate-buffered saline (PBS) to a solubilised collagen solution which neutralises the pH and promotes fibrillogenesis after a period of incubation.[103] Isometrically compacted collagen gels are constructed by applying an electric field to an aqueous collagen solution, inducing the electrolysis of water molecules which creates differing pH gradients at opposing electrodes (Figure 1.10). As collagen is ampholytic, this causes the isoelectric focusing of the molecules in solution, meaning the collagen molecules will migrate and accumulate at their isoelectric point forming dense electro-compacted (ECOM) collagen sheets.[102] This confers anisotropic order, mimicking native collagen and promotes fibrillogenesis within the collagen threads. Collagen gels created by this method showed a 5200-fold increase in in-plane tensile strength and a 2300-fold modular increase, making it comparable to native tendon strength.[102, 104]
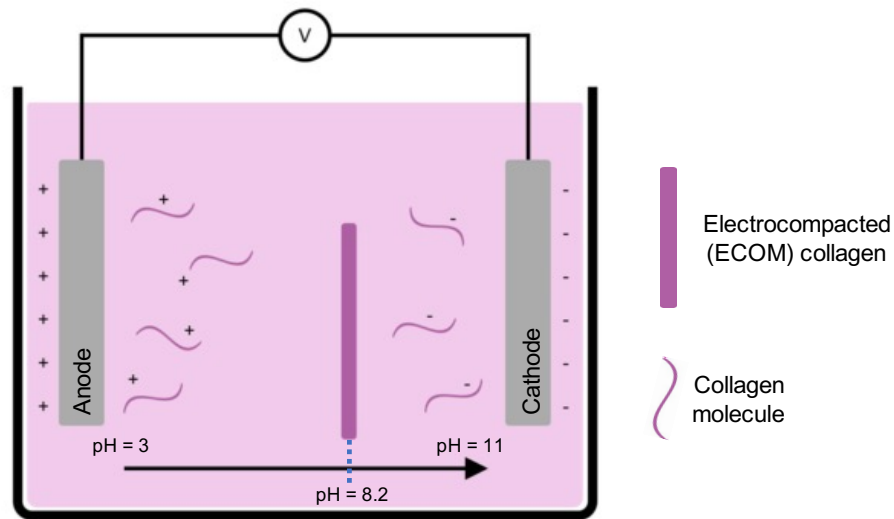
Figure 1.10 Schematic representing the formation of electro compacted (ECOM) collagen as shown in the work of Younesi et al.[102] The charged collagen molecules migrate towards their isoelectronic point (pH 8.2) when an appropriate current is applied to a solubilised collagen solution. This results in the formation of densely packed collagen sheets. Redrawn with permission from *Biofabrication*., 2015, **7**, 2. [102] © IOP Publishing. Reproduced with permission. All rights reserved.

Novel materials have been created using layer-by-layer assembly of ECOM collagen to construct 3D tissue and osteochondral scaffolds for ligaments, tendons and bones within minutes. Secondary nanoparticles and molecules can be incorporated into each layer such as hydroxyapatite which can be electrodeposited with collagen to create a scaffold with similar material properties to bone.[105] The increased stiffness of ECOM collagen sheets also saw a vast improvement in cell spreading, proliferation and adhesion.[102] However, cells cannot be added at the time of fabrication as the aqueous collagen solution is required to be salt-free and dialyzed before the electric field is generated. Studies have also incorporated polysaccharides and other key proteins such as elastin into electrochemically aligned collagen to construct bifunctional materials with many potential biomedical applications.[103]

1.6.1.3 Silk

Silk fibrous proteins extracted from silkworms and spiders are another biocompatible and biodegradable material that can form a hydrogel using electrochemical methods.[106] Silk hydrogel films are commonly formed by methods such as spin coating and solvent casting,

which can take up to several hours and require voltage potentials as high as >30 kV.[107, 108] The formation of silk electrochemical gels (e-gels) employs both an electrically fabricated pH gradient and weak electric fields.[109, 110] The electrogelation of silk employs a similar method to that seen in the fabrication of electro-compacted collagen gels. A current is applied to an aqueous silk fibroin solution which generates H^+ ions at the positive electrode and OH^- ions at the negative electrode. Silk has a relatively low isoelectric point (pI) of 4.2 due to the many acidic domains present in the protein structure. To induce the gelation of silk, the pH of the aqueous fibroin solution is decreased below the pI which results in the increased protonation of the acidic domains and the loss of its negative net charge. The reduction of the repulsive forces between adjacent proteins induces physical cross-links between the silk proteins and a sol-to-gel transition.[111] As silk fibroin has a negative net charge, the silk molecules migrate towards the positive electrode where the pH < pI, meaning gelation is governed by the formation of pH gradients and electric fields collectively.[109, 112] The electrogelation of silk fibroin has also been shown to be reversible, simply by reversing the polarity at the positive electrode.[108]

Omenetto and co-workers[92] have shown in their work that silk hydrogel films with high surface smoothness, varying 3D topologies and optical transparency can be created within 30 minutes using electrofabrication. This removes the secondary crystallisation step required in methods such as solvent casting and spin coating.[107] This method confers three-dimensionality and curvature by employing a closed-loop anode/positive electrode.[92] The chosen electrode geometry also overcame the common problem encountered in silk e-gels where oxygen bubbles formed at the anode became entrapped within the hydrogel. This results in inhomogeneity of the gel bulk properties, rendering them irreproducible with detrimental effects on the mechanical strength (weak regions within the gel).

The applications for this method extend to patient-specific engineered scaffolds, protein adhesives, drug delivery devices and biosensors with unconventional geometries. Other applications for deposited silk fibroin hydrogel films include drug-loaded orthopaedic implant coatings and e-gel coatings for titanium dental implants.[106, 113]

1.6.2 What is the need for multiple materials suitable for electrofabrication?

Materials generated by electrofabrication have a vast number of potential applications. Depending on the application, these materials must have specific and tailored mechanical properties. For example, in tissue engineering scaffolds, the implanted scaffold must possess a similar modulus and be able to withstand the applied pressure from the surrounding tissue

at the implanted site.[114] A review by Weaver et al.[115] describes the effect shear stress, hydrostatic pressure, compression and tension forces have on the response of cells within the matrix. There is a significant relationship between matrix rigidity and tissue phenotype. Weaver et al.[115] also show that the mechanical properties of the tissue can compromise cancer treatment and contribute to cancer progression. Therefore, the mechanical properties of the resultant mimetic or support material are highly important when choosing an appropriate material for a specific application. All the biocompatible hydrogels fabricated by electrofabrication mentioned above (chitosan, collagen, silk) have unique mechanical and chemical properties. As a result, a wide library of materials will be required alongside an extensive rheological analysis to apply them to various applications.

1.6.3 Electrofabrication of biologically derived gels versus synthetic dipeptide gels

It has been demonstrated that a wide range of *N*-protected dipeptide LMWG can be fabricated on an array of electrode surfaces, forming hydrogels of various morphologies and controllable mechanical properties.[79, 85, 116] These materials provide a synthetic alternative to biomaterials of natural origin, which have received a lot more attention and are much more established within the field. Hydrogels derived from biological sources such as chitosan, silk and alginate can mediate biocompatibility, often containing adhesion sites and essential cell cues within the gel network.[15] However, there are a number of limitations with these materials including lot-to-lot variation, higher risk of allergic reaction and the inability to finely tune the bulk mechanical properties. Batch-to-batch variation means these materials often have inconsistent chemical compositions, contamination and purity.[117] This often produces inconsistent results, losing the ability to finely tune the mechanical properties and produce reproducible materials, which is essential for drug testing and reliable research studies. Biologically sourced gelators can be purified, but this comes at an inflated cost and extra fabrication step.

Some of these issues can be overcome with synthetic gelators of defined chemical composition and tuneable mechanical properties. *N*-Protected dipeptide LMWGs are in general, easily synthesised, commercially available and chemically consistent. Therefore, these gelators do not suffer from batch-to-batch variation, forming highly reproducible hydrogels with defined chemical composition and easily tuned mechanical properties. Synthetic hydrogels can be tuned to mimic the mechanical strength of biological materials such as tissues. This is an essential feature when influencing cell differentiation, tissue development and homeostasis, with a direct correlation between matrix rigidity and tissue

phenotype.[97] However, biocompatibility for synthetic gelators is much more challenging than gelators derived from natural origin. To be used in biological applications, synthetic hydrogels must be formed without any cytotoxic materials and at a biocompatible pH. As *N*-protected dipeptide gelators are often triggered by extreme pH values and cytotoxic catechols, this can be difficult. The cell media in which hydrogels are placed for biological applications often contains salt buffers, antibiotics and glucose. This can alter the mechanical strength of the resultant materials, potentially negating the application they were designed for.

1.7 Localised self-assembly of LMWG on surfaces

As shown previously, electrofabrication can be used to induce the localised self-assembly of LMWGs on electrode surfaces to form hydrogels.[15, 85] This allows for the fabrication of spatially and temporally resolved hydrogels. As well as electrode surfaces, there are a number of techniques and chemical processes that can be used to induce the self-assembly of hydrogels on a variety of modified or unmodified surfaces depending on the application or desired material properties.[118, 119] This can be achieved by confining the self-assembly triggers to the vicinity of the surface, preventing any self-assembly or hydrogel formation from occurring in the bulk. Some of the techniques used to generate hydrogels directly at or near a surface include the localised hydrogelation of LMWGs via electrochemically generated pH/proton gradients[120], 'seeding' layers[121], electrostatic interactions[122], surface-confined enzymes,[123] acid catalysis[124] and hydrophobic/hydrophilic interactions.[125]

1.7.1 Seeding layers

The use of a 'seeding layer' to induce the localised self-assembly at a solid interface has been used by Cameron and co-workers[121] to grow thin hydrogel films of the LMWG Fmoc-LG on glass substrates (Figure 1.11). A thin seeding layer (80-100 nm thick) of Fmoc-LG was grown electrochemically on the electrode surface via the oxidation of hydroquinone to benzoquinone, which produces protons. The production of protons locally lowers the pH at the electrode surface below the pK_a of the Fmoc-LG molecules, which initiates their self-assembly. The thin gel layer that formed was subsequently used as the seeding layer and was placed in solutions of Fmoc-LG (pH = 7) for 48 hours. As a result, a thicker hydrogel layer (1-2 mm) grew outwards from the surface of the existing seeding layer throughout the 48-hours. In this study, they highlight two possible mechanisms that could be responsible for the growth of the thicker hydrogel film from the surface of the seeding layer. Firstly, they

hypothesise that the excess protons trapped within the electrochemically generated seeding layer slowly diffuse out of the seeding layer and into the Fmoc-LG solution. Thus, reducing the pH below the pK_a of the Fmoc-LG monomers at the seeding layer-solution interface to induce gelation from the seeding layer surface. Secondly, they draw on evidence that suggests the surface-induced pKa shift of the free Fmoc-LG monomers in solution, which would cause them to self-assemble at a higher pH value than their 'apparent' pK_a.
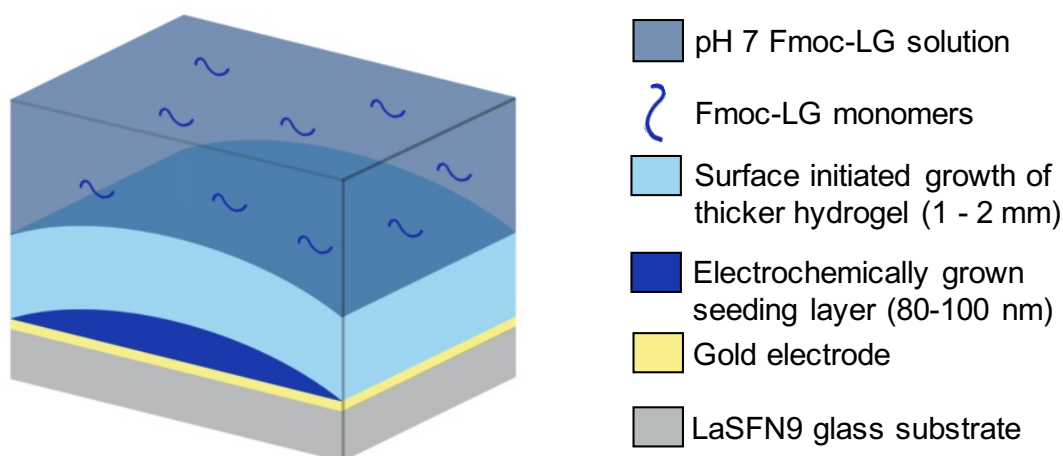
Figure 1.11 Schematic representation of the surface nucleated growth of Fmoc-LG hydrogels from electrochemically generated seeding layers. Image redrawn from *Chem. Commun.* 2013, **49**, 8698 with permission from the Royal Society of Chemistry.[121]

1.7.2 Surface confined enzymes

Over the last decade, using enzyme-instructed self-assembly to spatially control the localised growth of hydrogels has received notable attention and is particularly important for applications such as sensing and biocatalytic flow reactors.[126, 127] The use of enzymes as a gelation trigger is highly advantageous as it generally bestows the system with biocompatibility, high specificity and spatiotemporal control within cellular milieu.[128] Mai et al.[129] showed how enzymatic triggers can be used to confine gelation to the specific areas where the enzyme is immobilised by providing nucleation sites for self-assembly on the surface of urease-enzyme particles. The system exploits the autocatalytic reaction of the enzyme urease with urea which produces ammonia, subsequently reducing the local pH around the particle surface. In this work, urease-containing melon seed particles were suspended within an aqueous solution of urea and the water-soluble thiol and polyethylene glycol diacrylate (PEGDA) gelator. The autocatalytic reaction between the urease on the particle surface and urea in solution induces a propagating basic front from the particle

surface, triggering the polymerisation and growth of the thiol and PEGDA hydrogels exclusively on the particle.

1.7.3 Surface confined catalysts

The use of acidic surface confined catalysts is another strategy used to induce the localised self-assembly of hydrogels on an array of micropatterned surfaces. In 2014, van Esch[130] and co-workers used soft lithography to create micropatterns of sulfonic acid groups which were immobilised on glass surfaces (Figure 1.12). These patterned surfaces were then placed in solutions (pH 3-5) containing cyclohexane-1,3,5-tricarbohydrazide (**1**) and 3,4-bis[2-(2-methoxyethoxy) ethoxy] benzaldehyde (**2**) (Figure 1.12a). At this pH (3-5), the sulfonic acid groups are deprotonated ($pK_a = 1.4$) giving negatively charged sulfonic surfaces, leading to a localised increase in proton concentration at the patterned surface. The increased number of protons at the surface could then catalyse the condensation reaction of **1** with three molecules of **2** to produce the trishydrazone gelating molecule (**3**). This is seen in the formation of an array of precisely patterned hydrogel films of **3** with an excellent degree of spatiotemporal control.
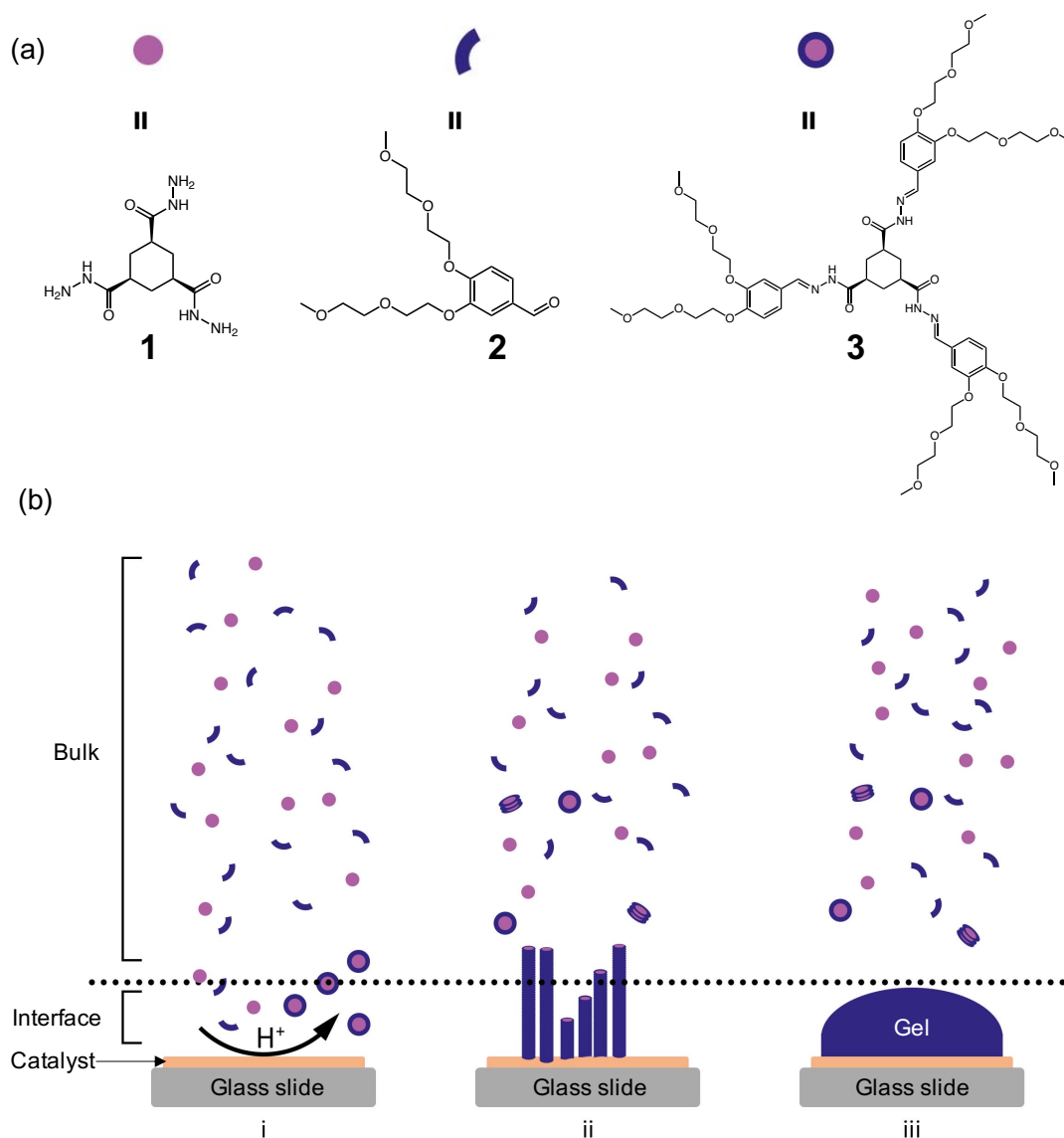
Figure 1.12 (a) Chemical structures of the insoluble trihydrazone gelating molecule (**3**) formed via the acid catalysed reaction of cyclohexane-1,3,5-tricarbohydrazide (**1**) and 3,4-bis[2-(2-methoxyethoxy) ethoxy] benzaldehyde (**2**) (b) Schematic representation of hydrogel formation of **3** on catalytic surfaces. (i) When the soluble building blocks of **1** and **2** come into contact with the catalytic surface (H$^+$ source), they form the insoluble gelating molecule (**3**). (ii) As the concentration of **3** surpasses the critical self-assembly concentration, a network of nanofibers begins to grow in a highly directional fashion, with their main axis perpendicular to the catalytic surface. (iii) When these fibers reach a certain concentration threshold, they form a supramolecular network that entraps the solvent, thus leading to hydrogel formation. Image redrawn with permission from *Angew. Chem. Int. Ed*. 2014, **126**, 4217.[130] © 2014 WILEY-VCH Verlag GmbH & Co. KGaA, Weinheim.

1.7.4 Surface charge or hydrophobic/hydrophilic balance

Another strategy that can be used to confine the self-assembly of hydrogels to surfaces is the adjustment of the surface charge or hydrophobicity/hydrophilicity balance. As a lot of gelator molecules present charged or hydrophobic/hydrophilic groups within their structure, tuning the surface properties can therefore be used to favour the attachment of the gelator molecules to the surface, often forming hydrogels at concentrations much lower than their minimum gelation concentrations. Yang and co-workers[131] prepared positively charged surfaces by modifying thin glass plates with (3-aminopropyl)triethoxysilane (APTES). The modified glass surfaces were then placed in solutions of the peptide based pro-gelator NBD-FFpY and the enzyme phosphatase. Incorporating the enzyme phosphatase converted the terminal phosphate group of NBD-FFpY to the corresponding phenol, giving the negatively charged gelator molecule NBD-FFY. This led to the successful surface-induced hydrogelation of NBD-FFY via electrostatic interactions of the positively charged surface and the negatively charged gelator molecule. It has also been shown that the surface's hydrophobicity/hydrophilicity balance has significant effects on the physical and mechanical properties of the attached hydrogels. In 2016, Angelerou et al.[132] also showed that hydrogels of the amphiphilic molecule C_{14} cytidine formed on hydrophilic (-OH presenting surface) and hydrophobic (-Ph presenting surface) surfaces displayed different fibre diameter and gel thickness due to alternation of the self-assembly kinetics. Thus, stressing the importance of the surface composition on the final properties of the hydrogel adhered to the surface.

1.8 Aim of the present study

The aim of this thesis is to understand the fabrication parameters and material properties of low molecular weight hydrogels formed on electrode surfaces via electrochemically generated pH gradients. To do this, we have used a wide array of material characterisation techniques to investigate the self-assembled structures across multiple length scales. Building upon previous knowledge, we employ the electrochemical oxidation of hydroquinone to trigger the gelation of various tri and dipeptide LMWGs. As well as this, we report the first known example of electrodeposition for a LMWG using a basic pH gradient by employing the galvanostatic reduction of hydrogen peroxide.

In chapter 2, we describe the largest reported tri and dipeptide-based hydrogels formed on electrode surfaces via the electrochemical oxidation of hydroquinone. In this work, we demonstrate that there is an upper limit to how large these materials can grow and that the

choice of gelator has a profound effect on the final material properties. We also build and design a system that allows the fabrication process to be undertaken in an inert nitrogen atmosphere. Thus, allowing the use of longer deposition times and an overall increase in gelation efficiency. As well as this, we show how this system can be used to grow multi-layered hydrogels, with the layers displaying vastly different chemical and mechanical properties.

In chapter 3, we report the first known example of electrodeposition for a LMWG using an electrochemically generated basic pH gradient. Previous studies have used this method to form hydrogels on electrode surfaces using the biopolymer chitosan. By adding hydrogen peroxide to gelator solutions, the application of a galvanostatic current can be used to electrochemically reduce hydrogen peroxide to generate hydroxide ions at the electrode. Thus, creating a localised basic pH gradient at the electrode-gelator solution interface. This sees the formation of immobilised hydrogels on the electrode with excellent spatiotemporal control. Using this approach, we report the first example of electrodeposition for a LMWG and show how the material properties can be vastly improved by increasing the concentration of hydrogen peroxide in gelator solutions. We also show the simultaneous formation of two LMWGs at opposing pH extremes by coupling the fabrication process aforementioned and the electrochemical oxidation of hydroquinone described in chapter 2.

In chapter 4, we describe the electrofabrication of five carbazole-protected amino acid-based hydrogels via the electrochemical oxidation of hydroquinone. We also report the full to partial polymerisation of these pre-assembled hydrogels to form electrochromic polymers on the electrode surface. The primary self-assembled structures of these materials are then probed during the fabrication processes in real time using small-angle X-ray scattering. We present a novel SAXS set-up using a custom-built electrochemical cell that allows data to be acquired from the hydrogels growing in-situ and their subsequent polymerisation in perchloric acid.

Chapter 1

1.9 References

1. M. Bustamante-Torres, D. Romero-Fierro, B. Arcentales-Vera, K. Palomino, H. Magaña and E. Bucio, *Gels*, 2021, **7**, 182.
2. A. Totosaus, J. G. Montejano, J. A. Salazar and I. Guerrero, *Int. J. Food Sci. Technol.*, 2002, **37**, 589-601.
3. A. S. Hoffman, *Adv. Drug Deliv. Rev.*, 2002, **54**, 3-12.
4. A. Vintiloiu and J.-C. Leroux, *J. Control. Release*, 2008, **125**, 179-192.
5. A. C. Pierre and G. M. Pajonk, *Chem. Rev.*, 2002, **102**, 4243-4266.
6. G. Guzel Kaya and H. Deveci, *J. Ind. Eng. Chem.*, 2020, **89**, 13-27.
7. M. Wu, J. Chen, Y. Ma, B. Yan, M. Pan, Q. Peng, W. Wang, L. Han, J. Liu and H. Zeng, *J. Mater. Chem. A*, 2020, **8**, 24718-24733.
8. S. Mitura, A. Sionkowska and A. Jaiswal, *J. Mater. Sci. Mater. Med.*, 2020, **31**, 50.
9. L. Fiorillo and G. L. Romano, *Gels*, 2020, **6**, 48.
10. X. Zhou, P. Zhang, F. Zhao and G. Yu, *ACS Mater. Lett.*, 2020, **2**, 1419-1422.
11. E. M. Ahmed, *J. Adv. Res.*, 2015, **6**, 105-121.
12. X. Qu, H. Liu, C. Zhang, Y. Lei, M. Lei, M. Xu, D. Jin, P. Li, M. Yin, G. F. Payne and C. Liu, *Acta Biomater.*, 2018, **73**, 190-203.
13. X. Ding, H. Zhao, Y. Li, A. L. Lee, Z. Li, M. Fu, C. Li, Y. Y. Yang and P. Yuan, *Adv. Drug Deliv. Rev.*, 2020, **160**, 78-104.
14. G. R. Deen and X. J. Loh, *Gels*, 2018, **4**, 13.
15. J. Li, S. Wu, E. Kim, K. Yan, H. Liu, C. Liu, H. Dong, X. Qu, X. Shi, J. Shen, W. E. Bentley and G. F. Payne, *Biofabrication*, 2019, **11**, 032002.
16. B. V. Slaughter, S. S. Khurshid, O. Z. Fisher, A. Khademhosseini and N. A. Peppas, *Adv. Mater.,* 2009, **21**, 3307-3329.
17. C. Vasile, D. Pamfil, E. Stoleru and M. Baican, *Molecules*, 2020, **25**, 1539.
18. S.-k. Ahn, R. M. Kasi, S.-C. Kim, N. Sharma and Y. Zhou, *Soft Matter*, 2008, **4**, 1151-1157.
19. X.-Q. Dou and C.-L. Feng, *Adv. Mater.*, 2017, **29**, 1604062.
20. F. Stapleton, S. Stretton, E. Papas, C. Skotnitsky and D. F. Sweeney, *Ocul. Surf.*, 2006, **4**, 24-43.
21. A. H. Karoyo and L. D. Wilson, *Gels*, 2017, **3**, 1.
22. E. Cheng, Y. Xing, P. Chen, Y. Yang, Y. Sun, D. Zhou, L. Xu, Q. Fan and D. Liu, *Angew. Chem., Int. Ed.*, 2009, **48**, 7660-7663.
23. Y. Shao, H. Jia, T. Cao and D. Liu, *Acc. Chem. Res.*, 2017, **50**, 659-668.

24. A. Alexander, Ajazuddin, J. Khan, S. Saraf and S. Saraf, *J. Control. Release*, 2013, **172**, 715-729.

25. E. Palleau, D. Morales, M. D. Dickey and O. D. Velev, *Nat. Commun.*, 2013, **4**, 2257.

26. E. R. Draper and D. J. Adams, *Chem*, 2017, **3**, 390-410.

27. R. N. Mitra, D. Das, S. Roy and P. K. Das, *J. Phys. Chem. B.*, 2007, **111**, 14107-14113.

28. S. Panja and D. J. Adams, *Chem. Commun.*, 2019, **55**, 47-50.

29. J. Morris, J. Bietsch, K. Bashaw and G. Wang, *Gels*, 2021, **7**, 24.

30. L. Johnson, M. G. Faidra Angelerou, B. T. Surikutchi, S. Allen, M. Zelzer and M. Marlow, *Mol. Pharmaceutics*, 2019, **16**, 462-467.

31. P. Terech and R. G. Weiss, *Chem. Rev.*, 1997, **97**, 3133-3160.

32. S. Manchineella and T. Govindaraju, *ChemPlusChem*, 2017, **82**, 88-106.

33. X. Yang, G. Zhang and D. Zhang, *J. Mater. Chem.*, 2012, **22**, 38-50.

34. X. Du, J. Zhou, J. Shi and B. Xu, *Chem. Rev.*, 2015, **115**, 13165-13307.

35. R. G. Weiss, *J. Am. Chem. Soc.*, 2014, **136**, 7519-7530.

36. G. M. Whitesides, J. P. Mathias and C. T. Seto, *Science*, 1991, **254**, 1312-1319.

37. J. Raeburn and D. J. Adams, *Chem. Commun.*, 2015, **51**, 5170-5180.

38. E. R. Draper and D. J. Adams, *Langmuir*, 2019, **35**, 6506-6521.

39. A. D. Martin, J. P. Wojciechowski, H. Warren, M. in het Panhuis and P. Thordarson, *Soft Matter*, 2016, **12**, 2700-2707.

40. L. Li, L. Xie, R. Zheng and R. Sun, *Front.Chem.*, 2021, **9**, 739791.

41. L. Chen, S. Revel, K. Morris, L. C. Serpell and D. J. Adams, *Langmuir*, 2010, **26**, 13466-13471.

42. E. K. Johnson, D. J. Adams and P. J. Cameron, *J. Mater.Chem.*, 2011, **21**, 2024-2027.

43. S. Fleming and R. V. Ulijn, *Chem. Soc. Rev.*, 2014, **43**, 8150-8177.

44. A. Dasgupta, J. H. Mondal and D. Das, *RSC Adv.*, 2013, **3**, 9117-9149.

45. K. Tao, A. Levin, L. Adler-Abramovich and E. Gazit, *Chem. Soc. Rev.*, 2016, **45**, 3935-3953.

46. W. T. Truong, Y. Su, D. Gloria, F. Braet and P. Thordarson, *Biomater. Sci.*, 2015, **3**, 298-307.

47. C. Tang, A. M. Smith, R. F. Collins, R. V. Ulijn and A. Saiani, *Langmuir*, 2009, **25**, 9447-9453.

48. K. A. Houton, K. L. Morris, L. Chen, M. Schmidtmann, J. T. A. Jones, L. C. Serpell, G. O. Lloyd and D. J. Adams, *Langmuir*, 2012, **28**, 9797-9806.

49. P. Abiman, A. Crossley, G. G. Wildgoose, J. H. Jones, R. G. Compton, *Langmuir*, 2009, **25**, 7768-7768.

50. A. Z. Cardoso, L. L. E. Mears, B. N. Cattoz, P. C. Griffiths, R. Schweins and D. J. Adams, *Soft Matter*, 2016, **12**, 3612-3621.

51. E. R. Draper, H. Su, C. Brasnett, R. J. Poole, S. Rogers, H. Cui, A. Seddon and D. J. Adams, *Ang. Chem. Int. Ed.*, 2017, **56**, 10467-10470.

52. L. Chen, T. O. McDonald and D. J. Adams, *RSC Adv.*, 2013, **3**, 8714-8720.

53. K. McAulay, L. Thomson, L. Porcar, R. Schweins, N. Mahmoudi, D. J. Adams and E. R. Draper, *Org. Mater.*, 2020, **02**, 108-115.

54. C. Colquhoun, E. R. Draper, R. Schweins, M. Marcello, D. Vadukul, L. C. Serpell and D. J. Adams, *Soft Matter*, 2017, **13**, 1914-1919.

55. V. Jayawarna, M. Ali, T. A. Jowitt, A. F. Miller, A. Saiani, J. E. Gough and R. V. Ulijn, *Adv. Mater.*, 2006, **18**, 611-614.

56. A. Mahler, M. Reches, M. Rechter, S. Cohen and E. Gazit, *Adv. Mater.,* 2006, **18**, 1365-1370.

57. Z. Yang, G. Liang and B. Xu, *Acc. Chem. Res.,* 2008, **41**, 315-326.

58. R. Vegners, I. Shestakova, I. Kalvinsh, R. M. Ezzell and P. A. Janmey, *J. Pept. Sci.*, 1995, **1**, 371-378.

59. M. E. Roth-Konforti, M. Comune, M. Halperin-Sternfeld, I. Grigoriants, D. Shabat and L. Adler-Abramovich, *Macromol. Rapid Commun.*, 2018, **39**, 1800588.

60. K. Sipa, K. Kowalewska, A. Leniart, A. Walcarius, G. Herzog, S. Skrzypek and L. Poltorak, *Electrochem. Commun.,* 2021, **123**, 106910.

61. J. Raeburn, A. Zamith Cardoso and D. J. Adams, *Chem. Soc. Rev.*, 2013, **42**, 5143-5156.

62. F. Tantakitti, J. Boekhoven, X. Wang, R. V. Kazantsev, T. Yu, J. Li, E. Zhuang, R. Zandi, J. H. Ortony, C. J. Newcomb, L. C. Palmer, G. S. Shekhawat, M. O. de la Cruz, G. C. Schatz and S. I. Stupp, *Nat. Mater.*, 2016, **15**, 469-476.

63. A. K. Patterson and D. K. Smith, *Chem.Commun.*, 2020, **56**, 11046-11049.

64. E. R. Draper and D. J. Adams, *Chem.Commun.*, 2016, **52**, 8196-8206.

65. H. M. D. Bandara and S. C. Burdette, *Chem. Soc. Rev.*, 2012, **41**, 1809-1825.

66. M. J. Clemente, R. M. Tejedor, P. Romero, J. Fitremann and L. Oriol, *New J. Chem.,* 2015, **39**, 4009-4019.

67. B. P. Nowak and B. J. Ravoo, *Soft Matter*, 2020, **16**, 7299-7304.

68.   A. M. Fuentes-Caparrós, Z. Canales-Galarza, M. Barrow, B. Dietrich, J. Läuger, M. Nemeth, E. R. Draper and D. J. Adams, *Biomacromolecules*, 2021, **22**, 1625-1638.

69.   J. Raeburn, C. Mendoza-Cuenca, B. N. Cattoz, M. A. Little, A. E. Terry, A. Zamith Cardoso, P. C. Griffiths and D. J. Adams, *Soft Matter*, 2015, **11**, 927-935.

70.   R. Huang, W. Qi, L. Feng, R. Su and Z. He, *Soft Matter*, 2011, **7**, 6222-6230.

71.   M. Zelzer, S. J. Todd, A. R. Hirst, T. O. McDonald and R. V. Ulijn, *Biomater. Sci.* 2013, **1**, 11-39.

72.   J. Hu, G. Zhang and S. Liu, *Chem. Soc. Rev.*, 2012, **41**, 5933-5949.

73.   J. W. Sadownik, J. Leckie and R. V. Ulijn, *Chem. Commun.*, 2011, **47**, 728-730.

74.   M. D. Segarra-Maset, V. J. Nebot, J. F. Miravet and B. Escuder, *Chem. Soc. Rev.*, 2013, **42**, 7086-7098.

75.   A. R. Hirst, S. Roy, M. Arora, A. K. Das, N. Hodson, P. Murray, S. Marshall, N. Javid, J. Sefcik, J. Boekhoven, J. H. van Esch, S. Santabarbara, N. T. Hunt and R. V. Ulijn, *Nat. Chem.*, 2010, **2**, 1089-1094.

76.   Z. Yang, H. Gu, D. Fu, P. Gao, J. K. Lam and B. Xu, *Adv. Mater.* 2004, **16**, 1440-1444.

77.   P. K. Vemula, G. A. Cruikshank, J. M. Karp and G. John, *Biomaterials*, 2009, **30**, 383-393.

78.   J. Raeburn, T. O. McDonald and D. J. Adams, *Chem. Commun.*, 2012, **48**, 9355-9357.

79.   J. Raeburn, B. Alston, J. Kroeger, T. O. McDonald, J. R. Howse, P. J. Cameron and D. J. Adams, *Mater. Horiz.*, 2014, **1**, 241-246.

80.   H. Svobodová, Nonappa, Z. Wimmer and E. Kolehmainen, *J. Colloid Interface Sci.*, 2011, **361**, 587-593.

81.   E. R. Draper, L. L. E. Mears, A. M. Castilla, S. M. King, T. O. McDonald, R. Akhtar and D. J. Adams, *RSC Adv.*, 2015, **5**, 95369-95378.

82.   D. J. Adams, M. F. Butler, W. J. Frith, M. Kirkland, L. Mullen and P. Sanderson, *Soft Matter*, 2009, **5**, 1856-1862.

83.   S. Toledano, R. J. Williams, V. Jayawarna and R. V. Ulijn, *J. Am. Chem. Soc.*, 2006, **128**, 1070-1071.

84.   B. P. Nowak, L. Schlichter and B. J. Ravoo, *Angew. Chem., Int. Ed.*, 2022, **61**, e202201791.

85.   E. R. Cross, *SN Appl. Sci.*, 2020, **2**, 397.

86.   Z. Yang, Z. Yuye, L. Houbin, D. Fuyuan and S. Xiaowen, *Curr. Med. Chem.,* 2019, **26**, 1-21.

87. K. Arcaute, B. K. Mann and R. B. Wicker, *Ann. Biomed. Eng.*, 2006, **34**, 1429-1441.

88. M. N. Cooke, J. P. Fisher, D. Dean, C. Rimnac and A. G. Mikos, *J. Biomed. Mater. Res. B,* 2003, **64B**, 65-69.

89. J. Li, C. Wu, P. K. Chu and M. Gelinsky, *Mater. Sci. Engi. R Rep.,* 2020, **140**, 100543.

90. K. Ino, F. Ozawa, N. Dang, K. Hiramoto, S. Hino, R. Akasaka, Y. Nashimoto and H. Shiku, *Adv. Biosyst.*, 2020, **4**, 1900234.

91. S. Wu, K. Yan, Y. Zhao, C.-C. Tsai, J. Shen, W. E. Bentley, Y. Chen, H. Deng, Y. Du, G. F. Payne and X. Shi, *Adv. Funct. Mater.*, 2018, **28**, 1803139.

92. J. E. Bressner, B. Marelli, G. Qin, L. E. Klinker, Y. Zhang, D. L. Kaplan and F. G. Omenetto, *J. Mater. Chem. B*, 2014, **2**, 4983-4987.

93. F. Ozawa, K. Ino, T. Arai, J. Ramón-Azcón, Y. Takahashi, H. Shiku and T. Matsue, *Lab Chip*, 2013, **13**, 3128-3135.

94. J. Li, D. Maniar, X. Qu, H. Liu, C.-Y. Tsao, E. Kim, W. E. Bentley, C. Liu and G. F. Payne, *Biomacromolecules*, 2019, **20**, 969-978.

95. M. Lei, X. Qu, H. Liu, Y. Liu, S. Wang, S. Wu, W. E. Bentley, G. F. Payne and C. Liu, *Adv. Funct. Mater.*, 2019, **29**, 1900065.

96. Z. Jin, G. Güven, V. Bocharova, J. Halámek, I. Tokarev, S. Minko, A. Melman, D. Mandler and E. Katz, *ACS Appl. Mater. Interfaces*, 2012, **4**, 466-475.

97. S. Ahadian, S. Yamada, J. Ramón-Azcón, M. Estili, X. Liang, K. Nakajima, H. Shiku, A. Khademhosseini and T. Matsue, *Acta Biomater.*, 2016, **31**, 134-143.

98. K. M. Gray, B. D. Liba, Y. Wang, Y. Cheng, G. W. Rubloff, W. E. Bentley, A. Montembault, I. Royaud, L. David and G. F. Payne, *Biomacromolecules*, 2012, **13**, 1181-1189.

99. Z. Geng, X. Wang, X. Guo, Z. Zhang, Y. Chen and Y. Wang, *J. Mater. Chem. B*, 2016, **4**, 3331-3338.

100. H. He, X. Cao, H. Dong, T. Ma and G. F. Payne, *Adv. Funct. Mater.*, 2017, **27**, 1605665.

101. M. D. Shoulders and R. T. Raines, *Annu. Rev. Biochem.*, 2009, **78**, 929-958.

102. M. Younesi, A. Islam, V. Kishore, S. Panit and O. Akkus, *Biofabrication*, 2015, **7**, 035001.

103. J. A. Uquillas, V. Kishore and O. Akkus, *Biomed. Mater.*, 2011, **6**, 035008.

104. M. Younesi, A. Islam, V. Kishore, J. M. Anderson and O. Akkus, *Adv. Funct. Mater.*, 2014, **24**, 5762-5770.

105. M. Kikuchi, *Biol. Pharm. Bull.*, 2013, **36**, 1666-1669.

106. C. Han, Y. Yao, X. Cheng, L. Jiaxin, P. Luo, Q. Wang, F. Yang, Q. Wei and Z. Zhang, *Biomacromolecules*, 2017, **18**, 3776-3787.

107. D. N. Rockwood, R. C. Preda, T. Yücel, X. Wang, M. L. Lovett and D. L. Kaplan, *Nat. Protoc.*, 2011, **6**, 1612-1631.

108. G. G. Leisk, T. J. Lo, T. Yucel, Q. Lu and D. L. Kaplan, *Adv. Mater.*, 2010, **22**, 711-715.

109. N. Kojic, M. J. Panzer, G. G. Leisk, W. K. Raja, M. Kojic and D. L. Kaplan, *Soft Matter*, 2012, **8**, 6897-6905.

110. Q. Lu, Y. Huang, M. Li, B. Zuo, S. Lu, J. Wang, H. Zhu and D. L. Kaplan, *Acta. Biomater.*, 2011, **7**, 2394-2400.

111. M. Floren, C. Migliaresi and A. Motta, *J. Funct. Biomater.,* 2016, **7**, 26.

112. T. Yucel, N. Kojic, G. G. Leisk, T. J. Lo and D. L. Kaplan, *J. Struct. Biol.,* 2010, **170**, 406-412.

113. R. Elia, C. D. Michelson, A. L. Perera, M. Harsono, G. G. Leisk, G. Kugel and D. L. Kaplan, *J. Biomater. Appl.*, 2015, **29**, 1247-1255.

114. S. Bhat and A. Kumar, *J. Biosci. Bioeng.*, 2012, **114**, 663-670.

115. D. T. Butcher, T. Alliston and V. M. Weaver, *Nat. Rev. Cancer*, 2009, **9**, 108-122.

116. C. Patterson, B. Dietrich, C. Wilson, A. R. Mount and D. J. Adams, *Soft Matter*, 2022.

117. H. Xiong, L. X. Yu and H. Qu, *AAPS PharmSciTech*, 2013, **14**, 802-810.

118. C. Vigier-Carrière, F. Boulmedais, P. Schaaf and L. Jierry, *Ang. Chem. Int. Ed.*, 2018, **57**, 1448-1456.

119. B. Yang, D. J. Adams, M. Marlow and M. Zelzer, *Langmuir*, 2018, **34**, 15109-15125.

120. R. Fernandes, L.-Q. Wu, T. Chen, H. Yi, G. W. Rubloff, R. Ghodssi, W. E. Bentley and G. F. Payne, *Langmuir*, 2003, **19**, 4058-4062.

121. E. K. Johnson, L. Chen, P. S. Kubiak, S. F. McDonald, D. J. Adams and P. J. Cameron, *Chem. Commun.*, 2013, **49**, 8698-8700.

122. A. M. Bieser and J. C. Tiller, *Chem. Commun.*, 2005, **31**, 3942-3944.

123. R. J. Williams, A. M. Smith, R. Collins, N. Hodson, A. K. Das and R. V. Ulijn, *Nat. Nanotechnol.*, 2009, **4**, 19-24.

124. Y. Wang, S. Oldenhof, F. Versluis, M. Shah, K. Zhang, V. van Steijn, X. Guo, R. Eelkema and J. H. van Esch, *Small*, 2019, **15**, 1804154.

125. Y. Liu, X.-D. Xu, J.-X. Chen, H. Cheng, X.-Z. Zhang and R.-X. Zhuo, *Colloids Surf., B,* 2011, **87**, 192-197.

126. V. Nele, J. P. Wojciechowski, J. P. K. Armstrong and M. M. Stevens, *Adv. Funct. Mater.,* 2020, **30**, 2002759.

127. N. Qureshi, B. A. Annous, T. C. Ezeji, P. Karcher and I. S. Maddox, *Microb. Cell Fact.,* 2005, **4**, 24.

128. Z. Zhang, S. Ai, Z. Yang and X. Li, *Adv. Drug Delivery Rev.*, 2021, **174**, 482-503.

129. A. Q. Mai, T. Bánsági, A. F. Taylor and J. A. Pojman, *Commun. Chem.*, 2021, **4**, 101.

130. A. G. L. Olive, N. H. Abdullah, I. Ziemecka, E. Mendes, R. Eelkema and J. H. van Esch, *Ang. Chem. Int. Ed.*, 2014, **53**, 4132-4136.

131. T. Xu, C. Liang, S. Ji, D. Ding, D. Kong, L. Wang and Z. Yang, *Anal. Chem.*, 2016, **88**, 7318-7323.

132. M. G. F. Angelerou, A. Sabri, R. Creasey, P. Angelerou, M. Marlow and M. Zelzer, *Chem. Commun.*, 2016, **52**, 4298-4300.

CHAPTER 2

The Electrofabrication of Large-Volume Di- and Tripeptide
Hydrogels *via* Hydroquinone Oxidation

This chapter is adapted in part from the following publication:

C. Patterson, B. Dietrich, C. Wilson, A. R. Mount, D. J. Adams

C. Wilson collected the X-ray crystallography measurements. Some of the molecules used in this chapter were synthesised by B. Dietrich, who also provided advice on the synthesis of other molecules. All other experiments were performed and collected by C. Patterson.

2.1 Introduction

Low molecular weight gelators (LMWGs) are small molecules that can self-assemble to form supramolecular hydrogels. Naphthalene-protected peptide gelator molecules are a class of LMWG known to self-assemble and form supramolecular hydrogels upon application of various external gelation triggers.[1-3] The structure of these LMWGs (Figure 2.1) are based around a naphthalene capping group on the *N*-terminus of the peptide.[4]
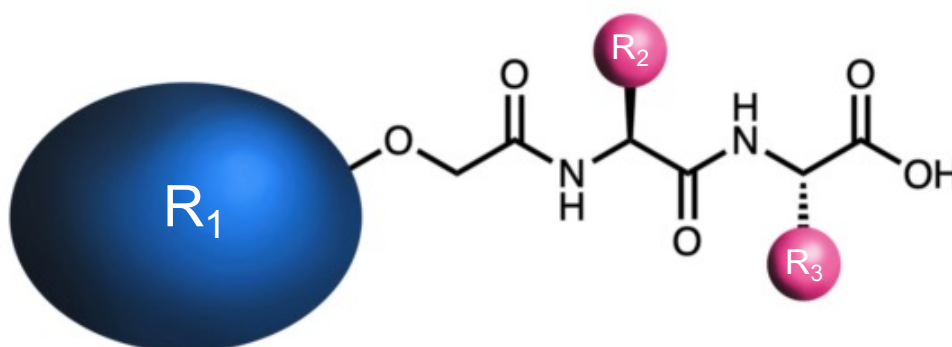
Figure 2.1 The general structure of naphthalene-protected peptide LMWG. R_1 = aromatic capping group, R_2 = amino acid, R_2 = amino acid.

The backbone of the gelator molecule consists of 2-3 amino acids and can be further functionalized by modifying the side chains with identical or different amino acids groups.[5] Finally, at the *C*-terminus of the molecule is the free carboxylic acid group. As *N*-protected peptide gelator molecules have a significant hydrophobic domain and charged head group, this renders them amphiphilic in nature.[6, 7] As a result, their solubility in water can be adjusted to trigger the self-assembly and gelation of *N*-protected peptide hydrogels.[8]

There are many examples where such LMWGs have been used to form gels by a change in pH.[9-11] One method used to trigger the self-assembly of *N*-protected LMWG using pH is electrodeposition, which is an electrochemical process that assembles solid or soft materials on electrode surfaces from ions or molecules in solution (see Chapter 1 for more details).[9-11] This technique has been used to form hydrogels, triggering the self-assembly of gelator molecules in solution upon application of an applied potential or electric field. Examples of

hydrogels fabricated using this method include various dipeptide gels[12], collagen[9], chitosan[13], silk[14], and alginate.[15] This approach has been used to self-assemble *N*-protected di and tri-peptide LMWG by electrochemically generating pH gradients at the electrode surface (Figure 2.2).[16, 17] By applying a direct potential or current to gelator solutions, a pH gradient can be generated at the electrode-solution interface. This can be achieved by exploiting various electrochemical acid-base or oxidation-reduction reactions.[10] The localised change in pH then initiates the self-assembly of the gelator molecules exclusively at the electrode surface with excellent spatiotemporal control over gelation. In many cases, this is due to the neutralisation of the pendant pH sensitive groups, removing the electrostatic repulsion between the charged groups on the gelator structure. As a result, the gelator molecules become less soluble in water and reduce their interactions with water by self-assembling to form the hydrogel network. An example of this at an acidic pH is the anodic-neutralisation reaction of *N*-protected dipeptide gelators via hydroquinone (HQ) oxidation (Figure 2.2).[18]
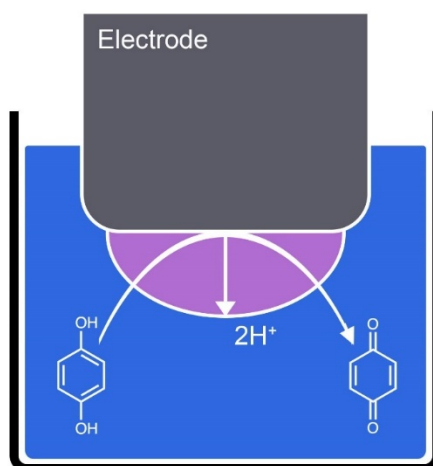
Figure 2.2 Schematic representation of electrochemical gelation via HQ oxidation. To trigger gelation, a constant current is applied to the electrode surface, electrochemically oxidising hydroquinone to benzoquinone which generates protons at the electrode-solution interface. As a result, the pH at the electrode surface decreases, resulting in gel formation on the electrode surface.

N-protected dipeptide gelators with free carboxylic acid groups on the *C*-terminus self-assemble via non-covalent interactions to form hydrogels when the pH drops below the pK_a of the terminal carboxylic acid. [19, 20] The electrochemical oxidation of hydroquinone (HQ) to benzoquinone (BQ) generates protons at the electrode-solution interface, creating a localised low-pH gradient at the electrode surface.[16, 18, 21] This causes the protonation of the charged carboxylate groups to form the neutral carboxylic acid in the proximity of the low-pH region. Therefore, gel formation occurs exclusively at the electrode surface. As a result, excellent spatiotemporal control over gelation is achieved while leaving the bulk of the gelator solution largely unaffected. This is one of the major benefits of this technique as the rate of gel growth, size, and thickness can be easily altered to suit the application, simply by changing the current and applied deposition time. The electrode material, size and geometry are also interchangeable, further widening the application range of the resultant hydrogels.[22]

A variety of *N*-protected peptide hydrogels have been fabricated using the electrochemical oxidation of HQ to form soft materials of various morphologies and sizes. Cameron and co-workers[23] first reported the surface nucleated growth of dipeptide gel membranes using this method, forming nanometre thick hydrogel films of the *N*-protected dipeptide Fmoc-LG. Using galvanostatic (constant current) conditions, the gel volume was found to increase with deposition time and the rate of gel growth from the electrode surface could be easily controlled by modifying the applied current. Cameron and co-workers[24] later showed that this method could be used to grow thin dipeptide layers on electrode surfaces, by placing seeding layers containing HQ in contact with dipeptide (Fmoc-LG) solutions for 24 hours (Figure 2.3a). Later, it was shown that it was possible to directly polymerise these electrochemically fabricated hydrogels to form microporous electrochromic polymers.[21]

The same electrochemical gelation approach was employed by Raeburn et al.,[18] growing millimetre thick dipeptide hydrogels of various chemical composition and size with excellent spatiotemporal control (Figure 2.3b-c). For these larger volume gels, increasing the current resulted in an increase in the rate of gel growth (Figure 2.3d) and a decrease in the pre-gelation lag time, which is the time taken for gelation to begin after the current has been switched on. In both cases, this was due to the increased rate of proton production at the electrode surface due to the higher current. Sequential assembly of two dipeptide LMWGs was also achieved (Figure 2.3i). By control of the current, the pH at the electrode-solution interface was first dropped to the pK_a of the first LMWG. This resulted in the assembly of the first LMWG while the other remained in solution. Increasing the current resulted in a

further drop in pH to the pK_a of the second LMWG, resulting in the self-assembly of this second LMWG in the presence of the gel formed from the first LMWG.[18]
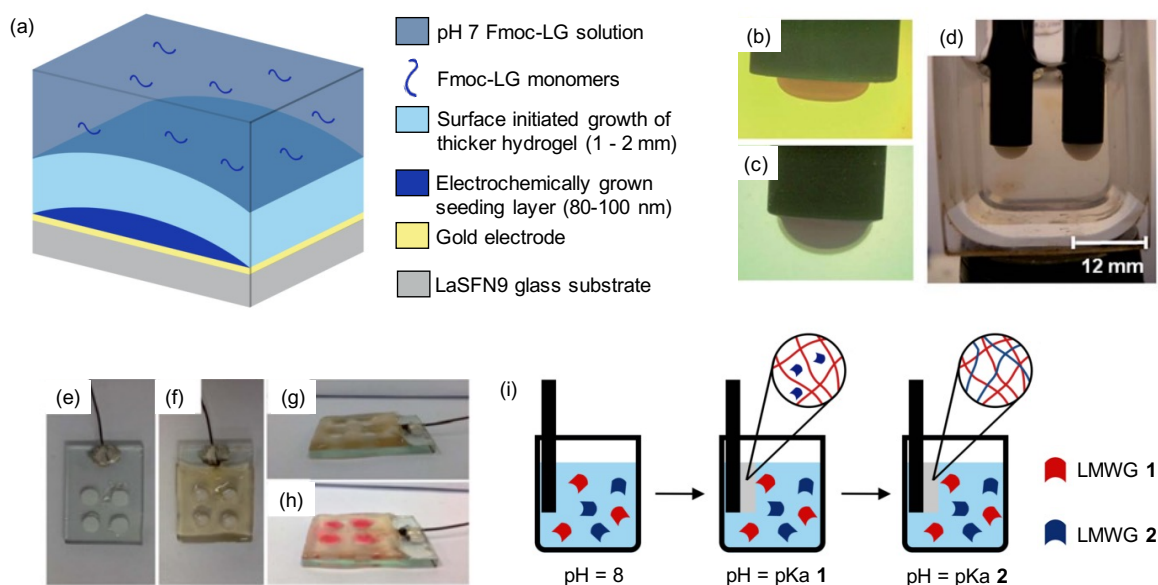
Figure 2.3 (a) Schematic representation of the surface nucleated growth of Fmoc-LG hydrogels from electrochemically generated seeding layers. Image reproduced from *Chem. Commun.* 2013, **49**, 8698 with permission from the Royal Society of Chemistry.[24] (b) Hydrogel of 6Br2NapFV grown via HQ oxidation on a glassy carbon electrode. Methyl red indicator was added to aid visualisation of the gel (low pH, pink) from the bulk solution (high pH, yellow) (c) A multi-layered gel was constructed by growing a second layer on top of the pre-existing gel of 6Br2NapFV (d) Two 6Br2NapFV gels were grown in parallel using different current rates of 10 μA (left) and 50 μA (right) (e) Non-conductive regions were created in FTO glass electrodes using four circular masks (f-g) Gel of 6Br2NapVF grown on masked FTO glass slide. No gel growth is observed on the masked non-conductive regions (h) GdL-triggered 6Br2NapVF hydrogels were formed in the non-conductive regions. Red dye was used to highlight the regions were the GdL gels were formed. (i) Schematic showing the sequential self-assembly of two LMWG from a multicomponent solution. As LMWG **1** has the highest pK_a, it self-assembles first when the pH is decreased while LMWG **2** remains in solution, giving hydrogels on electrodes solely composed of LMWG **1**. As the pH is decreased further, the pK_a of LMWG **2** is reached, triggering its self-assembly to give hydrogels composing of LMWG **1** and LMWG **2**. Image redrawn from *Mater. Horiz.* 2014, **1**, 245 with permission from the Royal Society of Chemistry.[18] Images b-h are reproduced from *Mater. Horiz.* 2014, **1**, 242-243 with permission from the Royal Society of Chemistry.[18]

Thus, temporal control of current resulted in temporal control of gelation. A variety of patterned hydrogels were also created on the electrode surface, further showing the versatility and practicality of this technique (Figure 2.3e-h). The electrochemical oxidation of HQ has also been used to successfully create peptide hydrogel-coated nanoelectrode biosensors, with the hydrogel allowing small biomarker molecules to diffuse through the gel matrix while simultaneously preventing biofouling.[25] Payne and co-workers[26] used this electrochemical method to form peptide hydrogels that act as temporary scaffolds for agarose hydrogels, which are widely used materials in biological sciences. A further study by Payne and co-workers[27] showed this could be performed within microfluidic channels, extending the potential of these materials to animal-on-a-chip applications.

All the work in this area has involved the formation of hydrogels on the nanometre to millimetre scales. Larger gel structures and their material properties have not yet been explored or reported. It has also been generally assumed that peptide hydrogels formed using this method have uniform mechanical properties and pH throughout, but due to the small scale on which these materials have been grown to date, this has not been determined. To investigate the maximum size to which these materials can grow, much longer deposition times are required. One of the most encountered problems with longer deposition times is the slow oxidation of HQ to BQ in air, as well as the formation of other quinhydrone species from various side reactions. This means some of the HQ is oxidised in solution before it can be consumed electrochemically, which inhibits the HQ electrochemical reaction and reduces gelation efficiency. This can be identified by the gelator/HQ solution turning a brown/red colour, indicating that the HQ has been oxidised to BQ or another quinhydrone species.

In this chapter, we report the formation of large gels formed from *N*-protected di- and tripeptides (around 3 cm^3 in size) via HQ oxidation and discuss the effect of size and time taken to grow the gels on their mechanical properties. To grow these electrochemically fabricated hydrogels to their maximum size, while simultaneously preventing the oxidation of HQ, we have used deposition times ranging from two to five hours under an inert nitrogen atmosphere. We also show this technique can be used to grow multi-layered hydrogels with vastly different chemical and material properties.

Chapter 2

2.2 Results and Discussion

2.2.1   Naphthalene-protected di and tripeptide gelator molecules

In this chapter, we focus on four naphthalene-protected di- and tripeptide gelators; **1**, **2**, **3** and **4** (Figure 2.4). These gelators were chosen as they were known to form self-supporting hydrogels under acidic conditions and were readily available for use.
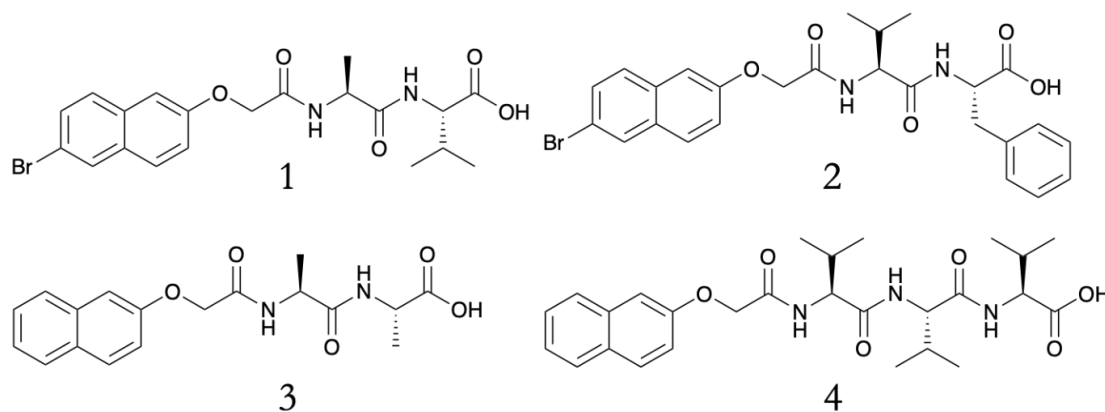
Figure 2.4 Chemical structures of the naphthalene-protected di and tripeptide gelator molecules **1**, **2**, **3** and **4** used throughout this chapter.

In all cases, we successfully grow hydrogels of pH 3-4 on electrode surfaces with excellent spatiotemporal control by applying a galvanostatic current to di- and tripeptide gelator solutions containing HQ (Figure 2.5). For **1**, **2**, **3** and **4**, gelator solutions were prepared at a concentration of 5 mg/mL and adjusted to pH 8 as HQ oxidation is accelerated above pH 10. To grow the hydrogels on electrode surfaces, 5 mg/mL of HQ was added to the gelator solutions immediately prior to gel deposition. For all gelators, deposition times of two to five hours were employed.
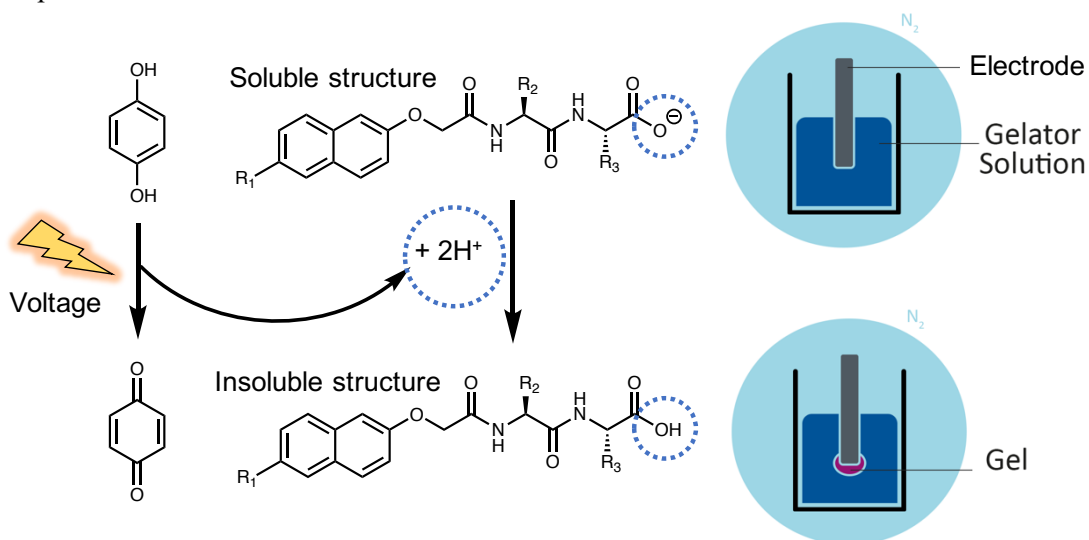
Figure 2.5 Schematic representation of electrochemical gelation via HQ oxidation. To prevent the oxidation of hydroquinone in air, the fabrication process is performed in an inert atmosphere using nitrogen.

2.2.2   Electrofabrication parameters

The three-electrode set up used to grow the gels consisted of a working electrode (glassy carbon), reference electrode (aq. 3 M Ag/AgCl) and counter electrode (platinum wire) (Figure 2.6).
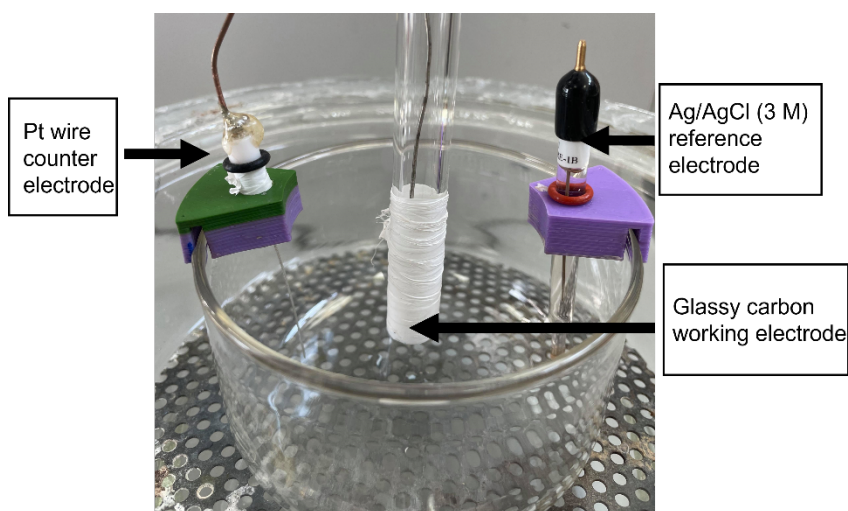
Figure 2.6 Electrochemical set-up used to electrochemically fabricate the *N*-protected peptide hydrogels via HQ oxidation. The three-electrode set-up consisted of a working electrode (glassy carbon), reference electrode (Ag/AgCl) and counter electrode (platinum wire). The set-up shown here was assembled within a degassed desiccator.

To ensure a satisfactory rate of gel growth by maintaining good gelation kinetics, a cyclic voltammogram (CV) (0.2 V/s) was taken of the HQ/gelator solution (Figure 2.7). A current value from the CV was then chosen to grow the gels using fast chronopotentiometry. Using this approach, a constant current density of 0.6 mA/cm^2 was chosen for **1**, **2** and **3**. For **4**, a current of 0.3 mA/cm^2 was applied. In all cases, a constant current was applied for five hours.
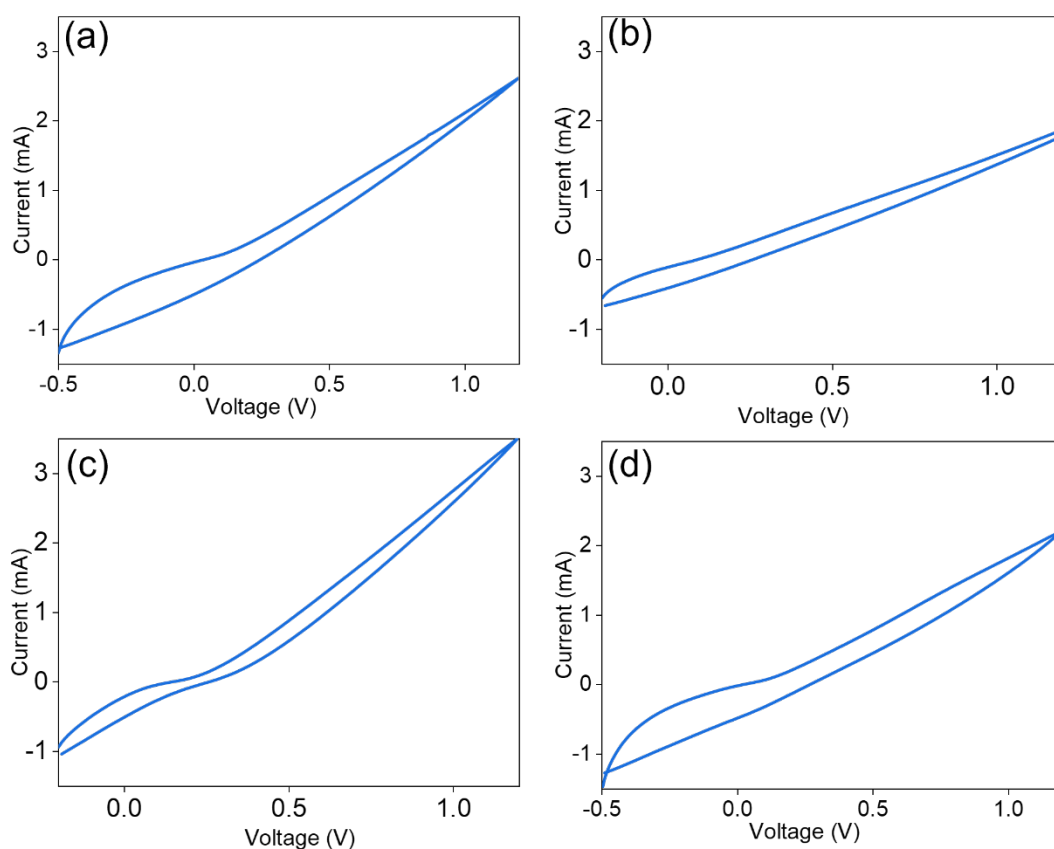
Figure 2.7 Cyclic Voltammograms of (a) **1** (b) **2** (c) **3** (d) **4**. Initial conditions [gelator] = 5 mg/mL, [HQ] = 5 mg/mL, [NaCl] = 0.1 M, [pH] = 8.

2.2.3 Electrofabrication in an inert atmosphere

Previous work within the Adams lab using this electrofabrication system has seen the formation of *N*-protected dipeptide hydrogels on a nanometre to millimetre scale.[18] Here, we show how this technique can be used to fabricate much larger materials of at least 3.35 cm^3 in size (Figure 2.8). As the size of the hydrogel is proportional to the deposition time (time of applied current), much longer deposition times are needed to fabricate larger hydrogels. Previously, this technique was performed on the benchtop, with the system open to the atmosphere. As HQ oxidises slowly in air, longer deposition times seen the oxidation of HQ in solution before it could be consumed electrochemically. This can be identified by the

gelator solution turning a red/brown colour. As we are attempting to use much longer deposition times in this work, we assembled a system that allowed us to perform the gel fabrication procedure under an inert atmosphere. To prevent the oxidation of HQ in air during the gel formation process, gelator/HQ solutions were deoxygenated under nitrogen for 30 minutes prior to each experiment. To grow the hydrogels under nitrogen, the deoxygenated gelator/HQ solutions were transferred to a desiccator that had been purged with nitrogen, which contained the three-electrode set-up used to grow the hydrogels. A desiccator was used as it could be fully deoxygenated prior to running the experiment. In theory, any air-tight container can be used.
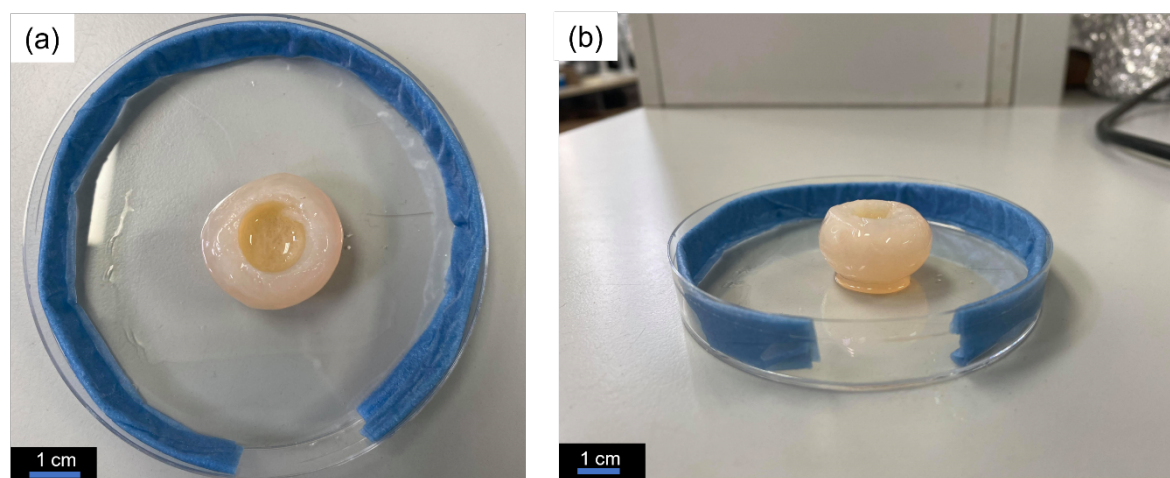
Figure 2.8 (a-b) Electrochemically grown hydrogels formed using **2**. To prevent the hydrogel drying out, wet tissue is placed around the edges of the petri dish. Reaction conditions: [**2**] = 5 mg/mL, [HQ] = 5 mg/mL, [NaCl] = 0.1 M, [starting pH] = 8, [current] = 0.6 mA/cm^2, [deposition time] = 5 hours.

2.2.4 Gel growth with time

When the current is applied to the gelator/HQ solutions, the local pH at the electrode surface drops due the oxidation of HQ, generating protons that diffuse away from the electrode surface into solution.[24] Previous studies have shown that gel area increases linearly with deposition time.[18] However, this has only been investigated for materials on the millimetre to nanometre scale. As a result, it was unknown if there was a maximum size these materials could grow to. The growth of the low pH region surrounding the electrode surface is likely governed by proton diffusion, with the size of this low pH zone limited to how far the protons

have diffused with time. To monitor the rate of gel growth with time, images of the hydrogels were taken at regular intervals (30 seconds) for the full deposition process (five hours). Unlike the other gelators, **2** does not form a translucent solution at 5 mg/mL, meaning we were unable to monitor gel growth in-situ with time. For **1**, **3** and **4**, images of the hydrogels at each interval were then uploaded to the image analysis software image ImageJ. The outline of the gel in each image was then traced, allowing the gel area to be calculated. Once the gel area of all the images were calculated, the rate of gel growth could be plotted. The hydrogels of **1**, **3** and **4** all showed the same growth trend, linearly increasing in area with deposition time before plateauing in size after a certain amount of time (Figure 2.9). For **1** and **3**, gels plateau in size at around two hours (Figure 2.9a-b). For **4**, a lower current value (0.3 mA/cm^2) was used to grow the hydrogels. As a result, three hours were needed to reach the plateau size (Figure 2.9c). As **2** does not form a translucent solution at 5 mg/mL, the plateau time could not be determined. For the purposes of this study, we assume **2** follows the same trend as **1** and **3**, plateauing after two hours as the same current value of 0.6 mA/cm^2 was used. In all cases, after five hours, gels of at least 3.35 cm^3 were fabricated (volume of gels was calculated manually immediately after gel deposition).
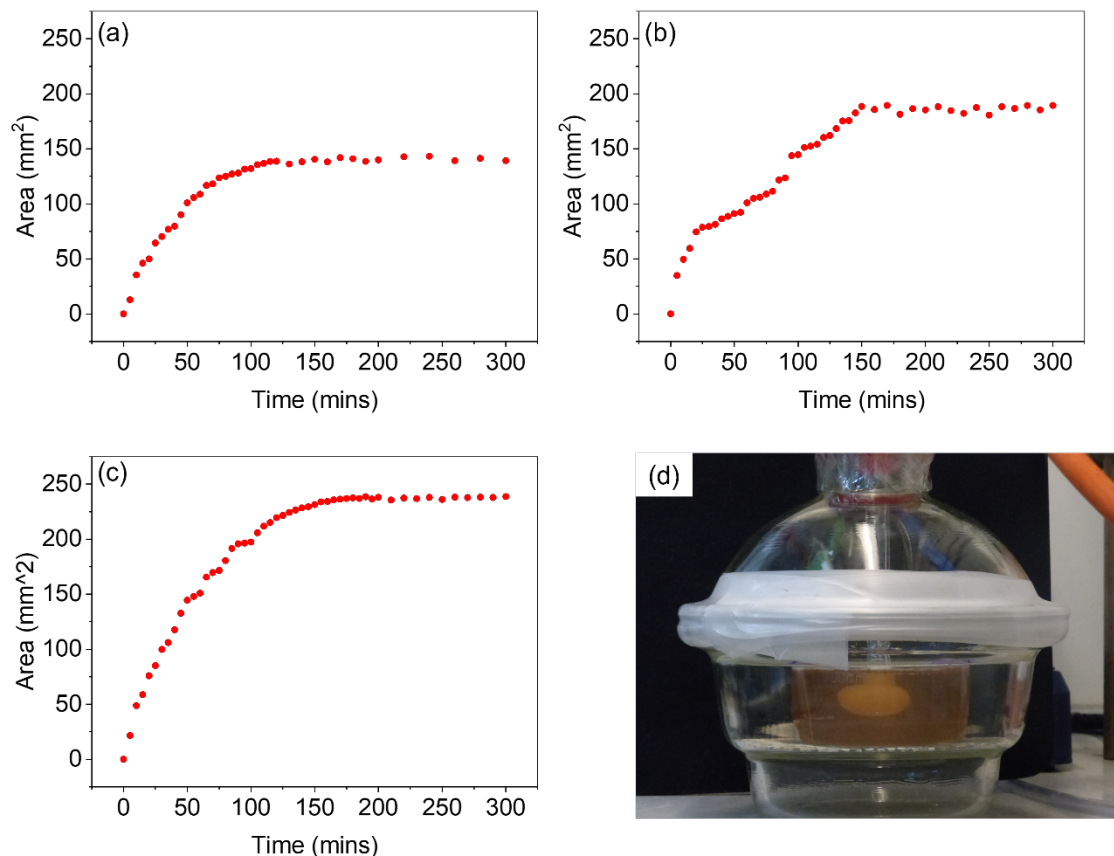
Figure 2.9 To monitor the rate of gel growth with time, images of the gels were taken at 30 second intervals for the entire deposition time (five hours). The area of the gels could then be plotted with time using the image processing program ImageJ (a-c) Shows the rate of gel growth with time for (a) **1**, (b) **3** and (c) **4**. (d) Image of the set-up used to grow the hydrogels in an inert nitrogen atmosphere with the gel attached to the electrode. The image is of gelator **3** at the end of the five-hour deposition process. Initial reaction conditions: [gelator] = 5 mg/mL, [HQ] = 5 mg/mL, [NaCl] = 0.1 M, [pH] = 8, [current] = 0.6 mA/cm², [deposition time] = 5 hours.

2.2.5 Rheological analysis

To determine the mechanical properties of the hydrogels fabricated from **1**, **2**, **3** and **4**, cavitation rheology was used. Due to the irregular shape of the gels formed using this technique, bulk rheology could not be used. Thus, cavitation rheology was used as a localized technique to probe the gels in their native environment.[28] To examine the mechanical properties using this technique, a syringe is lowered into the sample at a pre-defined depth. Air is then pumped through the syringe, forming a bubble within the sample. The critical pressure at which the bubble bursts can then be related to the elastic modulus of

the gel network, with higher critical pressures indicating a stiffer network. As this technique is localised, multiple measurements can be taken from the same sample. This is achieved by lifting the syringe out of the sample and repeating the measurement in another area. In all cases, three measurements were collected from each sample. The error was then calculated to show the standard deviation between the measurements. The first series of measurements were collected from the gels when they reached their plateau sizes. For **1**, **2**, **3**, this occurred after two hours. For **4**, three hours was needed to reach the plateau. The second measurements were then collected from the gels grown for five hours. This was the case for all gelators. Figure 2.10 shows that for **2** and **4**, the mechanical properties of the gels were identical at their plateau time and after five hours, giving very similar critical pressures as well as displaying very small variation between measurements. This indicates that there is little to no difference in the structural and mechanical properties of the gels collected at these times. It also suggests that the network underpinning the plateau and five-hour gel is the same as well as being homogenous throughout the sample. However, **1** and **3** show very different behaviour (Figure 2.10). In both cases, measurements taken from the five-hour samples show significantly higher critical pressure values when compared with the values collected at their plateau size. The three measurements collected from the five-hour gel also varied significantly, exhibiting much greater error within the sample. This indicates the gel network is inhomogeneous. Despite both gelators showing the same trend, we believe this behaviour is due to two separate phenomena, unique to each gel network.
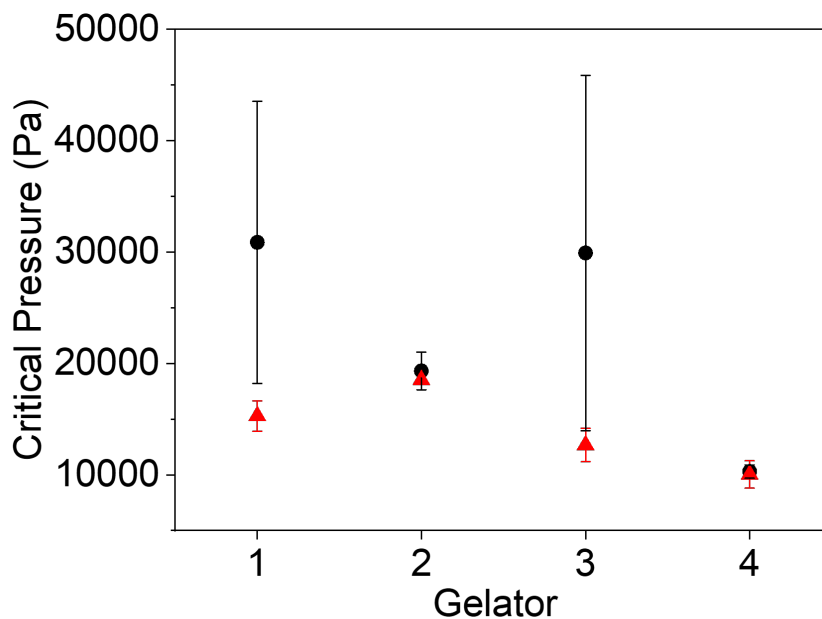
Figure 2.10 Cavitation rheology measurements of the electrochemically fabricated gels via HQ oxidation for gelators **1**, **2**, **3** and **4**. Measurements were taken from gels grown to their plateau size (red/triangle data) and gels grown for five hours (black/circle data). Measurements were performed in triplicate. Error bars show the standard deviation between measurements.

2.2.6 Behaviour of gelator 3

Giuri et. al. has shown that gels formed from **3** exhibit unusual ageing properties, undergoing a gel-to-crystal transition when triggered by certain concentrations of glucono-delta-lactone (GdL) (Figure 2.11a).[29] Their results show that the degree of crystallisation within the gel network increases with decreasing pH, driven by the excess protonation of the carboxylic acid groups on the gel network. Whilst here we use a different method to lower the pH, we hypothesised that the higher critical pressure values and variability seen for **3** were due to gel-to-crystal transitions. When the reaction was performed in the presence of bromophenol blue, the final gel was a uniform bright yellow indicating that the material has a homogenous pH of < 3 (Figure 2.11b). Giuri et al. report the gel-to-crystal transition occurs when the system drops below a pH of 4.1,[29] placing our gels within this pH range.
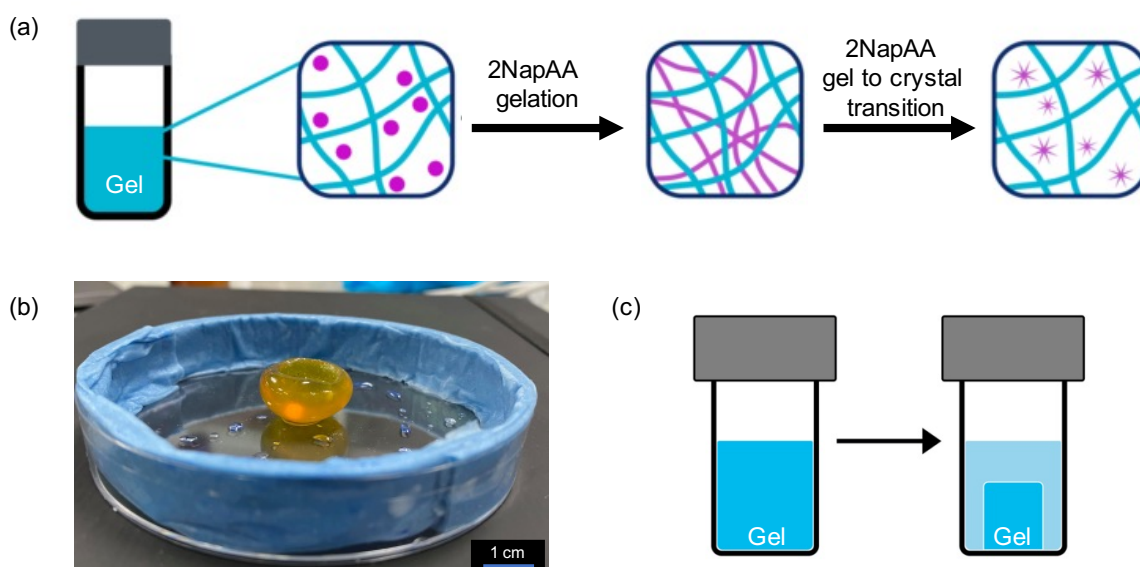
Figure 2.11. Schematic showing the sol-to-gel to-crystal transition of 2NapAA (pink) within 2NapFF hydrogels (blue). Redrawn from *Chem. Sci.* 2021, **12**, 9722 with permission from the Royal Society of Chemistry.[29] (b) Electrochemically grown hydrogel of **3** in the presence of bromophenol blue indicator. To prevent the hydrogel drying out, wet tissue is placed around the edges of the petri dish. Reaction conditions: [**3**] = 5 mg/mL, [HQ] = 5 mg/mL, [NaCl] = 0.1 M, [starting pH] = 8, [current] = 0.6 mA/cm^2, [deposition time] = 2 hours (c) Schematic showing the effect of syneresis on hydrogels.

2.2.6.1 pXRD

To confirm this gel-to-crystal transition, powder X-ray diffraction (pXRD) measurements were performed on gels formed from **3**. Measurements were taken from gels fabricated for two hours (i.e., at the point the gel reaches a plateau in volume) and after five hours. The pXRD data in Figure 2.12 show that after two hours an amorphous material is formed, with some weak peaks suggesting a small amount of crystalline material. In contrast to the two-hour sample, gels grown for five hours showed much sharper diffraction peaks, confirming substantially higher levels of crystalline material within the five-hour gel. As the degree of crystallisation increases with decreasing pH[29], this is to be expected. The application of current for longer times sees the prolonged production of protons at the electrode-solution interface, exposing the gel to a low pH environment for longer. As a result, the material has more time to undergo the gel-to-crystal transition. For the five-hour gels, these findings explain the high error and increased critical pressure values seen in the cavitation rheology data, with the increased level of crystalline material disrupting the homogenous gel network.
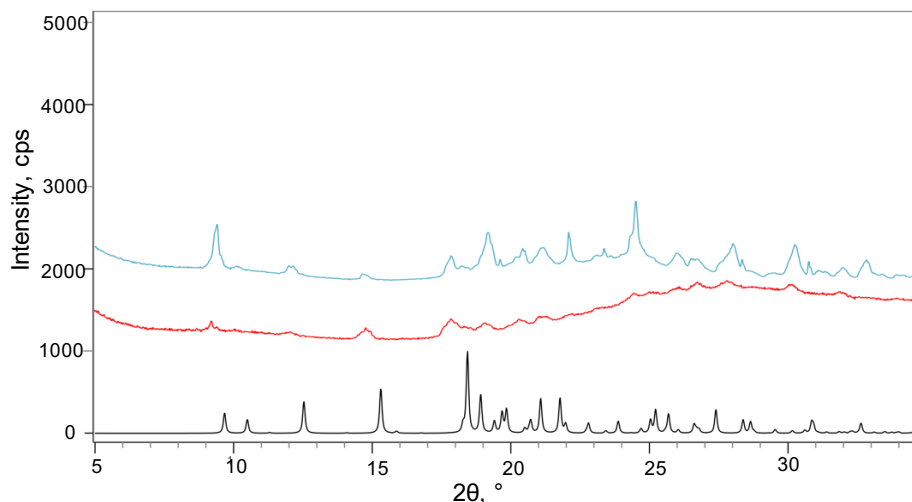
Figure 2.12 The calculated pXRD diffraction pattern of the room temperature single crystal structure of **3** (black data) and hydrogels grown from gelator **3** for two hours/plateau size (red data) and five hours (blue data).

2.2.7   Behaviour of gelator 1

For **1**, we believe a different ageing phenomenon is responsible for the increased critical pressure values and greater variability observed in the cavitation rheology data. Previous reports have shown that hydrogels of **1** undergo syneresis.[30] Syneresis causes the gel network to contract and shrink with time (Figure 2.11c).[31] For hydrogels formed from **1**, this is thought to be due to the removal of negative charge from the self-assembled structures, leading to hydrophobic interactions between the neutral fibres.[31] The contraction of the gel network results in the expulsion of water, leading to a denser, more compact network. This behaviour can usually be monitored using bulk rheology. However, due to the irregular shape of the gels formed using this technique, bulk rheology data could not be collected. The tendency for this material to behave in this way would explain the higher critical pressure values reported for the five-hour gels, as a denser, stiffer network would be present. As the gels grow, more gelator is needed to form the gels. After reaching a plateau in size, further changes may occur. Conceptually, this could be due to more gelator self-assembling within the pre- formed gel or by network stiffening as the pH changes, with no further gel formation.

2.2.7.1 Quantitative ^{1}H NMR

As bulk rheology could not be used, this behaviour was probed using quantitative ^{1}H NMR (qNMR). To determine the gelator concentration within the gels, gels fabricated from **1**, **2**, **3** and **4** were first freeze-dried at their plateau time and after five hours. ^{1}H NMR spectra were then collected of the freeze-dried gels in the presence of an external standard of known

concentration (1% PDMS in C_2Cl_4). The concentration of gelator within the gels could then be determined. The data shows that for **2**, **3** and **4**, the gelator concentration within the plateau and five-hour gels are very similar (Figure 2.13). The small difference is potentially due to the method used to select the plateau time. To track the rate of gel growth and determine the plateau time, a camera was set up in front of the electrode, capturing an image every 30 seconds. The outline of the gel in each image is then traced using ImageJ. This is used to determine the time the gel reaches a plateau in size. For **1**, there is a notable difference in concentration between the two gels, with the five-hour gel exhibiting a notably higher concentration of gelator in comparison with its plateau size gel. As mentioned previously, **1** has been shown to undergo syneresis with time.[30] This suggests that the gel network may be contracting and expelling water as it grows, causing it to shrink. As the gel does not visibly shrink in size, gel growth must continue in order to maintain its plateau size. This again shows that gel size is determined by proton diffusion, with the low pH region limited to a certain distance from the electrode surface. Consequently, this would account for the higher gelator concentration observed in the five-hour gel as the gel network becomes denser and more concentrated as it synereses, while simultaneously growing to maintain its plateau size.
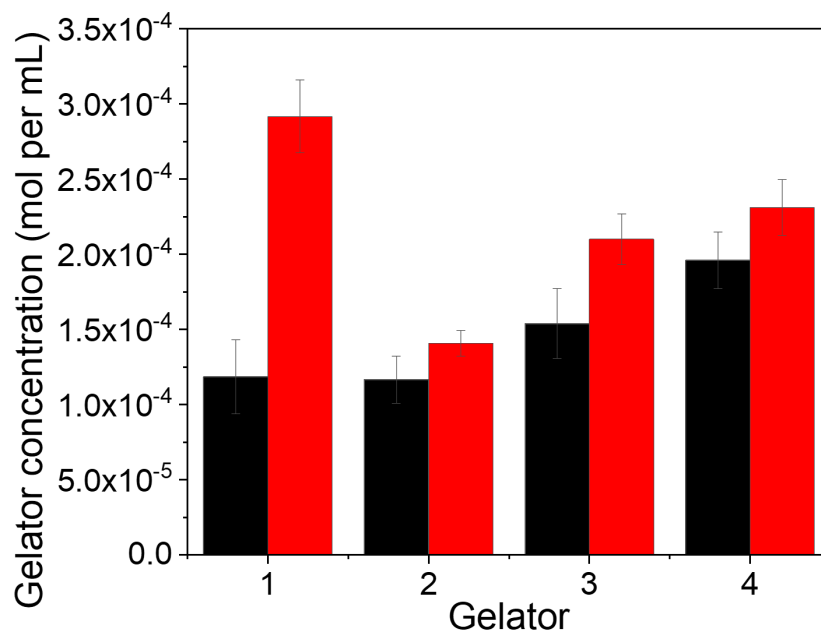
Figure 2.13 The relative gelator concentration of gelators **1**, **2**, **3** and **4** measured using quantitative ^{1}H NMR spectroscopy in DMSO-d^6. Measurements were taken from gels grown to their plateau size (red data) and gels grown for five hours (black data). Measurements were performed in triplicate. Error bars show the standard deviation between measurements.

2.2.8 Multi-layered gels from gelator molecules

An additional level of complexity was added by investigating multi-layered gels. As the gelators molecules **2** and **4** showed no unusual ageing properties, they were selected to grow the multi-layered hydrogel. As mentioned previously, gel area cannot be monitored in situ for **2**, as the solution at 5 mg/mL is not transparent. This meant gel growth could not be monitored in-situ for the multi-layered gels. As is the case for all the hydrogels in this chapter, gel fabrication was performed under an inert nitrogen atmosphere. To achieve this multi-layered gel structure, a gel core of **2** was grown for one hour at a current of 0.6 mA/cm^2 as is previously described (Figure 2.14a). The top of the desiccator was then removed and the electrode with gel attached was carefully placed to one side. The gelator solution of **2** was then drained, followed by rinsing the bowl thoroughly. The bowl was then secured back in the desiccator. The desiccator lid and electrode with the gel attached was then put back in position. The second degassed gelator solution of **4** was then immediately added to the desiccator bowl. A current of 0.6 mA/cm^2 was then applied for a further hour. After this time, the gel was carefully removed from the electrode surface with a spatula. Two distinct gel layers were formed within the structure, with the gel of **4** growing outwards from the surface of the pre-existing gel of **2** (Figure 2.14b-c). Visualisation of this was aided by adding universal indicator to the gelator solution of **4**. It is important to note that universal

indicator was not used when measuring the mechanical properties of the gel layers. A similar approach has been shown previously by Raeburn et al.[18], but with substantially smaller amounts of gel. Here, we can form much larger multi-layered gels.
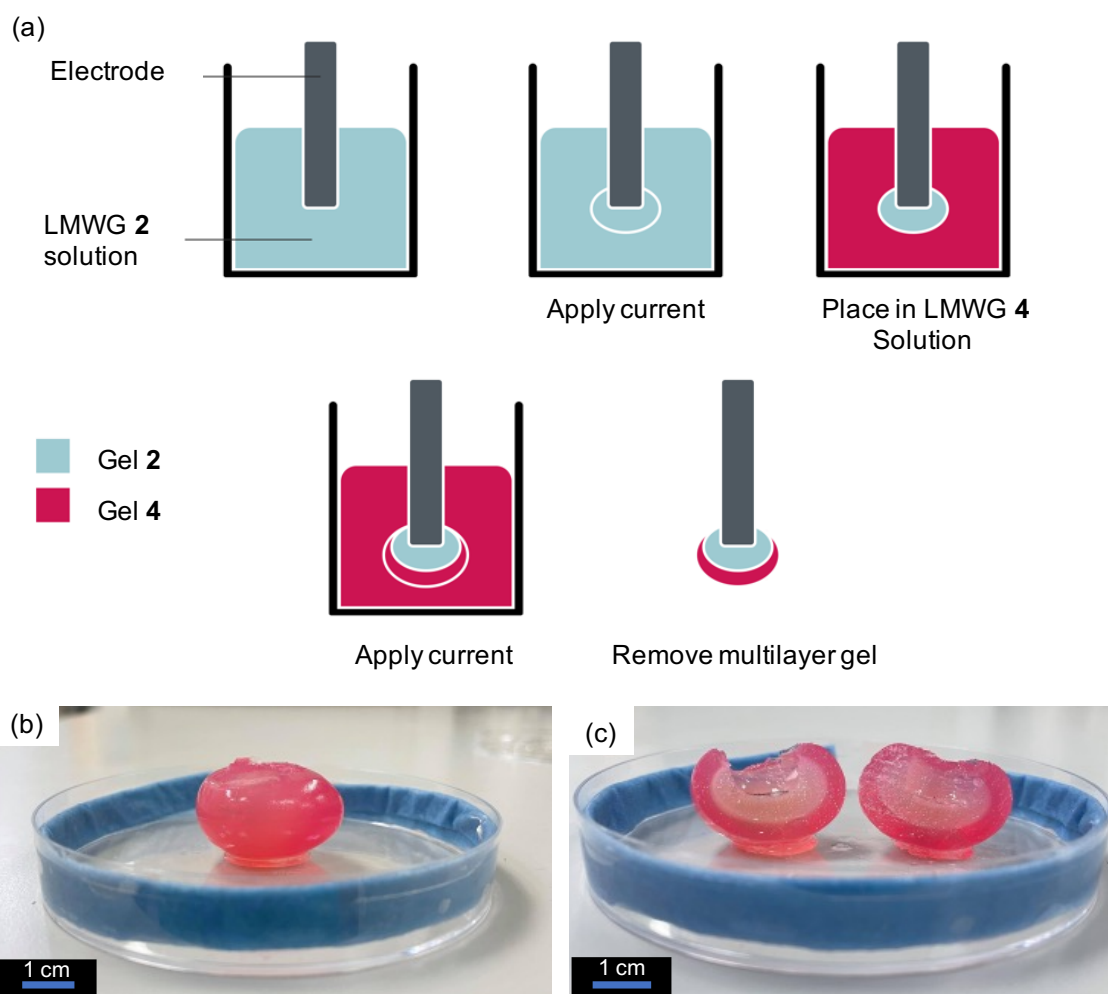
Figure 2.14 (a) Schematic representation of the electrochemical fabrication of multi-layered di- and tripeptide hydrogels via HQ oxidation (b) Image of the multilayer hydrogel immediately after it was removed from the electrode (c) cross section of the multi-layered hydrogel. In both cases (b-c) universal indicator was added to the second gelator solution to aid visualisation of the two gel layers. To prevent the hydrogel drying out, wet tissue is placed around the edges of the petri dish. Reaction conditions: [gelator] = 5 mg/mL, [HQ] = 5 mg/mL, [NaCl] = 0.1 M, [starting pH] = 8, [current] = 0.6 mA/cm^2, [total deposition time] = 2 hours.

As mentioned previously, there is a maximum distance over which protons can diffuse from the electrode surface, meaning there is a limit to how large these gels can grow. When the gel core of **2** was removed from its corresponding gelator solution and placed within the gelator solution of **4**, the acidic environment within the gel was retained. This is confirmed

by the stability of the gel when placed in the gelator solution of **4**. It is possible that there is some gel dissolution around the outside of the gel upon placing it in the pH 8 solution of **4.** However, turning on the current quickly re-establishes the acidic environment. Once the current is switched on protons can again diffuse away from the electrode surface, through the pre-existing gel and into the new gelator solution. This sees the formation of an outer gel layer which grows outwards from the edge of the preformed gel core of **2**.

2.2.8.1 ^{1}H NMR spectroscopy of the gel layers

To probe the chemical composition of the multi-layered gel, ^{1}H NMR spectra were generated from the freeze-dried sections of both layers (Figure 2.15). The spectra confirmed that each layer consisted of only their respective gelator as well as HQ and BQ generated during the fabrication process, showing that there is a well-defined interface between the layers. We hypothesise this is due to the micellar aggregates of the second gelator solution being too large to diffuse into the gel core. However, due to their much smaller size, protons can diffuse through the gel network and into the second gelator solution, allowing gel growth to continue. This means the second gelator cannot augment the inner layer.
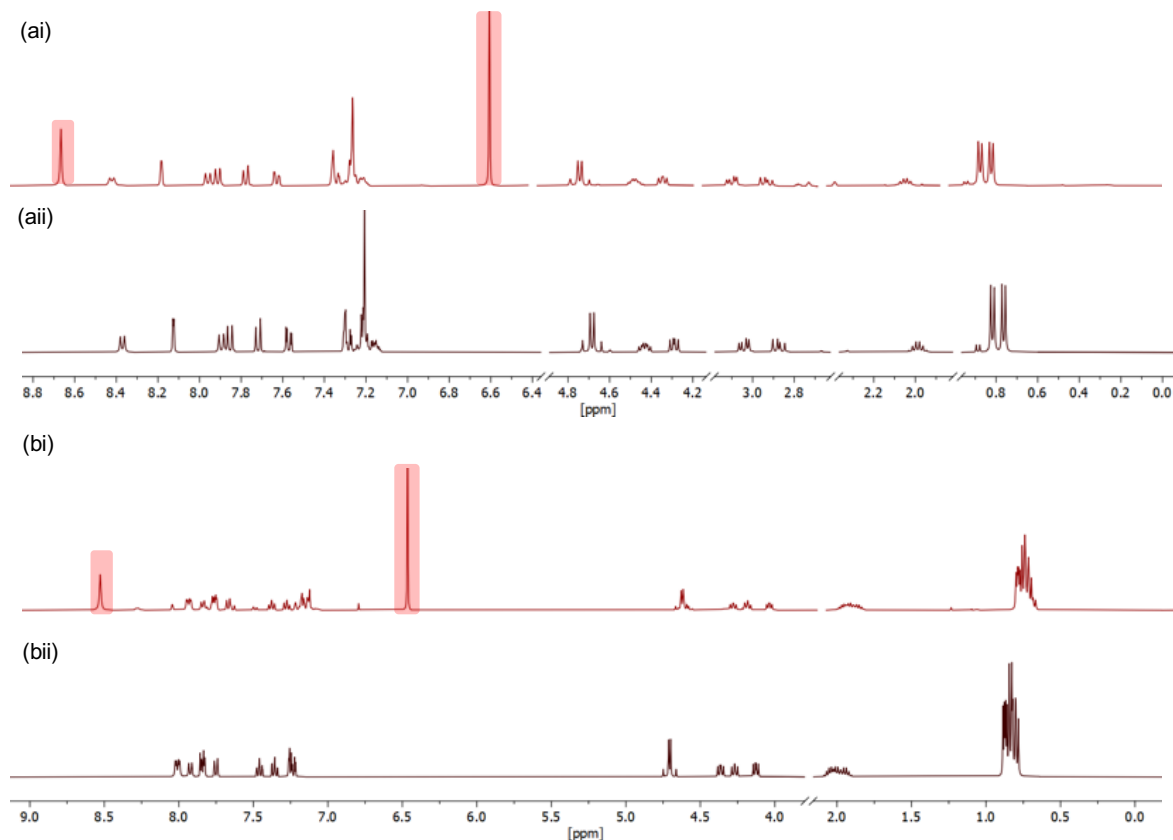
Figure 2.15 partial ^{1}HNMR spectra of the independent gel layers and compared with the partial spectra of the corresponding pure gelators in DMSO-d$_6$. This confirmed the gel layers consisted only of their respective gelators (ai) gel layer 1 of gelator **2** (aii) pure gelator **2** (bi) gel layer 2 of gelator **4** (bii) pure gelator **4**. Peaks corresponding to the HQ and BQ from the fabrication process are highlighted.

2.2.8.2 Rheological analysis of the gel layers

The mechanical properties of the gel layers were again investigated using cavitation rheology (Figure 2.16a). This was achieved by cutting a cross section from the gel to expose both the layers, followed by lowering the needle into the target layer (Figure 2.16b-c). To take measurements from each layer, the needle was moved and lowered into the target layer. It is important to highlight that the multi-layered material must be cut for the mechanical properties to be measured. Therefore, we focus on the trends observed rather than absolute values. Measurements taken from the gel layer of **2** gave significantly higher critical pressure values than the gel layer of **4**, producing a gel with two distinct regions of mechanical stiffness and chemical composition (Figure 2.16a). For this material, the **2** core is mechanically stiffer than the outer region containing **4**. To show that the mechanical and chemical properties of the gel layers are interchangeable, the fabrication process was repeated in reverse. To a solution of **4**, a current of 0.6 mA/cm^2 was applied for one hour, this time forming the core of the

multi-layered gel. The solution of **4** was then removed and replaced with the solution of **2**. Again, a current of 0.6 mA/cm^2 was applied for a further hour to fabricate the outer layer. The cavitation rheology data showed the same trend, with higher critical pressure values collected from the layer of **2** in comparison to the layer of **4**. This highlights the rheological and chemical properties within the material can be finely tuned, simply by interchanging the gelator solution.
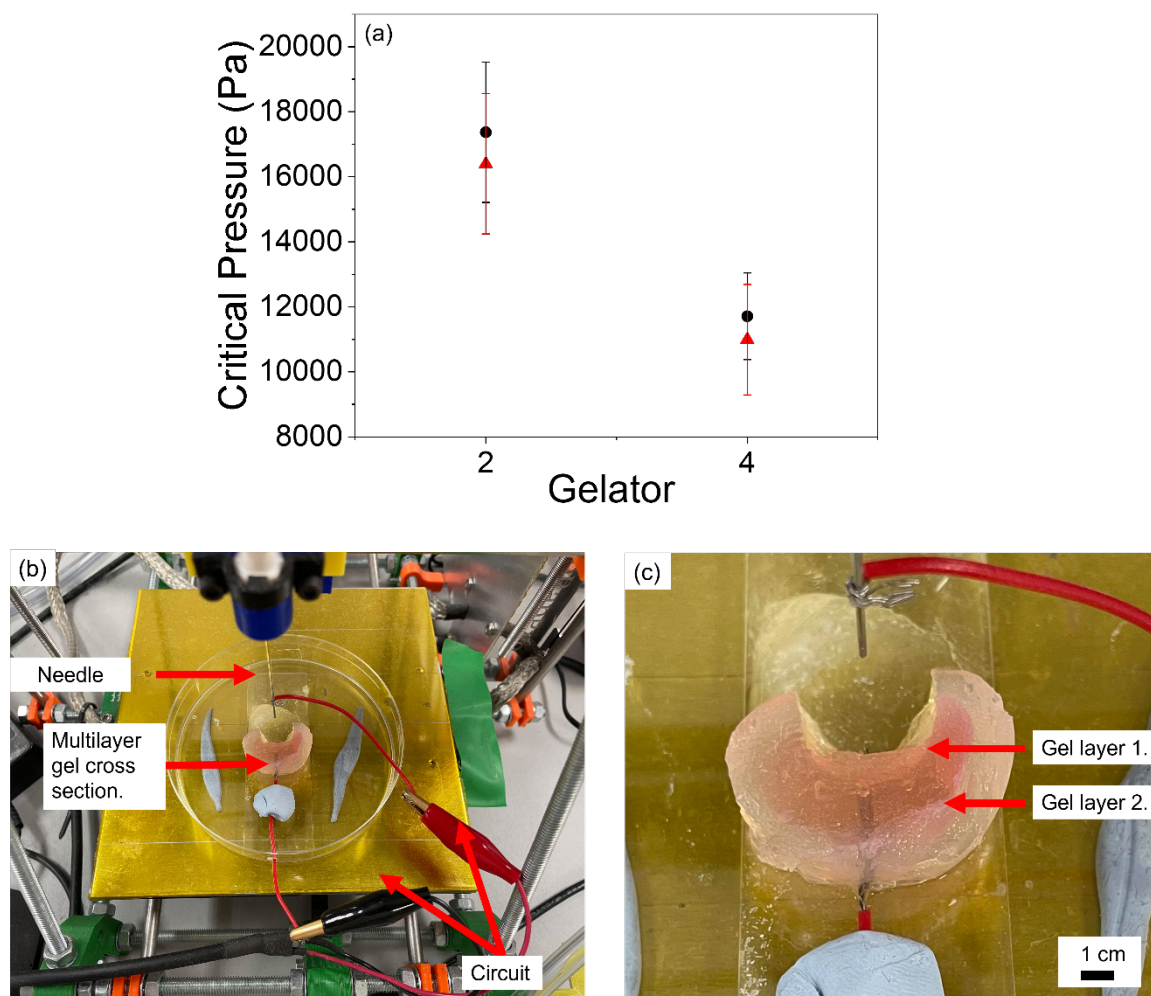
Figure 2.16 (a) Cavitation rheology measurements of the gel layers. Inner layer: gelator **2**, outer layer: gelator **4** (black/circle data). Inner layer: gelator **4**, outer layer: gelator **2** (red/triangle data). Measurements were performed in triplicate. Error bars show the standard deviation between measurements (b) Image showing how cavitation rheology measurements were collected from cross sections of the multi-layered hydrogel (c) Image showing the two distinct gel layers within the cross section of the multi-layered hydrogel.

2.3 Conclusions

In this chapter, we have shown that large hydrogels (of around 3-4 cm^3) of pH 3-4 can be grown on electrode surfaces via the electrochemical oxidation of HQ under an inert nitrogen atmosphere. All hydrogels showed the same trend, linearly increasing in volume until they plateaued in size. The mechanical properties of the plateau-sized gels and five-hour gels were investigated for all gelators. For gelators **2** and **4**, the mechanical properties of the five-hour gels and the plateau-sized gels were identical. Therefore, once this maximum size was reached, the gel network and their subsequent mechanical properties remained constant. For gelators **3** and **1**, the mechanical properties of the five-hour gels and the plateau-sized gels varied significantly. Using pXRD measurements we confirmed that gelator **3** undergoes a gel-to-crystal transition within the gel when the sample is exposed to a pH below 4.1. As the five-hour sample is exposed to a low pH environment for longer, increased crystalline material builds up within the gel in comparison to the two-hour sample. This means the mechanical stiffness of the five-hour sample is increased but not homogenously, leading to large intra-sample variation. The same trend was also observed for the five-hour sample of **1**. However, a different aging phenomenon called syneresis was found to be responsible which was examined using quantitative ^{1}H NMR spectroscopy. Finally, we have shown how this approach can be extended to growing multi-layered gels with varying mechanical and chemical properties, allowing for the easy fabrication of single and multicomponent materials with excellent spatiotemporal control.

All previous work within this area has focused on the fabrication of hydrogels on a nanometre to millimetre scales.[18, 21, 24, 25, 27] In this work, we successfully fabricate the largest reported di- and tri-peptide based hydrogels using this electrochemical method, employing deposition times of two to five hours. As much longer deposition times were required to grow hydrogels of this size, we built a system that could perform the fabrication process under an inert nitrogen atmosphere. Overcoming the oxidation of HQ in air, which occurs for this system when exposed to the atmosphere.

Due to the limited number of research groups investigating the electrofabrication of di- and tripeptide hydrogels, research within this area is in its preliminary stages. Through the work undertaken in this chapter we hope to have extended upon prior

research, providing a much deeper understanding of the fabrication parameters and characterisation of these systems than previously reported.

2.4 Experimental

2.4.1 Synthetic procedures

Materials

All chemicals and solvents were purchased from Sigma Aldrich and used as received. 2NapAA[1] (gelator **3**) and 6Br2NapAV[1] (gelator **1**) and were synthesized as previously described. Full synthesis of 2NapVVV (gelator **4**) and 6Br2NapVF (gelator **2**) are reported below. Deionized Milli-Q water was used consistently throughout every experiment.

2NapVVV (gelator 4) synthesis

Figure 2.17 Synthesis of 2NapVOMe

Iso-butyl chloroformate (5.18 mL, 40 mmol) and *N*-methylmorpholine (1 eq, 4.4 mL) were added to a suspension of 2-naphthoxyacetic acid (1 eq, 8.1 g) in chloroform (100 mL) at 0 °C using an ice-bath. This mixture was stirred for 20 minutes. A solution of L-valine methyl ester hydrochloride (1 eq, 6.71 g) and *N*-methylmorpholine (1 eq, 4.4 mL) in chloroform (100mL) was then added and the reaction was stirred overnight and allowed to warm to room temperature. After this time, the reaction mixture was diluted with chloroform and washed in turn with water (×2), 1M hydrochloric acid and brine. After drying over magnesium sulfate and evaporation *in vacuo*, the compound 2NapVOMe was obtained as a viscous orange oil (11.9 g, 89 %). This was used in the next step without further purification.

δ_H(400 MHz, DMSO-d_6): 8.39 (1H, d, *J* 8.3 Hz, NH), 7.87-7.22 (7H, m, HAro), 4.76 (1H, d, *J* 14.6 Hz, CH$_2$) 4.72 (1H, d, *J* 14.6 Hz, CH$_2$), 4.29 (1H, dd, *J* 8.3, 6.4, *CH), 3.65 (3H, s, OCH$_3$), 2.12 (1H, m, CH(CH$_3$)$_2$), 0.91 (3H, d, *J* 5.8 Hz, CH(CH$_3$)$_2$), 0.89 (3H, d, *J* 5.8 Hz, CH(CH$_3$)$_2$). δ_C (100 MHz, DMSO-d_6): 171.8, 167.9 (C=O), 155.7, 134.0, 129.3, 128.7, 127.5, 126.6, 126.5, 123.8, 118.6,107.2 (C$_{Aro}$), 66.5 (CH$_2$), 57.1 (*CH), 51.7 (OCH$_3$), 29.8 (CH(CH$_3$)$_2$), 18.9, 18.1 CH(CH$_3$)$_2$). HRMS (ESI) m/z: [M+Na]$^+$ accurate mass calculated for C$_{18}$H$_{21}$NNaO$_4$: 338.1363 Found: 338.1364.

Figure 2.18 Deprotection of 2NapVOMe

A solution of lithium hydroxide (4.73 g, 195 mmol) in water (120 mL) was added to a solution of 2NapVOMe (11.9 g, 39 mmol) in tetrahydrofuran (120 mL) and stirred vigorously for 30 minutes. The reaction was monitored using TLC (1:9 EtOAc:DCM). After this time, the TLC indicated the deprotection was complete. The reaction mixture was then poured into 1M hydrochloric acid (ca. 800 mL) and stirred for a further 20 minutes. The precipitate was filtered off and washed with several portions of water. Drying by azeotropic distillation with acetonitrile on a rotary evaporator, followed by keeping at 40 °C under vacuum overnight, afforded the compound 2NapVOH as a white solid (9.67 g, 86%). This was used in the next step without further purification.

δ_H(400 MHz, DMSO-d_6): 8.22 (1H, d, J, 8.6 Hz, NH), 8.14-7.24 (7H, m, H$_{Aro}$), 4.76 (1H, d, J 14.6 Hz, CH$_2$), 4.71 (1H, d, J 14.6 Hz, CH$_2$), 4.24 (1H, dd, J 8.6, 5.7 Hz,*CH), 2.12 (1H, m, CH(CH$_3$)$_2$), 0.89 (6H, d, J 6.8 Hz, CH(CH$_3$)$_2$). δ_C (100 MHz, DMSO-d_6): 172.7, 167.7 (C=O), 155.7, 134.0, 129.3, 128.7, 127.5, 126.6, 126.4, 123.8, 118.5, 107.2 (C$_{Aro}$), 66.6 (CH$_2$), 56.8 (*CH), 29.9 (CH(CH$_3$)$_2$), 19.1, 17.9 CH(CH$_3$)$_2$). HRMS (ESI) m/z: [M+H]$^+$ accurate mass calculated for C$_{17}$H$_{20}$NO$_4$: 302.1387. Found: 302.1390.

Figure 2.19 Synthesis of 2NapVVOMe

N-Methylmorpholine (3.7 mL, 33.7 mmol) was added to a suspension of 2NapVOH (1 eq, 9.67 g,) in chloroform (100 mL) and cooled to 0 °C using an ice-bath. *Iso*-butyl chloroformate (1 eq, 4.37 mL) was added (upon which all solids dissolved) and the mixture was stirred for 15 minutes. A solution of L-valine methyl ester hydrochloride (1 eq, 5.65 g) and N-methylmorpholine (1 eq, 3.7 mL) in chloroform (60 mL) was then added and the reaction mixture was stirred at ambient temperature overnight. After this time, it was diluted with an approximately equal amount of chloroform, washed in turn with water (2×), 1M hydrochloric acid and brine, dried (MgSO$_4$), filtered, and evaporated under reduced pressure. The compound 2NapVVOMe was obtained as a pale-brown solid (12.73 g, 91% crude

yield). The product was purified by column chromatography using 1:9 EtOAc:DCM to give a white solid.

δH(400 MHz, DMSO-d$_6$): 8.21 (1H, d, J 8.4 Hz, NH), 7.94 (1H, d, J 8.7 Hz, NH), 7.90-7.19 (7H, m, HAro), 4.73 (1H, d, J 14.7 Hz, CH$_2$), 4.69 (1H, d, J 14.7 Hz, CH$_2$), 4.45 (1H, dd, J 8.7, 6.8 Hz,*CH), 4.13 (1H, dd, J 8.3, 5.9 Hz,*CH), 3.65 (3H, s, OCH$_3$), 2.12 (1H, m, CH(CH$_3$)$_2$), 1.97 (1H, m CH(CH$_3$)$_2$), 0.91-0.81 (12H, m, CH(CH$_3$)$_2$. δC (100 MHz, DMSO-d$_6$): 171.7, 171.1, 167.2 (C=O), 155.5, 134.0, 129.4, 128.7, 127.5, 126.6, 126.4, 123.8, 118.9, 107.3 (CAro), 66.7 (CH$_2$), 57.6, 56.7 (*CH), 51.5 (OCH$_3$), 30.9, 29.6, (CH(CH$_3$)$_2$), 19.0, 18.8, 18.2, 17.9 CH(CH$_3$)$_2$ HRMS (ESI) m/z: [M+Na]$^+$ accurate mass calculated for C$_{23}$H$_{30}$N$_2$NaO$_5$: 437.2047. Found: 437.2048.
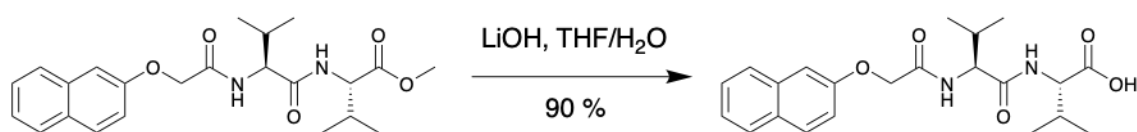
Figure 2.20 Deprotection of 2NapVVOMe

A solution of lithium hydroxide (3.68 g, 155 mmol) in water (120 mL) was added to a solution of 2NapVVOMe (12.73 g, 31 mmol) in tetrahydrofuran (120 mL) and stirred vigorously for 30 minutes. The reaction was monitored using TLC (1:9 EtOAc:DCM). After this time the TLC indicated the deprotection was complete. The reaction mixture was then poured into 1M hydrochloric acid (ca. 800 mL) and stirred for a further 20 minutes. The precipitate was filtered off and washed with several portions of water. Drying by azeotropic distillation with acetonitrile on a rotary evaporator, followed by keeping at 40 °C under vacuum overnight, afforded the compound 2NapVVOH as a white solid. (11.2 g, 90 %).

δH(400 MHz, DMSO-d$_6$): 12.57 (1H, s, OH), 8.13 (1H, d, J 8.1 Hz, NH), 7.9 (1H, d, J 9.0, NH), 7.87-7.21 (7H, m, HAro), 4.73 (1H, d, J 14.7 Hz, CH$_2$), 4.69 (1H, d, J 14.7 Hz, CH$_2$), 4.42 (1H, dd, J 9.0, 6.6 Hz,*CH), 4.11 (1H, dd, J 8.1, 5.9 Hz,*CH), 2.04 (1H, m, CH(CH$_3$)$_2$), 2.00 (1H, m CH(CH$_3$)$_2$), 0.91-0.81(12H, m, CH(CH$_3$)$_2$. δC (100 MHz, DMSO-d$_6$): 172.7, 171.0, 167.3 (C=O), 155.6, 134.0, 129.4, 128.7, 127.5, 126.6, 126.5, 123.8, 118.5, 107.3 (CAro), 66.8 (CH$_2$), 57.4, 56.8 (*CH), 31.0, 29.6 (CH(CH$_3$)$_2$), 19.1, 19.0, 18.1, 17.9 CH(CH$_3$)$_2$). HRMS (ESI) m/z: [M+H]$^+$ accurate mass calculated for C$_{22}$H$_{29}$N$_2$O$_5$: 401.2071 Found: 401.2070.

Figure 2.21 Synthesis of 2NapVVVOMe

A solution of *N*-methylmorpholine (3.1 mL, 28 mmol) was added to a suspension of 2NapVVOH (1 eq, 11.2 g) in chloroform (120 mL) was added and cooled to 0 °C using an ice-bath. *Iso*-butyl chloroformate (1 eq, 3.63 mL) was then added (upon which all solids dissolved) and the mixture was stirred for 20 minutes. A solution of L-valine methyl ester hydrochloride (1 eq, 4.69 g) and *N*-methylmorpholine (1 eq, 3.1 mL) in chloroform (50 mL) was then added and the reaction mixture was stirred at ambient temperature overnight. After this time, it was diluted with an approximately equal amount of chloroform, washed in turn with water (2×), 1M hydrochloric acid and brine, dried (MgSO₄), filtered, and evaporated under reduced pressure. The compound 2NapVVVOMe was obtained as a pale-brown solid (13.58 g, 94 % yield). This was used in the next step without further purification.

δH(400 MHz, DMSO-d_6): 8.12 (1H, d, *J* 7.7 Hz, NH), 7.83 (1H, d, *J* 7.9 Hz, NH), 7.75 (1H, d, *J* 8.2 Hz, NH), 8.04-7.21 (7H, m, HAro), 4.73 (1H, d, *J* 14.7 Hz, CH₂) 4.68 (1H, d, *J* 14.7 Hz, CH₂), 4.36 (1H, dd, *J* 8.9, 6.7 Hz, *CH), 4.26 (1H, dd, *J* 8.7, 7.4 Hz, *CH), 4.15 (1H, dd, *J* 7.8, 6.3 Hz, *CH), 3.61 (3H, s, OCH₃), 1.99 (3H, m, CH(CH₃)₂), 0.89-0.78 (18H, m, CH(CH₃)₂). δC (100 MHz, DMSO-d_6): 171.7, 171.1, 170.5, 167.3 (C=O), 155.5, 134.0, 129.4, 128.7, 127.5, 126.7, 126.4, 123.8, 118.5, 107.3 (C$_{Aro}$), 66.7 (CH₂), 57.5, 57.4, 57.1 (*CH), 51.5 (OCH₃), 30.8, 30.5, 29.6 (CH(CH₃)₂), 19.1 18.9, 18.8, 18.2, 18.1, 17.9 CH(CH₃)₂). HRMS (ESI) m/z: [M+Na]⁺ accurate mass calculated for C₂₈H₃₉N₃NaO₆: 536.2737. Found: 536.2741.
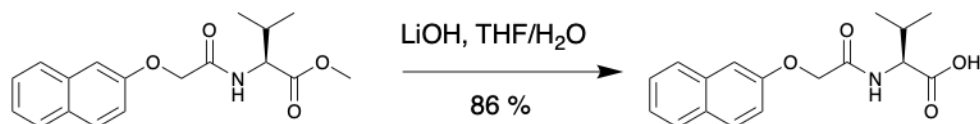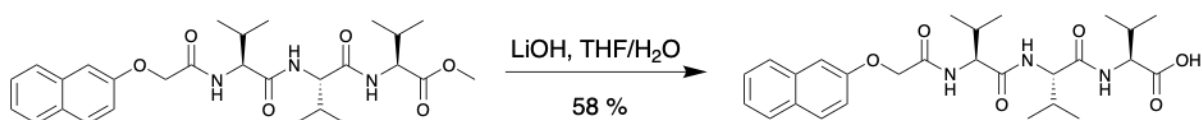

Figure 2.22 Deprotection of 2NapVVVOMe

A solution of lithium hydroxide (3.16 g, 130 mmol) in water (150 mL) was added to a solution of 2NapVVVOMe (13.58 g, 26 mmol) in tetrahydrofuran (150 mL) and was stirred vigorously for 30 minutes. The reaction was monitored using TLC (1:9 EtOAc: DCM). After this time, TLC indicated the deprotection was complete. The reaction mixture was then poured into 1M hydrochloric acid (ca. 800 mL) and stirred for a further 20 minutes. The precipitate was filtered off, then washed with several portions of water. Drying by azeotropic distillation with acetonitrile on a rotary evaporator, followed by keeping at 40 °C under

vacuum overnight, affording the compound 2NapVVVOH as a light brown solid (11.2 g, 90.25%). The ^{1}H NMR spectrum indicated the presence of an impurity and was recrystallised in acetonitrile to give the pure compound as a white solid (6.5 g, 58%).

δ_H(400 MHz, DMSO-d_6): 8.02 (1H, d, *J* 3.4 Hz, NH), 7.99 (1H, d, *J* 3.4 Hz, NH), 7.92 (1H, d, *J* 8.3 Hz, NH), 7.86-7.22 (m, 7H, HAro), 4.73 (1H, d, *J* 14.7 Hz, CH$_2$), 4.68 (1H, d, *J* 15.16 Hz, CH$_2$), 4.37 (1H, dd, *J* 8.9, 6.6 Hz, *CH), 4.3 (1H. dd, *J* 8.7, 7.3 Hz, *CH), 4.1 (1H, dd, *J* 8.2, 5.8 Hz, *CH), 1.99 (3H, m, CH(CH$_3$)$_2$), 0.89-0.79 (18H, m, CH(CH$_3$)$_2$). δ_C (100 MHz, DMSO-d_6): 172.8, 171.1, 170.6, 167.3 (C=O), 155.6, 134.1, 129.4, 128.7, 127.5, 126.7, 126.4, 123.8, 118.5, 107.3 (CAro), 66.8 (CH2) 57.6, 57.2, 57.2 (*CH), 30.9, 30.5, 29.7 (CH(CH$_3$)$_2$), 19.2, 19.1, 19.0, 18.2, 17.9, 17.9 (CH(CH$_3$)$_2$). HRMS (ESI) m/z: [M+Na]$^+$ accurate mass calculated for C$_{27}$H$_{37}$N$_3$NaO$_6$: 522.2575. Found: 522.2572.

6Br2NapVF (gelator 2) synthesis
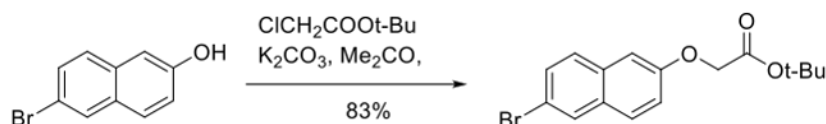
Figure 2.23 Synthesis of 6Br2NapO^{t}Bu.

A solution of potassium carbonate (7.13 g, 51.6 mmol) was added to a solution of 6-bromo-2-naphthol (1 eq, 11.5 g) in acetone (130 mL) and the mixture was stirred overnight in a flask equipped with a reflux condenser and CaCl$_2$ drying tube. After this time, *tert*-butyl chloroacetate (1.05 eq, 7.38 mL) and another portion of potassium carbonate (1 eq, 7.13 g) were added, and the mixture was heated at reflux (70 °C oil bath temperature) overnight. After this time, TLC (5:95 ethyl acetate/*n*-hexane) appeared to indicate the absence of starting the naphthol. The reaction mixture was evaporated to dryness under reduced pressure and the residue was partitioned between dichloromethane and water and stirred until all solids had dissolved. The layers were separated, and the aqueous phase was extracted with dichloromethane. The combined organics were washed in turn with water, and brine, dried (MgSO$_4$), filtered and evaporated under reduced pressure, affording a dark brown oil (17.0 g). ^{1}H NMR of this indicated the presence of a small amount of starting naphthol. Column chromatography (eluting with 4:6 dichloromethane/*n*-hexane, wet-loaded, 5×8 cm) afforded the title compound as a yellow oil which solidified on standing (14.5 g, 83 %). This was used in the next step without further purification. A small peak corresponding to *tert*-butyl chloroacetate is seen in the proton NMR around 4.25 ppm.

δ_H(400 MHz, DMSO-d_6): 8.12 (1H, d, J 1.9 Hz, HAro), 7.85 (1H, d, J 9.0 Hz, HAro), 7.76 (1H, d, J 8.8 Hz, HAro), 7.57 (1H, dd, J 8.7, 2.1 Hz, HAro), 7.29 (1H, d, J 2.5 Hz, HAro), 7.25 (1H, dd, J 8.9, 2.6 Hz, HAro), 4.77 (2H, s, CH$_2$), 1.43 (9H, s, C(CH$_3$)$_3$). δ_C (100 MHz, DMSO-d_6): 167.51 (C=O), 155.90, 132.60, 129.84, 129.32, 129.30, 128.89, 128.66, 119.47, 116.52, and 107.30 (CAro), 81.44 (C(CH$_3$)$_3$), 65.07 (CH$_2$), 27.65 (C(CH$_3$)$_3$). HRMS (ESI) m/z: [M]$^+$ accurate mass calculated for C$_{16}$H$_{17}$^{79}BrO$_3$: 336.0361; found: 336.037.
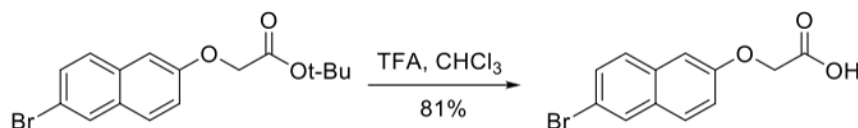
Figure 2.24 Synthesis of 6Br2NapOH

A solution of trifluoroacetic acid (42 mL, 549 mmol) was added to a solution of 6Br2NapOH (18.5 g, 54.9 mmol) in chloroform (80 mL) and the mixture was stirred overnight. After this time, the mixture was poured into diethyl ether (500 mL), stirred for 1 hour, then filtered. The solid in the filter was washed with several portions of diethyl ether and dried under vacuum. The title compound was thus obtained as a white solid (12.5 g, 81%).

δ_H(400 MHz, DMSO-d_6): 13.11 (1H, s, COOH), 8.12 (1H, d, J 1.9 Hz, HAro), 7.85 (1H, d, J 9.0 Hz, HAro), 7.77 (1H, d, J 8.80 Hz, HAro), 7.57 (1H, dd, J 8.76, 2.04 Hz, HAro), 7.32 (1H, d, J 2.48 Hz, HAro), 7.26 (1H, dd, J 8.96, 2.60 Hz, HAro), 4.80 (2H, s, OCH$_2$). δ_C (100 MHz, DMSO-d6): 169.96 (C=O), 156.06, 132.69, 129.87, 129.38, 129.33, 128.97, 128.72, 119.64, 116.54, and 107.16 (CAro), 64.58 (OCH$_2$). HRMS (ESI) m/z: [M+Na]$^+$ accurate mass calculated for C$_{12}$H$_9$^{79}BrNaO$_3$: 302.9627. Found: 302.9629.

Figure 2.25 Synthesis of 6Br2NapVOme

N-Methylmorpholine (2.1 mL, 19 mmol) and *Iso*-butyl chloroformate (1 eq, 2.46 mL) were added to a solution of 6Br2NapOH (1 eq, 5.4 g) in chloroform (60 mL) and cooled to 0 °C using an ice-bath. After stirring for 10 minutes, a solution of L-valine methyl ester hydrochloride (1 eq, 3.18 g) in chloroform and another portion of *N*-methylmorpholine (1 eq, 2.1 mL) were added and the reaction was stirred overnight. It was then diluted with chloroform, washed water (2×), 1M hydrochloric acid and brine, dried (MgSO$_4$), filtered, and evaporated under reduced pressure. The resulting white solid (7.3 g, 97% yield) was used directly in the next step.

δH(400 MHz, DMSO-d$_6$): 8.41 (1H, d, J 8.3 Hz, NH), 7.85 (1H, d, J 8.8 Hz, NH), 8.13-7.24 (6H, m, HAro), 4.76 (1H, d, J 14.4 Hz, CH$_2$), 4.71 (1H, d, J 14.6 Hz, CH$_2$), 4.26 (1H, dd, J 8.3, 6.4 Hz, *CH), 3.64 (3H, s, OCH$_3$), 2.11 (1H, m, CH(CH$_3$)$_2$), 0.89 (3H, d, J 5.4 Hz, CH(CH$_3$)$_2$), 0.88 (3H, d, J 5.4 Hz, CH(CH$_3$)$_2$).
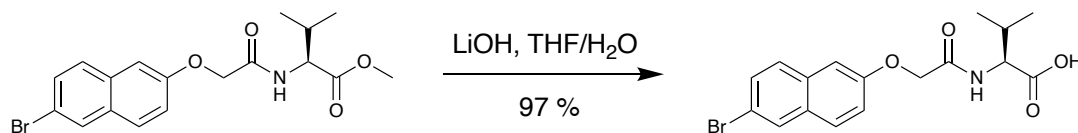
Figure 2.26 Synthesis of 6Br2NapVOH

A solution of lithium hydroxide (2.2 g, 92.5 mmol) in water (100 mL) was added to a solution of 6Br2NapVOMe (7.3 g, 18.5 mmol) in tetrahydrofuran (100 mL) and the reaction was monitored by TLC. After about one hour, the starting material had been consumed. The mixture was poured into 1M hydrochloric acid (ca. 500 mL) and stirred for one hour. The precipitated sticky solids were filtered off and rinsed with water in the filter. Recrystallization from boiling acetonitrile afforded the compound 6Br2NapVOH as a white solid (6.85 g, 97 %).

δH(400 MHz, DMSO-d$_6$): 8.39 (1H, d, J 8.4 Hz, NH), 7.45 (1H, d, J 8.6 Hz, NH), 8.26-7.31 (6H, m, HAro), 4.82 (1H, d, J 14.6 Hz, CH$_2$), 4.79 (1H, d, J 14.4 Hz, CH$_2$), 4.32 (1H, dd, J 8.5, 6.7 Hz, *CH), 2.09 (1H, m, CH(CH$_3$)$_2$), 0.89 (6H, d, J 6.8 Hz, CH(CH$_3$)$_2$). δC (100 MHz, DMSO-d6): 173.23 (C=O), 168.10 (C=O), 156.60, 133.12, 130.36, 129.87, 129.82, 129.31, 129.13, 120.24, 117.03, 107.83 (CAro), 67.13 (OCH$_2$), 57.39 (*CH), 30.36 (CH-(CH$_3$)$_2$), 19.60, 18.42 (CH-(CH$_3$)$_2$). HRMS (ESI) m/z: [M-H]$^-$ accurate mass calculated for C$_{17}$H$_{18}$NO$_4$^{79}Br: 378.0346, Found: 378.0345
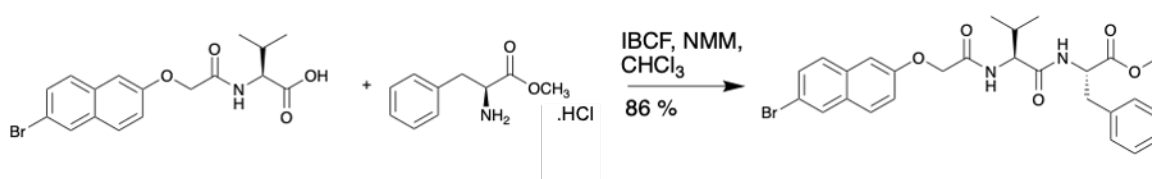
Figure 2.27 Synthesis of 6Br2NapVFOMe

N-Methylmorpholine (1.98 mL, 18 mmol) followed by *Iso*-butyl chloroformate (1 eq, 2.33 mL) was added to a suspension of 6Br2NapVOH (1 eq, 6.85 g) in chloroform (80 mL) and cooled to 0 °C using an ice-bath. After stirring for 10 minutes, L-phenylalanine methyl ester

hydrochloride (1.0 eq, 3.88 g) and another portion of *N*-methylmorpholine (1 eq, 1.98 mL) were added and the reaction was stirred overnight. After this time, it was diluted with an approximately equal amount of chloroform, washed in turn with water (2×), 1M

hydrochloric acid and brine, dried (MgSO₄), filtered, and evaporated under reduced pressure. The resulting white solid of 6Br2NapVFOMe (8.14 g, 86 % crude) was used as is in the next step.

δ_H(400 MHz, DMSO-d_6): 8.54 (1H, d, J 7.4 Hz, NH), 7.9 (1H, d, J 9.1 Hz, NH), 8.14-7.14 (11H, m, HAro), 4.71 (1H, d, J 14.6 Hz, CH₂), 4.66 (1H, d, J 14.4 Hz, CH₂), 4.48 (1H, m,*CH), 4.29 (1H, dd, J 9.0, 6.5 Hz, *CH), 3.56 (3H, s, OCH₃), 3.02 (1H, dd, J 14.0, 6.1 Hz, CH₂-Phe), 2.91 (1H, dd, J 13.9, 8.8 Hz, CH₂-Phe), 1.99 (1H, m, CH-CH₂-Phe), 0.82 (3H, d, J 6.8 Hz, CH(CH₃)₂) 0.77 (3H, d, J 6.8 Hz, CH(CH₃)₂).
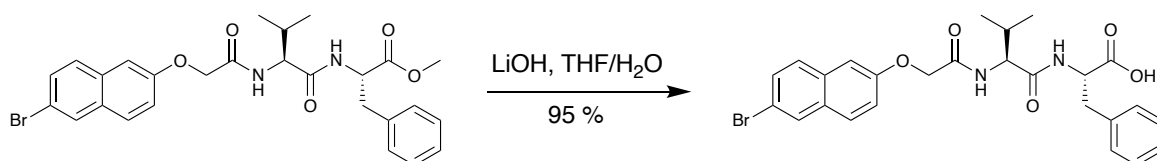
Figure 2.28 Synthesis of 6Br2NapVFOH

A solution of lithium hydroxide (1.8 g, 75 mmol) in water (100 mL) was added to a solution of 6Br2NapVFOMe (8.14 g, 15 mmol) in tetrahydrofuran (100 mL) and the reaction was monitored by TLC. After about one hour, the starting material had been consumed. The mixture was poured into 1M hydrochloric acid (ca. 500 mL) and stirred for one hour. The precipitate was filtered off, then washed with several portions of water. Drying by azeotropic distillation with acetonitrile on a rotary evaporator, followed by keeping at 40 °C under vacuum overnight, affording the compound 6Br2NapVFOH (7.50 g, 95 %).

δ_H(400 MHz, DMSO-d_6): 12.71 (1H, s, OH), 8.37 (1H, d, J 7.8 Hz, NH), 8.12 (1H, d, J 1.9 Hz, NH), 7.92-7.12 (11H, m, HAro), 4.71 (1H, d, J 14.7 Hz, CH₂), 4.66 (1H, d, J 14.6 Hz, CH₂), 4.43 (1H, m, *CH), 4.29 (1H, dd, J 9.0, 6.5 Hz, *CH), 3.04 (1H, dd, J 13.9 Hz, 5.2 Hz, CH-CH₂-Phe), 2.88 (1H, dd, J 13.9, 9.1 Hz, CH-CH₂-Phe), 1.99 (1H, m, CH-CH₂-Phe), 0.82 (3H, d, J 6.8 Hz, CH(CH₃)₂), 0.76 (3H, d, J 6.8 Hz, CH(CH₃)₂). δ_C (100 MHz, DMSO-d_6): 172.7, 170.6, 167.1 (C=O), 155.9, 137.5, 132.6, 129.9, 129.4, 129.4, 129.0, 128.8, 128.7, 128.1, 126.4, 119.6, 116.6, 107.4 (CAro), 66.8 (CH₂), 56.9, 53.4 (*CH), 36.6 (CH-(CH₃)₂, 30.9 (CH₂-Phe), 19.1, 17.7 (CH-(CH₃)₂). HRMS (ESI) m/z: [M+Na]⁺ accurate mass calculated for C₂₆H₂₇N₂NaO₅⁷⁹Br: 549.1001, Found: 549.0988.

2.4.2 Instrument and Procedures

Preparation of stock solutions

Each stock solution was prepared to a volume of 200 mL. The appropriate mass of gelator was weighed out in a 250 mL glass jar. 1 molar equivalent of NaOH (aq. 0.1 M) was added and then the stock solution made up to a volume of 200 mL using deionized water. Solutions were left to stir overnight to ensure all gelator had dissolved and the desired concentration was reached. Solutions were then adjusted to pH 8 using HCl (aq. 0.1/1 M) and NaOH (aq. 0.1/1 M) as necessary. All stock solutions were stored at room temperature and made fresh at the beginning of every week.

Image analysis

Images of the gel-forming on the electrode surface were taken every 30 seconds using a Panasonic Lumix DMC-FZ200 camera and custom-built programmable shutter release timer. These images were uploaded to the open-source image analysis software 'ImageJ'. The outline of the gel in each image was then traced, allowing the volume of the gel to be calculated (Figure 2.29). Once the area of all the images were calculated the rate of gel growth could then be plotted.
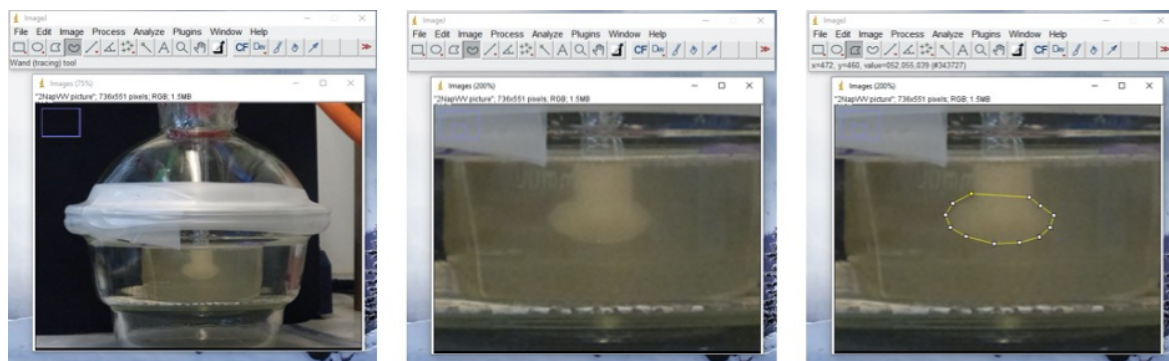
Figure 2.29 ImageJ software was used to trace around the gel to determine the change gel area with time.

pH measurements

A FC200 pH probe from HANNA instruments with a 6 mm x 10 mm conical tip was used for pH measurements. The stated accuracy of the pH measurements is ±0.1. The tip was placed in the stock solution and the pH was adjusted using HCl (aq. 0.1/1 M) and NaOH (aq. 0.1/1M). After the addition of each aliquot of HCl/NaOH, the solution was stirred for 30 seconds. The stirring was stopped, and another measurement was taken. This process was repeated until the desired pH of 8 was reached.

Chapter 2

Electrochemical measurements

The electrochemical set up shown in Figure 2.6 was used to carry out cyclic voltammetry and grow gels using fast chronopotentiometry. All experiments were run using a Dropsens potentiostat. Cyclic voltammetry measurements were carried out within a potential range of -0.5 to 1.2 V vs. an Ag/AgCl (aq. 3 M) ref. at a scan rate of 0.2 V/s. This was used to determine the current value to grow gels using fast chronopotentiometry. Each CV measurement consisted of one scan. An appropriate current value was then chosen from the middle of the oxidation curve, this current was then imposed on the gelator/HQ/electrolyte solution for the chosen time using fast chronopotentiometry. Once the experiment was finished the gel was removed using a spatula.

Gel forming procedure on 12 mm electrode under nitrogen

200 mL of gelator solution were transferred to a double-necked round bottom flask and degassed by stirring under vacuum for 30 minutes in a fume hood (Figure 2.30a). After this time, the stirring was stopped. The nitrogen inlet on the other neck of the flask was then turned on and the vacuum was continued for 3-5 seconds before turning both the vacuum and the nitrogen off. The stopper was then removed and 1 g of HQ and 2 mL of NaCl (0.1 M) were quickly added, and the stopper replaced. The solution was then stirred under vacuum for a further 10 minutes to ensure all HQ had dissolved. While the solution was degassing, the three-electrode system (12 mm glassy carbon working electrode, Pt wire counter electrode and Ag/AgCl (aq. 3 M) reference electrode) was set up in a 250 mL bowl within a desiccator (Figure 2.30c). The desiccator lid was replaced, and the rim secured with a layer of parafilm to prevent air leaks. A custom-made 3D printed lid with three holes (one for nitrogen inlet, one for electrode wires and one for working electrode) was placed on top of the desiccator neck and secured using sellotape (Figure 2.30b). A nitrogen inlet was placed inside the desiccator and a steady flow of nitrogen was applied for 30 minutes to degass the desiccator chamber. After the HQ had dissolved the stirring was stopped and the vacuum switched off. The stopper was then replaced with a Drechsel bottle head. One of the two bottle heads necks was attached to the nitrogen inlet and the other attached to a tube that feeds through the desiccator lid and into the bowl within the desiccator (Figure 2.30d). The nitrogen inlet tube for the desiccator chamber was turned off and removed to allow the Drechsel bottle tube to be inserted. The degassed solution was then transferred by turning on the nitrogen inlet, pushing the solution through the tube and into the bowl. Once the solution had been transferred, the tube is removed and replaced with the nitrogen inlet tube, again applying a steady flow of nitrogen for the remainder of the experiment. The gels were

then grown electrochemically as previously described. Once the gels were grown, they were removed from the solution and carefully slid off the electrode using a spatula.
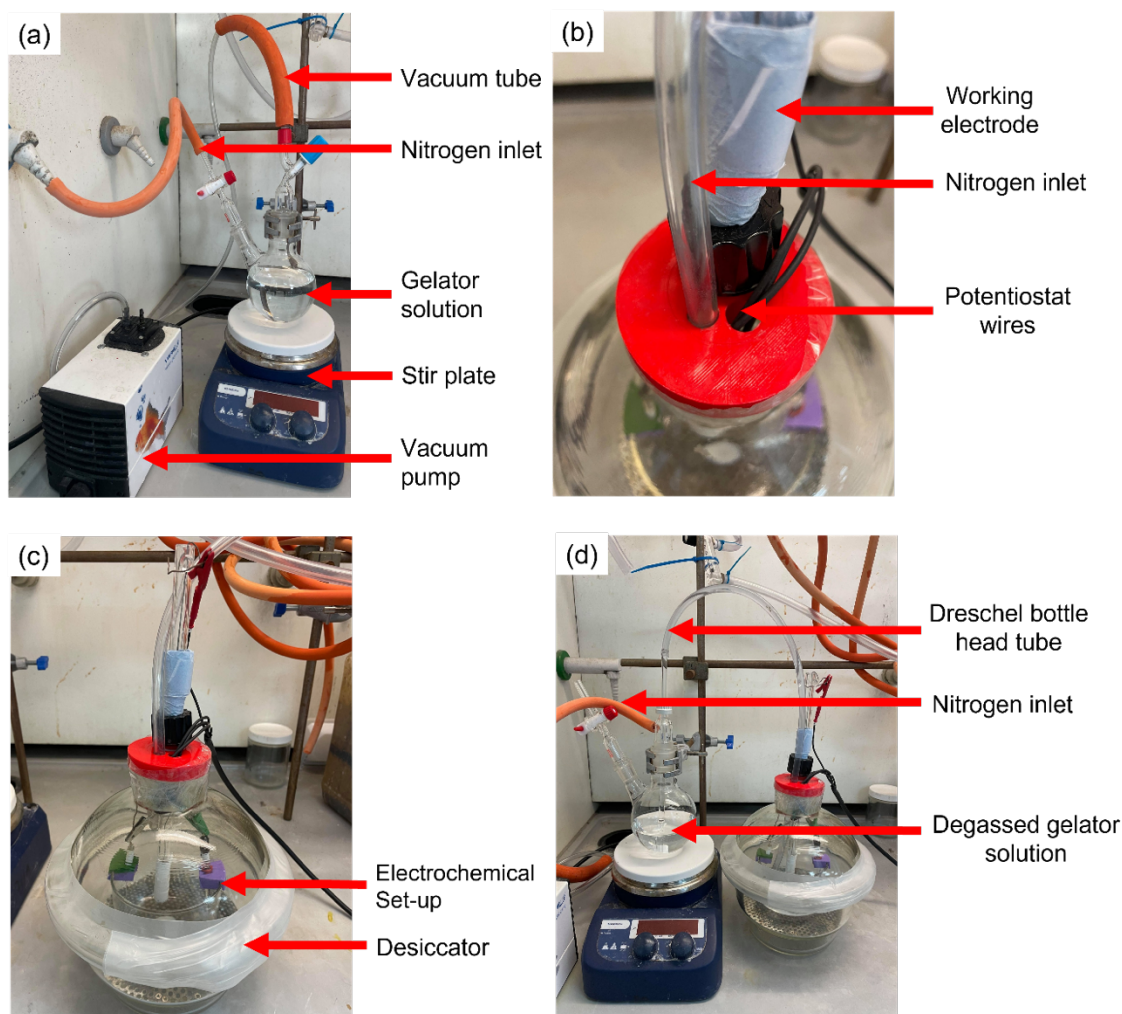
Figure 2.30 Set up for growing di and tri-peptide gels under nitrogen via the electrochemical oxidation of HQ (a) degassing of gelator/HQ solution (b) custom made 3D printed desiccator lid (c) Electrochemical set up within desiccator chamber (d) Set up used to transfer degassed gelator/HQ solution into desiccator chamber.

Multi-layered gel forming procedure on 12 mm electrode.

The first layer of the multi-layered gel was grown as previously described in. After the gel forming procedure was complete, the lid of the desiccator was lifted and the electrode with gel attached was carefully placed to one side. The remaining gelator solution in the bowl was drained and the bowl rinsed thoroughly. The bowl was then placed back in the desiccator, followed by fixing the desiccator lid and electrode with gel attached back in position. The second degassed gelator solution was then immediately added to the desiccator

bowl. The gel fabrication process was then repeated. Once the deposition process was complete the gel was removed from the solution and detached from the electrode using a spatula.

Cavitation Rheology

The cavitation rheometer was custom-made and the experimental procedures used here are as described previously (Figure 2.31).[28] Measurements were run using a 60 mL syringe (HSW HENKE-JECT Syringe with Luer-lock attachment) with an inner diameter of 0.41 mm (Fisher Scientific, HamiltonTM Kel-F Hub Blunt Point Needle with Luer-lock attachment). A 4.0 mL min^{-1} pump rate was used throughout.
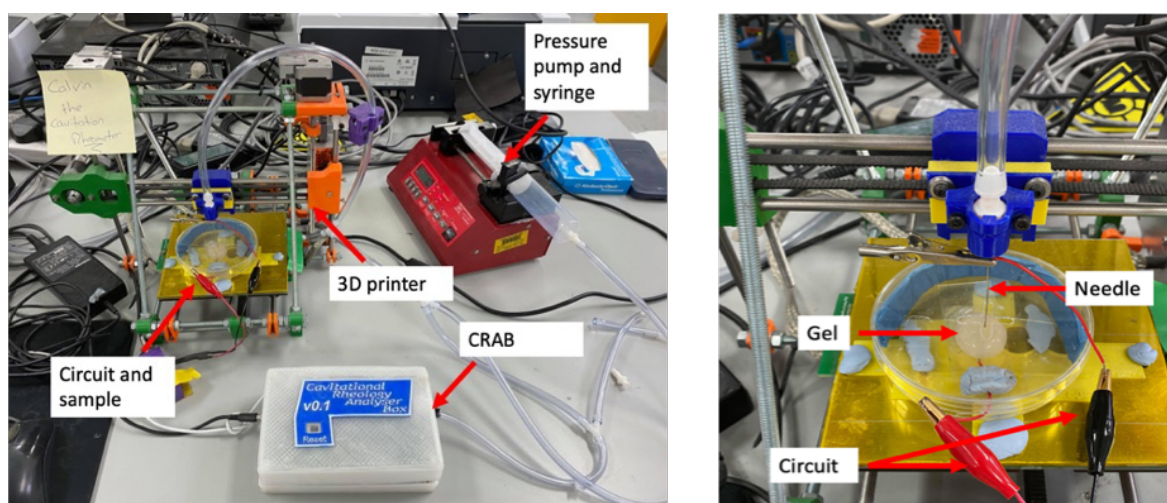
Figure 2.31. Cavitation rheology set-up.

Cavitation Rheology for multi-layered gels.

Cavitation rheology measurements were taken as previously described. However, in order to collect measurements from the multi-layered gel, the layers must be exposed. Using a scalpel, a cross section from the multi-layered gel was cut as shown in Figure 2.16 The cross section of the sample was then used to collect the measurements. To take measurements from each layer, the needle was moved and lowered into the target layer.

Determining relative gelator concentration using ^{1}H NMR spectroscopy

^{1}H NMR spectra were recorded using a Bruker Avance III 500 MHz spectrometer. Samples were run in DMSO-d_6. To determine the gelator concentration within the gels, ^{1}H NMR spectra were collected of the freeze-dried gel layers. Once gel deposition was complete the gels were removed from the electrode and placed in a freezer for two hours. The frozen gels were then transferred to the freeze dryer (CHRIST, Alpha 2-4 LSCbasic) and left overnight. The freeze-dried gels were then dissolved in 1 mL of DMSO-d_6 and pipetted into an NMR

tube containing a lock tube of known concentration (1% PDMS in C_2Cl_4). This was used as the external standard. The gelator concentration within the gels was then calculated using quantitative NMR (qNMR).

Powder X-Ray Diffraction (pXRD)

pXRD (powder X-ray diffraction) patterns were collected using a Rigaku MiniFlex 6G equipped with a D/teX Ultra detector, a 6-position (ASC-6) sample changer and Cu sealed tube (Kα1 and Kα2 wavelengths - 1.5406 and 1.5444 Å respectively). Patterns were measured as q/2θ scans typically. Data collection and analysis were carried out using Rigaku SmartLab Studio II software (Rigaku Corporation, 2014).

2.5 References

1. L. Chen, S. Revel, K. Morris, L. C. Serpell and D. J. Adams, *Langmuir*, 2010, **26**, 13466-13471.

2. E. R. Draper and D. J. Adams, *Chem*, 2017, **3**, 390-410.

3. Z. Yang, G. Liang, M. Ma, Y. Gao and B. Xu, *J. Mater. Chem.*, 2007, **17**, 850-854.

4. A. D. Martin and P. Thordarson, *J. Mater. Chem. B*, 2020, **8**, 863-877.

5. N. Habibi, N. Kamaly, A. Memic and H. Shafiee, *Nano Today*, 2016, **11**, 41-60.

6. L. Li, L. Xie, R. Zheng and R. Sun, *Front. Chem.*, 2021, **9**, 739791.

7. X. Du, J. Zhou, J. Shi and B. Xu, *Chem. Rev.*, 2015, **115**, 13165-13307.

8. E. R. Draper and D. J. Adams, *Langmuir*, 2019, **35**, 6506-6521.

9. J. Zhuang, S. Lin, L. Dong, K. Cheng and W. Weng, *ACS Biomater. Sci. Eng.*, 2018, **4**, 1528-1535.

10. J. Li, S. Wu, E. Kim, K. Yan, H. Liu, C. Liu, H. Dong, X. Qu, X. Shi, J. Shen, W. E. Bentley and G. F. Payne, *Biofabrication*, 2019, **11**, 032002.

11. Z. Yang, Z. Yuye, L. Houbin, D. Fuyuan and S. Xiaowen, *Curr. Med. Chem.*, 2019, **26**, 1-21.

12. C. Patterson, B. Dietrich, C. Wilson, A. R. Mount and D. J. Adams, *Soft Matter*, 2022, **18**, 1064-1070.

13. S. Wu, K. Yan, J. Li, R. N. Huynh, C. B. Raub, J. Shen, X. Shi and G. F. Payne, *React. Funct. Polym.*, 2020, **148**, 104492.

14. J. E. Bressner, B. Marelli, G. Qin, L. E. Klinker, Y. Zhang, D. L. Kaplan and F. G. Omenetto, *J. Mater. Chem. B*, 2014, **2**, 4983-4987.

15. F. Ozawa, K. Ino, T. Arai, J. Ramón-Azcón, Y. Takahashi, H. Shiku and T. Matsue, *Lab Chip*, 2013, **13**, 3128-3135.

16.   E. K. Johnson, D. J. Adams and P. J. Cameron, *J. Am. Chem. Soc.*, 2010, **132**, 5130-5136.

17.   M. Lei, X. Qu, H. Liu, Y. Liu, S. Wang, S. Wu, W. E. Bentley, G. F. Payne and C. Liu, *Adv. Funct. Mater.*, 2019, **29**, 1900065.

18.   J. Raeburn, B. Alston, J. Kroeger, T. O. McDonald, J. R. Howse, P. J. Cameron and D. J. Adams, *Mater. Horiz.*, 2014, **1**, 241-246.

19.   C. Tang, A. M. Smith, R. F. Collins, R. V. Ulijn and A. Saiani, *Langmuir*, 2009, **25**, 9447-9453.

20.   K. A. Houton, K. L. Morris, L. Chen, M. Schmidtmann, J. T. A. Jones, L. C. Serpell, G. O. Lloyd and D. J. Adams, *Langmuir*, 2012, **28**, 9797-9806.

21.   P. S. Kubiak, S. Awhida, C. Hotchen, W. Deng, B. Alston, T. O. McDonald, D. J. Adams and P. J. Cameron, *Chem. Commun.*, 2015, **51**, 10427-10430.

22.   E. R. Cross, *SN Appl. Sci.*, 2020, **2**, 397.

23.   E. K. Johnson, D. J. Adams and P. J. Cameron, *J. Mater. Chem.*, 2011, **21**, 2024-2027.

24.   E. K. Johnson, L. Chen, P. S. Kubiak, S. F. McDonald, D. J. Adams and P. J. Cameron, *Chem. Commun.*, 2013, **49**, 8698-8700.

25.   A. Piper, Ben M. Alston, D. J. Adams and A. R. Mount, *Faraday Discuss.*, 2018, **210**, 201-217.

26.   Y. Liu, Y. Cheng, H.-C. Wu, E. Kim, R. V. Ulijn, G. W. Rubloff, W. E. Bentley and G. F. Payne, *Langmuir*, 2011, **27**, 7380-7384.

27.   Y. Liu, E. Kim, R. V. Ulijn, W. E. Bentley and G. F. Payne, *Adv. Funct. Mater.*, 2011, **21**, 1575-1580.

28.   A. M. Fuentes-Caparrós, B. Dietrich, L. Thomson, C. Chauveau and D. J. Adams, *Soft Matter*, 2019, **15**, 6340-6347.

29.   D. Giuri, L. J. Marshall, B. Dietrich, D. McDowall, L. Thomson, J. Y. Newton, C. Wilson, R. Schweins and D. J. Adams, *Chem. Sci.,* 2021, **12**, 9720-9725.

30.   K. McAulay, L. Thomson, L. Porcar, R. Schweins, N. Mahmoudi, D. J. Adams and E. R. Draper, *Organic Materials*, 2020, **02**, 108-115.

31.   A. M. Castilla, M. Wallace, L. L. E. Mears, E. R. Draper, J. Doutch, S. Rogers and D. J. Adams, *Soft Matter*, 2016, **12**, 7848-7854.

CHAPTER 3

The First Electrofabrication of a Low Molecular Weight Hydrogel at High pH

This chapter is adapted in part from the following publication:

'Electrofabrication of a low molecular weight hydrogel at high pH'

Materials Chemistry Frontiers

C. Patterson, S. Panja, W. Liu, A. R. Mount, A. Squires, D. J. Adams

3.1 Introduction

Electrofabrication is an electrochemical process that can be used to assemble solid or soft materials on electrode surfaces (see Chapter 1).[1-4] This technique has been used to form hydrogels, triggering the self-assembly of gelling molecules or polymers upon application of a current or electric field. Hydrogels have been fabricated using this method from small molecule gelators such as dipeptides,[5] dibenzoyl cystine and functionalised amino acids.[6] Polymeric systems such as collagen,[7] chitosan,[8,9] silk[10] and alginate[11,12] have also been gelled using this same approach.

To fabricate pH-sensitive hydrogels from gelator solutions, electrofabrication can be used to generate localised pH gradients at electrode surfaces by exploiting various electrochemical acid-base or reduction-oxidation reactions.[2,13, 14] Within the localised region of pH change at the electrode, the charge is removed from the gelator structure, leading to the loss of electrostatic repulsion and self-assembly of the gelator to deposit a gel on the electrode surface. It should be noted that no gelation occurs in the bulk solution. As a result, excellent spatial and temporal control over gelation is achieved.

Depending on the system or additives used, the application of a galvanostatic current can result in the diffusion of hydrogen or hydroxyl ions from the electrode surface, creating a significantly more acidic or basic pH zone than the bulk solution. The size of this zone and as a consequence, the size of the hydrogel, is governed by the diffusion distance of the hydrogen or hydroxyl ions.[5] For low molecular weight gelators (LMWGs), electrofabrication has been used to form gels at low pH, typically by exploiting the hydroquinone-quinone couple[5, 15] or the direct oxidation of water.[16] Gelling at high pH by electrofabrication is yet to be described for a LMWG.

Despite no known examples of electrodeposition at high pH for LMWGs, gelling at high pH has been achieved for chitosan (Figure 3.1b; a biopolymer containing many primary amines, in the form of charged ammonium ions) using the galvanostatic reduction of hydrogen peroxide (Figure 3.1a).
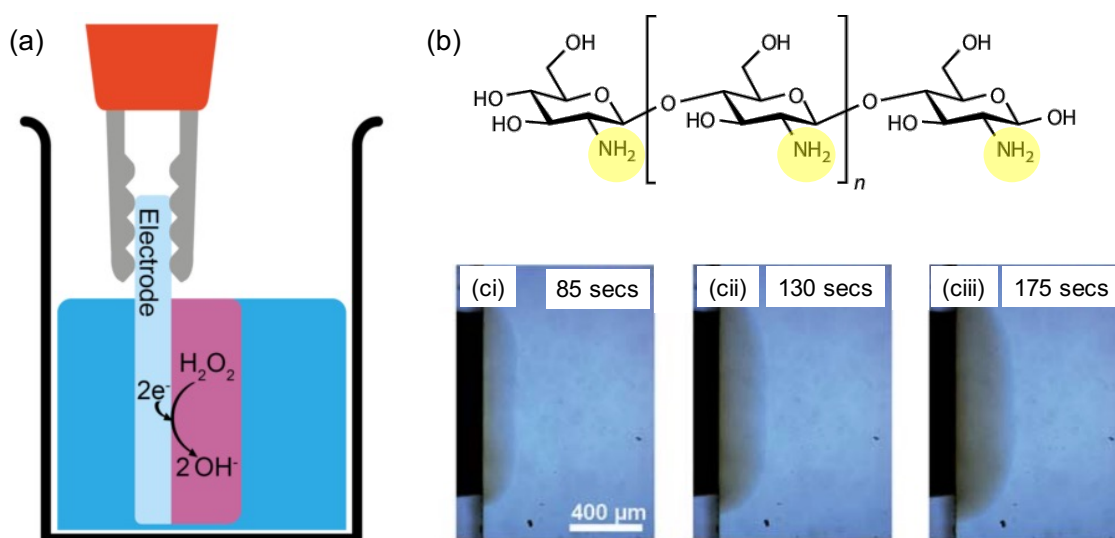
Figure 3.1 (a) Schematic representation of the electrochemical gelation of chitosan via the two-electron, electrochemical reduction of hydrogen peroxide, producing two hydroxide ions (b) chemical structure of the amino polysaccharide chitosan. The pH sensitive amino groups responsible for gelation have been highlighted. (c) Images showing the time-dependent electrofabrication of chitosan hydrogels on electrode surfaces via water electrolysis at deposition times of (ci) 85 secs (cii) 130 secs and (ciii) 175 secs. Scale bar 400 μm. Images reproduced from *Soft Matter*, 2010, **6**, 3179 with permission from the Royal Society of Chemistry.[17]

During the electrochemical reduction of hydrogen peroxide, hydroxide ions are produced at the electrode-solution interface, creating a basic pH zone.[14] This sees the deprotonation of chitosan's ammonium groups in this zone, decreasing chitosan's solubility to induce gelation at the electrode surface.[8] Electrofabrication of chitosan has also been achieved through the electrolysis of water, which produces hydroxide ions and hydrogen gas at the cathode surface (Figure 3.1c).[17, 18] Although the production of hydroxide ions can reduce the local pH enough to induce gelation, water electrolysis is often avoided when using longer deposition times. This is due to the production of hydrogen gas bubbles that perforate through the hydrogel surface which disrupts the materials homogeneity.[18]

In this chapter, we report the first known electrofabrication of a LMWG hydrogel using an electrochemically generated basic pH gradient at an electrode surface. We then show the simultaneous formation of two different LMWGs at opposing pH extremes by coupling an anodic and cathodic neutralisation method. Thus, fabricating materials with a high degree of spatiotemporal control.

Chapter 3

3.2 Results and Discussion

3.2.1 Fmoc-3

Fmoc-3 (Figure 3.2; mono-Fmoc 1,3-diaminopropane hydrochloride) is an effective LMWG. To form a hydrogel, the Fmoc-3 gelator molecules self-assemble in water to form fibrous structures that entangle when the pH of the solution is raised above the pK_a (8.4-8.7).[19] Previous work has shown that this can be achieved chemically via the autocatalytic reaction of urea and urease which produces ammonia.[19] The production of ammonia results in an increase in the pH, causing the deprotonation and neutralization of the Fmoc-3 molecules and hence the formation of a hydrogel.
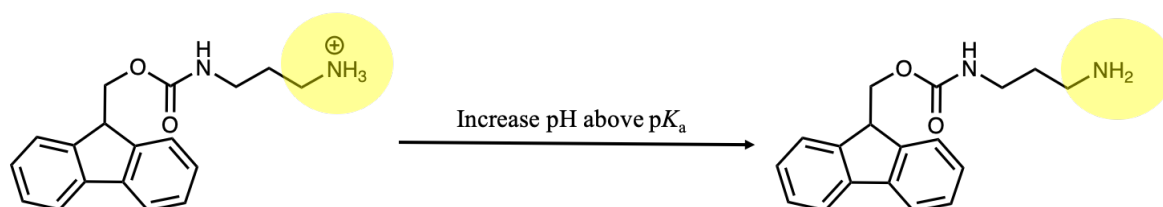
Figure 3.2 Chemical structures of the LMWG Fmoc-3. When the pH of the gelator solution is raised above the pK_a of the terminal amine, the charge is removed from the gelator structure, triggering the molecules to self-assemble and to form hydrogels. The pH sensitive amino groups are highlighted.

3.2.2 Fabrication parameters

To electrochemically gel the LMWG Fmoc-3, 7 mL solutions of Fmoc-3 (5 mg/mL in aq. NaCl 0.1 M) were prepared to give gelator solutions at a pH of 6.5. As carbon dioxide in the atmosphere dissolves in water, it is likely that the pH is fixed at 6.5 due to the natural buffering of dissolved carbon dioxide in the gelator solutions. To create the basic pH gradient at the electrode surface, 70 μL of hydrogen peroxide solution was added to the Fmoc-3 solutions immediately prior to gelation. The importance of hydrogen peroxide reduction on hydrogel formation was then investigated by growing Fmoc-3 hydrogels in the absence of hydrogen peroxide and varying the concentration of the hydrogen peroxide solution from 1 M to 4 M. As a result, the final concentration of hydrogen peroxide in the Fmoc-3 gelator solutions ranged from 10 - 40 mM. It is important to note that in the absence of hydrogen

peroxide, the gelation process relies on the electrochemical reduction of water which produces hydrogen gas as a by-product.

To grow the Fmoc-3 hydrogels, a three-electrode set-up under galvanostatic control consisted of an FTO glass slide (working electrode), platinum wire (counter electrode) and Ag/AgCl (reference electrode) (Figure 3.3a). A current density of -0.7 mA/cm^2 was found to be satisfactory for gel growth and was applied to all Fmoc-3 gelator solutions for 900 seconds using chronopotentiometry (Figure 3.3b).
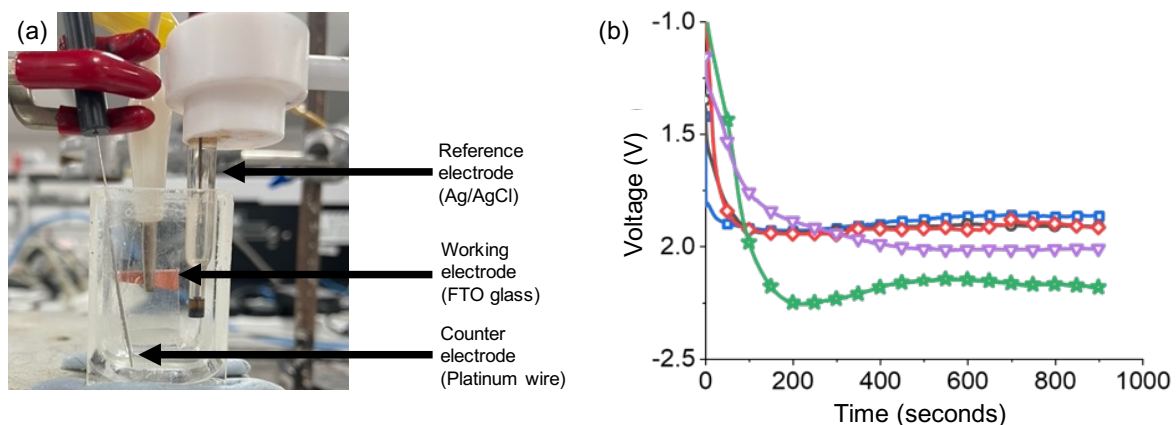
Figure 3.3 (a) Electrochemical set-up for Fmoc-3 hydrogel formation (b) Chronopotentiometry measurements of Fmoc-3 gelator solutions in the absence of hydrogen peroxide (green/star data) and 10mM (pink/triangle data), 20 mM (red/diamond data), 30 mM (black/circle data) and 40 mM (blue/square data) hydrogen peroxide solution. In all cases Fmoc-3 = [5 mg/mL], NaCl = [aq. 0.1 M], deposition time = [900 seconds], current density = [-0.7 mA/cm^2].

In the absence of hydrogen peroxide and across the entire hydrogen peroxide concentration range, hydrogel formation was observed at the working electrode surface (Figure 3.4a-b), giving hydrogels of pH 9.5 - 10.5. However, there were visible differences in the surface structure and smoothness of the resultant hydrogel films. In line with previous studies that look at electrodeposition of LMWGs, hydrogel growth increases with deposition time (Figure 3.4c).[5, 15]

Images of the hydrogel films show that in the absence of hydrogen peroxide and at lower concentrations of hydrogen peroxide, the hydrogel film contains many holes where the hydrogen gas bubbles have escaped through the material (Figure 3.4a-b). As the concentration of hydrogen peroxide is increased, the number of holes present on the hydrogel surface decreases significantly (Figure 3.4a-b). Previous work has shown that when the

gelation process relies on the electrolysis of water, the gaseous by-product (hydrogen gas) escapes through the hydrogel on the electrode surface, leaving holes.[10, 20] For most applications, material reproducibility and homogeneity are of the utmost importance. As the electrochemical reduction of water results in air bubble holes throughout the Fmoc-3 hydrogels, the fabrication process is unsuitable for the formation of reproducible hydrogels. The addition of hydrogen peroxide circumvents this issue; as the concentration of hydrogen peroxide is increased, the gelation process relies mostly on hydrogen peroxide reduction. Thus, there is a reduction in the presence of holes to produce hydrogels with smooth surfaces.
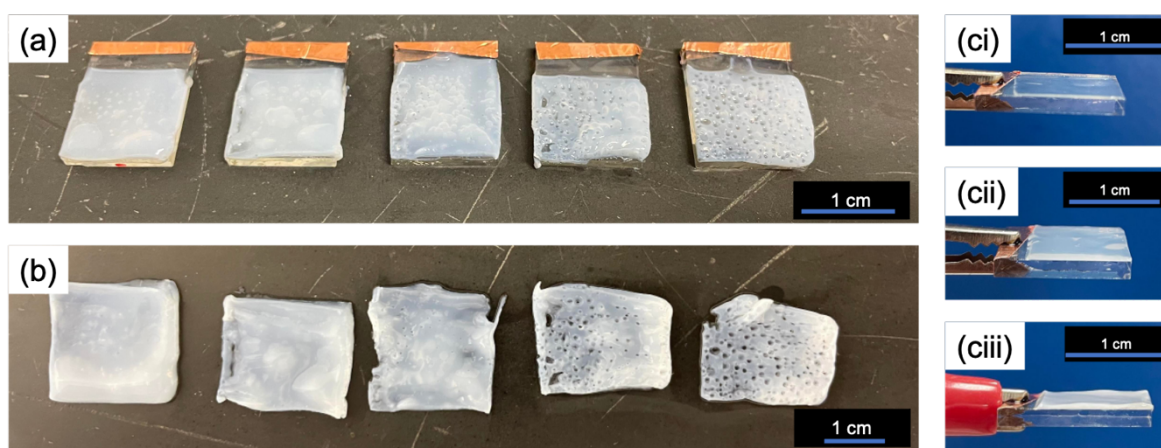
Figure 3.4 Fmoc-3 hydrogels formed via electrochemically generated basic pH gradients (a) on the FTO glass slides and (b) removed from FTO glass slide. Fmoc-3 hydrogels were grown in the absence of hydrogen peroxide (far right) and 10 mM, 20 mM, 30 mM and 40 mM hydrogen peroxide solution (right to left) (ci-iii) Images showing the time dependent growth of Fmoc-3 hydrogels on FTO glass slides grown for (ci) 300 (cii) 600 and (ciii) 900 seconds. Scale bars: 1 cm. In all cases Fmoc-3 = [5 mg/mL], NaCl = [aq. 0.1 M], current density = [-0.7 mA/cm^2].

As the Fmoc functionality is base labile, care must be taken to ensure that the high pH environment does not cleave the Fmoc group from the molecule to form dibenzofulvene.[21] To confirm that this does not occur during the electrodeposition process, ^{1}H NMR spectra of the freeze-dried gels were collected and compared with the spectra of the pure Fmoc-3 gelator (Figure 3.5). The spectra confirms that the Fmoc group does not cleave during the electrofabrication process. This cleavage is also usually accompanied by a yellow/orange colour change which was not observed for any of the hydrogels.
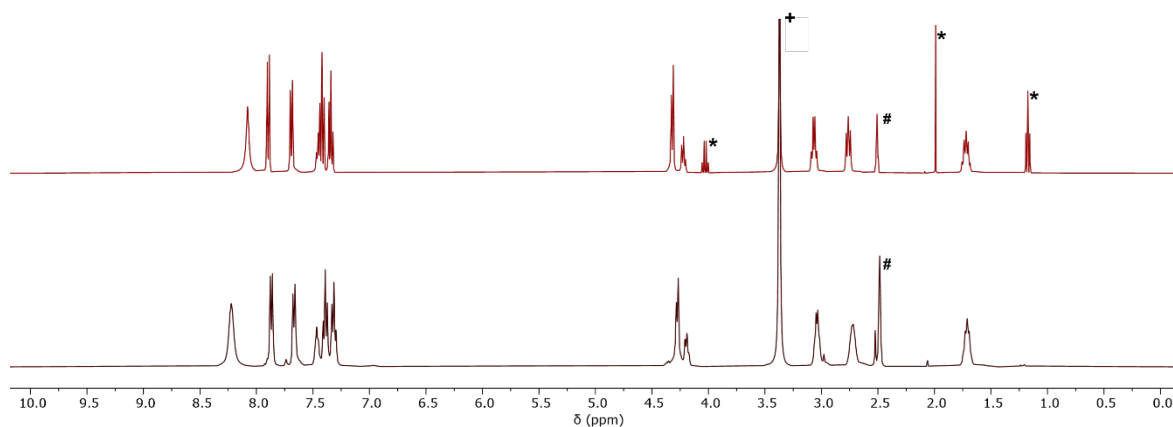
Figure 3.5 To confirm that the Fmoc group is not cleaved from the gelator molecule during the gelation process, ^{1}H NMR spectra of the freeze-dried Fmoc-3 gels were collected in DMSO-d[6] and compared with the spectrum of the pure Fmoc-3 gelator. Bottom spectrum: Freeze-dried Fmoc-3 gel. Top spectrum: pure Fmoc-3 gelator. To obtain a satisfactory ^{1}H NMR spectrum of the Fmoc-3 hydrogel, multiple hydrogels were combined. Peaks marked * = are ethyl acetate solvent, # = NMR solvent and + = water peak.

3.2.3 Rheological analysis

To investigate the effect of hydrogen peroxide concentration on the stiffness and breaking point of the resulting gels, bulk rheology was used. Due to the shape and thickness (≤ 2 mm) of the Fmoc-3 hydrogels fabricated on the glass FTO slides, a 'cup and vane' geometry could not be used. Instead, a parallel plate geometry was employed. When a 'cup and vane' geometry is used, hydrogels must be formed within vials of a specific size. This excludes our hydrogels which are formed on glass FTO slides. It is important to note that when a parallel plate geometry is used, the surface of the hydrogel has the greatest contribution to the average distribution of the bulk material properties relative to the rest of the material.[22] However, as the Fmoc-3 hydrogels on the electrode surface are relatively thin, this effect will most likely be less pronounced.

Cavitation rheology, a localised technique which is used to probe the mechanical properties of gels in their native environment,[23, 24] was also attempted to characterise the mechanical properties of the Fmoc-3 hydrogels. To examine the mechanical properties using this method, air is pumped through a syringe that penetrates the hydrogel at a pre-defined depth which causes a bubble to form within the hydrogel. The elastic modulus can then be related to the critical pressure at which this bubble bursts, with higher critical pressures corresponding to stiffer hydrogel networks. The main advantage of this technique is that hydrogels of any shape can be used and are not limited by the specific geometries or volumes

needed in bulk rheology.[23, 24] However, all attempts to collect rheological data using this method failed. Due to the thickness of the Fmoc-3 hydrogels ($\leq$ 2 mm) it is likely that the bubble formed within the hydrogel touches the surface of the glass FTO slide, causing it to burst prematurely.

As cavitation rheology measurements could not be collected, bulk rheology was chosen. Strain and frequency sweeps (Figure 3.6) were performed on the Fmoc-3 hydrogels grown in the absence of hydrogen peroxide and across the full hydrogen peroxide concentration range (from 10 to 40 mM). To collect these measurements, the glass FTO slides with the hydrogels attached were secured onto the parallel plate of the rheometer using tape to prevent slipping.

For all gels, strain sweeps were measured from 0.01 % to 100 % with a constant frequency of 10 rad/s. As the linear elastic region deviated at values >0.05% strain, frequency sweeps were performed from 1 rad/s to 100 rad/s under a constant strain of 0.05%. For all the hydrogels, the storage modulus (G$'$) and loss modulus (G$''$) values are the same (approximately G$'$= 10^5, G$'' = 10^4$ Pa). However, as the concentration of hydrogen peroxide is increased, these strain values become more reproducible between gels (Figure 3.6). From the rheology data, Fmoc-3 hydrogels grown in the presence of 40 mM hydrogen peroxide solution exhibit the lowest errors in both G$'$ and G$''$ showing that a hydrogen peroxide concentration of 40 mM is the optimal concentration for reproducible hydrogel formation out of all the concentration values investigated.
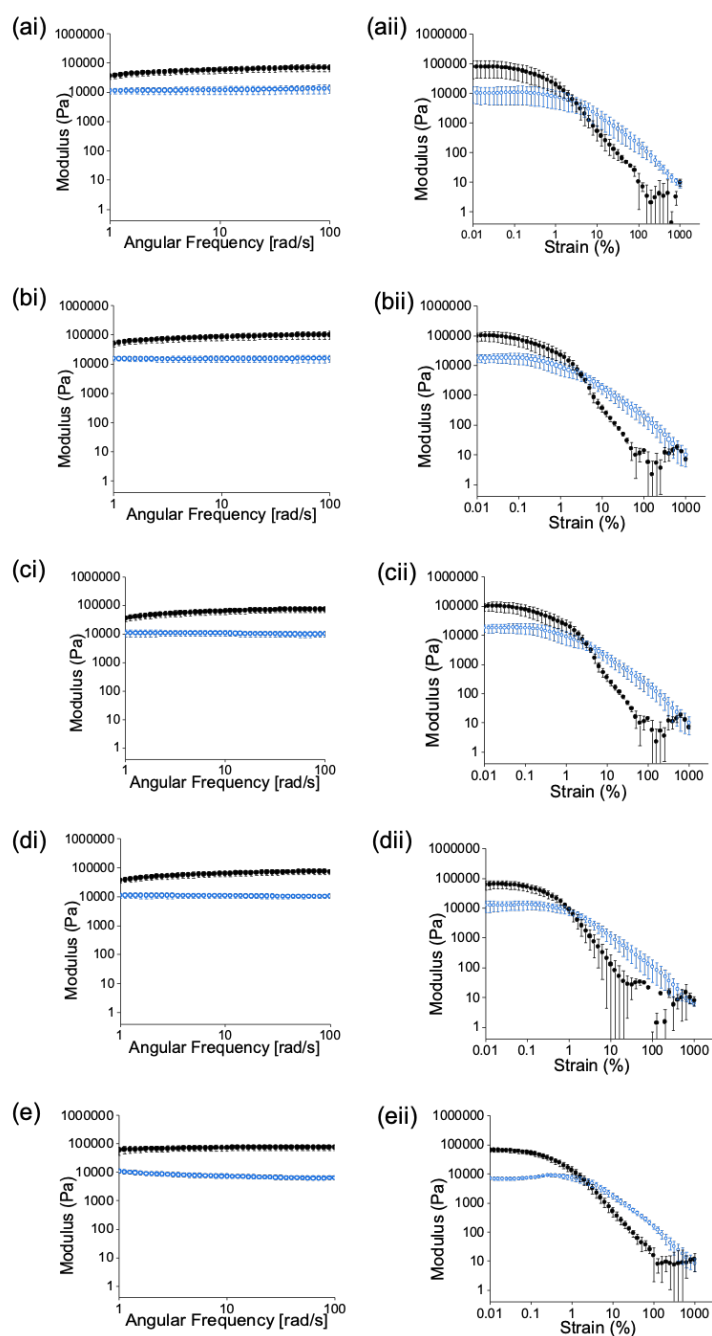
Figure 3.6 Frequency and strain sweeps showing the storage (G′, black/full circle data) and loss modulus (G″, blue/hollow circle data) of Fmoc-3 hydrogels (ai-aii) in the absence of hydrogen peroxide and in the presence of hydrogen peroxide solution at various concentrations (bi-ii) 10 mM (ci-cii) 20 mM (di-dii) 30 mM (ei-eii) 40 mM. Measurements performed in triplicate; error bars calculated by standard deviation. In all cases Fmoc-3 = [5 mg/mL], NaCl = [aq. 0.1 M], deposition time = [900 seconds], current density = [-0.7 mA/cm^2].

3.2.4 Time dependent gel growth

To monitor the rate of gel growth, the geometry of the electrode was changed to a circular glassy carbon macroelectrode (12 mm diameter). The hemispherical growth of hydrogels observed from a circular electrode means that the gel area can easily be calculated using the image processing software ImageJ. At lower concentrations of hydrogen peroxide, the number of holes created by hydrogen gas bubbles throughout the material increases, making it difficult to image and accurately calculate gel area. Therefore, results from concentrations below 40 mM are not included in this work. Photographs of the Fmoc-3 hydrogels were taken in situ at 30 second intervals for 900 seconds using a hydrogen peroxide concentration of 40 mM. The area of gel was then determined using the image processing program ImageJ by manually tracing around the hydrogel on the electrode surface. From the gel area vs time plot (Figure 3.7a), hydrogel growth increases with time up until 600 seconds after which the gel area appears to plateau.
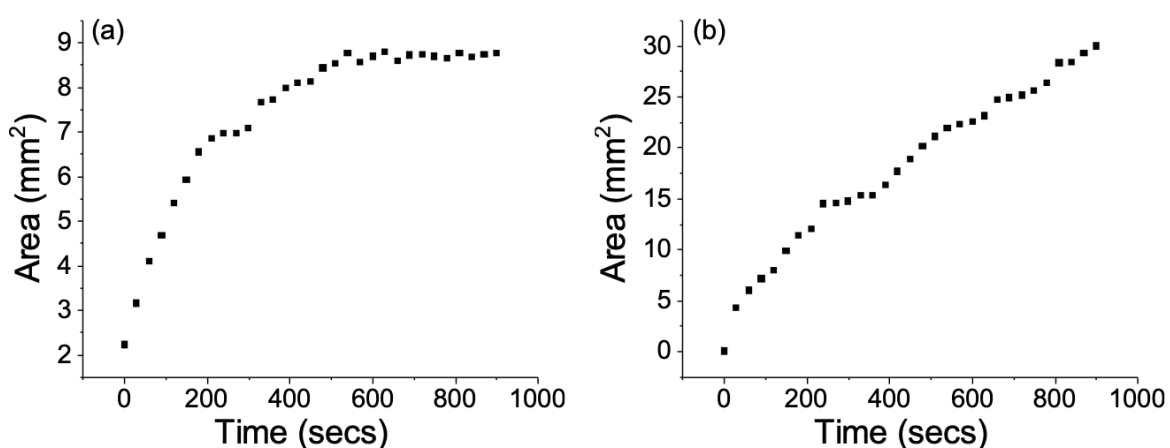
Figure 3.7 Gel area vs time plots of Fmoc-3 hydrogels with a starting solution of (a) pH 6.5 (b) pH 8. Initial conditions Fmoc-3 = [5 mg/mL], NaCl = [aq. 0.1 M], H_2O_2 = [40 mM], deposition time = [900 seconds], current density = [-0.7 mA/cm^2].

To determine whether the concentration of the Fmoc-3 hydrogel changes after this plateau point, quantitative ^{1}H NMR spectroscopy (qNMR) was used. To calculate the relative gelator concentration, the Fmoc-3 hydrogels were carefully removed from the FTO glass surface, frozen and then freeze dried overnight. The freeze-dried gels were then subsequently dissolved in 1 mL of DMSO-d_6 and transferred into an NMR tube with a lock tube/external standard of known concentration (1% PDMS in C_2Cl_4). From the qNMR data (Figure 3.8),

the concentrations of the Fmoc-3 hydrogels grown for 600 and 900 seconds are almost identical, indicating that gel growth stops after the plateau point of around 600 seconds. To ensure that hydrogen peroxide depletion was not the limiting factor to hydrogel growth, a second aliquot of hydrogen peroxide solution (70 µL, 4 M) was added at 600 seconds (gel growth plateau point), followed by applying the current for a further 600 seconds (1200 seconds total). Again, the qNMR results show no difference in concentration between the Fmoc-3 hydrogels grown for 600 and 1200 seconds, indicating there is a limit to how large these gels can grow using these conditions. It is likely that the reason for the plateau in gel growth seen for this system is that the carbon dioxide dissolved within the gelator solution acts as a buffer, buffering the pH at the high pH zone interface, preventing the gel from increasing in size.
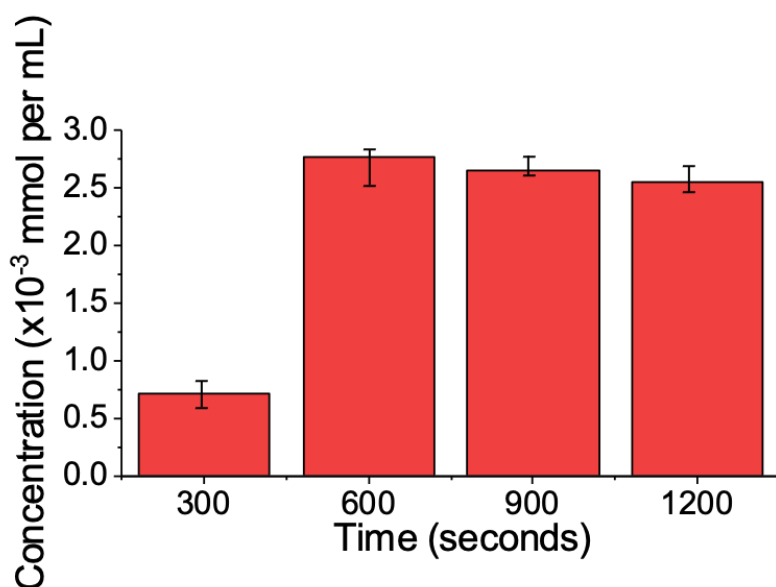
Figure 3.8 The relative gelator concentration of the Fmoc-3 hydrogels grown using various deposition times. For the 1200 second sample, a second aliquot (70 µL, 4 M) of hydrogen peroxide was added at 600 seconds. Measurements performed in triplicate; error bars calculated by standard deviation. Conditions Fmoc-3 = [5 mg/mL], NaCl = [aq. 0.1 M], H_2O_2 = [40 mM], current density = [-0.7 mA/cm^2].

To prevent carbon dioxide acting as a buffer, the pH of the gelator solutions were adjusted to pH 8 prior to hydrogel deposition. Again, photographs were taken in situ at 30 second intervals to monitor gel area with time using ImageJ software. When the starting pH was adjusted to pH 8, gel area does not plateau after 300 seconds but increases linearly with deposition time (Figure 3.7b). A larger gel is also formed when compared to hydrogels grown from the pH = 6.5 gelator solution. These results show that the size of the low pH

zone from the electrode surface is dependent on the starting pH of the gelator solution. As the pH of the gelator solution is increased, the dissolved carbon dioxide cannot act as a buffer. As a result, the size of the hydrogel is now governed by the diffusion path length of the hydroxide ions from the electrode surface. Assuming three-dimensional diffusion-controlled growth of a near hemispherical gel for which $r^2 = 6Dt$, the diffusion coefficient of the hydroxide ions travelling from the electrode surface can be calculated from the slope of the gel area vs time graphs. The calculated diffusion coefficient from the linear regions of the gel area vs time graphs for the gelator solutions of pH = 6.5 and pH = 8 are 3.67 x 10^{-5} cm^2 s^{-1} and 4.78 x 10^{-5} cm^2 s^{-1} respectively. These values are reassuring as they are a sensible comparison to the diffusion coefficient of hydroxide ions in water (5 x 10^{-5} cm^2 s^1).[25]

3.2.5 Confocal microscopy

Confocal microscopy is a highly useful tool used to examine the microstructure of soft materials such as hydrogels.[26] By adding fluorescent dyes such as Nile blue to gelator solutions, the dye can be incorporated into the hydrogel structures during the self-assembly process. This allows images of the self-assembled network to be collected in a non-invasive manner as well as controlling the depth of field of the image without penetrating the material. Notably, confocal microscopy allows the microstructure to be probed without dehydrating the sample which is needed for other imaging techniques such as SEM or TEM.[27] Previous work has shown that dehydrating the hydrogel before imaging often results in drying artefacts, producing images that are not representative of the hydrogel microstructure in the solvated state.[27] Within the Adams group, it is general practice to incorporate the fluorescent dye (2 µL/mL of a 0.1 wt% solution) into gelator solutions before inducing gelation, so that when gelation is triggered, the dye is incorporated into the hydrogel network as it forms.[28] This technique was attempted for the electrochemically fabricated Fmoc-3 hydrogels by adding Nile Blue to gelator solutions before applying a constant current to the FTO glass surface. However, when the hydrogels were removed from the FTO glass and exited under the confocal microscope, no clear images could be obtained. It was also noted that the hydrogels had a red/pink tinge to them. Previous work has shown that for Nile blue solutions, basic pH can cause hypsochromic shifts of the absorption maxima accompanied by a colorimetric change of blue to pink.[29] It is therefore likely that the pH at the electrode-solution interface is too basic, meaning the wavelength applied by the confocal microscope to excite the Nile blue in the Fmoc-3 hydrogels is no longer suitable. To circumvent this, once the gelation process was complete, the hydrogel was removed from the FTO glass slide and placed in 20 mL of Nile blue solution (2 µL/mL of a aq. 0.1 wt% solution) for 30 minutes

before imaging. This was found to a sufficient time for imaging as when the hydrogel was left in the Nile blue solution overnight, the hydrogel absorbed all of the dye from solution, causing it to disintegrate. After 30 minutes, the Fmoc-3 hydrogels were removed from the Nile blue solutions. Small sections of the gel were then cut out of the hydrogel using a scalpel and placed on a microscope slide. A cover slip was then placed on top of the gel before imaging.

To examine whether the microstructure of the Fmoc-3 hydrogels changes at various concentrations of hydrogen peroxide, confocal microscopy images were taken of gels grown in the absence of hydrogen peroxide and gels grown across the full hydrogen peroxide concentration range (Figure 3.9). Despite presenting different surface smoothness and topography, all the Fmoc-3 hydrogels appear to have a very similar microstructure, exhibiting long fibers with a number of spherulitic domains (Figure 3.9). Notably, for the 40 mM sample, the fibres appear to be longer in comparison to the other Fmoc-3 hydrogel microstructures as well as displaying a greater contrast with the solvent. As is seen previously, Fmoc-3 hydrogels formed in the presence of 40 mM hydrogen peroxide solution present little to no air bubble holes in the final material. It is therefore likely that the increase in contrast and fibre length are due to the increased homogeneity of the sample as the three-dimensional network is not disrupted/broken by hydrogen gas bubble holes.

 To examine the microstructure at different stages of the deposition process, confocal microscopy images were collected from gels grown for 300, 600 and 900 seconds. Again, the images show that long fibres and a number of spherulitic domains are present (Figure 3.9f-g). This suggests the microstructure remains very similar throughout the deposition process. However, images of the 300 and 600 second samples present poor contrast with the solvent, making it hard to obtain clear images. As the hydrogels are very thin at this stage (> 1.5 mm), it is likely that there is much less hydrogel network for the Nile blue dye to adhere to, resulting in poorer images. In all cases, multiple images were collected at various positions, confirming the microstructure was homogeneous throughout the sample.
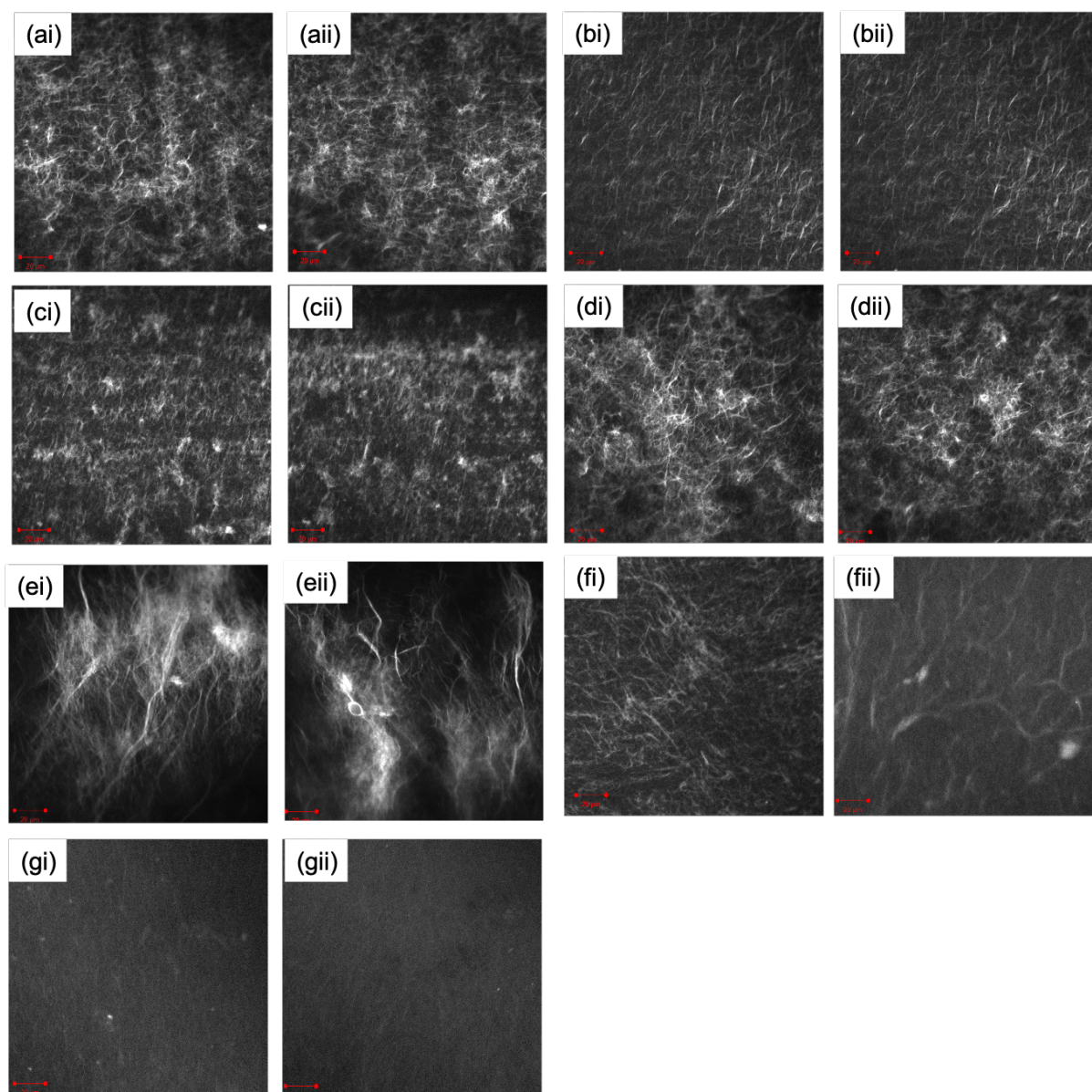
Figure 3.9 Confocal microscopy images of Fmoc-3 hydrogels fabricated (ai-ii) in the absence of hydrogen peroxide and in the presence of hydrogen peroxide solution of (bi-ii) 10 mM (ci-ii) 20 mM (di-ii) 30 mM and (ei-ii) 40 mM concentration. For the 40 mM sample, images were taken of the Fmoc-3 hydrogels at different stages of the deposition process (fi-i) 300 seconds (gi-ii) 600 seconds. Images of two different positions within the hydrogels are included to show that the microstructure is homogenous throughout the sample. In all cases a current density of -0.7 mA/cm^2 was applied. Conditions; Fmoc-3 = [5 mg/mL], NaCl = [aq. 0.1 M]. Scale bar: 20 μm.

3.2.6   Scanning electron microscope

To further probe the microstructure of the Fmoc-3 hydrogels, single electron microscope (SEM) images were collected from the dehydrated hydrogels/xerogels attached to the glass FTO slides. As is previously mentioned, SEM requires the hydrogel sample to be dehydrated prior to imaging and sputter coated to prevent charging. From the images collected of the xerogels (Figure 3.10), it is evident that in all cases the dehydrating process has caused a large number of drying artefacts. As a result, very little informative information can be drawn from these images as they do not represent the microstructure in its hydrated state. For other LMWG xerogels, it has been shown that informative images of the fibers can be collected using this method.[30] One reason that this method may have been unsuccessful for the Fmoc-3 hydrogels is due to their thickness (>2 mm), meaning that when they are dehydrated, very small amounts of xerogel are present on the glass FTO slides.
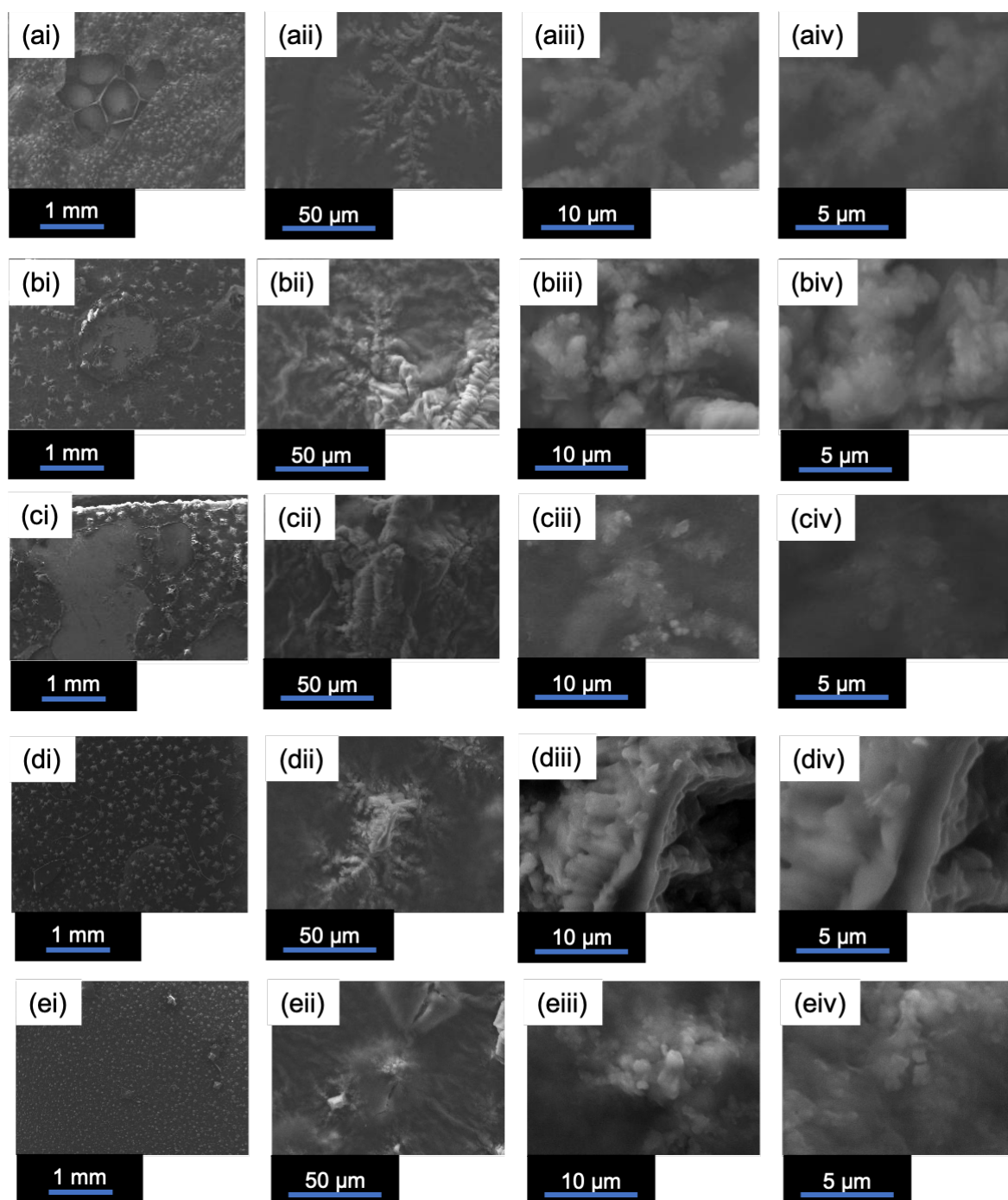
Figure 3.10. SEM images of dried Fmoc-3 hydrogels fabricated (ai-aiv) in the absence of hydrogen peroxide and in the presence of hydrogen peroxide solution of (bi-biv) 10 mM (ci-civ) 20 mM (di-div) 30 mM and (ei-eiv) 40 mM concentration. Magnification (i) 35 (ii) 1K (iii) 5K (iv) 10 K. In all cases a current density of -0.7 mA/cm^2 was applied. Conditions; Fmoc-3 = [5 mg/mL], NaCl = [aq. 0.1 M].

3.2.6 Small angle X-ray scattering

Whilst confocal microscopy probes the microstructure, small angle X-ray scattering (SAXS) can be used to probe the primary self-assembled structures underpinning the Fmoc-3 hydrogels. As a result, the combination of these techniques provides information across two different length scales. As in-situ SAXS measurements could not be collected during the deposition process using in-house SAXS, small sections of all the Fmoc-3 hydrogels (2 mm thickness) grown for 900 seconds were cut and sealed in paste cells with Kapton windows. 10 µL of deionised water was added to each section to prevent the hydrogel drying out or the formation of air pockets. SAXS data was then collected from hydrogels grown in the absence of hydrogen peroxide and across the full hydrogen peroxide concentration range (10 - 40 mM). In the next chapter, a much more in-depth explanation of SAXS data and the corresponding fitting parameters is discussed.

Fitting the SAXS data was carried out using SasView software.[31] Full fitting parameters for the Fmoc-3 hydrogels can be found in Table 3.1-2. In all cases, the SAXS data were best fit to a flexible elliptical cylinder model with a polydispersity in radius (Figure 3.11). As the length lies outside of the Q range of the experiment, an arbitrarily high value of 1000 Å was fixed and not allowed to refine with the other fitting parameters.

From the SAXS data in Table 3.2, hydrogels grown in the absence of hydrogen peroxide display a Kuhn length and radius of 7.1 nm and 4.3 nm respectively. As the concentration of hydrogen peroxide is increased from 10 to 40 mM, the general trend observed is that the Kuhn length and radius gradually decrease. For hydrogels grown in the presence of 40 mM hydrogen peroxide solution, the fits display a Kuhn length and radius of 4.8 nm and 3.5 nm respectively. As a result, the axis ratio increases in size with increasing hydrogen peroxide concentration from 0.60 nm (hydrogels grown in the absence of hydrogen peroxide) to 0.7 nm (40 mM hydrogen peroxide solution). This suggests the self-assembled structures are transitioning from tape-like to more spherical shaped structures as the concentration of hydrogen peroxide is reduced.

For hydrogels grown in the presence of 40 mM hydrogen peroxide solution, SAXS data were collected from hydrogels grown for 300 and 600 seconds to examine if deposition time effects the primary self-assembled structures. Again, all SAXS data were best fit to the same model (flexible elliptical cylinder with polydispersity of radius). For the Fmoc-3 hydrogels grown for 300 and 600-seconds, the SAXS data implies that the radius and axis ratio values are very similar. However, their Kuhn length values of 6.4 nm (300 secs) and 6.8 nm (600

secs) are notably higher than hydrogels grown for 900 seconds (4.8 nm). This suggests that the self-assembled structures are less flexible at shorter deposition times.

Sample	H_2O_2 concentration (mM)	Deposition time (secs)
1	40	300
2	40	600
3	40	900
4	30	900
5	20	900
6	10	900
7	N/A	900

Table 3.1. Sample list of electrochemically fabricated Fmoc-3 hydrogels. In all cases Fmoc-3 = [5 mg/mL], NaCl = [aq. 0.1 M].

	1	2	3	4	5	6	7
Model	FEC	FEC	FEC	FEC	FEC	FEC	FEC
Scale	0.02 ± 3.1 x 10^{-5}	0.007 ± 3.2 x 10^{-5}	0.01 ± 2.8 x 10^{-5}	0.013 ± 2.9 x 10^{-5}	0.016 ± 3.2 x 10^{-5}	0.02 ± 3.4 x 10^{-5}	0.016 ± 3.5 x 10^{-5}
Background	1.5 ± 0.04	1.6 ± 0.04	2.4 ± 0.04	2.2 ± 0.04	2.5 ± 0.04	2.6 ± 0.04	1.7 ± 0.04
Polydispersity of the radius	0.1*	0.1*	0.1*	0.1*	0.1*	0.1*	0.1*
Length (Å)	1000*	1000*	1000*	1000*	1000*	1000*	1000*
Kuhn Length (Å)	63.5 ± 0.3	68.4 ± 0.9	48.4 ± 0.2	45.4 ± 0.4	50.0 ± 0.3	67.8 ± 1.3	70.5 ± 0.1
Radius (Å)	34.1 ± 0.1	35.6 ± 0.2	34.7 ± 0.1	35.1 ± 0.1	37.7 ± 0.1	42.2 ± 0.1	43.2 ± 0.1
Axis ratio (Å)	7.5 ± 0.03	7.2 ± 0.07	7.4 ± 0.04	7.3 ± 0.05	6.3 ± 0.03	6.4 ± 0.04	6.0 ± 0.06
χ^2	2.9	1.3	1.8	1.6	2.2	2.5	1.6

Table 3.2 Fitting parameters of the electrochemically fabricated Fmoc-3 hydrogels listed in Table 3.1. Values annotated with an asterisk (*) were fixed and not allowed to refine during the fitting process. Fitting errors are provided as ± and are calculated by the fitting software. FEC: flexible elliptical cylinder.
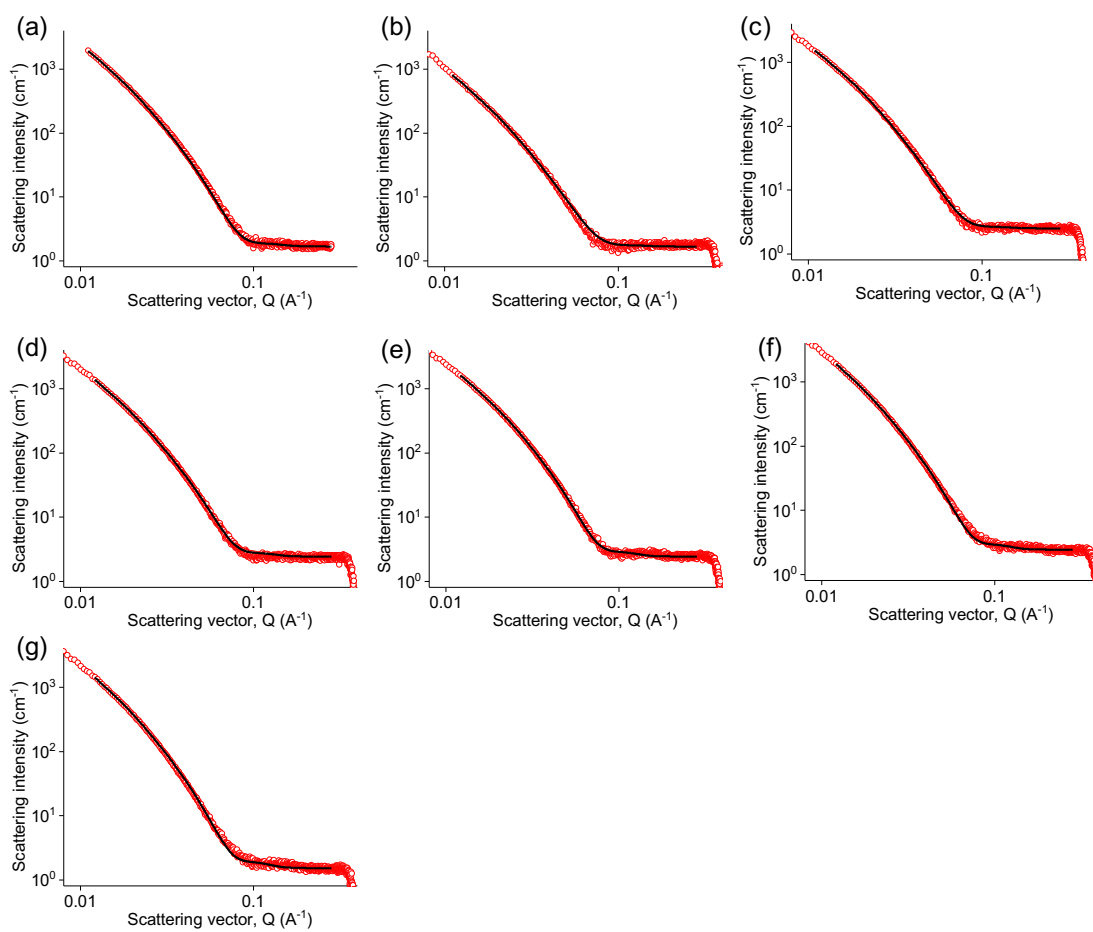
Figure 3.11 SAXS 1D I vs Q plots for hydrogels shown as open red circles and fits to the data (fitting parameters shown in Table 3.2) shown as black lines (a) **1**; (b) **2**; (c) **3**; (d) **4**; (e) **5**; (f) **6**; (g) **7**.

3.2.7 Dual hydrogel formation

To add a further level of complexity to this system, we have combined the techniques seen in this chapter with the fabrication methods seen in Chapter 2.

In this chapter, we have shown that we can electrochemically fabricate hydrogels of Fmoc-3 by employing the reduction of hydrogen peroxide and electrolysis of water at electrode surfaces. This electrochemical process produces hydroxide ions which diffuse from the electrode surface to create a basic pH zone extending from the electrode front. The reduction in pH within this zone removes the charge from the Fmoc-3 gelator structure leading to the loss of electrostatic repulsion between the gelator molecules to induce self-assembly exclusively on the electrode surface.

In Chapter 2, we showed the electrofabrication of various naphthalene-protected tri- and dipeptide hydrogels on electrode surfaces via the electrochemical oxidation of the hydroquinone (benzene-1,4-diol).[5, 13, 15] In short, the electrochemical oxidation of hydroquinone produces hydrogen ions at the electrode surface, creating an acidic pH zone at the electrode surface. Unlike the Fmoc-3 gelator structure, which presents free amine groups on the *C*-terminus, Naphthalene-protected tri- and dipeptide LMWGs present carboxylate groups which are negatively charged at high pH. When the pH is lowered below the pK_a of the carboxylate groups (i.e., within the acidic pH zone at the electrode surface) the carboxylate groups are protonated to form the neutral structure (protonated carboxylic acid). As a result, the electrostatic repulsion between the gelator molecules is removed to locally induce gelation at the electrode surface.

Thus far, we have shown that we can trigger the gelation of two different classes of LMWG molecules on electrode surfaces by employing electrochemically generated pH gradients. To couple both these systems, a custom-made H-cell (Figure 3.13) was built, consisting of two glass chambers separated by a Nafion membrane. This allowed the simultaneous formation of both classes of LMWG at opposing pH extremes within the same system.

To demonstrate this concept, two LMWG molecules were chosen that could be triggered at opposing pH extremes. To electrochemically trigger gelation of a LMWG at an acidic pH extreme, the Naphthalene-protected dipeptide 2NapVG was chosen (Figure 3.12b). For the basic pH extreme, Fmoc-3 was used (Figure 3.12a).
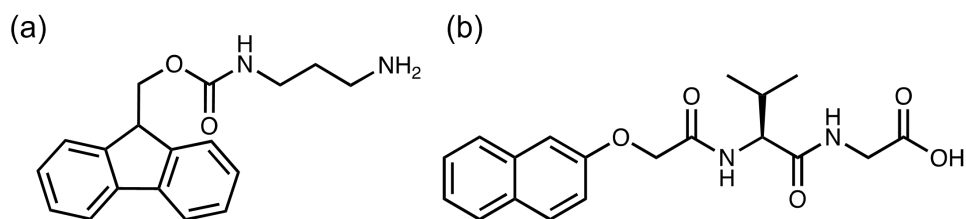
Figure 3.12 Chemical structure of the low molecular weight gelator molecules (a) Fmoc-3 and (b) 2NapVG.

In one chamber, the working electrode (glassy carbon) and reference electrode (aq. Ag/AgCl, 3 M) was placed in a 2NapVG and hydroquinone solution (Figure 3.14a). In the other chamber, the counter electrode (platinum wire) was placed in a Fmoc-3 and hydrogen peroxide solution. As is shown previously, the effect of hydrogen peroxide concentration on the formation of Fmoc-3 hydrogels was investigated. As the highest concentration of hydrogen peroxide solution investigated (40 mM) gave the most reproducible hydrogels, this was chosen to grow the Fmoc-3 hydrogels in this system.

To simultaneously grow the Fmoc-3 and 2NapVG hydrogels, a galvanostatic current was applied to the working electrode for 900 seconds. For this system, a high current density of 22 mA/cm^2, was required to grow the gels. Whenever lower current densities were attempted the rate of gel growth was significantly slower, producing very small amounts of hydrogel on the electrode surface. A potential reason for this could be the increased resistance of the system posed by the Nafion membrane used to separate the two gelator solutions. As well as this, the electrofabrication of Fmoc-3 hydrogels using hydrogen peroxide solution requires much higher current densities in comparison to dipeptide/hydroquinone systems.
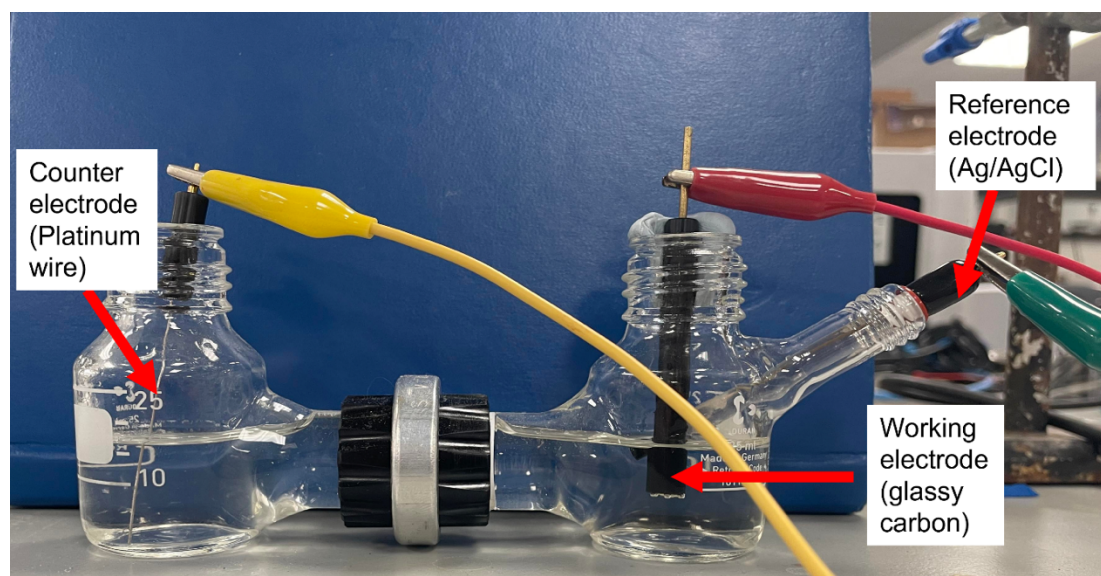
Figure 3.13. Electrochemical set-up for dual hydrogel formation. In the LHS chamber, initial reaction conditions; Fmoc-3 = [5 mg/mL], NaCl = [aq. 0.1 M], H_2O_2 = [40 mM]. In RHS chamber, initial reaction conditions; 2Nap-VG-OH = [5 mg/mL], hydroquinone [5 mg/mL], NaCl = [aq. 0.1 M], pH = [8].

Upon application of the current, hydrogel formation was observed on both working and counter electrode surfaces in their respective chambers (Figure 3.14b). The application of an anodic current to the working electrode in the right-hand side (RHS) chamber sees the oxidation of hydroquinone to benzoquinone, liberating protons at the electrode-solution interface. This localised decrease in pH triggers the 2NapVG molecules to self-assemble and form a hydrogel exclusively at the working electrode surface.[5, 15] To complete the electrochemical circuit, the hydrogen peroxide in the LHS chamber is reduced at the counter electrode, generating hydroxide ions. As a result, self-assembly of Fmoc-3 and formation of a hydrogel on the counter electrode surface is also achieved.
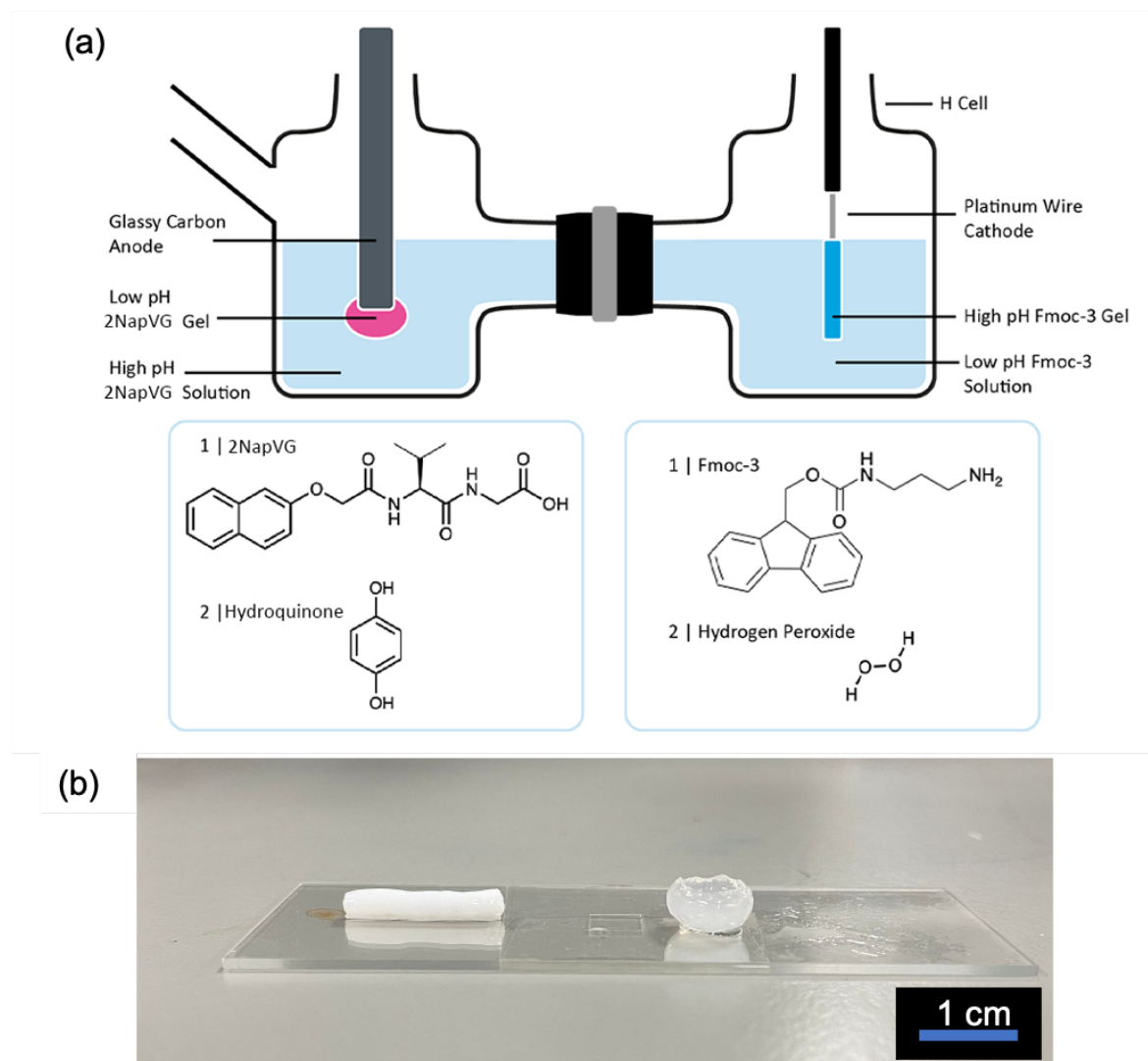
Figure 3.14 (a) Schematic representation of the electrochemical system used to simultaneously grow two different hydrogels at opposing pH extremes (b) Images of the 2NapVG (right) and Fmoc-3 (left) hydrogels grown using this technique. A current density of 22 mA/cm^2 was applied for 900 seconds. Scale bar: 1 cm. Initial reaction conditions; Fmoc-3 = [5 mg/mL], NaCl = [aq. 0.1 M], H$_2$O$_2$ = [40 mM], 2NapVG = [5 mg/mL], hydroquinone [5 mg/mL], NaCl = [aq. 0.1 M], pH = [8].

3.3 Conclusions

In summary, we have shown that we can deposit Fmoc-3 hydrogels at high pH on electrode surfaces via the electrochemical reduction of hydrogen peroxide or the electrolysis of water. In both cases, the generation of hydroxide ions at the electrode-solution interface creates a basic pH zone growing from the electrode front. However, unlike the electrochemical reduction of hydrogen peroxide which produces no gaseous by-products, the electrolysis of water produces hydrogen gas alongside hydroxide ions. As a result, when Fmoc-3 hydrogels are formed on electrode surfaces using the electrolysis of water, the final material is perforated with multiple holes where the hydrogen gas bubbles have escaped. In this chapter we have shown that the material properties can be greatly improved by the addition hydrogen peroxide. As the concentration of hydrogen peroxide is increased, the mechanical properties become much more reproducible and homogeneous, which is of the utmost importance for potential future material applications.

We have also shown that despite having very different surface topography and material homogeneity, Fmoc-3 hydrogels grown in the absence of hydrogen peroxide and across the full hydrogen peroxide concentration range (10 – 40 mM) display a very similar microstructure. Using confocal microscopy, images confirmed the presence of long fibers with a number of spherulitic domains in all cases. This was also observed at various deposition times (300, 600 and 900 seconds) indicating that the microstructure remains the same/very similar as the hydrogel grows with time. For the Fmoc-3 hydrogels grown in the presence of 40 mM hydrogen peroxide, confocal images show that the fibers appear to be longer as well as displaying a greater contrast with the solvent in comparison to the hydrogels grown in the absence of hydrogen peroxide and at lower hydrogen peroxide concentrations (10-30 mM). We attributed this difference to the lack of air bubble holes throughout the bulk material, meaning the gel network experiences less disruption/breakage. Thus, increasing the contrast with the solvent and the fibre length of the microstructure as a result of the increased homogeneity of the sample. To further investigate the microstructure of the Fmoc-3 hydrogels, we attempted to collect SEM images of the dehydrated hydrogels/xerogels. Unfortunately, no informative information could be drawn from these images due to the presence of significant drying artefacts.

Using SAXS, the primary self-assembled structures of the Fmoc-3 hydrogels were probed. Unlike the microstructure, changes to the structures were observed as the concentration of hydrogen peroxide was varied. The data suggests that as the concentration of hydrogen peroxide decreases, the self-assembled structures transition from tape-like to more spherical

shaped structures. As well as this, SAXS data were collected from Fmoc-3 hydrogels grown in 40 mM hydrogen peroxide solutions at various deposition times (300, 600 and 900 seconds). From the values collected, the data suggests that the self-assembled structures become more flexible as deposition time increases.

As an extension of the work in this chapter we have also shown that this system can be coupled with the electrofabrication method seen in chapter 2 by employing a custom-made H-cell. This sees the simultaneous formation of two hydrogels triggered at opposing pH extremes in a spatially and temporally controlled manner. This approach greatly expands the electrofabrication approach using LMWG.

In this work, we have shown the first electrodeposition of a LMWG at high pH via the electrochemical reduction of hydrogen peroxide and the electrolysis of water. As well as this, we have also reported the first known example of the gelation of two chemically different LMWG at opposing pH extremes on different electrodes simultaneously.

Almost all the previous work on the electrodeposition of hydrogels on electrode surfaces have focused on polymer-based hydrogels.[3, 11, 32, 33] We hope that through the work in this chapter, the addition of LMWG-based hydrogels and the unique material properties that they bestow will provide advances to the field of electrodeposition as well as promote the development of LMWG for future practical applications.

3.4 Experimental

3.4.1 Instrument and Procedures

Materials

Mono-Fmoc 1,3-diaminopropane hydrochloride (Fmoc-DAP.HCl, Fmoc-3) was purchased from Fluorochem Ltd and stored in a laboratory-grade fridge. 2NapVG was synthesized as previously reported[34] and stored at room temperature. Hydrogen peroxide (30 % stabilized) solution was purchased from Avantor and stored in a laboratory-grade fridge.

Preparation of solutions for electrochemical gelation

All solutions of Fmoc-3 and hydrogen peroxide were made fresh at the beginning of every day using deionized Milli-Q water. To prepare Fmoc-3 solutions at a concentration of 5 mg/mL, 35 mg of Fmoc-3 was weighed into a 10.5 mL glass vial. 7 mL of NaCl (aq. 0.1 M) was added. The solution was then stirred using a magnetic stirring plate and stir bar until all solids had dissolved. Solutions were stored in the fridge during the day prior to use.

Immediately before the gelation process, 70 μL of hydrogen peroxide solution (between 1 and 4 M, see main text) were pipetted to make up the final solution.

2NapVG stock solutions (200 mL) were prepared at a concentration of 5 mg/mL and adjusted to pH 8 using NaOH (aq. 0.1 M) and HCl (aq. 0.1 M). To make the stock solutions, the appropriate mass of 2NapVG was dissolved in NaCl (aq. 0.1 M) and 1 molar equivalent of NaOH (using 1 M aq. soln) in a 250 mL glass jar. The solution was then then left to stir overnight to ensure all solids had dissolved. The following day, the pH was adjusted to pH 8. As hydroquinone oxidizes above pH 10, the pH of the solutions must be adjusted. All 2NapVG solutions were stored at room temperature and made fresh at the beginning of every week using deionized Milli-Q water. To make the gelator solution used for the electrofabrication process, hydroquinone (5 mg/mL) was weighed into a glass vial. The appropriate volume of 2NapVG stock solution (5 mg/mL) was then pipetted into the vial and stirred using a magnetic stirring plate and stir bar until all the hydroquinone had dissolved. This solution was then used immediately.

pH measurements

All pH measurements were collected using A FC200 pH probe from HANNA instruments with a 6 mm x 10 mm conical tip. The stated error of each measurement is ±1. To adjust the pH of the 2Nap-VG-OH stock solutions to pH 8, 20 μL aliquots of NaOH (aq. 0.1 M)/HCl (aq. 0.1 M) were added to the solution. After the addition of each aliquot, the solution was stirred for 30 seconds before taking another measurement. This was repeated until the bulk solution reached the desired pH 8.

Fmoc gel forming procedure on FTO slide

To grow the Fmoc-3 hydrogels, the three-electrode set-up consisting of a working electrode (FTO glass slide 12 x 15 mm), reference electrode (Ag/AgCl) and counter electrode (platinum wire) was assembled in a glass chamber. 7 mL of the Fmoc-3 gelator solution was then pipetted into the chamber immediately prior to the electrochemical experiment. A current density of -0.7 mA/cm^2 was found to be satisfactory for sufficient gel growth and was applied to the working electrode surface (FTO slide) for 900 seconds using chronopotentiometry. After the 900 seconds, the FTO slide with the hydrogel attached was removed and placed within a petri dish. To prevent the hydrogel from drying out, a wet paper towel was placed around the edges of the petri dish and the lid secured. This procedure was repeated for hydrogels grown in the absence of hydrogen peroxide and all the concentrations of hydrogen peroxide used.

Confocal fluorescence microscopy

A Zeiss LSM510 on a Zeiss Observer Z1 (Zeiss, Jena, Germany) was used for imaging. The gel samples were prepared as previously mentioned and placed within an aqueous Nile blue solution (2 μL/mL of a 0.1 wt% solution) for 30 minutes before imaging. After leaving the gels in the aqueous Nile Blue solution for 30 minutes, the gel was removed, and small sections of the gel were cut using a scalpel and placed on a microscope slide (Thermo scientific, 76 x 26 mm). A cover slip was then placed on top of the gel. Images were then collected by exciting the sample at 633 nm and detected with a Zeiss Meta detector. Data were captured using Zeiss Zen software (Zeiss, Jena, Germany) and analysed using Zeiss LSM image browser (version 4.2.0.121). This was the same procedure for all samples.

Image analysis

Images of the Fmoc-3 hydrogels growing on the electrode surface were taken at 30 second intervals using an iPhone 12 camera. To analyze these images, the photos were uploaded to the open-source image processing program ImageJ. To calculate the change in gel area with time, the outline of the hydrogel on each image was traced, allowing a gel area vs time graph to be plotted on OriginLab software.

Quantitative NMR

Using a Bruker Avance III 500 MHz spectrometer, ^{1}H NMR spectra were recorded. To determine the concentration of Fmoc-3 within the hydrogels, the gels were first frozen for two-three hours in a laboratory grade freezer. Once frozen, the gels were placed into the freeze dryer (CHRIST, Alpha 2-4 LSCbasic) for two hours. The freeze-dried gels were then dissolved in in DMSO-d_6 and transferred into an NMR tube. To determine the relative concentration of the Fmoc-3 hydrogels, a lock tube of known concentration (1% PDMS in C_2Cl_4) was used as an external standard. The gelator concentration within the gels could then be calculated.

Electrochemical measurements

The three-electrode set up was used to run chronopotentiometry measurements. All electrochemical measurements and data were collected using a Dropsens potentiostat on the software PSTrace 5.8. To grow the gels, a current density of -0.7 mA/cm^2 was applied to the working electrode using chronopotentiometry for the allocated time.

Rheology

Rheological measurements were carried out using an Anton Paar Physica MCR301 rheometer (Figure 3.15). A parallel plate (12.5 mm diameter, smooth) was used to measure frequency and strain sweeps. For measuring the frequency and strain sweeps, the FTO slide with gel attached was placed onto the rheometer and secured onto the bottom plate using Sellotape to prevent slipping. As the hydrogel was not removed from the FTO surface after gel deposition, no damage occurred. Rheological measurements were recorded at 25 °C. Strain sweeps were measured from 0.01 % to 100 % with a constant frequency of 10 rad/s. Frequency scans were performed from 1 rad/s to 100 rad/s under a constant strain of 0.05%. All measurements were performed in triplicate and errors were calculated from the standard deviation.

Figure 3.15 Photograph of the experimental set-up used to collect rheological measurements from the Fmoc-3 hydrogels using a parallel plate geometry (12.5 mm). To prevent the hydrogel from slipping, the FTO glass slides with the hydrogels attached were secured to the plate using tape.

Scanning electron microscope (SEM)

SEM images were collected on a PC controlled environmental scanning electron microscope (FEI Phillips/ XL30 ESEM). The hydrogels were prepared as previously mentioned and left to dry overnight. To prevent charging and obtain better images, the dried hydrogels/xerogels

attached to the glass FTO electrodes were sputter coated prior to imaging using a Polaron SC7640 auto/manual high resolution sputter coater with a Gold/Palladium target. Images were then collected using a tungsten electron gun (accelerating voltage 1kV – 30kV) and standard SE and BSE detectors. This was the same procedure for all the samples.

Small angle X-ray scattering

Small-angle X-ray scattering (SAXS) measurements were performed using Anton Paar SAXS Point 2.0 (Cu, K_α= 1.54 Å) at the University of Bath. This beamline operates at a fixed energy of 8.04 keV and SAXS patterns were collected at a sample-detector distance of 572mm, resulting in a Q range of 0.07– 3.3 nm^{-1}. For each sample, 1 frame was acquired with an acquisition time of 30 mins. An Anton Paar Multiple-Solid Sample Holder (Figure 3.16a-b) was used to load the samples. It comprises two metal plates with 5*4 grids (11*11 mm for each grid) sandwiching a Kapton sheet. Appropriate amounts (ca. 10 mg each) of the electrochemically processed gels were transferred into different cells of the sample holder, followed by topping with 10µl of DI water. All 2D patterns were acquired on a Dectris Eiger detector and reduced by azimuthal integration into 1D I vs Q plots using the Anton Paar SAXS Analysis software.

The scattering length density of Fmoc-3 was calculated using the National Institute of Standards and Technology Neutron[35] activation and scattering calculator to give a value of 14.069 x 10^{-6}/Å^2. A scattering length density of 9.469 x 10^{-6} Å^{-2} was used for the solvent.

For all the samples, the collected water background resulted in an over-subtraction of the data. To account for this, the water background for each sample was normalized to the intensity of the Kapton peak (~4 nm^{-1}). For all the 1D I vs Q plots, the scaled water background was subtracted in excel before loading the subtracted data in the SasView software package (Version 5.0.5).[31] In all cases, the subtracted data were fitted to a flexible elliptical cylinder model with polydispersity of the radius to give low χ^2 values. It is important to note that the fitting error is obtained from the fitting software and does not consider any other sources of error.
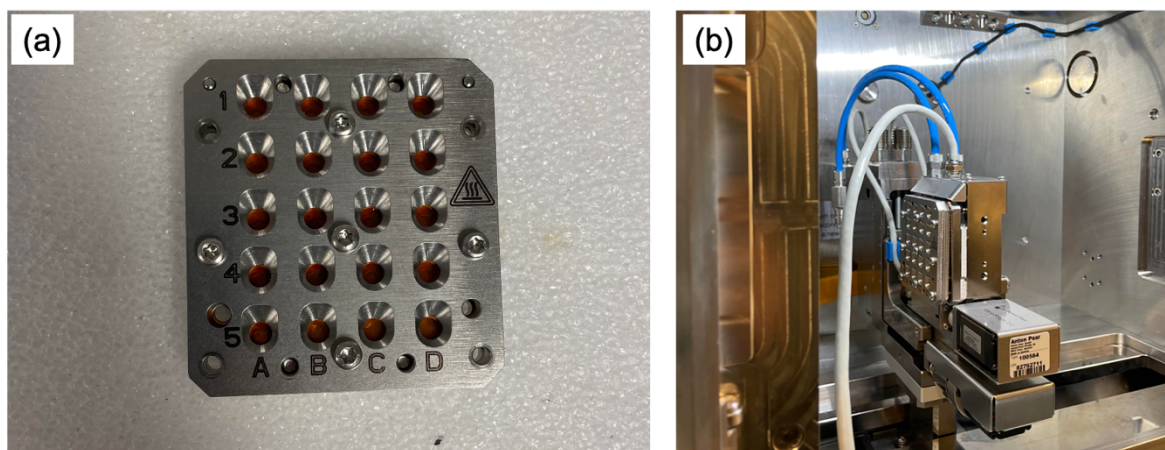
Figure 3.16. (a) Image of Anton Paar Multiple-Solid Sample Holder used to collect the SAXS measurements of the Fmoc-3 hydrogels (b) Image showing the set-up of the sample holder within the SAXS instrument.

Dual hydrogel formation in H-Cell

To grow Fmoc-3 and 2NapVG hydrogels simultaneously, a custom-built H-cell consisting of two 25 mL cell chambers separated by a Nafion membrane was used to connect the two gelator solutions. The right-hand side chamber used to grow the 2NapVG hydrogel consisted of the working electrode (1.2mm glassy carbon) and the reference electrode (aq. Ag/AgCl, 3 M). The left-hand side chamber used to grow the Fmoc-3 hydrogel consisted of the counter electrode (platinum wire).

Prior to gel deposition, 20 mL of 2NapVG/hydroquinone solution (pH 8) was pipetted into the right-hand side chamber followed by pipetting 20 mL of Fmoc-3/hydrogen peroxide solution into the left-hand side chamber. To grow the hydrogels simultaneously, a current density of 22 mA/cm^2 was applied to the working electrode (Figure 3.16b). This seen the formation of hydrogels on both the working and counter electrode surface.
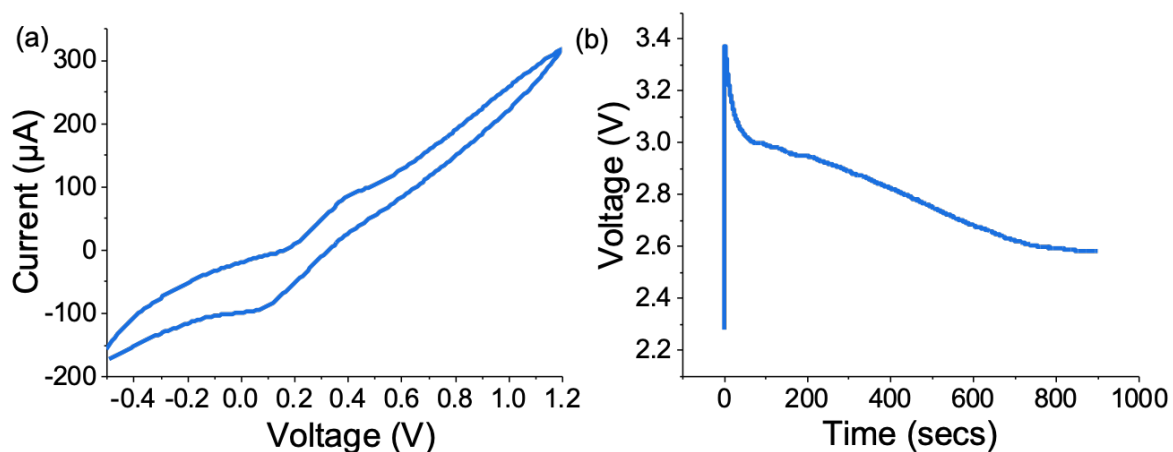
Figure 3.16. (a) Cyclic voltammetry and (b) chronopotentiometry measurements of the dual hydrogel system (Fmoc-3 = [5 mg/mL], NaCl = [aq. 0.1 M], H_2O_2 = [40 mM], 2NapVG = [5 mg/mL], hydroquinone [5 mg/mL], NaCl = [aq. 0.1 M], pH = [8]. Current density = [22 mA/cm^2], deposition time = [900 seconds].

3.5 References

1.   J. Zhuang, S. Lin, L. Dong, K. Cheng and W. Weng, *ACS Biomater. Sci. Eng.*, 2018, **4**, 1528-1535.

2.   J. Li, S. Wu, E. Kim, K. Yan, H. Liu, C. Liu, H. Dong, X. Qu, X. Shi, J. Shen, W. E. Bentley and G. F. Payne, *Biofabrication*, 2019, **11**, 032002.

3.   Z. Yang, Z. Yuye, L. Houbin, D. Fuyuan and S. Xiaowen, *Curr. Med. Chem.,* 2019, **26**, 1-21.

4.   K. Sipa, K. Kowalewska, A. Leniart, A. Walcarius, G. Herzog, S. Skrzypek and L. Poltorak, *Electrochem. Commun.* 2021, **123**, 106910.

5.   C. Patterson, B. Dietrich, C. Wilson, A. R. Mount and D. J. Adams, *Soft Matter*, 2022, **5**, 1064-1070.

6.   Y. Liu, E. Kim, R. V. Ulijn, W. E. Bentley and G. F. Payne, *Adv. Funct. Mater.*, 2011, **21**, 1575-1580.

7.   M. Lei, X. Qu, H. Wan, D. Jin, S. Wang, Z. Zhao, M. Yin, F. Payne Gregory and C. Liu, *Sci. Adv.*, 2022, **8**, eabl7506.

8.   S. Wu, K. Yan, J. Li, R. N. Huynh, C. B. Raub, J. Shen, X. Shi and G. F. Payne, *React. Funct. Polym.*, 2020, **148**, 104492.

9.   X. Qu, H. Liu, C. Zhang, Y. Lei, M. Lei, M. Xu, D. Jin, P. Li, M. Yin, G. F. Payne and C. Liu, *Acta Biomater.*, 2018, **73**, 190-203.

10.   J. E. Bressner, B. Marelli, G. Qin, L. E. Klinker, Y. Zhang, D. L. Kaplan and F. G. Omenetto, *J. Mater. Chem., B*, 2014, **2**, 4983-4987.

11.   F. Ozawa, K. Ino, T. Arai, J. Ramón-Azcón, Y. Takahashi, H. Shiku and T. Matsue, *Lab Chip*, 2013, **13**, 3128-3135.

12.   A. Gargava, S. Ahn, W. E. Bentley and S. R. Raghavan, *ACS Appl. Mater. Interfaces*, 2019, **11**, 37103-37111.

13.   E. K. Johnson, D. J. Adams and P. J. Cameron, *J. Am. Chem. Soc.,* 2010, **132**, 5130-5136.

14.   M. Lei, X. Qu, H. Liu, Y. Liu, S. Wang, S. Wu, W. E. Bentley, G. F. Payne and C. Liu, *Adv. Funct. Mater.*, 2019, **29**, 1900065.

15.   J. Raeburn, B. Alston, J. Kroeger, T. O. McDonald, J. R. Howse, P. J. Cameron and D. J. Adams, *Mater.Horiz.*, 2014, **1**, 241-246.

16.   V. Lakshminarayanan, L. Poltorak, E. J. R. Sudhölter, E. Mendes and J. van Esch, *Electrochim. Acta*, 2020, **350**, 136352.

17.   Y. Cheng, X. Luo, J. Betz, S. Buckhout-White, O. Bekdash, G. F. Payne, W. E. Bentley and G. W. Rubloff, *Soft Matter*, 2010, **6**, 3177-3183.

18.   R. A. Zangmeister, J. J. Park, G. W. Rubloff and M. J. Tarlov, *Electrochim. Acta*, 2006, **51**, 5324-5333.

19.   S. Panja and D. J. Adams, *Chem. Commun.*, 2019, **55**, 47-50.

20.   G. G. Leisk, T. J. Lo, T. Yucel, Q. Lu and D. L. Kaplan, *Adv. Mater.*, 2010, **22**, 711-715.

21.   D. A. Wellings and E. Atherton, in *Methods in Enzymology*, ed. G. B. Fields, Academic Press, Cambridge, 1st edn, 1997, vol. 289, pp. 44-67.

22.   A. M. Fuentes-Caparrós, Z. Canales-Galarza, M. Barrow, B. Dietrich, J. Läuger, M. Nemeth, E. R. Draper and D. J. Adams, *Biomacromolecules*, 2021, **22**, 1625-1638.

23.   J. A. Zimberlin, N. Sanabria-DeLong, G. N. Tew and A. J. Crosby, *Soft Matter*, 2007, **3**, 763-767.

24.   A. M. Fuentes-Caparrós, B. Dietrich, L. Thomson, C. Chauveau and D. J. Adams, *Soft Matter*, 2019, **15**, 6340-6347.

25.   S. Takai, S. Murakami, L. Zhang, K. Ohsasa and S. Watanabe, *ACS Appl. Eng. Mater.*, 2023, **1**, 80-86.

26.   J. Zhong, T. Zhao and M. Liu, *NPG Asia Materials*, 2022, **14**, 38.

27.   D. J. Adams, *Gels*, 2018, **4**, 32.

28.   J. Raeburn, C. Mendoza-Cuenca, B. N. Cattoz, M. A. Little, A. E. Terry, A. Zamith Cardoso, P. C. Griffiths and D. J. Adams, *Soft Matter*, 2015, **11**, 927-935.

29.   X.-L. Wang, R. Sun, W.-J. Zhu, X.-L. Sha and J.-F. Ge, *J. Fluores.*, 2017, **27**, 819-827.

30.   E. R. Draper and D. J. Adams, *Chem. Soc. Rev.*, 2018, **47**, 3395-3405.

31.   SasView, http://www.sasview.org/, (acessed 10 August 2022).

32.   R. Elia, C. D. Michelson, A. L. Perera, M. Harsono, G. G. Leisk, G. Kugel and D. L. Kaplan, *J. Biomater. Appl.,* 2015, **29**, 1247-1255.

33.   K. M. Gray, B. D. Liba, Y. Wang, Y. Cheng, G. W. Rubloff, W. E. Bentley, A. Montembault, I. Royaud, L. David and G. F. Payne, *Biomacromolecules*, 2012, **13**, 1181-1189.

34.   L. Chen, S. Revel, K. Morris, L. C. Serpell and D. J. Adams, *Langmuir*, 2010, **26**, 13466-13471.

35.   NIST, https://www.ncnr.nist.gov/resources/activation/ (acessed 10 August 2022).

CHAPTER 4

The Electrofabrication of Carbazole-Protected Amino Acid
Hydrogels and their Subsequent Polymerisation to Form
Electrochromic Polymers

4.1 Introduction

Short-chain *N*-protected peptides are a highly effective class of low molecular weight gelator molecules.[1-4] Hydrogels based on these small synthetic molecules have rapidly gained popularity in the fields of drug delivery, cell scaffolding and tissue engineering due several attractive properties.[5-8] Short-chained *N*-protected peptides are easily synthesized and can often be biocompatible due to the presence of biorelevant amino acid sequences on the gelator backbone.[9] They also offer a number of advantages over polymer-based hydrogels, owing to the non-covalent interactions that maintain the gel network.[10, 11] As the supramolecular network is easily perturbed, hydrogels formed from these materials can often display reversible and dynamic material properties.[12] As this class of gelator is synthetic, chemical homogeneity and reproducibility can often be improved relative to naturally derived gelator molecules. For example, it has been shown that for naturally derived polymeric gels such as collagen, very small changes in the sequence distribution can dramatically affect the function of encapsulated cells in the hydrogel matrix, leading to batch-to-batch variability.[13]

For short-chain *N*-protected peptides, the aromatic capping group on the *N*-terminus of the molecule is required to drive the gelation process via hydrophobic and π- π stacking interactions.[14] The choice of capping group has also been shown to have significant effects on the hierarchal self-assembly of the gelator molecules and as a result, the final material properties of the hydrogel.[15] Examples of various aromatic capping groups include; naphthalene[16], Fmoc[17], phenothiazine[18], carboxybenzyl[19] and azobenzene.[20]

As the Fmoc-group is a common orthogonal protecting in solid phase peptide synthesis (SPPS), it has become a popular choice of capping group for short-chained *N*-protected peptides due to its ease of synthesis and commercial availability (Figure 4.1a).[14, 21] However, studies have reported cytotoxicity *in vitro* at elevated concentrations.[22] A further drawback to using the Fmoc protecting group is that it is readily cleaved under mildly basic conditions. At pH values above 10, the acidic proton at the 9-position of the fluorene ring is abstracted, followed by β-elimination to give the highly reactive molecule dibenzofulvene.[23] To circumvent this issue, the Fmoc-capping group can be replaced with carbazole, which can be considered an analogue to the fluorene moiety that is present in the Fmoc-capping group. In comparison to the Fmoc-capping group, carbazole-protected peptides (Figure 4.1b) display reduced cytotoxicity and increased stability at high pH.[24] With this considered,

carbazole-capped peptide hydrogels present an attractive alternative to Fmoc-capped peptide hydrogels.
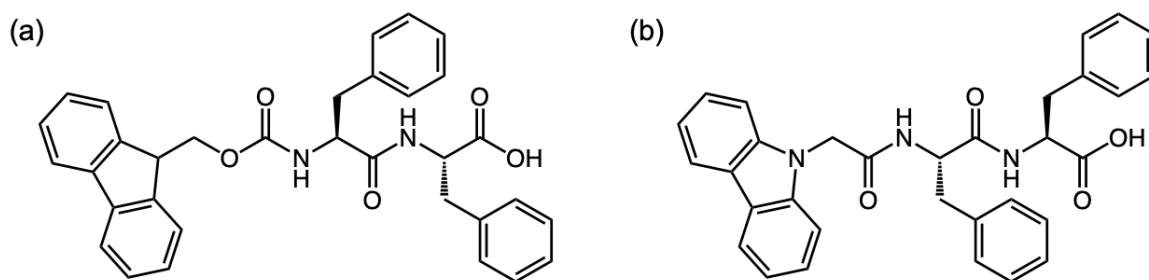
Figure 4.1 (a) Chemical structure of the Fmoc-protected peptide Fmoc-Phe-Phe and (b) the carbazole protected peptide Carb-Phe-Phe (three letter code used to represent amino acid).

As well as being used to form supramolecular hydrogels, Fmoc-capped and carbazole-capped peptides can both be electrochemically polymerised to form redox polymers in organic solvents.[25, 26] For both classes of materials, deposition of conductive polymers can be achieved on electrode surfaces via the direct electrochemical oxidation of the corresponding monomers in organic solutions. This technique sees many distinct advantages as the fabrication of polymers can be done in one step, is catalyst free and only requires a very small amount of the corresponding monomer in solution. The thickness of the resultant polymer films can also be easily controlled by adjusting the time of the applied anodic potential. As a result, these conductive materials show great potential as photovoltaic devices, light emitting diodes and sensors.[27-29]

For Fmoc-protected amino acids, anodic oxidation can be used to form polyfluorene-based polymers which display thermal and oxidative stability, excellent charge transport properties and high luminesce yields (Figure 4.2).[25, 30, 31] As well as this, the presence of the amino acid on the polymer side chain renders the material a biological macromolecule. This opens up the materials to applications such as DNA sensors as the carboxylate groups on the amino acids can form covalent bonds with biologically active materials. In 1999, Rault-Berthelot et al.[30] showed the electrochemical oxidation of various Fmoc-protected amino-acids in solutions of acetonitrile and tetrabutylammonium tetrafluoroborate including; Fmoc-Ala, Fmoc-Val and Fmoc-Iso (three-letter code used to represent amino acids). In all cases, insoluble electroactive polymers were formed on electrode surfaces with a polyfluorene backbone and retention of the amino acid side chain.[30] It was also shown that these polymers displayed chiral discrimination towards pure enantiomers, allowing them to function as

highly effective chiral sensors. Lai et al.[31] also showed that blue-light emitting polyfluorene-based polymers could be deposited on ITO electrodes using an applied potential of 1.6 V from solutions of Fmoc-Phe (Figure 4.2). In contrast to previous work, the anodic polymerisation of Fmoc-Phe was undertaken in solutions of boron trifluoride diethyl etherate (BFEE). The subsequent use of BFEE lowered the oxidation potential required to electropolymerize the aromatic monomer due to interactions between the aromatic monomer and the medium-strong Lewis acid BFEE.[31] In 2016, Zhang and et. al.[25] electropolymerized Fmoc-Gly in a mixed solution of BFEE and dichloromethane, confirming the electropolymerisation occurred at the C2 and C7 positions of the fluorene units. They then went on to show that this polyfluorene-based film could function as an optical sensor, detecting Fe^{3+}, Cu^{2+} and $Cr_2O_7^{2-}$ via UV and fluorescence responses.[25]
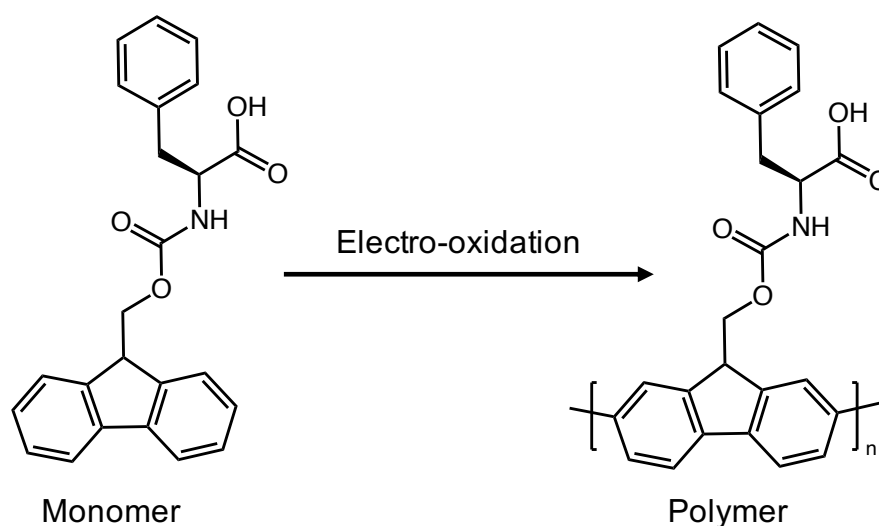
Figure 4.2 The electrochemical oxidation of the Fmoc-protected amino acid (Fmoc-Phe) to give the polyfluorene-based polymer with retention of the amino acid side chain.

In comparison to Fmoc-protected amino acids, the direct electropolymerisation of carbazole-protected amino acids in organic solutions is much less researched. Polycarbazole is a well-established redox polymer known for its unique electrochemical and optical properties and can be formed via the anodic oxidation of carbazole in organic solutions.[32] In 2015, Thordarson et al.[24] reported the first example of a carbazole-protected dipeptide and tripeptide. In the same year, Cameron and co-workers[26] then went on to show the first electropolymerisation of the carbazole-protected amino acid Carb-Ala (Figure 4.3a) in

acetonitrile. In comparison to Fmoc-Ala (which forms fluorene-based polymers), they reported a significant decrease in the onset oxidation potential required to electropolymerize Carb-Ala in acetonitrile.[26] For polymer fabrication, this decrease of the onset oxidation potential is highly desirable as it lowers the chances of side reactions, leading to higher quality polymer films.

However, the main focus of this study was the fabrication of an electrochromic polymer with a unique structure from pre-assembled hydrogels of Carb-Ala on electrode surfaces.[26] In comparison to the dense polymers formed from Carb-Ala in acetonitrile, the polymers fabricated from the pre-assembled hydrogels displayed a much more open, fibrous structure (Figure 4.3d).[26] For conjugated polymers, the morphology plays a significant role in determining the bulk physical properties of the final material.[33] To meet the demands of multiple material applications, it is therefore highly desirable to fabricate polymers with a controlled and unique morphology.
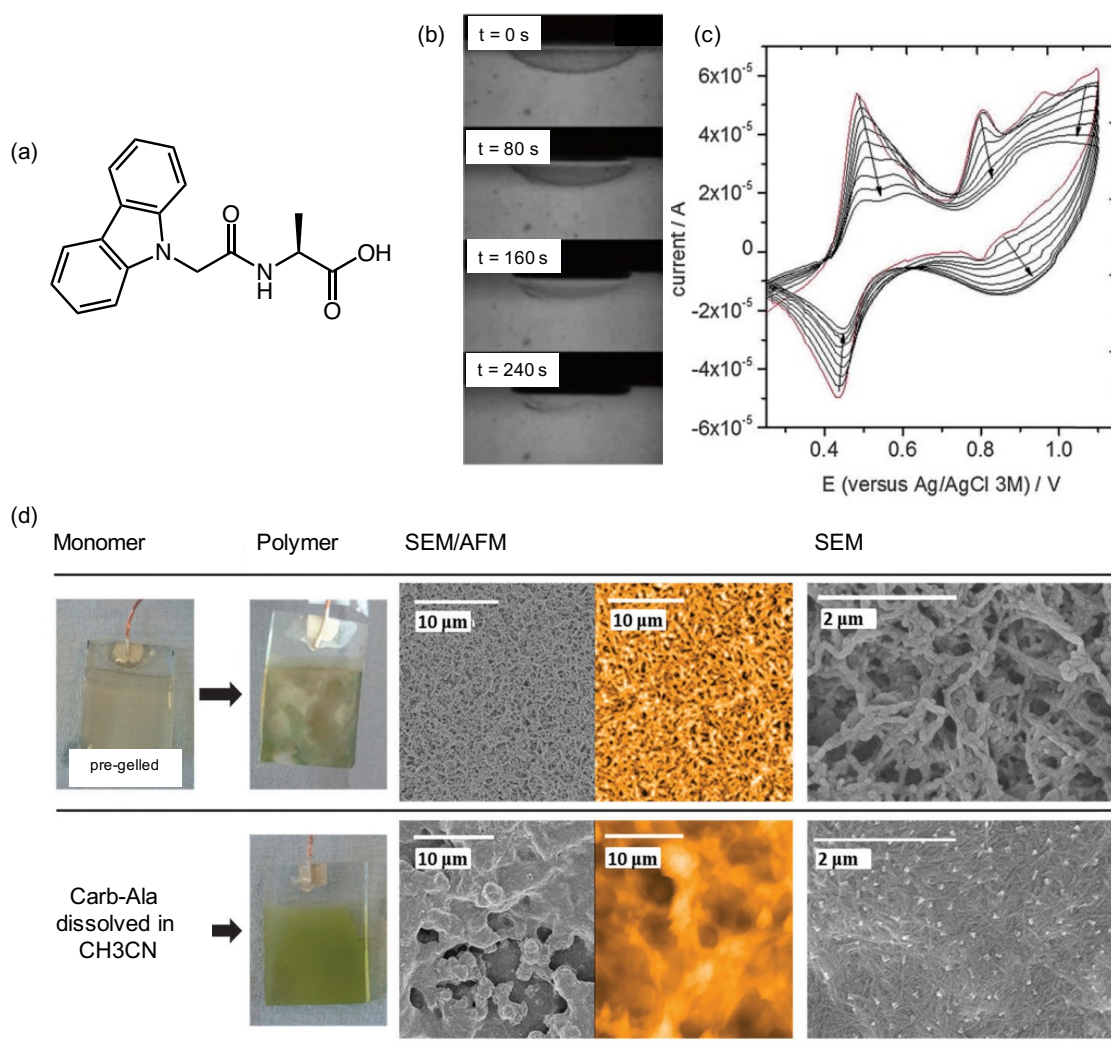
Figure 4.3 (a) Chemical structure of the carbazole-protected amino acid Carb-Ala (b) Images showing the electropolymerisation of pre-formed Carb-Ala hydrogels on electrode surfaces. Cyclic voltammograms (CVs) were repeatedly cycled above the oxidation potential of Carb-Ala, causing the gel to collapse into a dense polymer film. The images show the hydrogel collapsing during the first 8 CV cycles (50 mV, 34 secs per scan) (c) CV cycles taken during the electropolymerisation of Carb-Ala as shown in part (b). The peaks above 0.75 V correspond to the oxidation of Carb-Ala (d) Images comparing the different polymer morphologies of poly(carb-Ala) formed as a result of different electropolymerisation conditions. The top row shows the morphology of the polymer formed from the electropolymerized hydrogel. The bottom row shows polymers formed from the anodic oxidation of Cab-Ala in acetonitrile. SEM and AFM images show the large differences in the microstructures of the poly(Carb-Ala) materials. Images reproduced from *Chem. Comm.,* 2015, **51**, 10427-10430 with permission from the Royal Society of Chemistry.[26]

To deposit the unique polymer films on electrode surfaces, Cameron and co-workers[26] first grew Carb-Ala hydrogels on electrodes via an electrochemically generated pH gradient. For short-chained *N*-protected peptides such as Carb-Ala, the free carboxylic acid group on the *C*-terminus renders the molecule is pH sensitive in aqueous solutions.[34] When the pH of the Carb-Ala solution drops below the pK_a of the terminal carboxylic acid, protonation of the charged carboxylate groups occurs to form the neutral carboxylic acid. Consequently, the electrostatic repulsion between the charged groups on the gelator structure is removed. The gelator molecules are then rendered less soluble in water. This causes the gelator molecules to self-assemble via non-covalent interactions to give long one-dimensional fibres which entangle to form the hydrogel network.[35, 36] To achieve this exclusively on electrode surfaces, hydroquinone (HQ) can be incorporated into gelator solutions. [26, 37, 38] The electrochemical oxidation of HQ to benzoquinone (BQ), generates protons, creating a localised acidic pH region at the electrode-solution interface. As the pH of the bulk gelator solution is unaffected, gelation occurs exclusively on the electrode surface, fabricating localised materials with excellent spatiotemporal control. [39, 40] Using this method, Cameron and co-workers fabricated transparent hydrogels of Carb-Ala on electrode surfaces prior to electropolymerisation (Figure 3.4b). To electropolymerize the Carb-Ala hydrogels, the electrode with the hydrogel attached was removed from the gelator/HQ solution and placed within a 1 mol dm^3 perchloric acid solution. The Carb-Ala hydrogel was then polymerised by the repeated cycling of cyclic voltammograms (Figure 4.3c) between 0.2 and 1.1 V (versus Ag/AgCl, 3 mol dm^3). This saw the collapse of the pre-assembled hydrogel to become part of an electrochromic polymer film on the electrode surface (Figure 4.3b). Using Fourier transform infrared (FTIR) and NMR spectroscopy, retention of the alanine group on the polycarbazole film was confirmed. SEM and AFM images (Figure 4.3d) of the electropolymerized films revealed a unique and open fibrous structure, whereas films of poly(carb-Ala) deposited from Carb-Ala in acetonitrile displayed a much denser morphology. In summary, Cameron and co-workers[26] have shown that the fibrous structures underpinning Carb-Ala hydrogels can be used as a 'template' for accessing polymers with a unique morphology.

4.2 Results and Discussion

4.2.1 Carbazole-protected amino acids

In this chapter, we expand upon the work described above[26], reporting the electrofabrication of hydrogels via the electrochemical oxidation of hydroquinone (HQ) for Carb-Ala, Carb-Gly, Carb-Val, Carb-Ile and Carb-Leu (Figure 4.4). As well as this, we report the full to partial electropolymerisation of the pre-assembled hydrogels in in perchloric acid (1 mol/L).
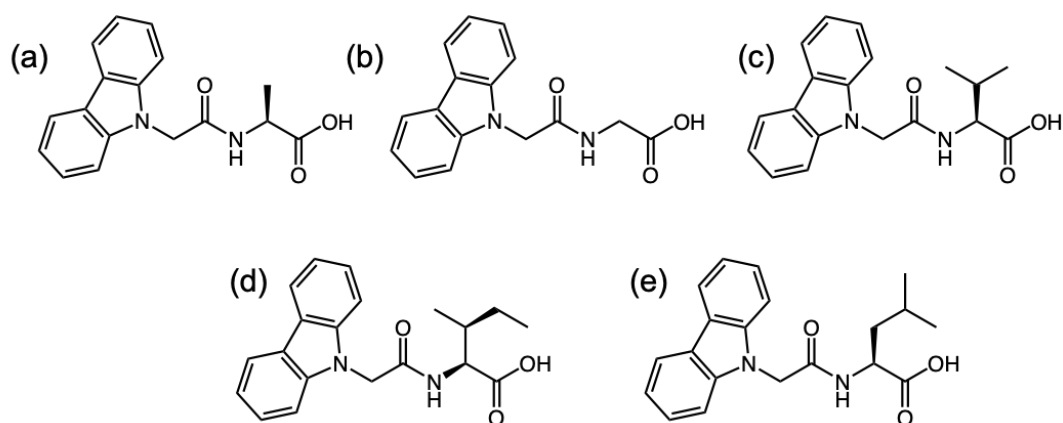
Figure 4.4 Chemical structures of the carbazole-protected amino acids (a) Carb-Ala (b) Carb-Gly (c) Carb-Val (d) Carb-Ile (e) Carb-Leu. A three-letter code is used to represent the amino acids.

To probe the primary self-assembled structures of the carbazole-based hydrogels growing in real time and their subsequent electropolymerisation in perchloric acid, a first-of-its-kind experiment was performed using small-angle X-ray scattering (SAXS) at Diamond Light Source (I22 beamline, Oxfordshire, UK).

4.2.2 Polymerisation of carbazole-protected amino acids in acetonitrile

For future comparison of the polycarbazole polymers formed from the pre-assembled hydrogels, the electropolymerisation of the carbazole-protected amino acids were first carried out in anhydrous acetonitrile. This was performed using a standard three-electrode set-up, consisting of a working electrode (FTO glass slide 12 x 15 mm), reference electrode (Ag/AgNO₃) and counter electrode (platinum wire). To deposit the polymers, 25 mg (5 mg/mL) of the carbazole-protected amino acid and 194 g (0.1 M) of the supporting electrolyte tetra-n-butylammonium hexafluorophosphate (Bu₄NPF₆) were dissolved in 5 mL of degassed anhydrous acetonitrile. As polymer deposition occurs as a result of monomer

oxidation, cyclic voltammetry (CV) measurements were carried out within a potential range of 0 to 1.1.V vs Ag/AgNO$_3$ (Figure 4.5).
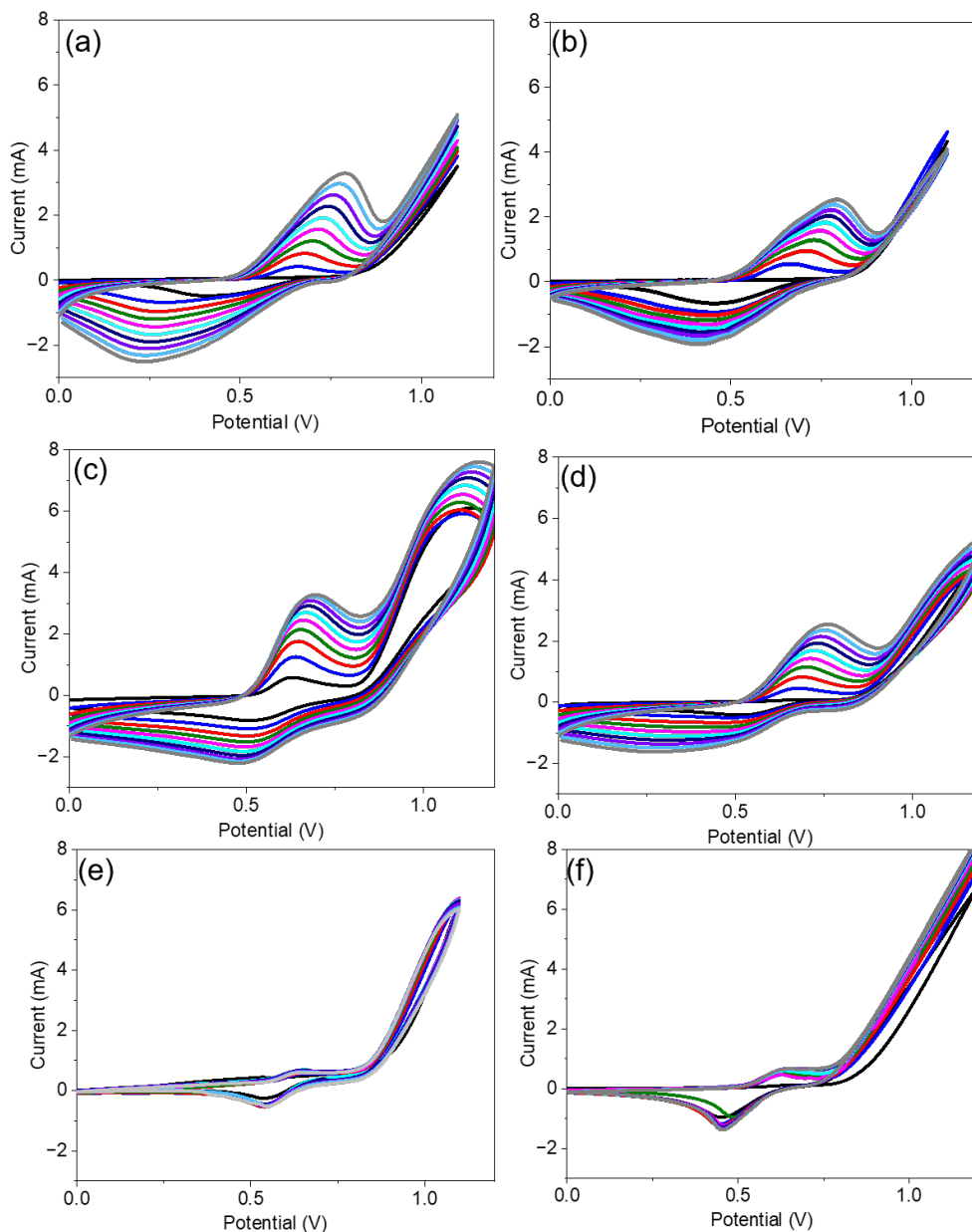
Figure 4.5 The first 10 CV measurements of the electropolymerisation of the carbazole-protected amino acids (a) Carb-Ala (b) Carb-Gly (c) Carb-Val (d) Carb-Ile (e) Carb-Leu and (f) Carbazole in anhydrous acetonitrile. Redox wave current densities increased as CV scans were cycled (black to grey). Conditions; [monomer] = 5 mg/mL, [Bu$_4$NPF$_6$] = 0.1 M, [scan rate] = 40 mV/s.

To deposit the polycarbazole films on the FTO glass surface (Figure 4.6), CV measurements were repeatedly cycled for 20 scans using a scan rate of 40 mV/s. In all cases, electrochromic polymer films were formed (Figure 4.6), cycling between green (oxidised form) and colourless (reduced form) with each CV. For all the carbazole-protected amino acids, the peaks corresponding to monomer oxidation and polymer formation occurred above 0.75 V. It is important to note that for Carb-Leu, the polymer film did not adhere/deposit onto the FTO glass surface. However, as the electropolymerisation process progressed, the colour of the solution around the electrode and at the bottom of the container turned increasingly green. This indicates that the oligomers formed at the electrode surface are partly soluble, causing them to diffuse away from the electrode into the bulk solution. As a result, no material characterisation is included for Carb-Leu in anhydrous acetonitrile.

Figure 4.6 Polycarbazole-based films of the carbazole-protected amino acids deposited on glass FTO slides via the electrochemical oxidation of monomers in anhydrous acetonitrile. From left to right; Carb-Ala, Carb-Gly, Carb-Val, and Carb-Ile. Carb-Leu excluded as the polymer does not adhere to the FTO glass surface. Conditions; [monomer] = 5 mg/mL, [Bu$_4$NPF$_6$] = 0.1 M, [scan rate] = 40 mV/s. Scale bar: 1 cm.

4.2.3 Electrochemical growth of carbazole-protected hydrogels

To fabricate the spatially resolved hydrogels of the carbazole-protected amino acids, the electrochemical oxidation of hydroquinone (HQ) was employed. Again, a three-electrode set-up was used, involving a working electrode (FTO glass slide, 12 x 15 mm), reference electrode (aq. Ag/AgCl, 3 M) and counter electrode (platinum wire). To grow the carbazole-protected amino acid hydrogels, the pH of the gelator solutions (5 mg/mL) in NaCl (aq. 0.1 M) were adjusted from pH 11 to pH 7. As the oxidation of HQ is accelerated at high pH, the adjustment of pH prevents the HQ in solution oxidizing before it can be consumed

electrochemically. 7 mL of gelator solutions containing HQ (5 mg/mL) were then pipetted into the glass chamber containing the three-electrode set-up. A galvanostatic current of current density 0.7 mA/cm^2 was then applied to the working electrode (FTO slide) for 300 seconds. For all the carbazole-protected amino acids, this seen the formation of hydrogels of pH 3-4 on the FTO glass surface (Figure 4.7).
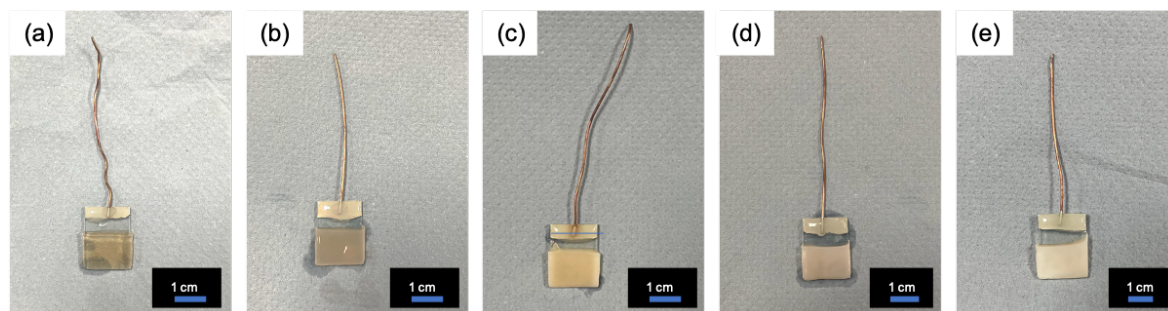
Figure 4.7 Images of spatially resolved hydrogels grown via the electrochemical oxidation of HQ: (a) Carb-Ala (b) Carb-Gly (c) Carb-Val (d) Carb-Ile (e) Carb-Leu. In all cases, conditions: [monomer] = 5 mg/mL, [HQ] = 5 mg/mL, [NaCl] = aq. 0.1 M, [current density] = 0.7 mA/cm^2, [deposition time] = 300 seconds. Scale bar = 1 cm.

4.2.4 Electropolymerisation of pre-assembled hydrogels

In 2015, Cameron and co-workers reported the first electrochemical polymerisation of Carb-Ala hydrogels in perchloric acid (aq. 1 mol/L). As a continuation of this work, we attempted to electropolymerise hydrogels of the carbazole-protected amino acids; Carb-Gly, Carb-Val, Carb-Ile and Carb-Leu. As the electropolymerisation of Carb-Ala has previously been reported, it was included as a control. It is important to note that due to the limited solubility of the polycarbazole materials, all the polymer films reported could only be dissolved in dimethylformamide (DMF). This meant that all characterisation of the polycarbazole materials by gel permeation chromatography (GPC) failed due to an insufficient difference in the refractive index of the polymer and the solvent.[26] As a result, we can only confirm that oligomerisation and possible polymerisation occurs. However, for convenience and in line with previous work, we will call it polymerisation for the entirety of this thesis chapter.

To electropolymerise the pre-assembled hydrogels, the hydrogels were first deposited on the FTO glass slides via the electrochemical oxidation of HQ as previously described. The FTO glass slide with the hydrogel attached was then removed from the gelator/HQ solution and placed in 7 mL of perchloric acid (1 mol/L). It is important to note that at this stage, there is

no free monomer in the perchloric acid solution. To electropolymerise the pre-assembled hydrogels in perchloric acid, CVs were repeatedly cycled from 0 to 1.1 V using a scan rate of 40 mV/s. In total, 100 scans were cycled, taking approximately one hour and thirty minutes to complete. Out of all the carbazole-protected amino acids investigated, only the pre-assembled hydrogels of Carb-Ala and Carb-Gly fully collapsed to become part of a denser polymer film on the FTO glass surface (Figure 4.8).
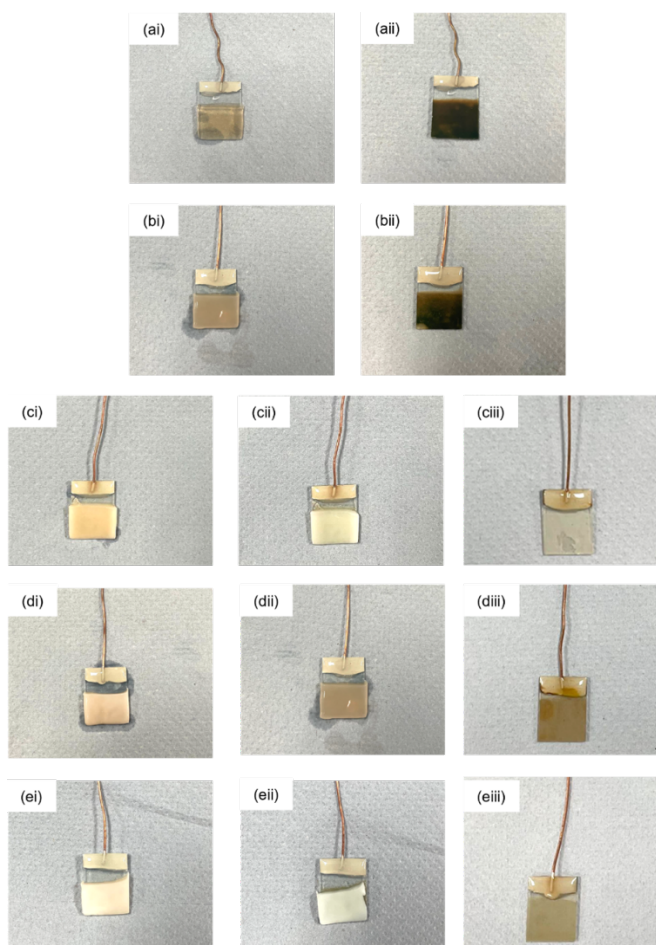
Figure 4.8 Images of the carbazole-protected amino acid hydrogels before (i) and after (ii) 100 successive CV cycles in perchloric acid (1 mol/L) for (a) Carb-Ala (b) Carb-Gly (c) Carb-Val (d) Carb-Ile (e) Carb-Leu. For Carb-Val (c), Carb-Ile (d) and Carb-Leu (e), complete collapse and electropolymerisation of the pre-assembled hydrogel does not occur. However, upon removing the remaining hydrogel from the electrode surface (iii), discolouration of the glass FTO slides can be seen underneath.

Like the polycarbazole films formed in anhydrous acetonitrile, the polymers deposited in perchloric acid were electrochromic, cycling between a green (oxidation) and colourless (reduction) during successive CV cycles. However, once the polymer films were rinsed with water and dried overnight in a vacuum oven (60 °C), they turned brown (Figure 4.8). This is most likely due to residual HQ/quinone trapped within the polymer film. Unlike Carb-Ala and Carb-Gly, the pre-assembled hydrogels of Carb-Val, Carb-Leu and Carb-Ile were still present on the FTO glass surface after the successive CV cycles were complete (Figure 4.8). Despite not collapsing to form a polymer film, electrochromic colour changes were observed with each CV at the FTO glass surface for Carb-Ile and Carb-Leu. For Carb-Val, no colour changes were observed during the successive CV cycles. Upon removing the hydrogels from the electrode surface, green discolouration was observed for Carb-Leu and Carb-Ile where the hydrogels had previously been attached (Figure 4.8d-e). This indicated that some degree of polymerisation had taken place. Upon drying, these films also turned a light brown colour due to residual HQ/quinone. For Carb-Val, no green discolouration was observed on the FTO glass slide upon removal of the hydrogel. Upon drying, a white coloured film was observed (Figure 4.8c).

In comparison to Carb-Ala and Carb-Gly, the amino acid side chains for Carb-Val, Carb-Ile and Carb-Leu are much bulkier and less flexible. It is therefore likely that the orientation and organisation of the Carb-Val, Carb-Ile and Carb-Leu molecules in the hydrogel network are more restricted. For this reason, it is possible that the π- π stacked gels cannot undergo the molecular reorganisation required to fully collapse into conjugated polymer films. As only the surface of the FTO glass under the pre-formed hydrogel is discoloured for Carb-Leu and Carb-Ile, it may be that only the carbazole-protected molecules in direct contact with the FTO glass can be electropolymerized. As Carb-Val is the bulkiest carbazole-protected amino acid in the group, this may be why no evidence of electropolymerisation is seen at this stage.

Firstly, the electrochemical behaviour and current response of the polymerisation process was investigated with successive CV scans for Carb-Ala (Figure 4.9).
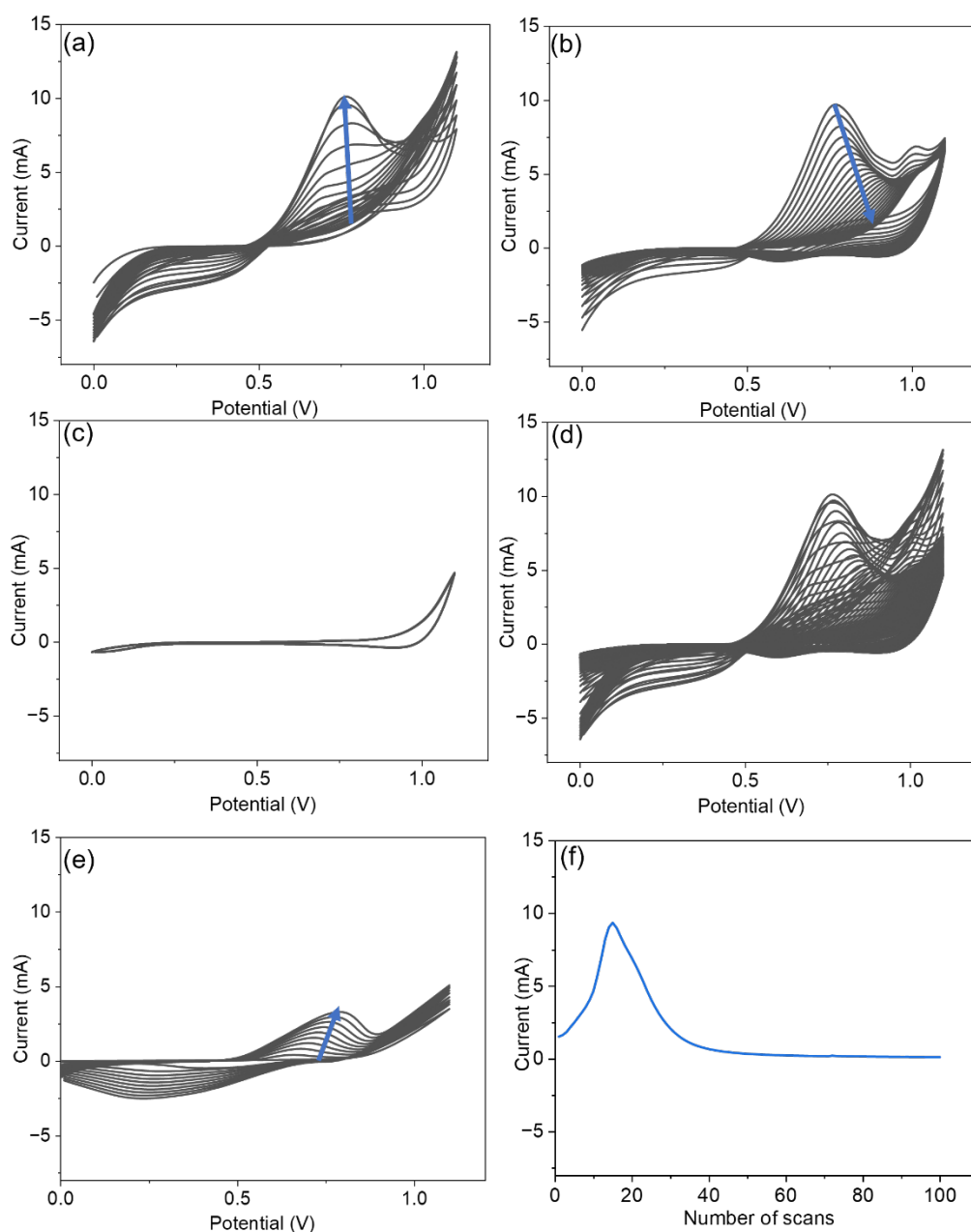
Figure 4.9 CV cycles taken during the electropolymerisation of Carb-Ala hydrogels (a) Cycles 1-15 (b) Cycles 16-40 (c) Cycles 95-100 (d) Cycles 1-100 (e) First ten CV cycles taken during the electropolymerisation of Carb-Ala in anhydrous acetonitrile (f) Current response at 0.8 V taken from (d) vs number of CV scans.   In all cases, CVs were scanned from 0 to 1.1 V using a scan rate of 40 mV/s. The order of CV cycles is shown by the direction of the arrows. For a-d, conditions: [monomer] = 5 mg/mL, [HClO$_4$] = 1 M. For e, conditions: [monomer] = 5 mg/mL, [Bu$_4$NPF$_6$] = 0.1 M.

For the first fifteen successive CV cycles (Figure 4.9a), the oxidation peak at 0.8 V increases in intensity with recurrent CV scans. The increase of the oxidation peak current density with increasing CV cycles indicates an increase in the amount of the conductive polymer being deposited on the FTO glass surface.[41] Unlike the polymer films formed in acetonitrile (Figure 4.9e), no reduction peak is observed, indicating that this oxidation process is non-reversible. This is to be expected as there are no free monomers present in the perchloric acid solution. After scan 15, the oxidation peak current density begins to decrease (Figure 4.9b). Due to the large number of total CV cycles, it was difficult to visualise the peak current density for all 100 successive CVs (Figure 4.9d). To aid understanding, current values at 0.8 V were plotted as a function of scan number (Figure 4.9f). As can be seen in Figure 4.9f, the current increases linearly with recurrent CVs for 15 cycles, before decreasing. The gradual decrease in current observed after 15 scans towards zero implies that the surface of the electrode has become saturated as the thickness of the polymer film increases.[41] This increase in polymer thickness on the FTO glass surface is directly proportional to the resistance, thus leading to a decrease in current as the deposited material becomes less conductive than the FTO glass surface.[42]

As the current is also dependent on the concentration and diffusion of monomers to the electrode surface, it is likely that this decrease in current is also due to the poor mobility of the Carb-Ala molecules in the stationary hydrogel.[41] Up until 15 CV cycles, it is highly probable that only the Carb-Ala molecules in contact with the electrode surface are readily polymerised. With progressive CV cycles, the number of Carb-Ala molecules available for electropolymerisation at the electrode surface are depleted, meaning the Carb-Ala within the hydrogel must then diffuse to the electrode or else wait for the hydrogel to collapse further towards the surface. As there is no free Carb-Ala molecules present in the perchloric acid solution, the concentration of the Carb-Ala is also limited to what is present in the hydrogel, further impeding electropolymerisation. For the last five scans of the electrochemical experiment (Figure 4.9c) the oxidation peak at 0.8 V is no longer visible. However, a small degree of oxidation of the polymer film can be seen at higher potentials from 0.9 V.

As well as Carb-Ala, pre-assembled hydrogels of Carb-Gly fully collapsed to form electrochromic polymer films on the FTO glass surface. From Figure 4.10, we can see that like Carb-Ala, current density increases with the number of scans before steadily decreasing towards zero. However, the current begins to decrease after six scans, unlike Carb-Ala, which increases for fifteen scans before beginning to fall.

For Carb-Leu and Carb-Ile, the pre-assembled hydrogels did not collapse to form a polymer film. However, electrochromic colour responses were observed during successive CV cycles and green discolouration was observed on the FTO glass surface upon removal of the hydrogel. This indicates that some degree of polymerisation has occurred. Like Carb-Ala and Carb-Gly, current density increased with the number of scans for eight and nine CV scans respectively before decreasing (Figure 4.10).
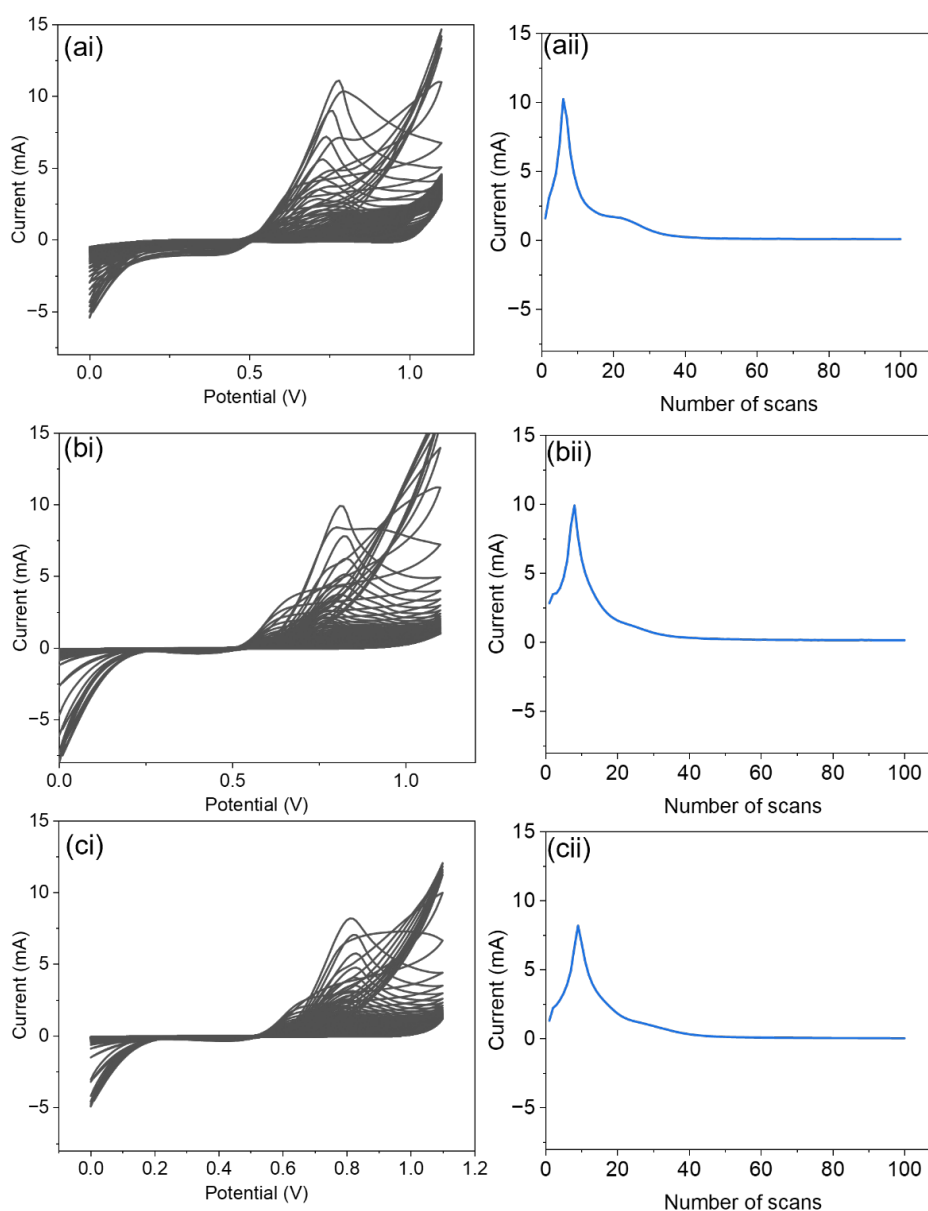
Figure 4.10 (i) CV cycles taken during the electropolymerisation of the pre-assembled carbazole protected hydrogels (ii) Current values at 0.8 V taken from (i) vs number of CV scans for (a) Carb-Gly (b) Carb-Ile and (c) Carb-Leu. Conditions: [monomer] = 5 mg/mL, [HClO$_4$] = 1 M.

Like Carb-Ile and Carb-Leu, hydrogels of Carb-Val did not collapse to form a polymer film on the FTO glass surface. However, unlike Carb-Ile and Carb-Leu, CV cycles were not accompanied by electrochromic colour changes, nor was any green discolouration observed on the FTO glass when the hydrogel was removed. From the CV cycles (Figure 4.11ai), we can see that in comparison to the other carbazole amino acids (Figure 4.9 and Figure 4.10), the CVs are very similar, showing an oxidation peak at 0.8V. From Figure 4.11ai, we can also see that like the other carbazole-protected amino acids, current density increases with the number of scans before decreasing. However, the current values in response to the scanned potential are significantly lower. For the other carbazole-protected amino acids, the current increases sharply with increasing scan rate for 6-15 scans before steadily decreasing. For Carb-Val, the current increases for much longer (30 scans) before steadily decreasing (Figure 4.11aii).
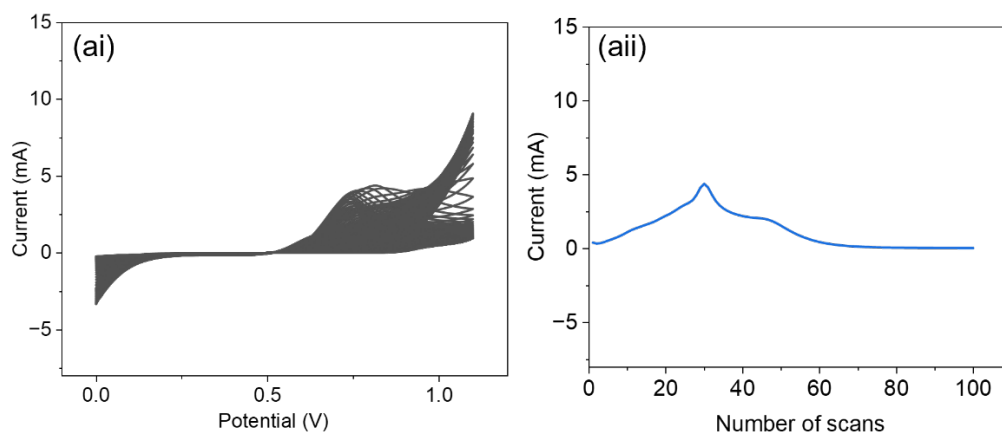
Figure 4.11 (ai) CV cycles taken during the electropolymerisation of the pre-assembled of Carb-Val (aii) Current values at 0.8 V taken from (ai) vs number of CV scans. In all cases, 100 CVs were scanned from 0 to 1.1 V using a scan rate of 40 mV/s. Conditions: [monomer] = 5 mg/mL, [$HClO_4$] = 1 M.

Despite no visual evidence of polymerisation, it may be that a very small amount of polymer is deposited on the FTO glass surface with each CV cycle in comparison to the others. This may explain why current increases for a larger number of cycles as it would take longer for the electrode to become saturated which would cause the current to start decreasing. As Carb-Val is the bulkiest amino acid investigated, it may be that steric effects prevent the π-π stacked gels from undergoing the extensive molecular reorganisation required to fully/partially collapse into a conjugated polymer film.

4.2.5 SEM

To examine the microstructure of the hydrogels and the morphology of the polycarbazole films on the FTO glass surface, SEM images were collected (Figure 4.12).
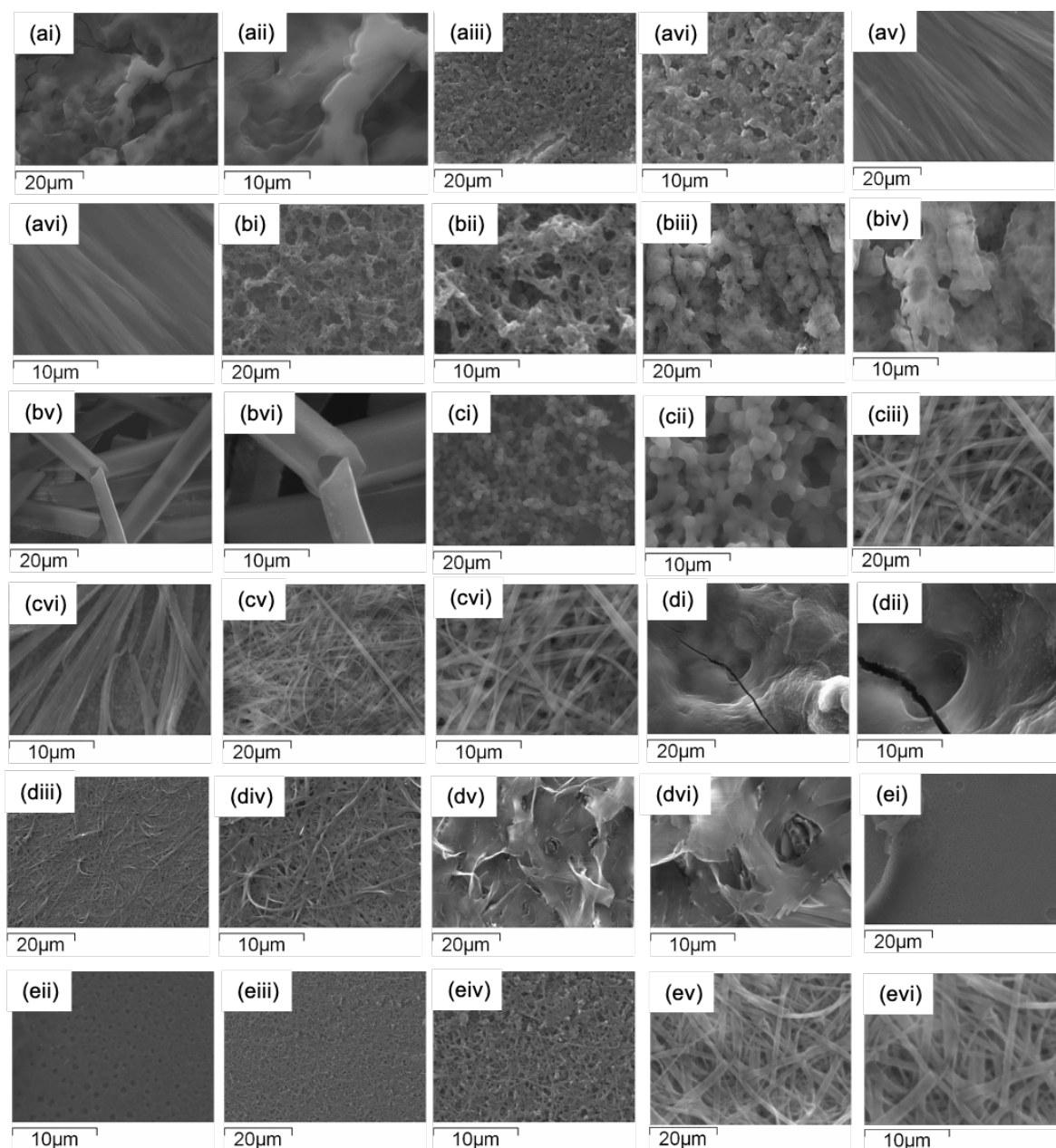
Figure 4.12 SEM images of the carbazole-protected amino acid polymers formed in acetonitrile (i-ii), polymers formed form the electropolymerisation of the pre-assembled hydrogels (iii-iv), and xerogels (v-vi) for (a) Carb-Ala (b) Carb-Gly (c) Carb-Val (d) Carb-Ile (e) Carb-Leu. Scale bar: 20 μm (2 K mag), Scale bar: 10 μm (5 K mag).

For SEM, all samples must be dehydrated before imaging, meaning the pre-formed hydrogels of the carbazole-protected amino acids were left to airdry overnight, giving the corresponding xerogels. It is important to highlight that while SEM is a useful tool for probing the microstructure, it is possible that the dehydrating process can cause a number of drying artefacts and increased aggregation of hydrogel fibres.[43, 44] As a result, the images may not be a full representation the material in its hydrated state. Upon drying, all of the xerogels investigated display a network of fibers which is very typical for this type of material (Figure 4.12). Out of all the carbazole-protected amino acids investigated, only the hydrogels of Carb-Ala and Carb-Gly fully collapse to form electrochromic polymer films. Interestingly, Carb-Ala is the only xerogel that displays compact, directional fibers on the FTO glass surface (Figure 4.12av). This arrangement of fibers may aid the molecular reorganization and collapse of the Carb-Ala molecules to form conjugated polymers as the other xerogels present a network of non-directional, mesh-like fibers (Figure 4.12). For Carb-Gly, the fibers/structures of the xerogels are significantly larger than all of the carbazole-protected amino acids investigated (Figure 4.12bv), this may also aid the molecular reorganization required for full collapse of the self-assembled hydrogel.

For Carb-Ala and Carb-Gly, SEM images were taken of the polymers deposited in acetonitrile and the polymers formed from the electropolymerisation of the gel phase (Figure 4.12). As has been previously reported for Carb-Ala, the microstructure of the two polymers displays large differences. For Carb-Ala, the polymers formed in acetonitrile are much denser than the polymers grown from the gel phase, which display a much more open, fibrous structure. For Carb-Gly, the differences in the microstructure are less pronounced. However, in comparison to the polymers formed in acetonitrile, the polymers formed from the gel phase seem to be denser and less porous (Figure 4.12).

For Carb-Val and Carb-Ile, images were taken of the polymers deposited in acetonitrile. Despite not adhering to the FTO glass surface, images were taken of the FTO glass slide after the electropolymerisation of Carb-Leu in acetonitrile (Figure 4.12ei). For Carb-Val and Carb-Ile, dense polymer structures are present. As would be expected, images of the FTO glass taken after the electropolymerisation of Carb-Leu are consistent with the FTO glass surface as no polymer adheres to the FTO glass surface during the electropolymerisation process. Interestingly, all the polymer films formed from the carbazole-protected amino acids in acetonitrile have a unique morphology, demonstrating the pronounced effect of the amino acid side chain on the final polymer structure.

In an attempt to image the polymers under the surface of the hydrogels for Carb-Val, Crab-Ile and Carb-Leu, the hydrogels were carefully removed from the glass FTO slide and rinsed thoroughly with water before drying. For these materials, the images collected show structures that resemble an entangled network of fibers, which would be expected from dried hydrogels/xerogels (Figure 4.12). It is therefore likely that small amounts of hydrogel were still present on the surface after rinsing, preventing the thin polymer underneath from being imaged.

4.2.6 UV-Vis

To measure the absorbance properties of the monomers and polycarbazole materials, UV-vis spectra were collected in DMF solution. As the UV cut-off for DMF is 268 nm, spectra were collected from 268 to 800 nm. For the carbazole monomer (Figure 4.13), three main absorption peaks were observed between 268 and 350 nm at 290, 325 and 340 nm respectively. In line with previous studies[45], the absorption peak at 290 nm can be attributed to the $\pi - \pi^*$ electron transition and the absorption peaks at 325 and 340 nm can be mainly denoted to the n - π^* electron transitions of the whole conjugated molecule.[45] The absorption spectra of the carbazole-protected amino acids (Figure 4.13) were then collected. In all cases, the addition of the amino acid substituent to the carbazole molecule results in a slight red shift of the absorption peaks at 325 and 340 nm but is otherwise identical to the carbazole spectra.
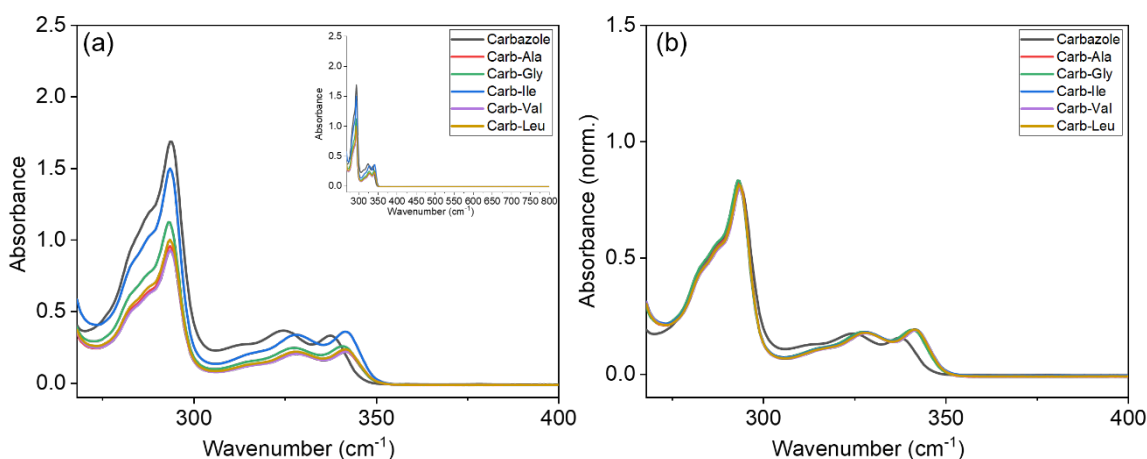
Figure 4.13 (a) UV-vis spectra of carbazole and the carbazole-protected amino acid monomers in DMF. The inset graph shows (a) until 800 nm (b) Normalization of (a) to individual λ_{max}.

To collect the absorption spectra of the polycarbazole-based films, the polymers on the FTO glass slides were dried and dissolved in DMF. For the polycarbazole-based films deposited in acetonitrile (Figure 4.14), all the spectra show bathochromic shifts and spectral broadening of the carbazole absorption peak at 290 nm, giving a broad peak ranging from 275 - 310 nm. This indicates enhanced $\pi - \pi^*$ stacking and stronger intramolecular interactions of the polycarbazole-based films in comparison to the carbazole and the carbazole-protected amino acids monomers.[46] This would be expected from the oligomerisation and polymerisation of the carbazole-protected into conjugated films. Again, Carb-Leu was not included in these results as the polymer does not adhere to the FTO glass surface.
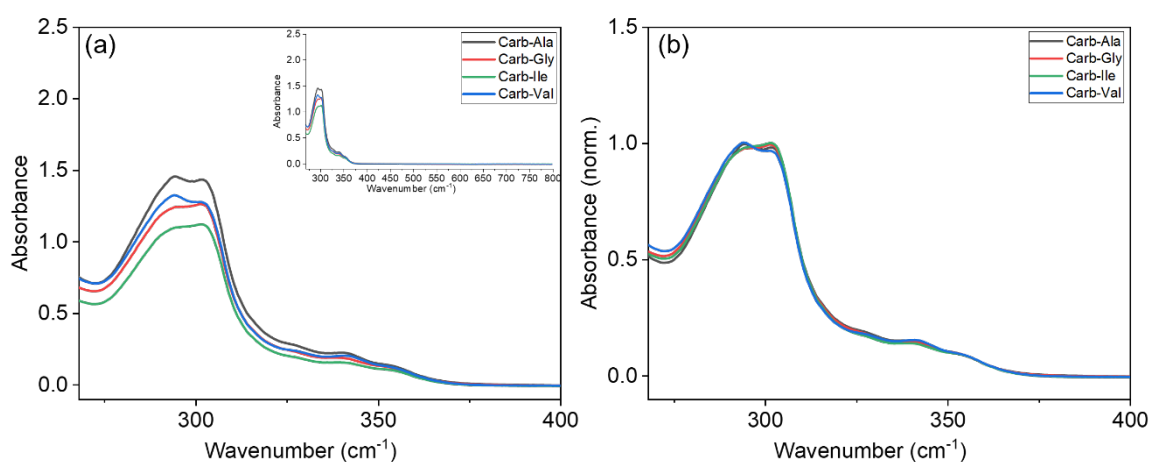
Figure 4.14 (a) UV-vis spectra of polycarbazole-based films deposited in anhydrous acetonitrile. The inset graph shows (a) until 800 nm (b) Normalization of (a) to individual λ_{max}.

Absorbance spectra of the polycarbazole films formed from the electropolymerisation of the gel phase were collected by dissolving freeze-dried films in DMF (Figure 4.15). For Carb-Val, Carb-Ile and Carb-Leu, the pre-assembled hydrogels do not fully collapse to form polymer films on the FTO glass surface. However, upon removing the hydrogel from the electrode surface, discolouration of the FTO glass was observed where the hydrogel had been. To collect the absorbance spectra of the deposited materials on the surface of the FTO glass, the hydrogels were removed to expose the FTO glass surface and deposited material. For these cases, much lower concentrations of material are deposited in comparison to Carb-Ala and Carb-Gly. As a result, multiple FTO glass slides were combined in order to collect the absorbance spectra in DMF.

Figure 4.15 shows the absorbance spectra of the polymers formed from the electropolymerisation of Carb-Ala and Carb-Gly hydrogels and the deposited materials underneath the hydrogels of Carb-Val, Carb-Leu and Carb-Ile. For Carb-Ala and Carb-Gly, the absorbance spectra show spectral broadening of the carbazole absorption peak at 290 nm. Just like the polymers formed in acetonitrile, this indicates enhanced $\pi - \pi^*$ stacking of the carbazole groups, which is conducive to the increased conjugation seen in oligomerisation and polymerisation.[46] This is also seen in the absorbance spectra of Carb-Leu and Carb-Ile, which would suggest that although the hydrogels do not fully collapse during the successive CV cycles, some degree of polymerisation is occurring on the surface/underneath the hydrogel. For Carb-Val, the spectrum is almost identical to that of the carbazole molecule and the Carb-Val monomer, indicating that little to no polymer has been formed on the FTO glass surface. The deposited material underneath the hydrogel is therefore most likely residual gelator/xerogel.
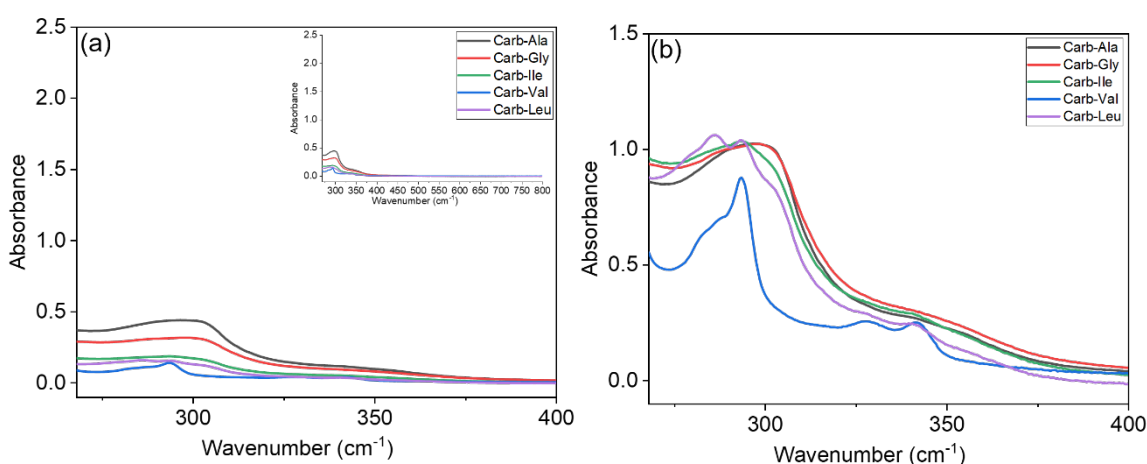
Figure 4.15 (a) UV-vis spectra of polycarbazole-based films formed from the electropolymerisation of the gel phase. The inset graph shows (a) until 800 nm (b) Normalization of (a) to individual λ_{max}.

4.2.7 NMR spectroscopy

For Carb-Val, Carb-Leu and Carb-Ile, NMR spectra of the deposited material/polymer films underneath the hydrogels could not be collected due to the low concentration of material present on the FTO glass surface. Even when material from multiple FTO slides were combined, the signal-to-noise ratio was too low to obtain a readable spectrum. Due to this, NMR spectra of these materials are not included.

For Carb-Ala and Carb-Gly, NMR spectra of the monomers were collected in DMSO-d$_6$ (Figure 4.16). Due to the additional CH$_3$ group on the alanine side chain, a singlet peak at 1.3 ppm is observed. In both cases, the peak corresponding to the carboxylic acid on the C-terminus of the molecule can be seen at 12.6 ppm.
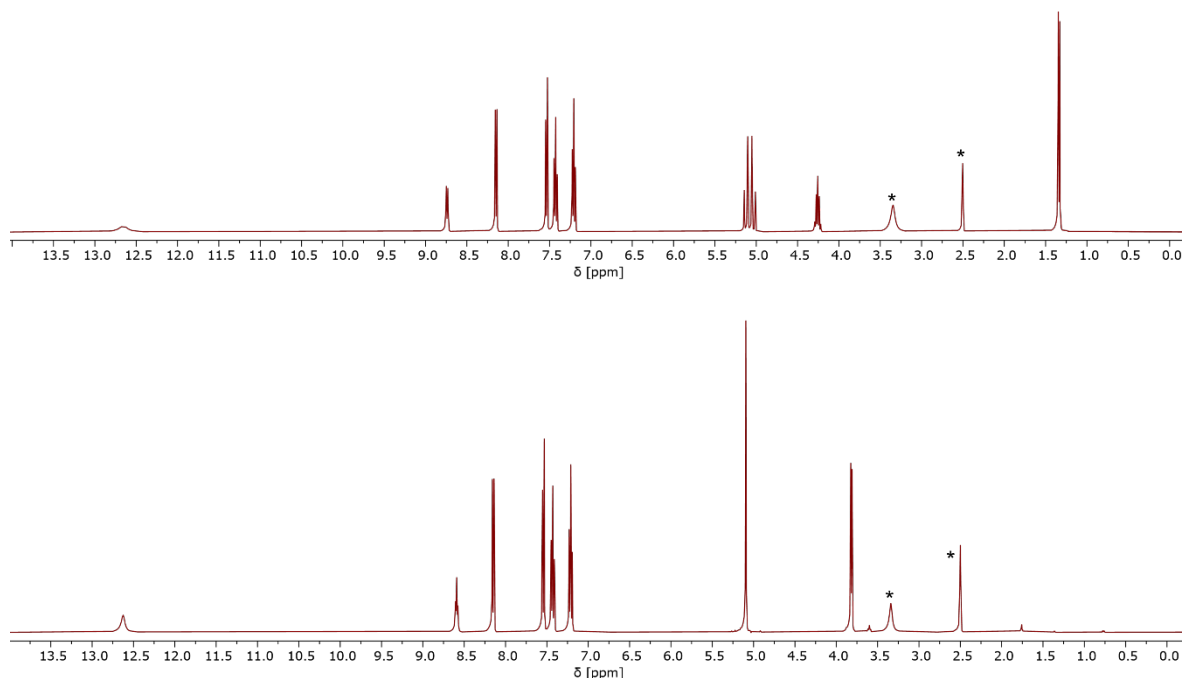
Figure 4.16 Top spectrum: ^{1}H NMR spectrum of Carb-Ala monomer. Bottom spectrum: ^{1}H NMR spectrum of Carb-Gly monomer. Both spectra are collected in DMSO-d$_6$. Solvent peaks are marked with a *.

For Carb-Ala and Carb-Gly, NMR spectra of the polycarbazole films deposited in acetonitrile and the electropolymerisation of the gel phase were collected. For the polymers deposited from the gel phase, multiple FTO slides had to be combined due to the low concentration of the deposited polymer films. Due to the limited solubility of the polymer films, NMR spectra of the polymers were collected in deuterated DMF (DMF-d$_7$).

For poly(Carb-Ala), both the polymers formed in acetonitrile and the gel phase show retention of alanine group at 1.4 ppm (Figure 4.17). As can be seen from the aromatic region (7-9 ppm), the polymerization of Carb-Ala has fabricated oligomers of various lengths. Unlike the Carb-Ala monomer (Figure 4.16), the carbazole group is no longer symmetrical as it is covalently bonded to other carbazole groups via the electrochemical oxidation process. This is why we observe multiple peaks in the aromatic region for the poly(Carb-Ala) materials formed from the electropolymerisation process in acetonitrile and the gel

phase (Figure 4.17). By comparison of the Carb-Ala monomer spectrum in DMSO-d_6 (Figure 4.16), we can see that there is residual monomer is present in the spectrum of the electropolymerized gel. This is not observed in the spectrum of the samples polymerized in acetonitrile (Figure 4.17). This could be due to the remanence of residual hydrogel left on the electrode surface after the polymerization process had concluded.
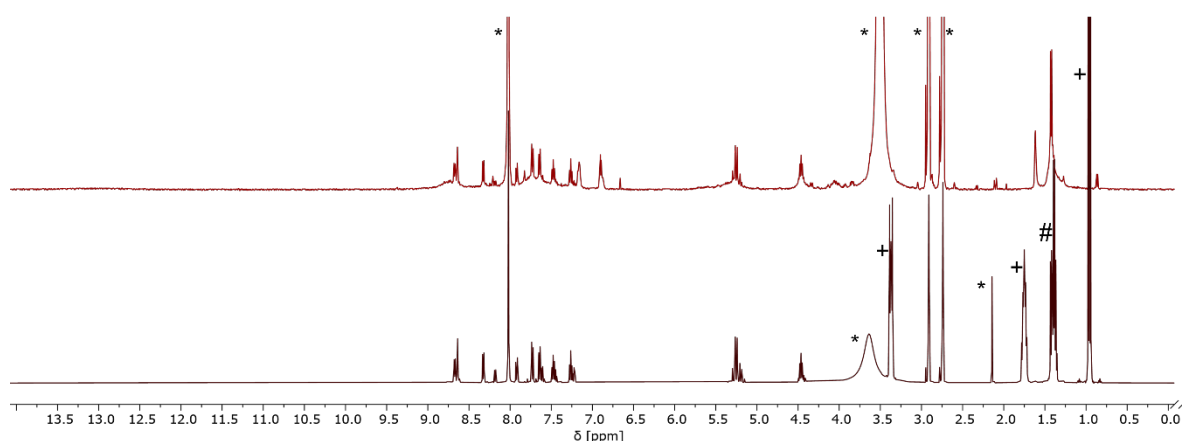
Figure 4.17 Bottom spectrum: ^{1}H NMR spectrum of poly(Carb-Ala) films grown in anhydrous acetonitrile. Top spectrum: ^{1}H NMR spectrum of poly(Carb-Ala) films grown via the electropolymerisation of pre-assembled Carb-Ala hydrogels. Due to the limited solubility of the polymer films, the NMR spectra were collected in d_7-DMF. Solvent peaks are marked with a *. The peaks due to the Bu$_4$NPF$_6$ electrolyte are marked with a +. The peak marked with a # includes one of the CH$_2$ groups in the Bu$_4$NPF$_6$ electrolyte and the CH$_3$ group from the alanine.

For poly(Carb-Gly), NMR spectra of the polymers formed in acetonitrile and the gel phase were also collected (Figure 4.18). Like the poly(Carb-Ala) materials (Figure 4.17), multiple peaks in the aromatic range are observed due to the formation of multiple oligomers in the electropolymerisation process. Again, by comparison of the Carb-Gly monomer spectrum in DMSO-d_6 (Figure 4.16), we can see that NMR spectrum of the polymerized gel shows evidence of residual monomer. It is therefore likely that some of the unpolymerized hydrogel is present on the electrode surface after the experiment had concluded. This is not observed for the samples polymerized in acetonitrile (Figure 4.18).
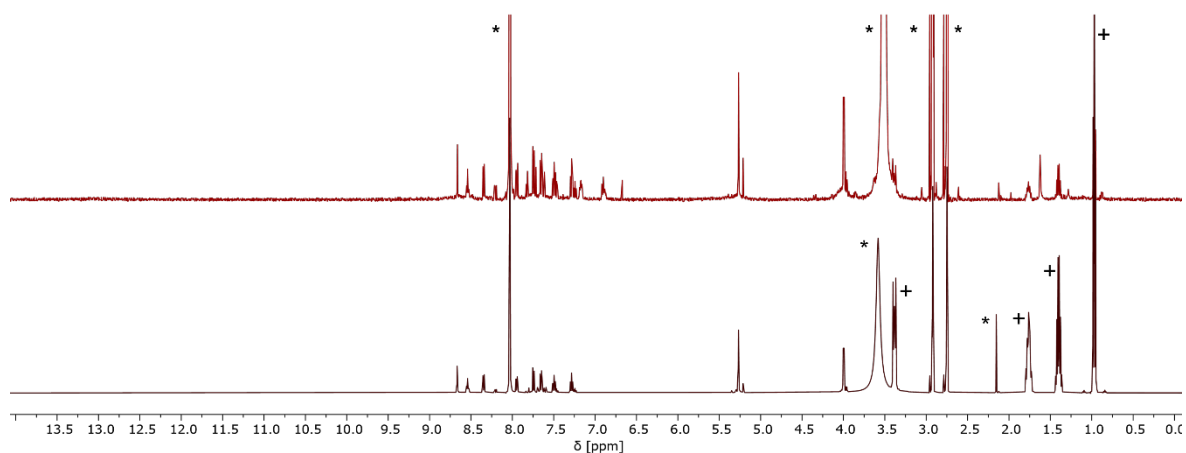
Figure 4.18 Bottom spectrum: ^{1}H NMR spectrum of poly(Carb-Gly) films grown in anhydrous acetonitrile. Top spectrum: ^{1}H NMR spectrum of poly(Carb-Gly) films grown via the electropolymerisation of pre-assembled Carb-Gly hydrogels. Due to the limited solubility of the polymer films, the NMR spectra were collected in d_7-DMF. Solvent peaks are marked with a *. The peaks due to the Bu$_4$NPF$_6$ electrolyte are marked with a +.

Further characterisation of the polycarbazole materials was attempted by running gel permeation chromatography (GPC). However, all attempts failed due to an insufficient difference in the refractive index of the polymer and the solvent.[26] Unfortunately, this meant that the relative molecular weights and distribution of the molecular weights could not be determined for the oligomers/polymers.

4.2.8 SAXS

To probe the primary self-assembled structures of the hydrogels growing in real time and the following electropolymerisation process in perchloric acid, a first-of-its-kind experiment was performed using small-angle X-ray scattering (SAXS) at Diamond Light Source (I22 beamline, Oxfordshire, UK). Unlike other material characterization methods such as SEM, SAXS allows the size and morphology of nanostructures (1-100 nm) to be studied in situ and in their hydrated state. As a relatively large volume of hydrogel is irradiated with the X-ray beam, a representative data set of the hydrogel structures is produced. For localized microscopy techniques, only a very small section of the sample is investigated which may not be fully representative of all the structures present in the bulk. Despite these benefits, SAXS data can be prone to large errors and care must be taken during data collection and background subtraction. To interpret the SAXS data, data is plotted as a scattering vector (Q) vs Intensity (I) plot and fitted to a structural model on SasView software. At this stage care must be taken to not overfit the data to the wrong structural model as this would not be

a true representation of the structures present in the hydrogel network. To prevent this, a χ^2 value is generated with each fit. A sensible value for χ^2 can be between 1-10, indicating that the chosen structural model is suitable and not overfitting the data.

To perform these in situ SAXS measurements, a custom-built, 3D printed electrochemical cell (Echem cell) was generated in Blender by Joshua White and printed using the Formlabs preform printing software on a Formlabs Form 2 printer in Resin V4 at the B21 beamline (Figure 4.19a).
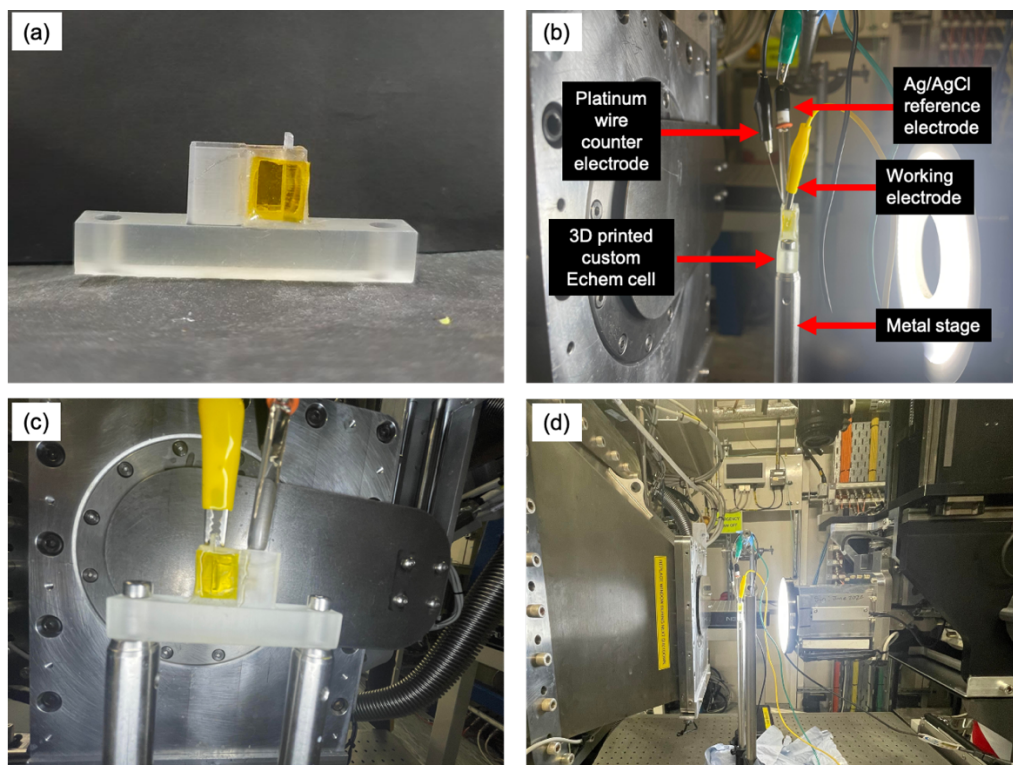
Figure 4.19 (a) Custom-built 3D Echem cell used to perform the electrochemical experiments (b) Three-electrode set-up assembled within the Echem cell (c) Front view of the Echem cell positioned in front of the beamline (d) Full view of the electrochemical experiment within the experimental hutch at the I22 beamline at Diamond Light Source (Oxfordshire, UK).

This novel Echem cell was secured in front of the I22 beamline on a metal stage (Figure 4.19). Within the custom cell, a three-electrode set up consisting of a working electrode (small fragment of FTO glass), reference electrode (aq. Ag/AgCl 3M) and counter electrode (platinum wire) was assembled (Figure 4.19b). The working electrode was secured perpendicular to the incoming beam, with a window for the beam to pass through in order to monitor the gel growth away from the electrode and the electropolymerisation (Figure

4.19c). Windows on the cell were made from Kapton tape and sealed with epoxy resin to make the cell leakproof. To perform the electrochemical experiments, the potentiostat within the experimental hutch was connected to a computer that could be controlled from a monitor outside the experimental hutch. All these experiments were performed with the help of Simona Bianco (University of Glasgow), Adam Squires (University of Bath) and Joshua White (University of Southampton).

To take in situ SAXS measurements of the hydrogel growing with time, the three-electrode set-up was assembled within the custom Echem cell. The gelator/HQ solution was then pipetted into the cell immediately before the experiment. For the SAXS measurements, a script was written to program the SAXS beamline to collect scattering at multiple locations across the hydrogel as it grows from the FTO glass surface. This script and the electrochemical experiment were started simultaneously. The growth of the hydrogel from the electrode surface could also be followed in real-time using a camera. This allowed us to calculate the final size of the hydrogel. In all cases, the distance between the SAXS measurement positions were 2 mm. After the first full set of SAXS measurements at each position, the process would be cycled from the starting position until the electrochemical experiment was finished. Each full scan set across the surface took approximately 30 seconds to complete. Finally, once the electrochemical experiment was complete, a final scan set across the hydrogel was collected at each position.

To collect in situ SAXS measurements for the electropolymerisation of the carbazole-protected hydrogels, the gelator solution used to grow the hydrogels was removed from the Echem cell using a glass pipette and replaced with perchloric acid (aq. 1 M). During this time, the FTO glass slide with the hydrogel attached remained in the same position. Again, a script was written to perform the in situ SAXS measurements and followed with a camera. As the CVs were repeatedly cycled, SAXS scans were taken at multiple positions across the hydrogel from the FTO glass surface. As the electropolymerisation experiment took approximately 1.5 hours to complete, scans were taken for the entirety of this time.

4.2.8.1 In situ SAXS of hydrogel growth

To grow hydrogels of the carbazole-protected amino acids within the custom Echem cell, gelator/HQ solutions were made as aforementioned. Immediately before the electrochemical/SAXS experiment began, the gelator/HQ solution was pipetted into the Echem cell containing the three-electrode set-up. Outside of the experimental hutch, the potentiostat was controlled using a monitor in the neighboring room. Using a current density

of 0.7 mA/cm^2, a galvanostatic current was applied to the working electrode (FTO slide) for 300 seconds. In all cases, this saw the formation of hydrogels on the FTO glass surface. To collect the SAXS measurements of the hydrogel growing with time, the SAXS script was run concurrently with the electrochemical experiment. This gave multiple SAXS measurements at multiple positions for the full experimental time (300 seconds). A final scan of the hydrogel was also performed at all positions immediately after the electrochemical experiment had concluded.

To access the raw data collected at Diamond Light source, the data were processed using Dawn Science software (version 2.27), according to a standard I22 pipeline. As part of the processing, a full azimuthal integration was performed on the raw 2D SAXS data to reduce the data to a 1D I vs Q plot. The files were then exported to .txt files using Dawn Science software. These .txt files could then be loaded into the fitting software (SasView 4.2.2).[47] To perform the background subtraction, the collected background was manually subtracted from the 1D I vs Q plots within SasView.

All fitting of the SAXS data to structural models was carried out using SasView software. The scattering length density of the carbazole-protected amino acids were calculated using the National Institute of Standards and Technology Neutron activation and scattering calculator.[48] Assuming a density of 1.55 g/cm^3, the calculated scattering length density of the carbazole-protected amino acids are shown in Table 4.1. In all cases, a scattering length density of 9.469 x 10^{-6} Å^{-2} was used for the solvent (water).

Gelator	Calculated scattering length density (10^{-6}/Å^2)
Carb-Ala	13.896
Carb-Gly	13.840
Carb-Val	13.995
Carb-Leu	14.038
Carb-Ile	14.038

Table 4.1 The calculated scattering length densities of the Carbazole-protected amino acids assuming a density of 1.55 g/cm^3.

4.2.8.1.1 In situ SAXS for Carb-Ala hydrogel growth

Firstly, SAXS measurements were collected from the Carb-Ala hydrogel growing in situ from the electrode surface with time. To collect these measurements, the FTO glass was secured perpendicular to the incoming beam. As the hydrogel grew, SAXS measurements were taken at multiple positions from the electrode surface to see if the nanostructures changed as the hydrogel grew from the electrode surface. For this sample, six positions across the hydrogel were chosen, with position 0 being closest to the FTO glass surface and position 5 being the furthest away. Each position was separated by a distance of 2 mm. For position 0, care had to be taken to ensure the beam was not too close to the FTO glass surface. If the beam hit the FTO glass, flaring occurred, which caused the detector to receive too much noise. This caused the shutter to close and prevent any further data collection. To prevent this, position 0 was collected at least 1 mm away from the FTO glass surface.

To see if the structures remained the same as the Carb-Ala hydrogel grew with time, a singular position was investigated. In this case, position 2 was chosen. In total, six scans at position 2 were collected during the 300 second experiment, with scan 1 being the first scan collected and scan 6 being the last. Using SasView, all six scans at position 2 were fitted to an elliptical cylinder model and a power law (Figure 4.20). As is very typical for these systems, a power law is used to capture the increase in scattering seen at low Q, which may be due to the increased presence of the large self-assembled structures of the hydrogel network. From the fitting model, it is likely that the hydrogel fibres grow from the surface of the electrode and laterally associate to form structures which are elliptical in cross-section.
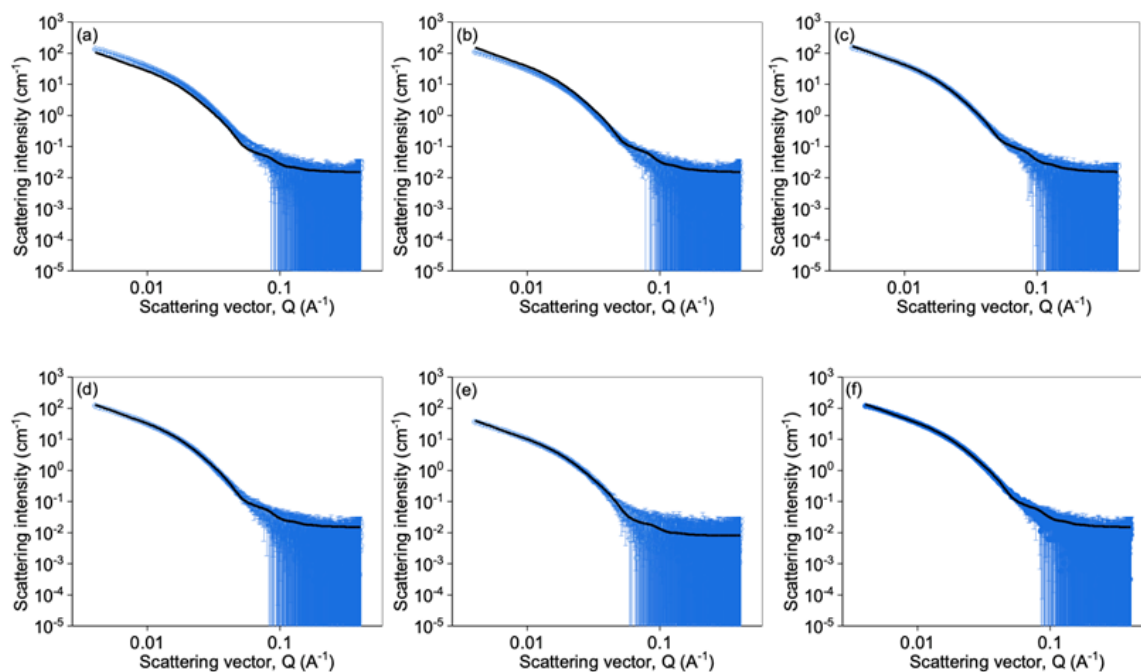
Figure 4.20 SAXS 1D I vs Q plots from position 2 of the Carb-Ala hydrogel growing on the FTO glass surface. Data shown as open blue circles and corresponding fit shown as black line (Fitting parameters shown in Table 4.2). In total, six scans were collected during the 300 second experiment, with scan 1 being the first scan collected and scan 6 being the last (a) scan 1, 130 s (b) scan 2, 160 s (c) scan 3, 190 s (d) scan 4, 220 s (e) scan 5, 250 s (f) scan 6, 280 s.

For all six scans, the fitting parameters shown in Table 4.2 are very similar, indicating that the structures are identical throughout the hydrogel as it grows from the electrode surface. In all cases, the elliptical cylinders have a radius ranging from 61.1-61.9 Å, an axis ratio of 2.4 and a power law ranging from 2.6-2.7. For these systems, the absolute length is beyond the resolution of this fit. Therefore, the length was fixed at an arbitrarily large value of 1000 Å and not allowed to refine with the other parameters. This was done for all the fits included in this chapter. In all cases, the fits generated χ^2 values between 1.2 and 1.4, indicating that the structural model selected was appropriate.

Carb-Ala	Scan 1	Scan 2	Scan 3	Scan 4	Scan 5	Scan 6
Model	EC+PL	EC+PL	EC+PL	EC+PL	EC+PL	EC+PL
Scale	1.0*	1.0*	1.0*	1.0*	1.0*	1.0*
Background	0.015*	0.015*	0.015*	0.015*	0.015*	0.015*
Background error	-	-	-	-	-	-
A scale	3.0×10^{-3}	2.0×10^{-3}	3.0×10^{-3}	2.0×10^{-3}	2.0×10^{-3}	2.0×10^{-3}
A scale error	*1.4×10^{-5}*	*1.5×10^{-5}*	*1.4×10^{-5}*	*1.5×10^{-5}*	*1.5×10^{-5}*	*1.5×10^{-5}*
A radius (Å)	61.8	61.2	61.3	61.9	61.1	61.6
A radius error	*0.2*	*0.3*	*0.2*	*0.3*	*0.2*	*0.3*
A axis ratio	2.4	2.4	2.4	2.4	2.4	2.4
A axis ratio error	*0.01*	*0.02*	*0.01*	*0.02*	*0.02*	*0.02*
A length (Å)	1000*	1000*	1000*	1000*	1000*	1000*
A length error	-	-	-	-	-	-
B scale	2.3×10^{-5}	1.9×10^{-5}	3.3×10^{-5}	1.6×10^{-5}	2.0×10^{-5}	1.6×10^{-5}
B scale error	*2.5×10^{-6}*	*2.5×10^{-6}*	*2.8×10^{-6}*	*2.2×10^{-6}*	*2.5×10^{-6}*	*2.4×10^{-6}*
B power	2.7	2.7	2.6	2.7	2.7	2.7
B power error	*0.02*	*0.02*	*0.02*	*0.02*	*0.02*	*0.02*
χ^2	1.4	1.2	1.3	1.2	1.2	1.3

Table 4.2 Fitting parameters of the 1D I vs Q plots shown in Figure 4.20. Values annotated with an asterisk (*) were fixed and not allowed to refine during the fitting process.

Secondly, SAXS measurements were collected from the Carb-Ala hydrogel after it had finished growing on the electrode surface and the electrochemical experiment had concluded. Thus, investigating whether the structures present during hydrogel growth are the same as the structures present in the final hydrogel. To collect this data, a scan was collected at all six positions (0-5). Again, the I vs Q plots were fitted to a structural model using SasView (Figure 4.21). For position five, no scattering data could be collected as the hydrogel did not grow large enough to reach the final position.
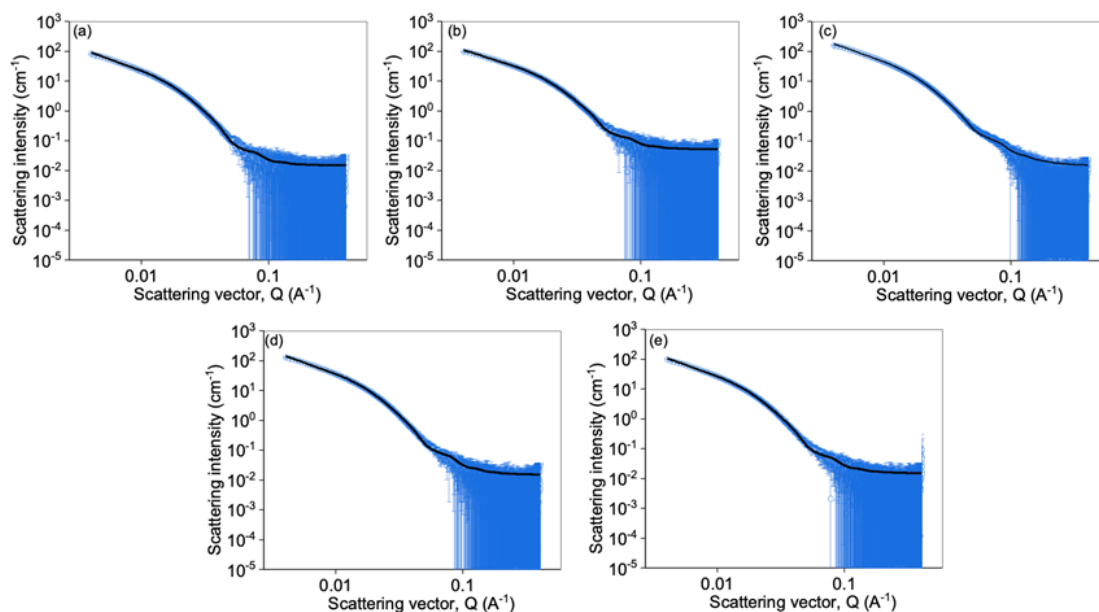
Figure 4.21 SAXS 1D I vs Q plots from positions 1-4 of the Carb-Ala hydrogel after the electrochemical experiment had concluded. Data shown as open blue circles and corresponding fit shown as black lines (Fitting parameters shown in Table 4.3). In total, SAXS measurements could be collected from five positions, with position 0 being closest to the electrode surface and 4 the furthest away. (a) position 0 (b) position 1 (c) position 2 (d) position 3 (e) position 4.

For positions 0-4, the data were again fitted to an elliptical cylinder model and power law. For all the positions, the fitting parameters shown in Table 4.3 are very similar, indicating that the structures are identical at each position across the hydrogel. In all cases, the elliptical cylinders have a radius ranging from 59.5-61.8 Å, an axis ratio ranging from 2.3-2.5 and a power law ranging from 2.5-2.7. Again, as the fibre length lay outside the length scale that can be probed using SAXS, the length was set to an arbitrarily large value of 1000 Å and not allowed to refine with the other fitting parameters. For all five positions, the fits generated χ^2 values between 1.1 and 1.7, again indicating that the chosen structural model is appropriate.

Carb-Ala	Position 0	Position 1	Position 2	Position 3	Position 4
Model	EC+PL	EC+PL	EC+PL	EC+PL	EC+PL
Scale	1.0*	1.0*	1.0*	1.0*	1.0*
Background	0.015*	0.015*	0.015*	0.015*	0.015*
Background error	-	-	-	-	-
A scale	1.6×10^{-3}	1.5×10^{-3}	3.1×10^{-3}	2.5×10^{-3}	1.9×10^{-3}
A scale error	*1.5×10^{-5}*	*1.6×10^{-5}*	*1.3×10^{-5}*	*1.4×10^{-5}*	*1.5×10^{-5}*
A radius (Å)	61.3	59.5	60.9	61.8	60.5
A radius error	*0.4*	*0.4*	*0.2*	*0.2*	*0.3*
A axis ratio	2.4	2.5	2.3	2.4	2.4
A axis ratio error	*0.02*	*0.03*	*0.01*	*0.02*	*0.02*
A length (Å)	1000*	1000*	1000*	1000*	1000*
A length error	-	-	-	-	-
B scale	9.9×10^{-6}	8.8×10^{-6}	8.2×10^{-5}	2.3×10^{-5}	1.6×10^{-5}
B scale error	*2.1×10^{-6}*	*2.2×10^{-6}*	*4.0×10^{-6}*	*2.5×10^{-6}*	*2.5×10^{-6}*
B power	2.7	2.7	2.5	2.7	2.7
B power error	*0.04*	*0.04*	*0.01*	*0.02*	*0.03*
χ^2	1.1	1.2	1.7	1.2	1.1

Table 4.3 Fitting parameters of the 1D I vs Q plots shown in Figure 4.21. Values annotated with an asterisk (*) were fixed and not allowed to refine during the fitting process.

Using the collected SAXS data, hydrogel growth was followed at all six positions (0-5) by overlaying the scans taken at each position during the full electrochemical experiment. To visualize gel growth at each position, the multiple scans from each position were plotted in singular scatter plots (Figure 4.22). These plots were then used to monitor gel growth from the electrode surface as it occurred. The corresponding colour spectrum attached to each plot progresses from blue for the first scan to red for the final scan collected. Using this data, a complimentary heatmap was generated (Figure 4.23), where the position is along the x axis and time along the y axis. For the heatmap, the colour corresponds to the intensity of the scattered X-Rays at a single, user-defined, q value, set to q = 0.01 nm^{-1} from the plots in Figure 4.22. Again, this allowed us to view the evolution of the scattering intensity at multiple different positions in time. From the single position scattering plots and the heatmap

(Figure 4.22 and Figure 4.23) we can see that for positions 0-4, scattering intensity increases with each scan, showing that the concentration of self-assembled structures increases as the hydrogel grows with time. For position 5, no plottable scattering data could be collected as the hydrogel never grew large enough to reach the final collected position (Figure 4.22f). As would be expected, the scattering intensity is greatest for the positions closest to the electrode surface at earlier times. As time continues, the scattering intensity for the positions further away from the electrode surface also begin to increase as the hydrogel grows bigger in size.

For these data sets, data processing was performed by Jack Macklin (University of Bath). Data were accessed from the Diamond Light Source data storage servers using Globus Connect. All the data were obtained as .nxs files which use the high performance HDF5 file format. Using the HDF5 interface, these binary data were extracted and converted to standard NumPy arrays for ease of use in further Pythonic processing. Each .nxs file was formed of multiple scans, where each scan is of a different location on the hydrogel. Data analysis was performed in Python using a custom script that was separated into three main functions; background subtraction, multiple time single position scatter plots and a gel growth heatmap, which all operated on the extracted NumPy arrays.
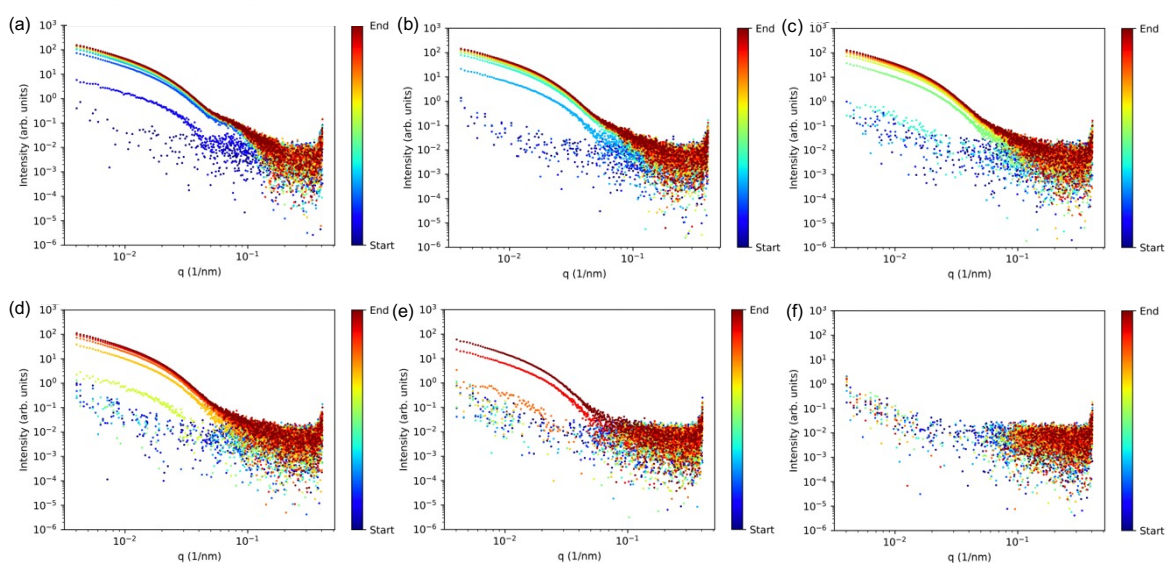
Figure 4.22 Series of singular plots showing the SAXS data for each position of the Carb-Ala hydrogel from the electrode surface with time. A background subtraction was performed before plotting each of the data series as a scatter plot. Position 0 is the closest position to the electrode surface and position 4 is the furthest away. (a) Position 0 (b) Position 1 (c) Position 2 (d) Position 3 (e) Position 4 (f) Position 5. Using the colour spectrum to the right of the plot, gel growth can be followed with time from the start of the experiment (blue) to the end (red).
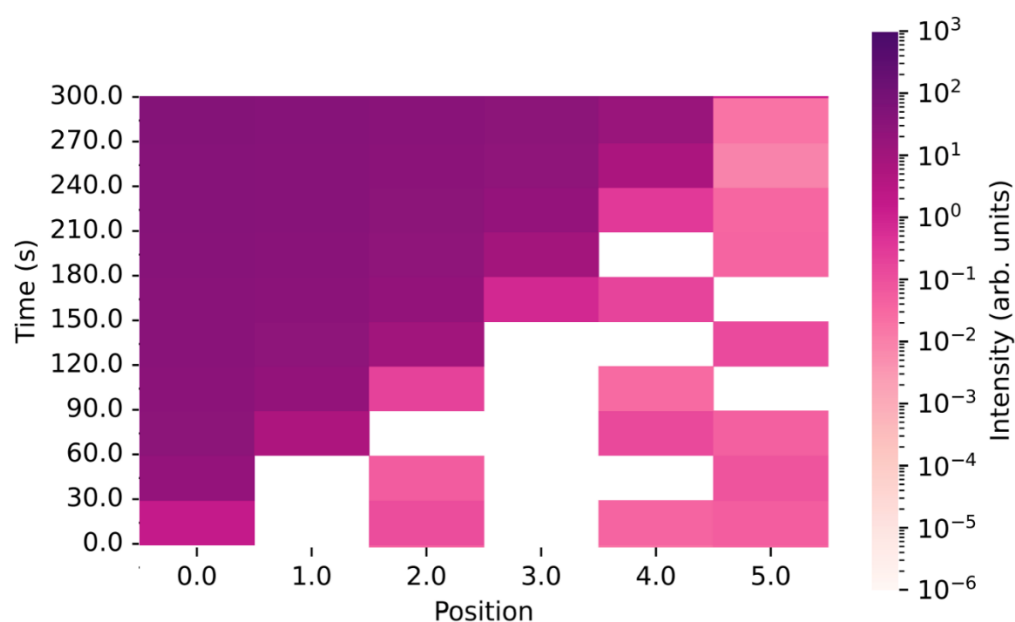
Figure 4.23 Complimentary heatmap generated from the single position scatter plots shown in Figure 4.22. The intensity of the scattered X-rays can be followed using the corresponding colour map to the right of the plot, with the intensity taken from the scattering intensity of Figure 4.21 at a single, user-defined, q value, set to $q = 0.01$ nm^{-1}.

For the gelators Carb-Gly, Carb-Val and Carb-Leu, the exact same SAXS procedure was followed as Carb-Ala. Unfortunately, due to the limited amount of time allocated at Diamond light source, SAXS measurements for the final gelator in this thesis, Carb-Ile, were not collected. For clarity, all further I vs Q plots, parameter tables and colour maps are included in Appendix: A.

4.2.8.1.2 In situ SAXS for Carb-Gly hydrogel growth

For Carb-Gly, SAXS measurements were collected from the hydrogel growing with time from the electrode surface. Again, six different positions across the hydrogel were investigated. To see if the structures remain the same as the hydrogel grows with time, a singular position (position 2) was studied. In comparison to Carb-Ala, Carb-Gly had a slower rate of growth, meaning it took longer for the gel to reach position 2. As a result, only four scans from position 2 are included from the 300 second experiment. Using the SasView software, all four scans from position 2 were fitted to a cylinder model and a power law (Figure A.1, Appendix). As aforementioned, the power law is used to capture the increase in scattering seen at low Q from the large structures in the hydrogel network. For all four consecutive scans, the fitting parameters shown in Table A.1 show that the radius gradually

increases with time from 124.2 to 178.1 Å. In comparison to Carb-Ala, the radius of these fibres is much larger. However, if we look at the SEM images (Figure 4.12), we can see that the dried xerogels of Carb-Gly show substantially larger gel fibres than the xerogel of Carb-Ala. From the Table A.1, we also observe an increase in the axis-ratio and power law. From this fitting model, it is therefore likely that the gel fibres grow from the electrode surface to form cylinder shaped structures. As the electrochemical experiment progresses, the radii of this cylinder-shaped structures gradually increase.

SAXS measurements were then collected from the Carb-Gly hydrogel after the electrochemical experiment had concluded to investigate whether the structures present during hydrogel growth are the same as the structures present in the final hydrogel. Again, SAXS measurements from six positions (separated by 2 mm) were collected across the hydrogel and fitted in SasView (Figure A.2). Again, no plottable SAXS data could be collected from position five. As expected, positions 0-4 were fitted to a cylinder model and a power law. From the parameters table (Table A.2), the trend observed is that the radius decreases the further away from electrode surface the data were collected, with the exception of position 2.

To visualise hydrogel growth at all five positions across the hydrogel, the multiple SAXS measurements collected at each position were plotted in a singular scatter plot (Figure A.3). From these plots, a complementary colour map was generated showing the scattering intensity of the hydrogel structures vs time at each position (Figure A.4). Both the scatter plots and the heatmap allow us to visualise the evolution of the hydrogel as it grows. Just like the scatter plots and heatmaps shown for Carb-Ala (Figure 4.22 and Figure 4.23), we can see that for all five positions, scattering intensity increases with experimental time. For the positions closest to the electrode surface, scattering intensity from the hydrogel structures is present at earlier times. As the hydrogel grows and reaches the positions further away from the electrode, scattering intensity begins to appear and increases with experimental time.

4.2.8.1.3 In situ SAXS for Carb-Val hydrogel growth

For Carb-Val, SAXS measurements from the in situ gel growth were collected at multiple positions, followed by a final scan of each position after the electrochemical experiment had finished. Out of all the gelators in this thesis, hydrogels of Carb-Val deposited after 300 seconds were the smallest. As a result, only five positions were investigated (0-4). Due to the hydrogels small size, SAXS measurements from only three positions (0-2) could be

collected and fitted to a structural model in SasView. To follow the in situ gel growth of the Carb-Val hydrogels, six consecutive SAXS measurements from position 1 were fitted in SasView (Figure A.5). For all six scans, the plots were fitted to an elliptical cylinder model and a power law. From the parameters table (Table A.3), the values are all very similar, indicating that for this gelator, the elliptical cylinders growing from the electrode surface remain the same during the electrochemical experiment.

For Carb-Val, the calculated radii (59.0–63.2 Å) of the elliptical cylinders are very similar to the radii reported for the Carb-Ala elliptical cylinders (61.1-61.9 Å) as well as fitting to the same structural model in SasView. This is reassuring as the fibre network of the dried xerogels seen in the SEM images (Figure 4.12) are very similar for Carb-Val and Carb-Ala.

Once the electrochemical experiment had concluded, SAXS measurements were collected from the Carb-Val hydrogel at all three positions (0-2). Again, the structures were fitted to an elliptical cylinder model and a power law (Figure A.6). For all the positions, the parameters shown in Table A.4 show that the values are all very similar, again implying that the self-assembled structures throughout the hydrogel are the same.

Just like the previous examples, hydrogel growth at all positions was visualised by plotting the multiple SAXS measurements collected at each position in a singular scatter plot (Figure A.7). In all cases, scattering intensity increases with time as the concentration of the self-assembled structures increases during the electrochemical experiment. This increase in scattering intensity with time can also be followed using the complementary colour map (Figure A.8).

4.2.8.1.4 In situ SAXS for Carb-Leu hydrogel growth

Finally, in situ SAXS measurements of gel growth was collected from Carb-Leu hydrogels at multiple positions across the hydrogel. However, for this system, several problems were encountered upon fitting the experimental data due to significant over subtraction of the background. When the 1D I vs Q plots were background subtracted, large gaps in the data were observed at high Q. To overcome the over subtraction observed at high Q, the intensity of the background was reduced by multiplying the background data by 0.7. This reduced background was then subtracted from the experimental data to give the 1D I vs Q plots shown in Figure A.9. Again, SAXS measurements from the in situ gel growth were collected at five positions from the electrode surface (0-4), followed by a final scan of each position after the electrochemical experiment had finished. For the in situ SAXS measurements, six

consecutive scans from position 2 were fitted in Sasview (Figure A.9). For all six scans, the plots were fitted to a cylinder model and a power law. For all the scans, the parameters shown in Table A.5 are very similar. This was also observed for the final scan of all five positions (Figure A.10 and Table A.6). However, in all cases, the calculated radius is significantly smaller than would be expected for these systems (Table A.5 and Table A.6). We believe that for this example, a large amount of information has been lost during the removal of the background intensity. It is reassuring that all the collected SAXS measurements have similar parameters and fit to the same structural model. Thus, indicating that the structures are the same throughout the hydrogel and during the fabrication process. However, in this case, we would recommend focusing on trends rather than absolute values. As a result, no further SAXS analysis is included for this gelator.

4.2.8.2 Attempted electropolymerisation of pre-assembled hydrogels

Once SAXS measurements were collected from the carbazole-protected hydrogels growing with time, SAXS measurements were then collected from the subsequent electropolymerisation of the hydrogels in perchloric acid. As aforementioned, once the hydrogels had finished growing on the electrode surface, the gelator/HQ solutions were removed from the Echem cell using a glass pipette. The solution was then replaced with perchloric acid (aq. 1 M). During this time, the FTO glass with the hydrogel attached remained untouched. In an attempt to electropolymerise the hydrogels within the SAXS beamline, the same electrochemical procedure was followed as previously mentioned in this thesis. As discussed, CVs were cycled repeatedly for 100 scans between 0 – 1.1 V using a scan rate of 40 mV/s. This took approximately 1 hour and 30 minutes to complete. In the lab-based set-up, this procedure saw the collapse of Carb-Ala and Carb-Gly based hydrogels into electrochromic polymers on the electrode surface. For Carb-Val, the pre-formed hydrogel remained attached to the electrode surface, with little to no evidence of any polymerization on the electrode surface.

To follow this procedure using SAXS, regular measurements were taken at multiple positions across the hydrogel for the entirety of the electrochemical experiment. Due to the large number of scans collected (around 200 scans at each position), the process was followed by plotting all the scans collected at each position in singular scattering plots. Again, these scattering plots were generated by Jack Macklin (University of Bath) using Python. To see if the self-assembled structures of the hydrogels changed during this experiment, a single position from across the hydrogel was investigated. Due to the large

number of collected scans, batch fitting of the SAXS measurements were performed in SasView. This sequentially fitted all the selected data sets to the same model. To perform batch fitting, a single SAXS measurement must first be fitted to the selected structural model. Using the same model and the parameters from this initial fit, the rest of the data sets can be fitted in batch mode to these values. This then generates a table, showing the parameter and χ^2 results for each individual SAXS measurement included in the batch. These results can then be used to show if any structural changes occur during the experiment.

4.2.8.2.1 Attempted electropolymerisation of Carb-Ala hydrogels

Unfortunately, unlike what was observed in a lab set-up, hydrogels of Carb-Ala did not fully collapse to form polymers on the FTO glass during the SAXS experiment. Once the electropolymerisation experiment had concluded, the hydrogel was still present on the electrode surface. However, upon removal of the hydrogel, green discoloration of the FTO glass was observed, indicating that some degree of polymerization had occurred. We believe there are a number of potential reasons the hydrogel does not fully collapse under these conditions. These reasons will be discussed at a later stage in this chapter.

Firstly, all the SAXS scans collected from each position were plotted in singular scatter plots (Figure 4.24). To collect the background data for these data sets, a SAXS measurement was collected from pure perchloric acid (aq. 1 M) in the Echem cell. However, when this background was subtracted from the collected SAXS measurements at each position, over subtraction occurred at high Q. This over subtraction left large gaps in the experimental data which prevented the data from being fit to a structural model. We believe that the reason for this over subtraction may be due to residual gelator/HQ solution being left in the Echem cell when the solution was replaced with perchloric acid. This would mean that the pure perchloric acid chosen as the background would not represent the 'true' background of the sample. To prevent large over subtraction of the data at high Q, the intensity of the collected background was reduced by multiplying the data by 0.8. Despite this, some over subtraction is still observed at position 0 (Figure 4.24).

From scatter plots (Figure 4.24), we can see no significant changes occurs. However, as the experiment progresses, we can see a slight reduction in intensity of the collected SAXS measurements. This observation is most pronounced at position 0. From these results, we believe that some degree of polymerization is occurring for the hydrogel closest to the electrode surface. Thus, causing the scattering intensity of position 0 to decrease with time.
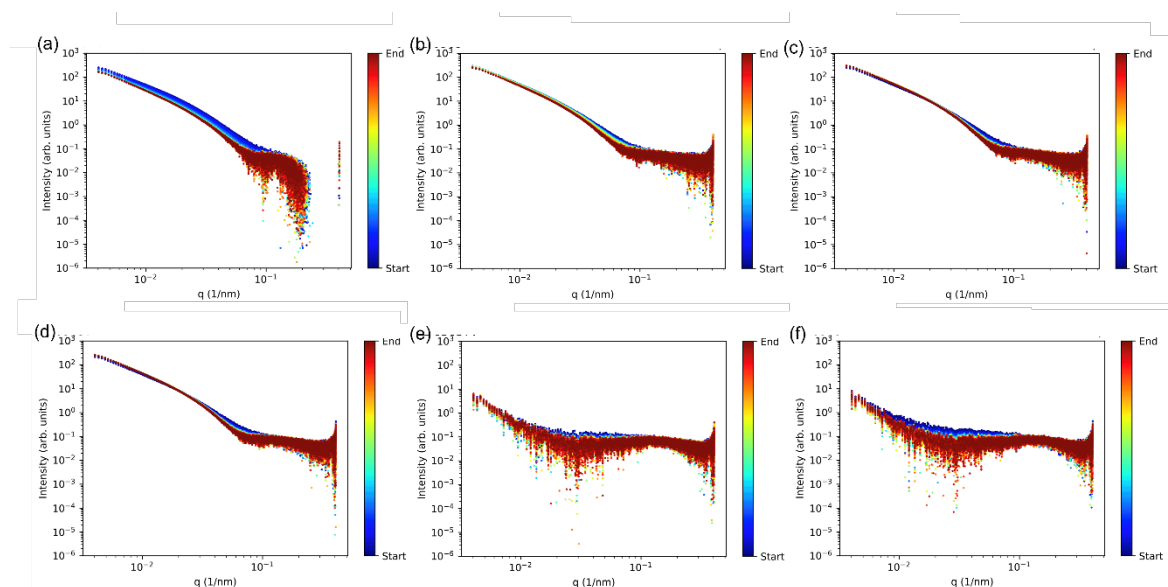
Figure 4.24 Series of plots showing the SAXS data from each position of the Carb-Ala hydrogel during the attempted electropolymerisation in perchloric acid. A background subtraction was performed before plotting each of the data series as a scatter plot. Position 0 is the closest position to the electrode surface and position 5 is the furthest away (a) position 0 (b) position 1 (c) position 2 (d) position 3 (e) position 4 (f) position 5. Using the colour spectrum to the right of the plot, gel growth can be followed with time from the start of the experiment (blue) to the end (red).

To see if any structural changes occur during the electrochemical experiment, SAXS measurements from position 2 were batch fitted in SasView. In total 200 scans at position 2 were collected. To perform batch fitting, every 20th scan was collected and loaded in SasView, giving 10 scans in total. To generate the initial fit needed for batch fitting process, the model and parameters were copied from the final scan of the Carb-Ala hydrogel at position 2 as seen in Table 4.3. These parameters were then copied and pasted into the first scan collected at position 2 for the electropolymerisation experiment. As can be seen from Figure 4.25, the first SAXS measurement in the batch collected at position 2 fit well to these parameters and structural model (elliptical cylinder + power law).
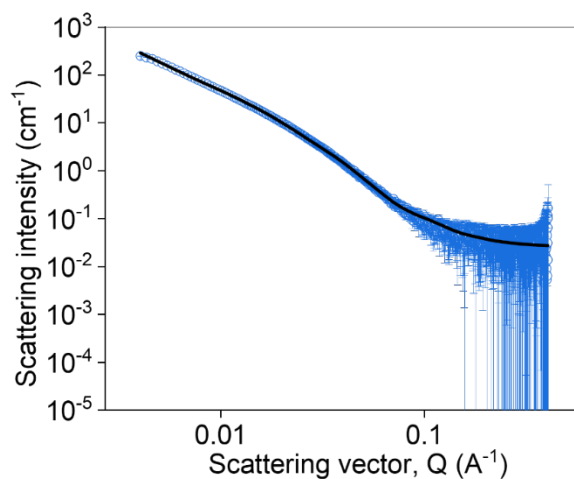
Figure 4.25. 1D I vs Q plot of scan 1 of position 2 taken during the attempted electropolymerisation of the Carb-Ala hydrogel in perchloric acid. The model and parameters from this fit were then used to perform the batch fitting process.

Using the same model and the parameters from this fit, the remainder of the data sets were fitted in batch mode to these values (Table 4.4).

Scan number	Background	A scale	A radius (Å)	Axis ratio	A length (Å)	B scale	B power	χ^2
1	0.025*	2.9×10^{-3}	42.8	3.4	1000*	2.0×10^{-4}	2.5	1.0
2	0.025*	2.9×10^{-3}	47.5	3.3	1000*	1.2×10^{-4}	2.6	1.1
3	0.025*	2.9×10^{-3}	48.2	3.3	1000*	1.1×10^{-4}	2.7	1.2
4	0.025*	2.8×10^{-3}	48.5	3.3	1000*	9.2×10^{-5}	2.7	1.2
5	0.025*	2.8×10^{-3}	49.4	3.3	1000*	8.3×10^{-5}	2.7	1.2
6	0.025*	2.6×10^{-3}	50.0	3.3	1000*	7.3×10^{-5}	2.7	1.2
7	0.025*	2.5×10^{-3}	51.0	3.2	1000*	6.3×10^{-5}	2.7	1.2
8	0.025*	2.5×10^{-3}	51.5	3.3	1000*	5.5×10^{-5}	2.8	1.3
9	0.025*	2.4×10^{-3}	52.2	3.2	1000*	5.0×10^{-5}	2.8	1.3
10	0.025*	2.4×10^{-3}	51.9	3.3	1000*	4.4×10^{-5}	2.8	1.2

Table 4.4 Batch fitting parameters of the 1D I vs Q plots taken from position 2 of the Carb-Ala hydrogel during the attempted electropolymerisation experiment. Values annotated with an asterisk (*) were fixed and not allowed to refine during the fitting process.

As can be seen from Table 4.4, the parameters of all the scans are almost identical, generating χ^2 values between 1.0-1.3. This indicates that the self-assembled structures remain the same during the full electrochemical experiment.

4.2.8.2.1 Attempted electropolymerisation of Carb-Gly hydrogels

In this chapter, we have shown that pre-assembled hydrogels of Carb-Gly on electrode surfaces can be made to collapse into electrochromic polymers in perchloric acid using successive cycles of CVs. However, when we attempted this in the SAXS beamline, hydrogels of Carb-Gly did not fully collapse to form polymers. Once the CV cycles were complete, the hydrogel was still present on the electrode surface. Despite not fully collapsing to form a polymer, green discoloration of the FTO glass was observed underneath the hydrogel implying a small amount of polymerization had occurred.

To follow this process using SAXS, the exact same procedure was followed as that used for Carb-Ala. Firstly, all the SAXS measurements collected at each position across the hydrogel were plotted as singular scatter plots (Figure A.11). Again, pure perchloric acid (aq. 1 M) was used as the background for the collected SAXS measurements. To prevent over subtraction of the SAXS data at high Q, the background intensity was reduced by multiplying the background data points by 0.8.

From the scatter plots (Figure A.11), we can see that the intensity of the collected SAXS measurements decreases at each position as the experiment progresses. This reduction in intensity may be due to the partial collapse of the hydrogel into an electrochromic polymer on the electrode surface.

Alongside these scatter plots, in situ SAXS measurements from position 2 were batch fitted in SasView. In total, 200 measurements were collected at position 2. From this data set, every 20th scan was loaded in the SasView software, giving 10 SAXS measurements in the batch. For the initial fit needed for the batch fitting process, the model (cylinder + power law) and parameters from the final scan of the Carb-Gly hydrogel (position 2, Table A.2) were copied and pasted into the first scan included in the batch. As can be seen in Figure A.12, the structural model and parameters fit well to the first batch scan as well as generating a sensible χ^2 value of 1.2. The remainder of the data sets in the batch were then fitted to this model and parameters in batch mode (Table A.7). From Table 4.4, the fits generate χ^2 values between 1.0-1.2. For these scans, the radius ranges from 199.4 to 229.9 Å, indicating that the radius of the fibres changes during the successive CV cycles. This could possibly be due to the reorganisation of the fibres as the hydrogel partially collapses to form a polymer on the FTO glass surface.

4.2.8.2.2 Attempted electropolymerisation of Carb-Val hydrogels

Finally, the attempted electropolymerisation of Carb-Val hydrogels was followed using SAXS. Unlike Carb-Ala and Carb-Gly, we have shown that pre-assembled hydrogels of Carb-Val do not collapse to form polymers in perchloric acid upon successive CV cycles. However, using the same setup and procedure, we followed the experiment using SAXS. Again, a pure perchloric acid (aq. 1M) background of reduced intensity (data points multiplied by 0.8) was used to generate the 1D I vs Q plots.

To follow the procedure at each position in the hydrogel using SAXS, singular scatter plots were used (Figure A.13). As can be seen in Figure A.13, a slight reduction in scattering intensity is observed at position 0 as the experiment progresses. For the other positions, little to no change of the scattering intensity is observed. These results correlate with what we observe in a lab setting as the hydrogel remains attached to the electrode surface after the electrochemical experiment had concluded. The reduction in intensity of the self-assembled structures at position 0 might be due to a small degree of polymerization of the hydrogel in direct contact with the FTO glass slide. However, unlike Carb-Ala and Carb-Gly, no green discoloration was observed on the electrode surface.

To see if any structural changes occur during the successive CV cycles, SAXS measurements from position 1 were batch fitted in SasView. Again, every 20th scan was collected and loaded in SasView, giving 10 scans in total. The initial fit for the batch fitting process was performed on the first scan in the batch. To generate the initial fit, the model (elliptical cylinder + power law) and parameters were copied from the final scan of the Carb-Val hydrogel at position 1 as seen in Table A.6. This generated a sensible χ^2 value of 1.6 (Table A.8). Using batch mode on SasView, the remainder of the scans in the batch were fitted to these initial parameters. From Table A.8 we can see that the parameters of all the scans are almost identical. Thus, implying that the structures at position 1 of the hydrogel remain the same during the successive CV scans in perchloric acid.

4.2.8.3 Future experimental improvements

As aforementioned, pre-assembled hydrogels of Carb-Ala and Carb-Gly collapse to form electrochromic polymers in perchloric acid when successive CV cycles are applied to the FTO glass surface. However, when we attempted to replicate this experiment in front of a SAXS beamline, the hydrogels were still present on the FTO glass surface. Upon removal of the hydrogel, green discolorations of the FTO glass were observed where the hydrogel had previously been attached. This indicates that some degree of polymerization has occurred.

There are a number of potential reasons why the hydrogels of Carb-Ala and Carb-Gly did not collapse to form electrochromic polymers during the SAXS experiment. However, we believe that the main reason for this was due to the small size of the 3D printed Echem cell. This meant that the working, reference and counter electrodes were in a very confined space. For the set-up used in the lab, the electrodes were not as confined spatially which seen the successful collapse and polymerization of the Carb-Ala and Carb-Gly hydrogels. Due to the

small size of Echem cell in the beamline, the hydrogel growing on the FTO glass slide was pressed against the walls of the Echem cell. In the lab set up, this does not occur. It is therefore possible that the confinement of the hydrogel to the sides of the Echem cell prevented the hydrogel from collapsing. To investigate whether this is the cause, we would recommend repeating the aforementioned SAXS experiments using an Echem cell identical in size to that used in the lab set up.

4.2.9 Conclusions

In this chapter, we first grow hydrogels of the carbazole-protected amino acids on electrode surfaces via the electrochemical oxidation of hydroquinone. We then go onto show the electropolymerisation of Carb-Ala and Carb-Gly based hydrogels to form electrochromic polymers on the electrode surface. For Carb-Leu and Carb-Ile based hydrogels, we observed that despite not fully collapsing to form a polymer, some degree of polymerization occurs underneath the hydrogel surface. However, for Carb-Val, there is little to no evidence of polymerization even underneath the pre-formed hydrogel. We hypothesized that this is due to the bulky side chain on gelator backbone which potentially prevents the reorganization and collapse of the Carb-Val molecules within the hydrogel to form a polymer.

For the final section of this thesis, in-situ SAXS measurements were used to probe the primary self-assembled structures of Carb-Ala, Carb-Gly, Carb-Val and Carb-Leu hydrogels growing in real time. To do this, a first-of-its-kind experiment was performed using a novel 3D printed Echem cell at Diamond Light Source (I22 beamline, Oxfordshire, UK). The final gelator in this thesis, Carb-Ile, was not included due to the limited time allocated at the I22 beamline. As well as the in situ SAXS measurements, the homogeneity of the structures throughout the hydrogel were investigated by collecting SAXS measurements at multiple positions across the hydrogel once it had finished growing on the electrode surface.

Using this set-up, the subsequent electropolymerisation of the pre-assembled hydrogels of Carb-Ala and Carb-Gly in perchloric acid was attempted in front of the beamline. However, unlike what is observed in the lab set-up, the hydrogels did not collapse to form electrochromic polymers. Instead, the hydrogel was still present after the electrochemical experiment had concluded. This experiment was also performed on pre-assembled hydrogels of Carb-Val despite no evidence of polymerization occurring in perchloric acid for this gelator.

For Carb-Ala and Carb-Gly, we believe the hydrogels were not able to collapse to form polymers due to the small size of the 3D printed Echem cell. When this Echem cell was used, the hydrogel on the electrode surface was pressed against the cell walls. Despite the hydrogel not collapsing, in situ SAXS measurements were collected at each position across the hydrogel for the entirety of the attempted electropolymerisation process. For both Carb-Ala and Carb-Gly, position 0 of the hydrogel (closest to the electrode) saw a reduction in scattering intensity as the experiment progressed. We believe this is due to some degree of electropolymerisation occurring from the hydrogel in direct contact with the electrode surface. As well as this, green discoloration of the FTO was observed where the hydrogel had previously been attached, again implying that a small degree of polymerization had occurred. We believe that this experiment could be successful in the future if a larger Echem cell is employed, with identical measurements and geometry to the Echem cell used in the lab set up.

To the best of our knowledge, there is only one other reported example for the polymerization of LMWG hydrogels to form electrochromic polymers on electrode surfaces.[26] Through the work in this chapter, we hope to contribute and expand upon the small amount of research undertaken in this area. As polycarbazole is a well-established redox polymer with many attractive optical and electrochemical properties, we believe that the materials discussed show great potential in a number of applications. As well as this, we hope that the novel SAXS set-up discussed allows other research groups investigating the electrodeposition of hydrogels access to a greater level of understating of their systems.

4.3 Experimental

4.3.1 Synthetic procedures

Materials

The carbazole-1-acetic acid and the amino acids; L-Alanine methyl ester hydrochloride, Glycine methyl ester hydrochloride, L-Valine methyl ester hydrochloride, L-Isoleucine methyl ester hydrochloride and L-Leucine methyl ester hydrochloride were purchased from Sigma-Aldrich. Tetrabutylammonium tetrafluoroborate was also purchased from Sigma Aldrich. Acetonitrile, anhydrous, 99.8+% was purchased from Alfa-Aesar. The synthesis of the Carbazole-protected amino acids Carb-Ala, and Carb-Ile were followed according to previously reported literature procedures.[26,48]

Synthesis of 2-(9*H*-Carbazol-9-yl)acetic acid

Figure 4.26. Synthesis of 2-(9*H*-Carbazol-9-yl)acetic acid.

In a round bottom flask, carbazole (12.3 g, 73.6 mmol) and crushed sodium hydroxide pellets (3 eq, 8.83 g) were heated in DMSO (50 mL) for 30 minutes at 85 °C using an oil bath. After heating for 30 minutes, bromoacetic acid (1.2 eq, 12.3 g) was carefully added in small portions. This was then left to stir overnight at 85 °C. The heat was then turned off and excess water (250 mL) was added to the hot reaction mixture. This resulted in the formation of a white precipitate. Once the reaction mixture was cooled to room temperature, a centrifugation was used to remove the bulk of the fine precipitate. To the filtrate, concentrated hydrochloric acid (approx. 1 eq, 12 mL) was added resulting in a thick white precipitate. This was stirred for one hour. The precipitate was then filtered and washed thoroughly with water. The final compound was then afforded as a white solid (7.52 g, 45 %) using suction drying and azeotropic distillation.

δ_H(400 MHz, DMSO-d_6): 8.22-7.16 (8H, m, HAro), 5.22 (2H, s, CH$_2$). δ_C (100 MHz, DMSO-d_6): 170.73 (C=O), 140.94, 126.19, 122.71, 120.64, 119.56, 109.73 (CAro), 44.44 (CH$_2$). HRMS (ESI) m/z: [M+H]$^+$ accurate mass calculated for C$_{14}$H$_{12}$NO$_2$: 226.0863 Found: 226.0863.

Synthesis of CarbG

Figure 4.27. Synthesis of CarbGOMe

2-(9*H*-Carbazol-9-yl)acetic acid (1.5 g, 6.7 mmol) was dissolved in chloroform (10 mL) at 0 °C using an ice-bath. To the solution, *N*-methylmorpholine (1 eq, 0.74 mL) and *Iso*-butyl chloroformate (1eq, 0.87 mL) were added and left to stir for 20 minutes. A solution of glycine methyl ester hydrochloride (1 eq, 0.84 g) and *N*-methylmorpholine (1 eq, 0.74 mL)

in chloroform (10 mL) was then added and the reaction was stirred overnight and allowed to warm to room temperature. The reaction mixture was then diluted with excess chloroform (40 mL) and washed in turn with water (×2), 1M hydrochloric acid and brine. After drying over magnesium sulfate and evaporation *in vacuo*, the compound CarbGOMe was obtained as a cream solid (1.54 g, 78 %). This was used in the next step without further purification.

δ_H(400 MHz, DMSO-d_6): 8.64 (1H, m ,NH), 8.18-7.18 (8H, m, HAro), 5.10 (2H, s, CH$_2$), 3.89 (2H, d, *J* 5.9 Hz, CH$_2$), 3.62 (3H, s, CH$_3$). δ_C (100 MHz, DMSO-d_6): 170.55, 168.68 (C=O), 141.06, 126.14, 122.77, 120.60, 119.53 109.86 (CAro), 52.20, 45.86 (CH$_2$), 41.14 (OCH$_3$). HRMS (ESI) m/z: [M+H] $^+$ accurate mass calculated for C$_{17}$H$_{17}$N$_2$O$_3$: 297.1234. Found: 297.1233.

Figure 4.28. Deprotection of CarbGOMe to afford the final compound, CarbG

A solution of lithium hydroxide (0.5 g, 20.5 mmol) in water (10 mL) was added to a solution of CarbGOMe (1.2g, 4.1 mmol) in tetrahydrofuran (10 mL) and stirred vigorously overnight. The reaction was monitored using TLC (1:9 EtOAc:DCM). Once the TLC indicated the deprotection was complete, the reaction mixture was then poured into 1M hydrochloric acid (ca. 40 mL) and stirred for a further 20 minutes. The precipitate was filtered off and washed with several portions of water. Drying by azeotropic distillation with acetonitrile on a rotary evaporator, followed by keeping at 40 °C under vacuum overnight, afforded the compound CarbG as a white solid (0.8 g, 70 %). This was used in the next step without further purification.

δ_H(400 MHz, DMSO-d_6): 8.59 (1H, m, NH), 8.19 (8H, m, HAro), 5.09 (2H, s, CH$_2$), 3.81 (2H, d, *J* 5.8 Hz, CH$_2$). δ_C (100 MHz, DMSO-d_6): 171.47, 168.44 (C=O), 141.07, 126.12, 122.74, 120.59, 119.49, 109.89 (CAro), 45.86, 41.22 (CH$_2$). HRMS (ESI) m/z: [M+H] $^+$ accurate mass calculated for C$_{16}$H$_{15}$N$_2$O$_3$: 283.1334. Found: 283.1335.
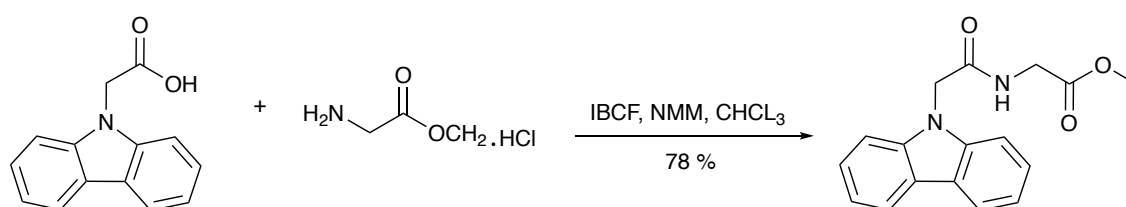
Synthesis of CarbV

Figure 4.29. Synthesis of CarbVOMe

2-(9*H*-Carbazol-9-yl)acetic acid (1.5 g, 6.7 mmol) was dissolved in chloroform (10 mL) at 0°C using an ice-bath. To the solution, *N*-methylmorpholine (1 eq, 0.74 mL) and *Iso*-butyl chloroformate (1 eq, 0.87 mL) were added and left to stir for 20 minutes. A solution of L-valine methyl ester hydrochloride (1 eq, 1.22 g) and *N*-methylmorpholine (1 eq, 0.74 mL) in chloroform (10 mL) was then added and the reaction was stirred overnight and allowed to warm to room temperature. The reaction mixture was then diluted with excess chloroform (40 mL) and washed in turn with water (×2), 1M hydrochloric acid and brine. After drying over magnesium sulfate and evaporation *in vacuo*, the compound CarbVOMe was obtained as a white solid (1.91 g, 84 %). This was used in the next step without further purification.

δH(400 MHz, DMSO-d_6): 8.74 (1H, d, *J* 8.2 Hz, NH), 8.18-7.16 (8H, m, HAro), 5.15 (1H, d, *J* 16.8 Hz, CH_2), 5.11(1H, d, *J* 16.8 Hz, CH_2), 4.21 (1H, m, *CH), 3.64 (3H, s, OCH_3), 2.10 (1H, m, $CH(CH_3)_2$), 0.94 (3H, d, *J* 6.8 Hz, CH_3), 0.89 (3H, d, *J* 6.8 Hz, CH_3). δC (100 MHz, DMSO-d_6): 173.48, 168.24 (C=O), 141.22, 126.35, 122.62, 120.57, 119.60, 109.91 (CAro), 51.35 (OCH_3), 57.55 (*CH), 45.55 (CH_2), 30.11 ($CH(CH_3)_2$) 18.37, 19.69 (CH_3). HRMS (ESI) m/z: [M+H]$^+$ accurate mass calculated for $C_{20}H_{23}N_2O_3$: 339.1703. Found: 339.1702.
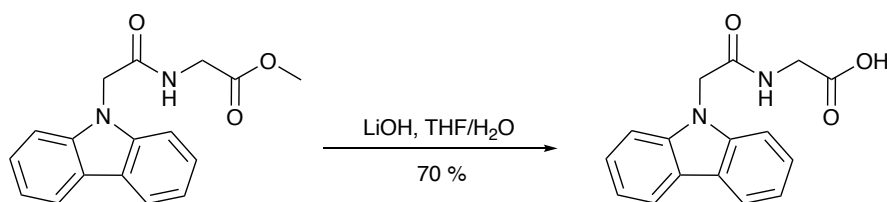

Figure 4.30. Deprotection of CarbGOMe to afford the final compound, CarbG

A solution of lithium hydroxide (0.5 g, 22.2 mmol) in water (10 mL) was added to a solution of CarbVOMe (1.5 g, 4.4 mmol) in tetrahydrofuran (10 mL) and stirred vigorously overnight. The reaction was monitored using TLC (1:9 EtOAc:DCM). Once the TLC indicated the deprotection was complete, the reaction mixture was then poured into 1M hydrochloric acid (ca. X mL) and stirred for a further 20 minutes. The precipitate was filtered

off and washed with several portions of water. Drying by azeotropic distillation with acetonitrile on a rotary evaporator, followed by keeping at 40 °C under vacuum overnight, afforded the compound CarbV as a white solid (1.1 g, 77 %). This was used in the next step without further purification.

δ_H(400 MHz, DMSO-d_6): 12.75 (1H, s, COOH), 8.57 (1H, d, J 8.7 Hz, NH), 8.18-7.12 (8H, m, HAro), 5.19 (1H, d, J 16.7 Hz, CH$_2$), 5.12 (1H, d, J 16.7 Hz, CH$_2$), 4.19 (1H, m,*CH), 2.11 (1H, m, CH(CH$_3$)$_2$), 0.94 (3H, d, J 6.8 Hz, CH(CH$_3$)$_2$), 0.90 (3H, d, J 6.8 Hz, CH(CH$_3$)$_2$). δ_C (100 MHz, DMSO-d_6): 173.28, 168.22 (C=O), 141.06, 126.06, 122.62, 120.59, 119.40, 109.84 (CAro), 57.64 (*CH), 45.61 (CH$_2$) 30.49 (CH(CH$_3$)$_2$) 18.37, 19.64 (CH$_3$). HRMS (ESI) m/z: [M+H] $^+$ accurate mass calculated for C$_{19}$H$_{21}$N$_2$O$_3$: 325.1547. Found: 325.1551.
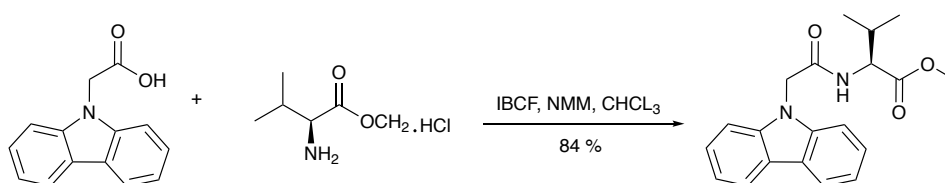
Synthesis of CarbL

Figure 4.31. Synthesis of CarbLOMe

2-(9H-Carbazol-9-yl)acetic acid (1.5 g, 6.7 mmol) was dissolved in chloroform (10 mL) at 0°C using an ice-bath. To the solution, N-methylmorpholine (1 eq, 0.74 mL) and *Iso*-butyl chloroformate (1 eq, 0.87 mL) were added and left to stir for 20 minutes. A solution of L-leucine methyl ester hydrochloride (1 eq, 1.2 g) and N-methylmorpholine (1 eq, 0.74 mL) in chloroform (10 mL) was then added and the reaction was stirred overnight and allowed to warm to room temperature. The reaction mixture was then diluted with excess chloroform (40 mL) and washed in turn with water (×2), 1M hydrochloric acid and brine. After drying over magnesium sulfate and evaporation *in vacuo*, the compound CarbLOMe was obtained as a white solid (1.92 g, 81 %). This was used in the next step without further purification.

δ_H(400 MHz, DMSO-d_6): 8.8 (1H, d, J 7.8 Hz, NH), 8.18-7.12 (8H, m, HAro), 5.14 (1H, d, J 16.7 Hz, CH$_2$), 5.05 (1H, d, J 16.6 Hz, CH$_2$), 4.32 (1H, m,*CH), 3.61 (3H, s, OCH$_3$), 1.62 (1H, m, CH(CH$_3$)$_2$), 1.55 (2H, m *CH(CH$_2$), 0.93 (3H, d, J 6.5 Hz, CH(CH$_3$)$_2$), 0.83 (3H, d, J 6.5 Hz, CH(CH$_3$)$_2$). δ_C (100 MHz, DMSO-d_6): 173.19, 168.22 (C=O), 141.05, 126.17, 122.81, 120.59, 119.45, 109.73 (CAro), 52.37 (OCH$_3$), 50.86 (CH$_2$), 45.68 (*CH),

44.45 $\underline{C}H(CH_3)_2$, 24.75 ($\underline{C}H_2C(CH_3)_2H$), 23.25, 21.70 ($CH_3$). HRMS (ESI) m/z: [M+Na] $^+$ accurate mass calculated for $C_{21}H_{24}N_2NaO_3$: 375.1679. Found: 375.1686.
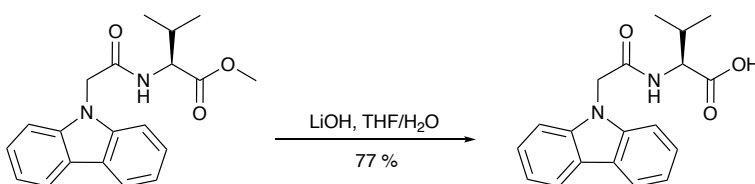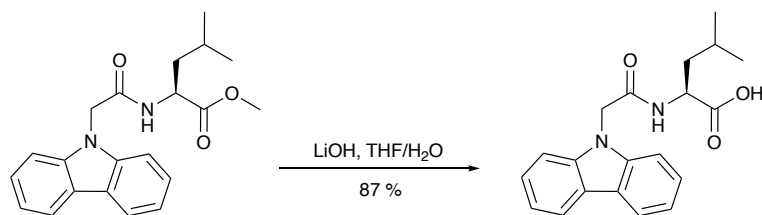

Figure 4.32. Deprotection of CarbLOMe to afford the final compound, CarbL

A solution of lithium hydroxide (0.6 g, 25.5 mmol) in water (10 mL) was added to a solution of CarbLOMe (1.8 g, 5.1 mmol) in tetrahydrofuran (10 mL) and stirred vigorously overnight. The reaction was monitored using TLC (1:9 EtOAc:DCM). Once the TLC indicated the deprotection was complete, the reaction mixture was then poured into 1M hydrochloric acid (ca. X mL) and stirred for a further 20 minutes. The precipitate was filtered off and washed with several portions of water. Drying by azeotropic distillation with acetonitrile on a rotary evaporator, followed by keeping at 40 °C under vacuum overnight, afforded the compound CarbL as a white solid (1.5 g, 87 %). This was used in the next step without further purification.

δ_H(400 MHz, DMSO-d_6): 8.71 (1H, d, J 8.1 Hz, NH), 8.17-7.16 (8H, m, HAro), 5.12 (1H, d, J 16.7 Hz, CH_2), 5.04 (1H, d, J 16.7 Hz, CH_2), 4.26 (1H, m, *CH), 1.71 (1H, m, $CH(CH_3)_2$), 1.57 (2H, m *CH(CH_2), 0.91 (3H, d, J 6.6 Hz, $CH(CH_3)_2$), 0.89 (3H, d, J 6.5 Hz, $CH(CH_3)_2$). δ_C (100 MHz, DMSO-d_6): 174.33, 168.02 (C=O), 141.07, 126.04, 122.66, 120.58, 119.42, 109.84 (CAro), 50.84 (CH_2), 45.75 (*CH), 40.55 $\underline{C}H(CH_3)_2$, 24.83 ($\underline{C}H_2C(CH_3)_2H$) 23.36, 21.74 ($CH_3$). HRMS (ESI) m/z: [M+H] $^+$ accurate mass calculated for $C_{20}H_{23}N_2O_3$: 339.1703. Found: 339.1711.

4.3.2 Instrument and Procedures

Preparation of Gelator solutions

Each stock solution of gelator was prepared at the beginning of each week at a concentration of 5 mg/mL and stored at room temperature. To make the solutions, 1.5 g of gelator was weighed into a falcon tube. NaCl (aq. 0.1 M) and 1 molar equivalent of NaOH (aq. 0.1 M) was added and made up to a volume of 30 mL. To ensure the desired concentration was reached, gelator solutions were stirred for 1-2 hours until all solids had dissolved. The pH of the gelator solutions were then adjusted to pH 7 using NaOH (aq. 0.1 M) and HCl (aq. 0.1

M). Immediately before the gelation process, 7 mL of gelator solution was transferred into a glass vial containing 35 mg of hydroquinone (5 mg/mL) and stirred until all the solids had dissolved. This solution was then used for the electrochemical fabrication of the hydrogels on the electrode surface.

pH measurements

To adjust the pH of the gelator solutions, a FC200 pH probe from HANNA instruments (6 mm x 10 mm conical tip) was used. To collect the pH measurements, the tip of the probe was placed in the gelator solutions. The pH of the gelator solution was then adjusted using aliquots of NaOH (aq. 0.1 M) and HCl (aq.0.1 M) solution. Upon addition of each aliquot, the solution was stirred for 20-30 seconds before taking a new pH reading. The prob was rinsed with deionised water before each reading. This process was repeated until a pH of 7 was reached with an accuracy of ±0.1.

Electrochemical measurements

All cyclic voltammetry (CV) and chronopotentiometry measurements were performed using a Dropsens potentiostat and processed using the PSTrace 5.8 software.

Electrochemical gelation

To grow hydrogels of the Carbazole-protected amino acids on glass FTO surfaces, a working electrode (FTO glass slide, 12 x 15 mm), reference electrode (aq. Ag/AgCl 3 M) and counter electrode (platinum wire) was assembled in a glass chamber. To electrochemically deposit the hydrogels on the glass FTO surface, 7 mL of the gelator/HQ solution was pipetted into the chamber. A current density of -0.7 mA/cm^2 was then applied to the working electrode (FTO slide) for 300 seconds. In all cases, this seen the formation of hydrogels on the electrode surface.

Electropolymerisation of Carbazole-protected amino acids in acetonitrile

Cyclic voltammetry measurements were carried out within a potential range of 0 to 1.1.V vs (Ag/AgNO$_3$). Tetra-n-butylammonium hexafluorophosphate/ Bu4NPF6 (0.1 M) was used as the supporting electrolyte and was weighed at the bottom of the electrochemical cell along with 25 mg (5 mg/mL) of the carbazole-protected amino acid. The solids were then dissolved in 5 mL of anhydrous acetonitrile and degassed by bubbling nitrogen through the solution for 30 minutes before each CV experiment. Each measurement consisted of 20 scans at a scan rate of 40 mV/s.

Electropolymerisation of pre-assembled hydrogels on electrode surfaces

To electropolymerize the hydrogels on the glass FTO slides, the gelator/HQ solution used to grow the hydrogels was removed from the glass chamber. The chamber was then rinsed thoroughly with water before adding 7 mL of perchloric acid (1 mol/mL). The FTO slide with the hydrogel attached was then placed in the chamber along with the reference and counter electrode. To electropolymerize the hydrogels, cyclic voltammetry scans were repeatedly cycled from 0 to 1.1 V at a scan rate of 40 mV/s. Each measurement consisted of 100 scans.

Scanning electron microscope (SEM)

All SEM images were taken on a PC controlled environmental scanning electron microscope (FEI Phillips/ XL30 ESEM). To obtain images of the fibers underpinning the Carbazole-protected amino acid hydrogels, the hydrogels were prepared as previously described on the glass FTO slides and left to air-dry overnight. Images of the polycarbazole amino acids formed in acetonitrile and perchloric acid were taken of the films formed on the FTO slides. In all cases, the FTO glass slides were sputter coated before imaging using a Polaron SC7640 auto/manual high resolution sputter coater with a Gold/Palladium target. Images of the hydrogel fibers and polymer films were then taken using a tungsten electron gun (Accelerating voltage 1kV – 30kV) and standard SE and BSE detectors.

UV-Vis Spectroscopy

Absorption spectra were collected on Agilent Technologies Cary 60 UV-Vis spectrophotometer. All measurements were performed within a 0.1 mm quartz cuvette. To collect absorption spectra of the Carbazole-protected amino acid monomers, the monomers were dissolved in DMF and diluted until the samples displayed an absorption maximum < 2. For the polycarbazole amino acids polymers made in anhydrous acetonitrile, films were washed thoroughly with acetonitrile before air-drying overnight. The films were then dissolved in 0.5 mL of DMF. An aliquot of this sample was then transferred to the cuvette to collect the spectra. For the polycarbazole amino acids polymers made in perchloric acid, films were washed thoroughly with water and placed in a vacuum oven (60°C) overnight before dissolving in DMF. To collect the spectra, an aliquot of this solution was transferred to the cuvette.

Chapter 4

Small angle X-ray scattering

Small-angle X-ray scattering (SAXS) measurements were performed using the X-ray beam of the I22 beamline (Diamond Light Source, Oxfordshire, UK). This beamline operates at a fixed energy of 12.4 keV and a camera length of 4.725 m, resulting in a Q range of 0.004 – 0.406 $Å^{-1}$. To perform the SAXS measurements, a 3D printed electrochemical cell was generated in Blender by Joshua White and printed using the Formlabs preform printing software on a Formlabs Form 2 printer in Resin V4 at the B21 beamline. This novel Echem cell was secured in front of the I22 beamline on a metal stage. Within the custom cell, a three-electrode set up was assembled. To perform the electrochemical experiments, the potentiostat within the experimental hutch was connected to a computer that could be controlled from a monitor outside the hutch. Full experimental details can be found in the main text.

4.4 References

1.   J. Raeburn and D. J. Adams, *Chem. Commun.*, 2015, **51**, 5170-5180.

2.   X.-Q. Dou and C.-L. Feng, *Adv. Mater.*, 2017, **29**, 1604062.

3.   E. K. Johnson, D. J. Adams and P. J. Cameron, *J. Mater. Chem.*, 2011, **21**, 2024-2027.

4.   L. Li, L. Xie, R. Zheng and R. Sun, *Front. Chem.*, 2021, **9**, 739791.

5.   C. J. Newcomb, S. Sur, J. H. Ortony, O.-S. Lee, J. B. Matson, J. Boekhoven, J. M. Yu, G. C. Schatz and S. I. Stupp, *Nat. Commun.*, 2014, **5**, 3321.

6.   M. Ikeda, T. Tanida, T. Yoshii, K. Kurotani, S. Onogi, K. Urayama and I. Hamachi, *Nat. Chem.*, 2014, **6**, 511-518.

7.   D. V, S. P. J, N. Rajeev, A. L. S, A. Chandran, G. G. B and S. Sadanandan, *Mol. Pharmaceutics*, 2022, **19**, 1999-2021.

8.   X. Ding, H. Zhao, Y. Li, A. L. Lee, Z. Li, M. Fu, C. Li, Y. Y. Yang and P. Yuan, *Adv. Drug Delivery Rev.*, 2020, **160**, 78-104.

9.   A. Dasgupta, J. H. Mondal and D. Das, *RSC Adv.*, 2013, **3**, 9117-9149.

10.   G. Fichman and E. Gazit, *Acta Biomater.*, 2014, **10**, 1671-1682.

11.   X. Du, J. Zhou, J. Shi and B. Xu, *Chem. Rev.*, 2015, **115**, 13165-13307.

12.   S. S. Babu, V. K. Praveen and A. Ajayaghosh, *Chem. Rev.*, 2014, **114**, 1973-2129.

13.   A. K. Kundu and A. J. Putnam, *Biochem. Biophys. Res. Commun.*, 2006, **347**, 347-357.

14.   A. D. Martin and P. Thordarson, *J. Mater. Chem. B*, 2020, **8**, 863-877.

15.   A. D. Martin, J. P. Wojciechowski, H. Warren, M. in het Panhuis and P. Thordarson, *Soft Matter*, 2016, **12**, 2700-2707.

16.   L. Chen, S. Revel, K. Morris, L. C. Serpell and D. J. Adams, *Langmuir*, 2010, **26**, 13466-13471.

17.   K. Tao, A. Levin, L. Adler-Abramovich and E. Gazit, *Chem. Soc. Rev.*, 2016, **45**, 3935-3953.

18.   C. Ou, J. Zhang, X. Zhang, Z. Yang and M. Chen, *Chem. Commun.*, 2013, **49**, 1853-1855.

19.   S. R. S. Veloso, P. J. Jervis, J. F. G. Silva, L. Hilliou, C. Moura, D. M. Pereira, P. J. G. Coutinho, J. A. Martins, E. M. S. Castanheira and P. M. T. Ferreira, *Mater. Sci. Eng. C*, 2021, **122**, 111869.

20.   D. Inoue, M. Suzuki, H. Shirai and K. Hanabusa, *Bull. Chem. Soc. Jpn.*, 2005, **78**, 721-726.

21.   S. Fleming, S. Debnath, P. W. J. M. Frederix, T. Tuttle and R. V. Ulijn, *Chem. Commun.*, 2013, **49**, 10587-10589.

22.   W. T. Truong, Y. Su, D. Gloria, F. Braet and P. Thordarson, *Biomater. Sci.*, 2015, **3**, 298-307.

23.   L. A. Carpino, *Acc. Chem. Res.*, 1987, **20**, 401-407.

24.   A. D. Martin, A. B. Robinson and P. Thordarson, *J. Mater. Chem. B*, 2015, **3**, 2277-2280.

25.   H. Zhang, G. Zhang, J.-k. Xu, Y.-p. Wen, W.-c. Ding, J. Zhang, S.-l. Ming and S. Zhen, *Chin. J. Polym. Sci.*, 2016, **34**, 229-241.

26.   P. S. Kubiak, S. Awhida, C. Hotchen, W. Deng, B. Alston, T. O. McDonald, D. J. Adams and P. J. Cameron, *Chem. Commun.*, 2015, **51**, 10427-10430.

27.   D.-H. Hwang, S.-K. Kim, M.-J. Park, J.-H. Lee, B.-W. Koo, I.-N. Kang, S.-H. Kim and T. Zyung, *Chem. Mater.*, 2004, **16**, 1298-1303.

28.   J. Li and A. C. Grimsdale, *Chem. Soc. Rev.*, 2010, **39**, 2399-2410.

29.   M. Ates, A. S. Sarac, C. M. Turhan and N. E. Ayaz, *Fibers Polym.*, 2009, **10**, 46-52.

30.   J. Rault-Berthelot, E. Raoult, J. Tahri-Hassani, H. Le Deit and J. Simonet, *Electrochim. Acta*, 1999, **44**, 3409-3419.

31.   C. Lai, W. Guo, X. Tang and M. Pei, *Chin. J. Chem.*, 2012, **30**, 507-511.

32.   J.-F. Morin, M. Leclerc, D. Adès and A. Siove, *Macromol. Rapid Commun.*, 2005, **26**, 761-778.

33.   Z. Hu, B. Shao, G. T. Geberth, D. A. Vanden Bout, *Chem. Sci.,* 2018, **19**, 1101-1111.

34.   E. R. Draper and D. J. Adams, *Chem*, 2017, **3**, 390-410.

35.   E. R. Draper and D. J. Adams, *Langmuir*, 2019, **35**, 6506-6521.

36.   A. R. Hirst, I. A. Coates, T. R. Boucheteau, J. F. Miravet, B. Escuder, V. Castelletto, I. W. Hamley and D. K. Smith, *J. Am. Chem. Soc.*, 2008, **130**, 9113-9121.

37.   J. Raeburn, B. Alston, J. Kroeger, T. O. McDonald, J. R. Howse, P. J. Cameron and D. J. Adams, *Mater. Horiz.*, 2014, **1**, 241-246.

38.   E. K. Johnson, D. J. Adams and P. J. Cameron, *J. Am. Chem. Soc.*, 2010, **132**, 5130-5136.

39.   C. Tang, A. M. Smith, R. F. Collins, R. V. Ulijn and A. Saiani, *Langmuir*, 2009, **25**, 9447-9453.

40.   K. A. Houton, K. L. Morris, L. Chen, M. Schmidtmann, J. T. A. Jones, L. C. Serpell, G. O. Lloyd and D. J. Adams, *Langmuir*, 2012, **28**, 9797-9806.

41.   F. Scholz, *ChemTexts*, 2015, **1**, 17.

42.   Z. Wei, J. Xu, G. Nie, Y. Du and S. Pu, *J. Electroanal. Chem.*, 2006, **589**, 112-119.

43.   D. J. Adams, *Gels*, 2018, **4**, 32.

44.   L. L. E. Mears, E. R. Draper, A. M. Castilla, H. Su, Zhuola, B. Dietrich, M. C. Nolan, G. N. Smith, J. Doutch, S. Rogers, R. Akhtar, H. Cui and D. J. Adams, *Biomacromolecules*, 2017, **18**, 3531-3540.

45.   H. A. Abro, T. Zhou, W. Han, T. Xue and T. Wang, *RSC Adv.*, 2017, **7**, 55382-55388.

46.   Y. Zhang, L. Kong, X. Ju, H. Du, J. Zhao and Y. Xie, *RSC Adv.*, 2018, **8**, 21252-21264.

47.   SasView, http://www.sasview.org/ (acessed 9th January 2023)

48.   NIST, https://www.ncnr.nist.gov/resources/activation/ (acessed 9th January 2023)

CHAPTER 5

Conclusions

5. Conclusions

Hydrogels fabricated from short chain peptide based LMWGs show great promise in a number of potential material applications due to their ease of synthesis, commercial availability, tuneable properties and their biological relevance. However, fabricating these materials using electrical signals, a term coined electrofabrication, is highly under researched. For the most part, research within this area has been performed on biological materials such as chitosan, collagen, silk and alginate, with the aim of eventually producing materials that can mimic complex biological contexts in areas such as regenerative medicine, tissue engineering, wound dressings and animal-on-a-chip. We believe that hydrogels of short chain peptide based LMWGs deposited using electrofabrication can provide a synthetic alternative to these biomaterials of natural origin. In this thesis, we show how electrofabrication can be used to deposit hydrogels from LMWGs on electrode surfaces and report on their subsequent material properties. Furthermore, we show how these hydrogels can be fabricated with excellent spatial and temporal control, effectively controlling the self-assembly of the LMWGs at electrode surfaces.

For the electrofabrication of LMWGs, all of the research to date has focused on the fabrication of hydrogels on a nanometre to millimetre scale. In chapter 2, we report the largest examples of di and tripeptide-based hydrogels deposited on electrode surfaces using the electrochemical oxidation of hydroquinone as a gelation trigger. Due to the larger size of the final hydrogels, much longer deposition times are required for the hydrogel to reach that size. However, when the hydroquinone is exposed to open air for this long, it begins to oxidise before it can be consumed at the electrode surface. To prevent this, we built a system that could perform the fabrication process in an inert atmosphere using nitrogen. In total, four di and tripeptide LMWGs were investigated. In all cases, hydrogels of at least 3 cm^3 were formed on circular glassy carbon electrodes within a nitrogen purged chamber. Using cavitation rheology, a localised technique that probes the material in its native environment, the mechanical properties of the hydrogel were investigated at the time its growth plateaued and at the end of the fabrication process. For two of the LMWGs investigated, the mechanical properties at the plateau and end point remained identical. For the other two LMWGs, the mechanical properties at the plateau and end point varied significantly. Using an array of characterisation techniques, we report the material phenomena that cause these differences. Thus, highlighting the importance of the gelators chemical composition on the final material properties. As well as this, we show how this approach can be used to grow multi-layered hydrogels with the layers presenting different chemical and mechanical

properties to one another. We hope that this will open up these materials to applications that require peptide-based hydrogels on a larger scale than previously reported.

For peptide based LMWGs, the electrofabrication of hydrogels has been performed by employing acidic pH gradients at the electrode-solution interface. In general, this has been achieved using the oxidation of water or the oxidation of hydroquinone in gelator solutions (both liberate hydrogen ions). To expand upon this work, we wanted to create a system that uses electrodeposition to trigger gelation of a LMWG at basic pH. For the biopolymer chitosan (biopolymer containing many primary amines in the form of charged ammonium ions), hydrogels of this polymer have been deposited from gelator solutions on electrode surfaces via the electrochemical reduction of hydrogen peroxide or the electrolysis of water (both produce hydroxide ions). This increase in pH triggers gelation of the chitosan in solution at the electrode surface due to the neutralisation of the amine groups on the polymer chain. Thus, inducing the self-assembly of the polymer chains to form a hydrogel. To apply this to a LMWG, we chose the Fmoc-protected amine Fmoc-3 as it had previously been reported as an effective LMWG that could be triggered to self-assemble at high pH. In chapter 3, we successfully show that we can deposit Fmoc-3 hydrogels via the electrochemical reduction hydrogen peroxide and the electrolysis of water. Through this work, we have shown how sample homogeneity and the material properties of the hydrogels can be vastly improved by the addition and increased concentration of hydrogen peroxide in gelator solutions. To the best of our knowledge, this is the first reported example of electrodeposition for a LMWG at high pH. As an addition to this work, we coupled this approach with the fabrication process used in chapter 2 to simultaneously grow two chemically different LMWG at opposing pH extremes. By using a H-cell set-up, which contains two chambers physically separated by a nafion membrane, an Fmoc-3 hydrogel was grown via the electrochemical reduction of hydrogen peroxide in one chamber. At the same time, a naphthalene-protected dipeptide hydrogel was grown in the other chamber using the electrochemical oxidation of hydroquinone. We hope that through the work undertaken in this chapter we have provided advances to the field of electrodeposition for LMWG as well as showing the versatility of this fabrication technique.

Finally, in chapter 4, we report the electrodeposition of LMWG based hydrogels from five carbazole-protected amino acids via the electrochemical oxidation of hydroquinone. For two of these carbazole-protected amino acids we showed that pre-assembled hydrogels on the electrode could act as a 'template' for forming electrochromic polymers with a unique microstructure and morphology. For the other three carbazole-protected amino acids, partial

to no polymerisation occurs for the pre-assembled hydrogels. We believe this is due to the bulkier side chains on the amino acid preventing the molecular reorganisation required for polymerisation to occur. To follow hydrogel growth and the subsequent polymerisation experiment in real-time, we used SAXS measurements to monitor any changes of the primary self-assembled structures in-situ. To perform these measurements, a first of its kind experiment was ran on the samples using a novel 3D printed electrochemical cell. Unfortunately, during the SAXS experiment, the polymerisation of the pre-assembled hydrogels on the electrode surfaces did not occur. However, very informative data was collected from the hydrogels growing via hydroquinone oxidation at multiple different locations from the electrode surface. We believe that the subsequent electropolymerisation reaction was not successful due to the small size of the electrochemical cell used. It is therefore our belief that with some experimental set-up changes, this experiment could be successful in the future.

In conclusion, we have successfully used electrofabrication to deposit LMWG based hydrogels on electrode surfaces with a high degree of spatial and temporal control. Due to the lack of research in this area, the electrofabrication of peptide based LMWG hydrogels is in its preliminary stages with no real-world applications as of yet. Through the work in this thesis, we hope to have greatly contributed to the field of electrodeposition, highlighting the advantages of using synthetic based LMWG over other gelators of natural origin. As some of the fabrication processes and experiments described in this thesis are novel, we hope to have provided a deeper understanding of these materials than previously reported.

6. Appendix: A
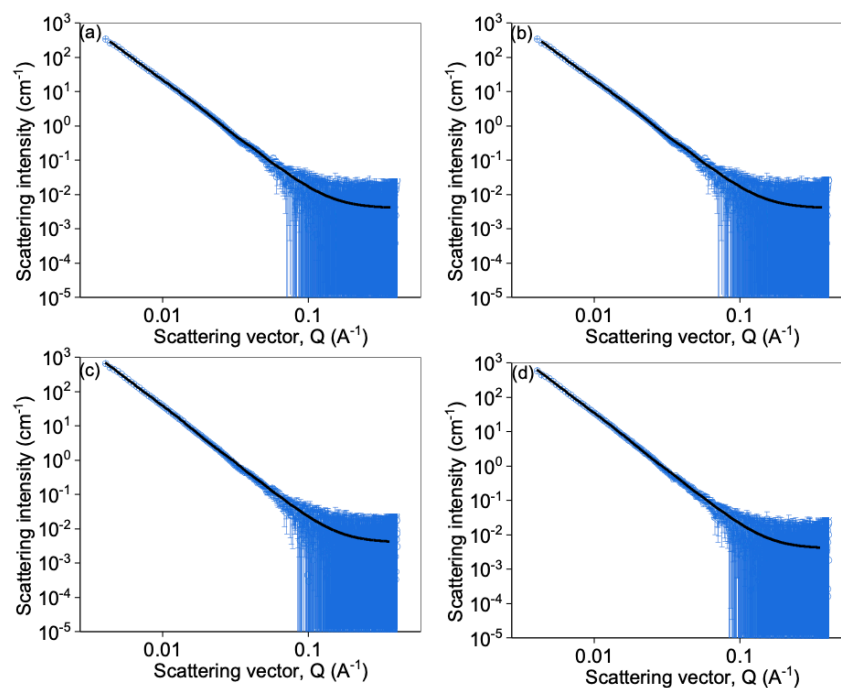
Figure A.1 SAXS 1D I vs Q plots from position 2 of the Carb-Gly hydrogel growing with time. Data shown as open blue circles and corresponding fit shown as black line (fitting parameters shown in Table A.1). In total, four scans were collected during the 300 second experiment, with scan 1 being the first scan collected and scan 4 being the last (a) scan 1, 190 s (b) scan 2, 220 s (c) scan 3, 250 s (d) scan 4, 280 s.

Appendix: A

Carb-Gly	Scan 1	Scan 2	Scan 3	Scan 4
Model	C+PL	C+PL	C+PL	C+PL
Scale	1.0*	1.0*	1.0*	1.0*
Background	0.004*	0.004*	0.004*	0.004*
Background error	-	-	-	-
A scale	1.0×10^{-4}	1.0×10^{-4}	1.2×10^{-4}	1.3×10^{-4}
A scale error	*4.6×10^{-6}*	*4.2×10^{-6}*	*4.0×10^{-6}*	*3.7×10^{-6}*
A radius (Å)	124.2	140.7	150.4	178.1
A radius error	*1.8*	*1.7*	*1.7*	*1.7*
A length (Å)	1000*	1000*	1000*	1000*
A length error	-	-	-	-
B scale	8.3×10^{-6}	9.1×10^{-5}	9.2×10^{-6}	1.0×10^{-5}
B scale error	*1.9×10^{-7}*	*1.4×10^{-7}*	*1.2×10^{-7}*	*9.5×10^{-8}*
B power	3.2	3.2	3.3	3.3
B power error	*4.0×10^{-3}*	*3.0×10^{-3}*	*2.0×10^{-3}*	*2.0×10^{-3}*
χ^2	1.1	1.5	1.8	1.9

Table A.1 Fitting parameters of the 1D I vs Q plots shown in Figure A.1. Values annotated with an asterisk (*) were fixed and not allowed to refine during the fitting process.
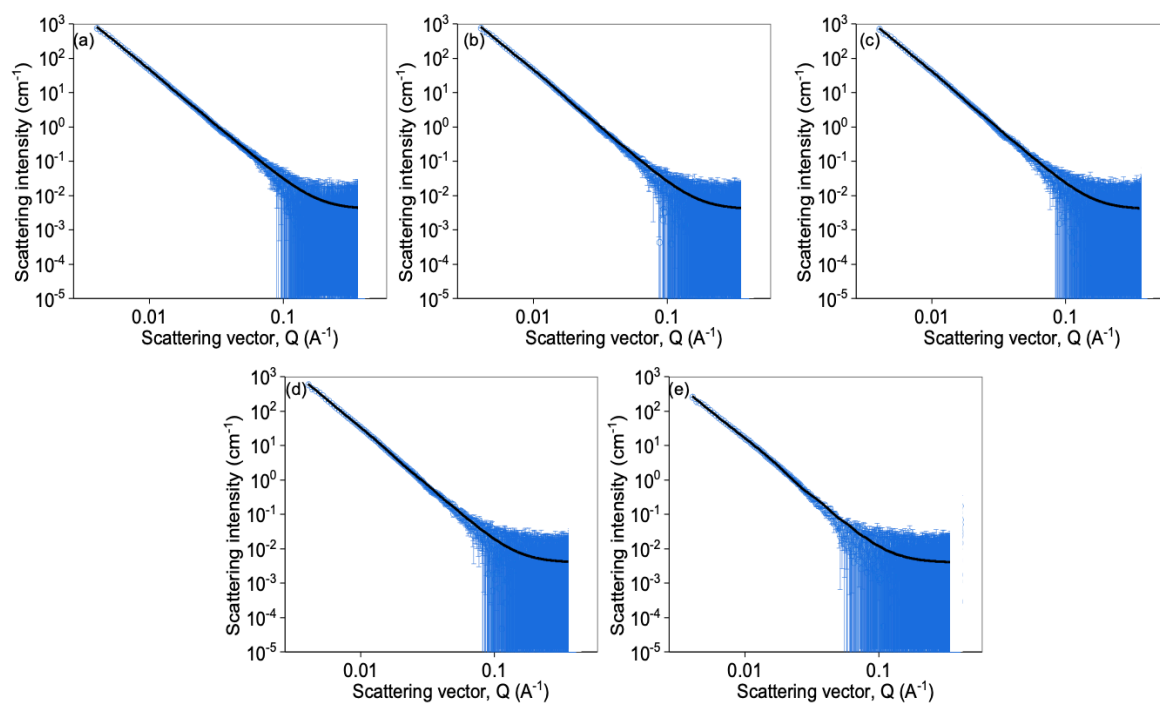
Figure A.2 SAXS 1D I vs Q plots from all five positions of the Carb-Gly hydrogel after the electrochemical experiment had concluded. Data shown as open blue circles and corresponding fit shown as black lines (Fitting parameters shown in Table A.2). In total, SAXS measurements from five positions were collected, with position 0 being closest to the electrode surface and 4 the furthest away (a) position 0 (b) position 1 (c) position 2 (d) position 3 (e) position 4.

Appendix: A

Carb-Gly	Position 0	Position 1	Position 2	Position 3	Position 4
Model	C+PL	C+PL	C+PL	C+PL	C+PL
Scale	1.0*	1.0*	1.0*	1.0*	1.0*
Background	0.004*	0.004*	0.004*	0.004*	0.004*
Background error	-	-	-	-	-
A scale	1.2×10^{-4}	1.8×10^{-4}	1.4×10^{-4}	1.2×10^{-4}	1.0×10^{-4}
A scale error	*4.6×10^{-6}*	*4.0×10^{-6}*	*3.8×10^{-6}*	*3.7×10^{-6}*	*3.6×10^{-6}*
A radius (Å)	218.9	170.4	188.1	167.9	143.8
A radius error	*2.3*	*1.3*	*1.6*	*1.8*	*1.6*
A length (Å)	1000*	1000*	1000*	1000*	1000*
A length error	-	-	-	-	-
B scale	1.7×10^{-5}	1.9×10^{-5}	1.0×10^{-5}	7.7×10^{-6}	4.3×10^{-6}
B scale error	*1.2×10^{-7}*	*1.0×10^{-7}*	*8.9×10^{-8}*	*9.1×10^{-8}*	*1.3×10^{-7}*
B power	3.2	3.3	3.3	3.3	3.3
B power error	*2.0×10^{-3}*	*2.0×10^{-3}*	*2.0×10^{-3}*	*2.0×10^{-3}*	*6.0×10^{-3}*
χ^2	1.3	1.6	1.7	1.1	1.0

Table A.2 Fitting parameters of the 1D I vs Q plots shown in Figure A.2. Values annotated with an asterisk (*) were fixed and not allowed to refine during the fitting process.

Appendix: A
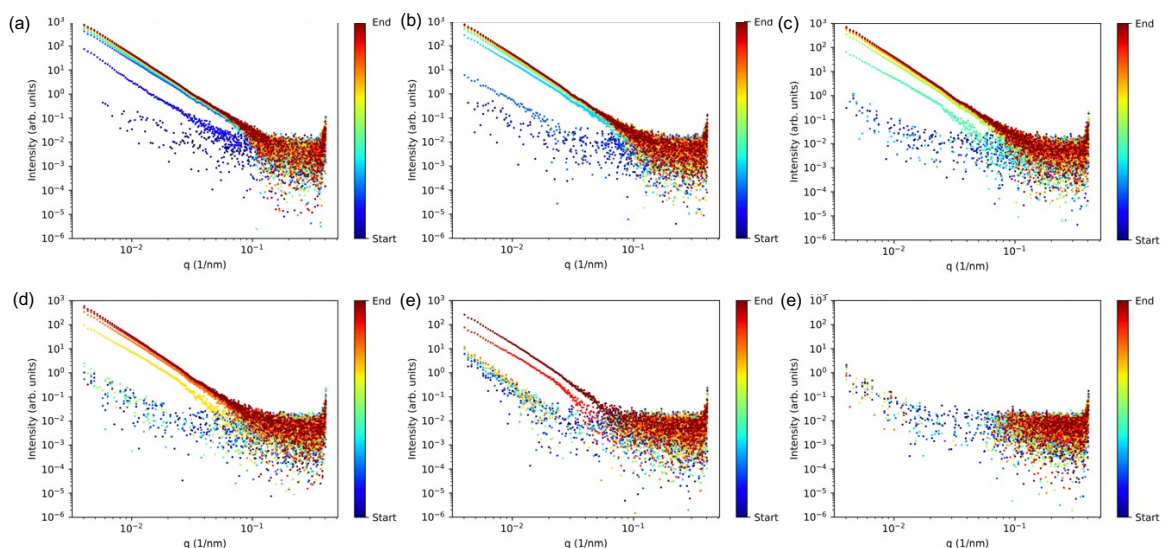
Figure A.3 Series of singular plots showing the SAXS data for each position of the Carb-Gly hydrogel from the electrode surface with time. A background subtraction was performed before plotting each of the data series as a scatter plot. Position 0 is the closest position to the electrode surface and position 4 is the furthest away. (a) Position 0 (b) Position 1 (c) Position 2 (d) Position 3 (e) Position 4 (e) Position 5. Using the colour spectrum to the right of the plot, gel growth can be followed with time from the start of the experiment (blue) to the end (red).
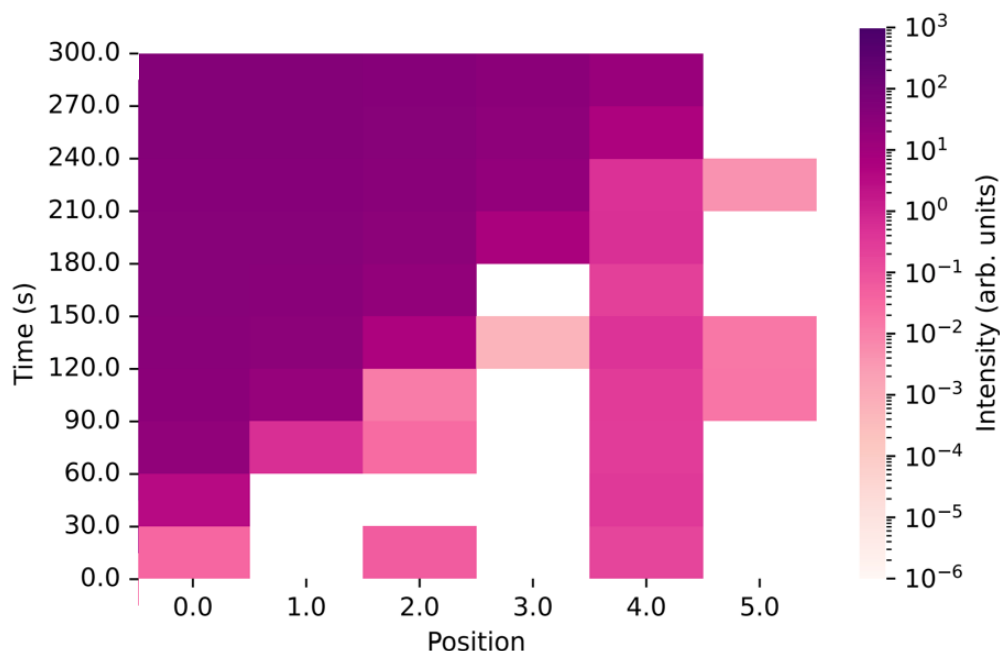
Figure A.4 Complimentary heatmap generated from the single position scatter plots shown in Figure A.3. The intensity of the scattered X-rays can be followed using the corresponding colour map to the right of the plot, with the intensity taken from the scattered intensity from Figure A.3 at a single, user-defined, q value, set to $q = 0.01$ nm^{-1}.

Appendix: A
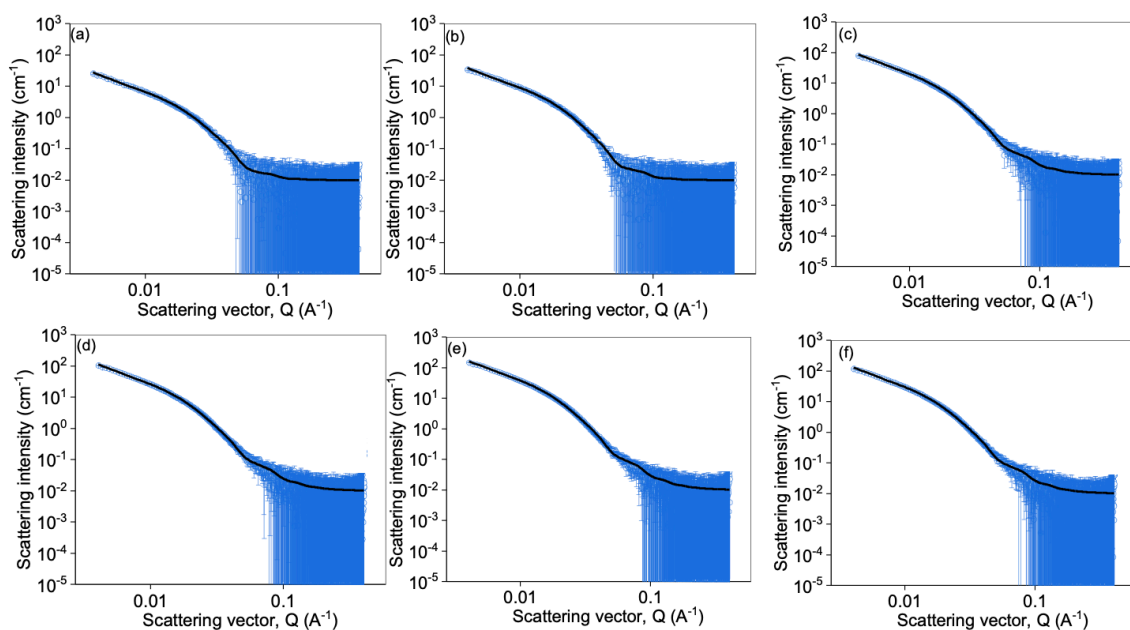
Figure A.5 SAXS 1D I vs Q plots from position 1 of the Carb-Val hydrogel growing with time. Data shown as open blue circles and corresponding fit shown as black line (Fitting parameters shown in Table A.3). In total, six scans were collected during the 300 second experiment, with scan 1 being the first scan collected and scan 6 being the last (a) scan 1, 125 s (b) scan 2, 155 s (c) scan 3, 185 s (d) scan 4, 215 s (e) scan 5, 245 s (f) scan 6, 275 s.

Appendix: A

Carb-Val	Scan 1	Scan 2	Scan 3	Scan 4	Scan 5	Scan 6
Model	EC+PL	EC+PL	EC+PL	EC+PL	EC+PL	EC+PL
Scale	1.0*	1.0*	1.0*	1.0*	1.0*	1.0*
Background	0.01*	0.01*	0.01*	0.01*	0.01*	0.01*
Background error	-	-	-	-	-	-
A scale	4.0×10^{-4}	1.2×10^{-4}	2.0×10^{-4}	2.0×10^{-4}	2.0×10^{-4}	2.0×10^{-4}
A scale error	*3.7×10^{-5}*	*1.6×10^{-5}*	*1.4×10^{-5}*	*1.5×10^{-5}*	*1.5×10^{-5}*	*1.5×10^{-5}*
A radius (Å)	55.0	61.1	62.7	62.6	62.9	63.2
A radius error	*1.1*	*0.5*	*0.4*	*0.3*	*0.3*	*0.3*
A axis ratio	2.5	2.4	2.4	2.4	2.3	2.3
A axis ratio error	*0.09*	*0.03*	*0.02*	*0.02*	*0.02*	*0.02*
A length (Å)	1000*	1000*	1000*	1000*	1000*	1000*
A length error	-	-	-	-	-	-
B scale	6.6×10^{-7}	1.5×10^{-5}	2.4×10^{-5}	2.6×10^{-5}	2.8×10^{-5}	2.9×10^{-5}
B scale error	*9.4×10^{-7}*	*2.7×10^{-6}*	*2.9×10^{-6}*	*2.9×10^{-6}*	*2.8×10^{-6}*	*2.7×10^{-6}*
B power	3.0	2.7	2.6	2.6	2.7	2.7
B power error	*0.3*	*0.03*	*0.02*	*0.02*	*0.02*	*0.02*
χ^2	1.0	1.2	1.6	2.1	1.8	1.0

Table A.3 Fitting parameters of the 1D I vs Q plots shown in Figure A.5. Values annotated with an asterisk (*) were fixed and not allowed to refine during the fitting process.
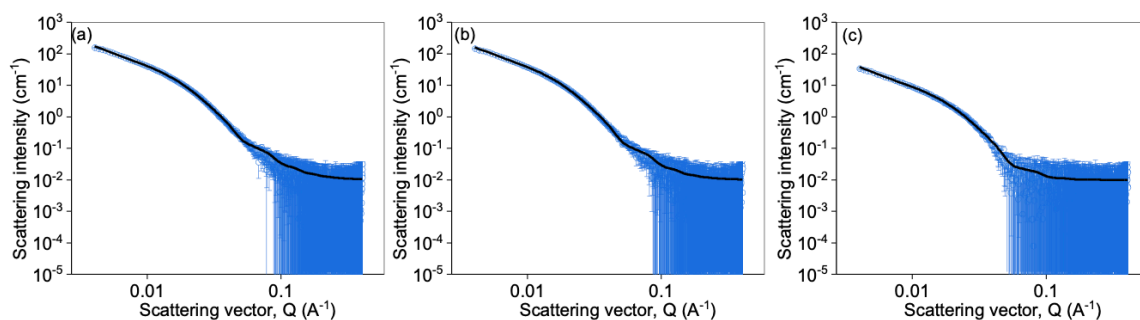
Appendix: A

Figure A.6 SAXS 1D I vs Q plots from all three positions of the Carb-Val hydrogel after the electrochemical experiment had concluded. Data shown as open blue circles and corresponding fit shown as black lines (Fitting parameters shown in Table A.4). In total, SAXS measurements from three positions were collected, with position 0 being closest to the electrode surface and 2 the furthest away (a) position 0 (b) position 1 (c) position 2.

Carb-Val	Position 0	Position 1	Position 2
Model	EC+PL	EC+PL	EC+PL
Scale	1.0*	1.0*	1.0*
Background	0.01*	0.01*	0.01*
Background error	-	-	-
A scale	6.6×10^{-4}	2.5×10^{-3}	2.4×10^{-3}
A scale error	*1.9×10^{-5}*	*1.6×10^{-6}*	*1.5×10^{-5}*
A radius (Å)	59.0	63.6	63.2
A radius error	*0.9*	*0.3*	*0.3*
A axis ratio	2.3	2.4	2.4
A axis ratio error	*0.06*	*0.02*	*0.02*
A length (Å)	1000*	1000*	1000*
A length error	-	-	-
B scale	8.9×10^{-7}	4.6×10^{-5}	3.0×10^{-5}
B scale error	*8.8×10^{-7}*	*4.4×10^{-5}*	*5.0×10^{-5}*
B power	3.0	2.6	2.7
B power error	*0.2*	*0.01*	*0.02*
χ^2	1.1	1.1	1.1

Table A.4 Fitting parameters of the 1D I vs Q plots shown in Figure A.6. Values annotated with an asterisk (*) were fixed and not allowed to refine during the fitting process.
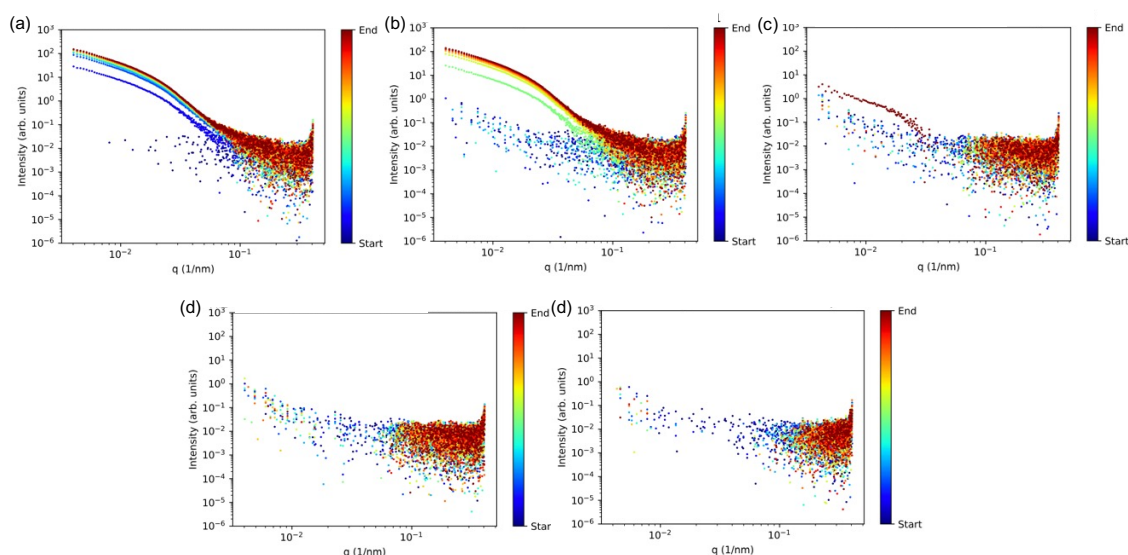
Figure A.7 Series of singular plots showing the SAXS data for each position of the Carb-Val hydrogel from the electrode surface with time. A background subtraction was performed before plotting each of the data series as a scatter plot. Position 0 is the closest position to the electrode surface and position 4 is the furthest away. (a) Position 0 (b) Position 1 (c) Position 2 (d) Position 3 (e) Position 4. Using the colour spectrum to the right of the plot, gel growth can be followed with time from the start of the experiment (blue) to the end (red).
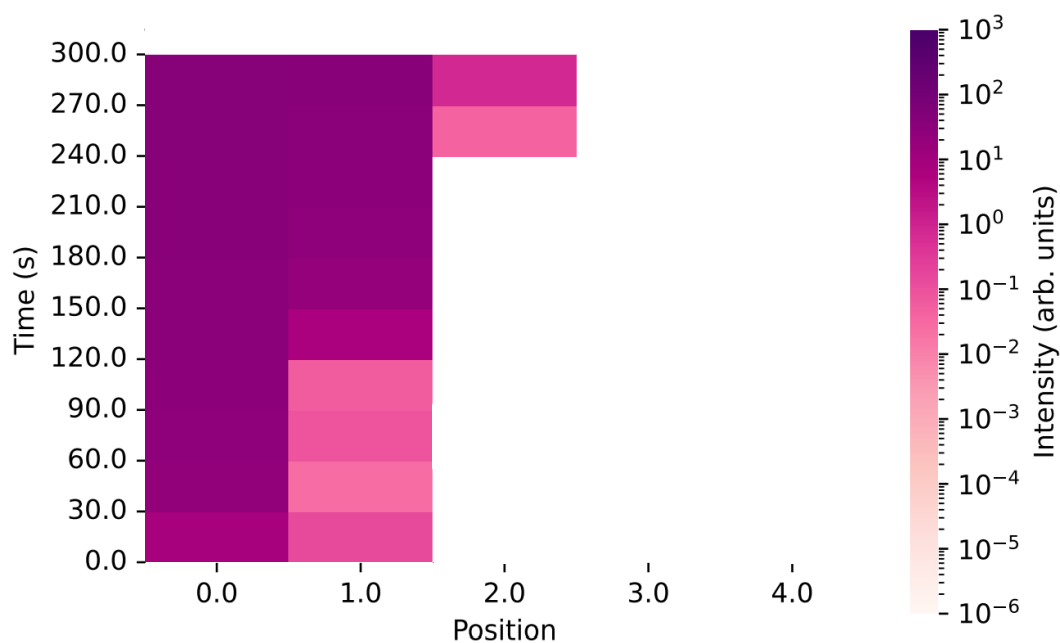
Figure A.8 Complimentary heatmap generated from the single position scatter plots shown in Figure A.7 The intensity of the scattered X-rays can be followed using the corresponding colour map to the right of the plot, with the intensity taken from the intensity from Figure A.7 at a single, user-defined, q value, set to q = 0.01 nm^{-1}.
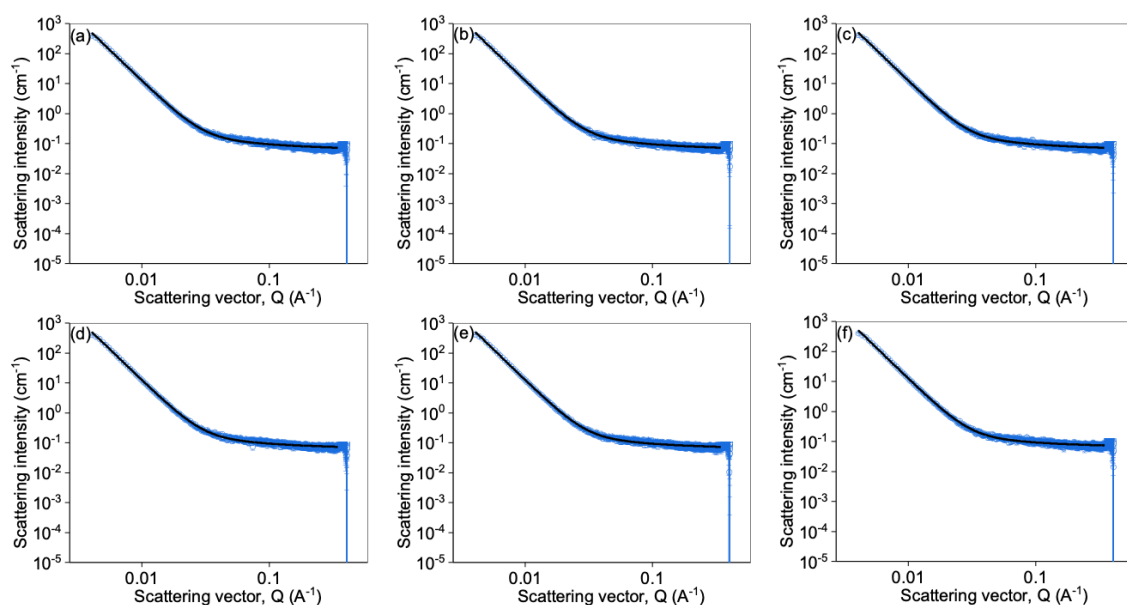
Figure A.9 SAXS 1D I vs Q plots from position 2 of the Carb-Leu hydrogel growing with time. Data shown as open blue circles and corresponding fit shown as black line (Fitting parameters shown in Table A.5). In total, six scans were collected during the 300 second experiment, with scan 1 being the first scan collected and scan 6 being the last (a) scan 1, 130 s (b) scan 2, 160 s (c) scan 3, 190 s (d) scan 4, 220 s (e) scan 5, 250 s (f) scan 6, 280 s.

Appendix: A

Carb-Leu	Scan 1	Scan 2	Scan 3	Scan 4	Scan 5	Scan 6
Model	C+PL	C+PL	C+PL	C+PL	C+PL	C+PL
Scale	1.0*	1.0*	1.0*	1.0*	1.0*	1.0*
Background	0.07*	0.07*	0.07*	0.07*	0.07*	0.07*
Background error	-	-	-	-	-	-
A scale	4.0×10^{-3}	5.0×10^{-3}	5.0×10^{-3}	5.0×10^{-3}	5.0×10^{-3}	7.0×10^{-3}
A scale error	7.0×10^{-4}	8.0×10^{-4}	8.0×10^{-4}	1.1×10^{-3}	1.1×10^{-3}	2.0×10^{-3}
A radius (Å)	5.4	5.2	5.3	4.8	4.9	4.1
A radius error	*0.5*	*0.5*	*0.5*	*0.6*	*0.6*	*0.6*
A length (Å)	1000*	1000*	1000*	1000*	1000*	1000*
A length error	-	-	-	-	-	-
B scale	8.2×10^{-8}	7.7×10^{-8}	7.3×10^{-8}	7.3×10^{-8}	7.2×10^{-8}	7.4×10^{-8}
B scale error	1.5×10^{-9}	1.4×10^{-9}	1.3×10^{-9}	1.3×10^{-9}	1.3×10^{-9}	1.3×10^{-9}
B power	4.1	4.1	4.1	4.1	4.1	4.1
B power error	4.0×10^{-3}	3.0×10^{-3}	4.0×10^{-3}	3.0×10^{-3}	4.0×10^{-3}	4.0×10^{-3}
χ^2	1.7	1.7	1.6	1.9	1.7	2.0

Table A.5 Fitting parameters of the 1D I vs Q plots shown in Figure A.9. Values annotated with an asterisk (*) were fixed and not allowed to refine during the fitting process.
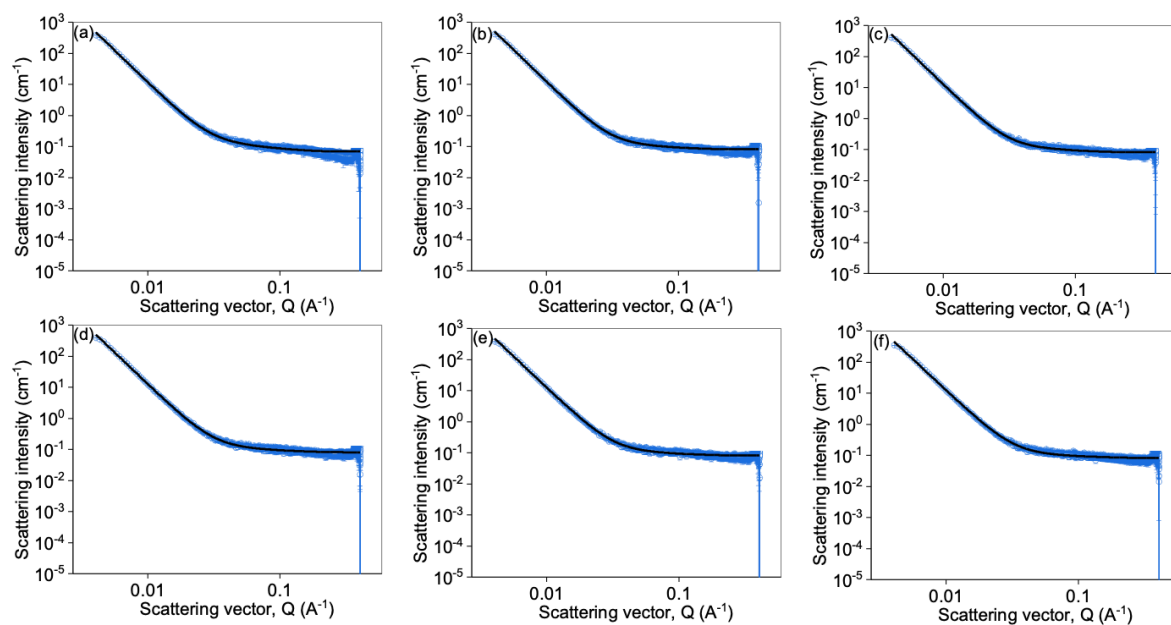
Figure A.10 SAXS 1D I vs Q plots from all five positions of the Carb-Leu hydrogel after the electrochemical experiment had concluded. Data shown as open blue circles and corresponding fit shown as black lines (Fitting parameters shown in Table A.6). In total, SAXS measurements from five positions were collected, with position 0 being closest to the electrode surface and 2 the furthest away (a) position 0 (b) position 1 (c) position 2 (d) position 3 (e) position 4 (f) position 5.

Appendix: A

Carb-Leu	Position 0	Position 1	Position 2	Position 3	Position 4	Position 5
Model	C+PL	C+PL	C+PL	C+PL	C+PL	C+PL
Scale	1.0*	1.0*	1.0*	1.0*	1.0*	1.0*
Background	0.07*	0.07*	0.07*	0.07*	0.07*	0.07*
Background error	-	-	-	-	-	-
A scale	8.0×10^{-4}	8.0×10^{-4}	7.0×10^{-4}	5.0×10^{-4}	3.0×10^{-4}	4.0×10^{-4}
A scale error	*8.9×10^{-5}*	*7.6×10^{-5}*	*5.1×10^{-5}*	*4.4×10^{-5}*	*6.4×10^{-5}*	*5.0×10^{-5}*
A radius (Å)	12.2	13.1	15.7	16.8	14.1	15.9
A radius error	*0.8*	*0.8*	*0.7*	*0.8*	*1.6*	*1.1*
A length (Å)	1000*	1000*	1000*	1000*	1000*	1000*
A length error	-	-	-	-	-	-
B scale	*6.8×10^{-8}*	*6.3×10^{-8}*	*6.2×10^{-8}*	*6.4×10^{-8}*	*6.5×10^{-8}*	*6.1×10^{-8}*
B scale error	*1.4×10^{-9}*	*1.3×10^{-9}*	*1.3×10^{-9}*	*1.3×10^{-9}*	*1.3×10^{-9}*	*1.2×10^{-9}*
B power	4.1	4.1	4.1	4.1	4.1	4.1
B power error	*4.0×10^{-3}*	*4.0×10^{-3}*	*4.0×10^{-3}*	*4.0×10^{-3}*	*3.0×10^{-3}*	*4.0×10^{-3}*
χ^2	1.9	2.9	2.0	2.1	2.0	2.2

Table A.6 Fitting parameters of the 1D I vs Q plots shown in Figure A.10. Values annotated with an asterisk (*) were fixed and not allowed to refine during the fitting process.
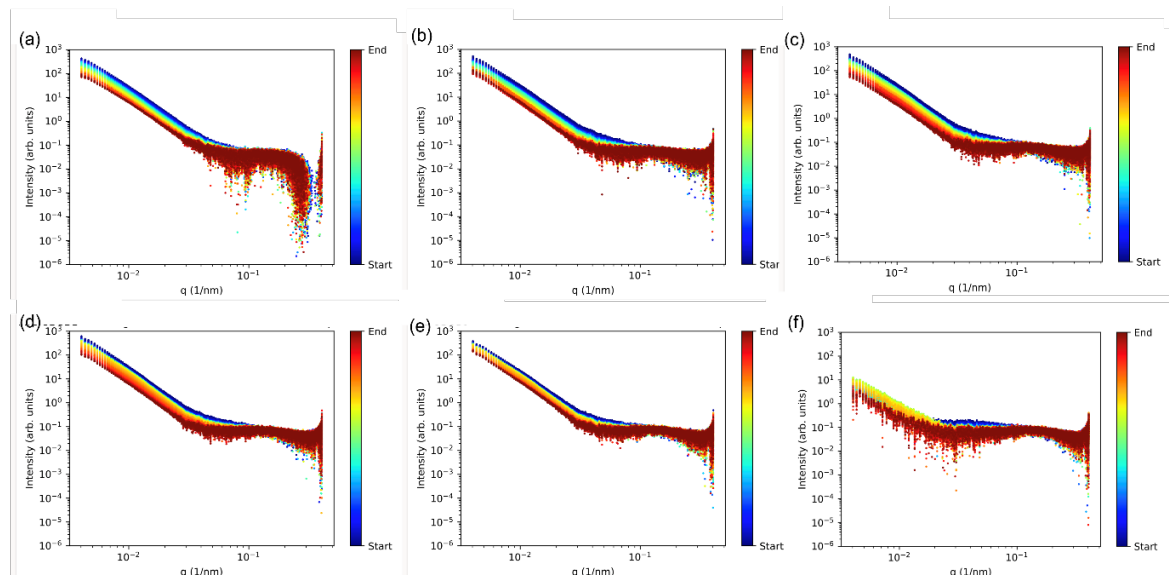
Figure A.11 Series of plots showing the SAXS data from each position of the Carb-Gly hydrogel during the attempted electropolymerisation reaction in perchloric acid. A background subtraction was performed before plotting each of the data series as a scatter plot. Position 0 is the closest position to the electrode surface and position 5 is the furthest away (a) position 0 (b) position 1 (c) position 2 (d) position 3 (e) position 4 (f) position 5. Using the colour spectrum to the right of the plot, gel growth can be followed with time from the start of the experiment (blue) to the end (red).
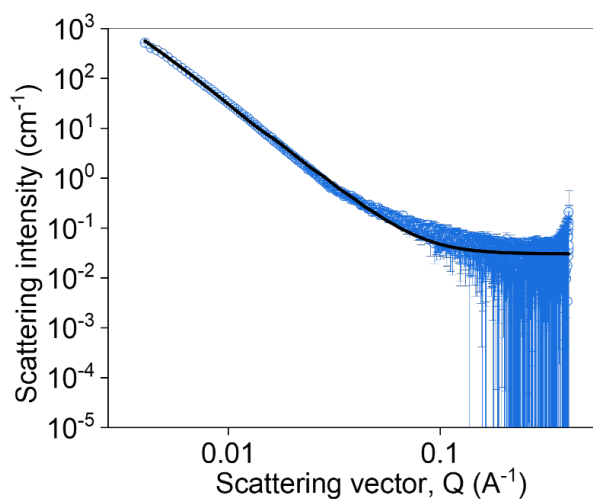

Figure A.12 1D I vs Q plot of scan 1 of position 2 taken during the attempted electropolymerisation of the Carb-Gly hydrogel in perchloric acid. The model and parameters from this fit were then used to perform the batch fitting process.

Appendix: A

Scan number	Background	A scale	A radius (Å)	A length (Å)	B scale	B power	χ^2
1	0.025*	1.7×10^{-4}	210.9	1000*	4.3×10^{-6}	3.3	1.2
2	0.025*	1.6×10^{-4}	213.6	1000*	3.6×10^{-6}	3.3	1.2
3	0.025*	1.6×10^{-4}	211.9	1000*	3.1×10^{-6}	3.3	1.1
4	0.025*	1.5×10^{-4}	213.9	1000*	3.1×10^{-5}	3.3	1.1
5	0.025*	1.1×10^{-4}	199.4	1000*	2.9×10^{-5}	3.3	1.1
6	0.025*	9.4×10^{-5}	209.4	1000*	2.5×10^{-5}	3.3	1.0
7	0.025*	6.2×10^{-5}	220.5	1000*	1.6×10^{-5}	3.3	1.0
8	0.025*	8.5×10^{-5}	229.4	1000*	1.7×10^{-5}	3.3	1.0
9	0.025*	2.9×10^{-3}	229.9	1000*	9.7×10^{-7}	3.4	1.0
10	0.025*	2.8×10^{-3}	224.0	1000*	5.1×10^{-7}	3.5	1.0

Table A.7 Batch fitting parameters of the 1D I vs Q plots taken from position 1 of the Carb-Val hydrogel during the attempted electropolymerisation experiment. Values annotated with an asterisk (*) were fixed and not allowed to refine during the fitting process.
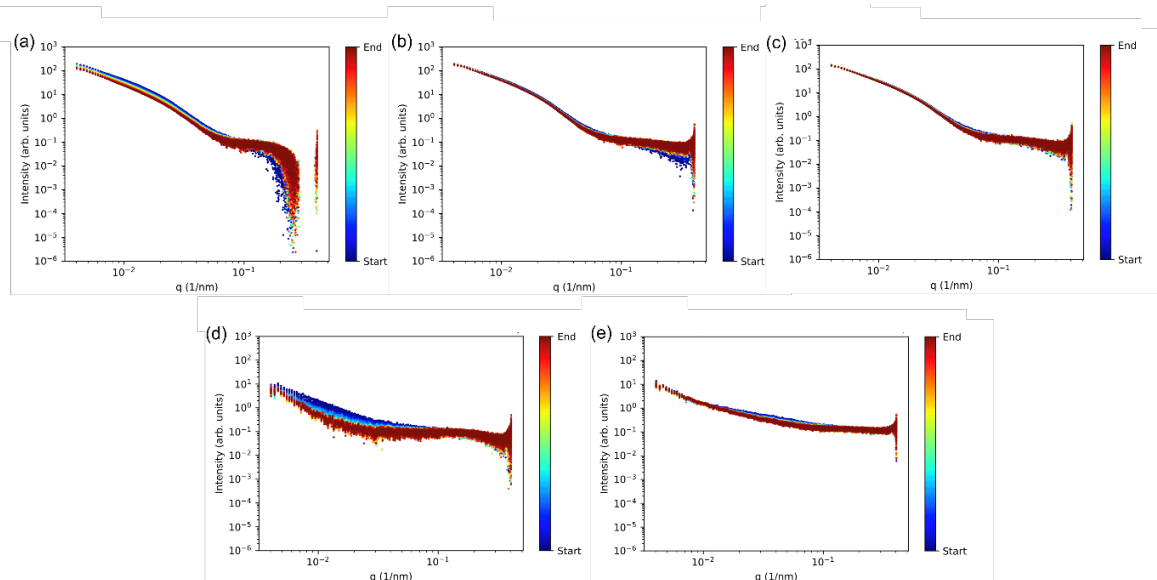
Figure A.13 Series of plots showing the SAXS data from each position of the Carb-Val hydrogel during the attempted electropolymerisation reaction in perchloric acid. A background subtraction was performed before plotting each of the data series as a scatter plot. Position 0 is the closest position to the electrode surface and position 5 is the furthest away (a) position 0 (b) position 1 (c) position 2 (d) position 3 (e) position 4 (f) position 5. Using the colour spectrum to the right of the plot, gel growth can be followed with time from the start of the experiment (blue) to the end (red).
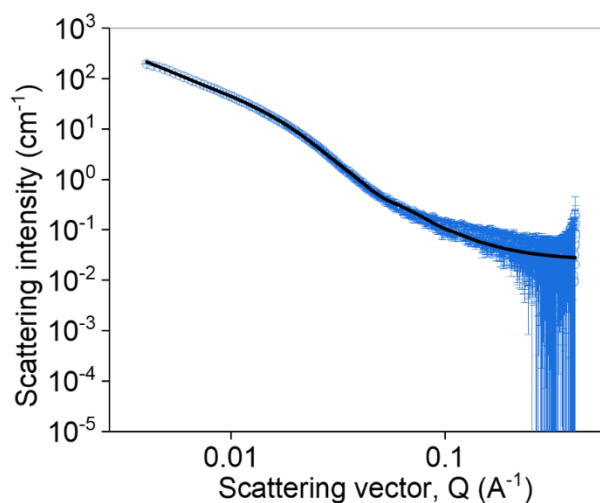

Figure A.14 1D I vs Q plot of scan 1 of position 2 taken during the attempted electropolymerisation of the Carb-Val hydrogel in perchloric acid. The model and parameters from this fit were then used to perform the batch fitting process.

Appendix: A

Scan number	Background	A scale	A radius (Å)	Axis ratio	A length (Å)	B scale	B power	χ^2
1	0.025*	1.7×10^{-3}	69.3	2.1	1000*	3.3×10^{-4}	2.3	1.6
2	0.025*	1.7×10^{-3}	69.7	2.1	1000*	3.0×10^{-4}	2.4	1.9
3	0.025*	1.7×10^{-3}	70.1	2.1	1000*	2.7×10^{-4}	2.4	2.1
4	0.025*	1.7×10^{-3}	70.0	2.1	1000*	2.7×10^{-5}	2.4	2.2
5	0.025*	1.7×10^{-3}	70.2	2.1	1000*	2.6×10^{-5}	2.4	2.2
6	0.025*	1.8×10^{-3}	69.4	2.2	1000*	2.6×10^{-5}	2.4	2.4
7	0.025*	1.7×10^{-3}	70.0	2.1	1000*	2.5×10^{-5}	2.4	2.3
8	0.025*	1.7×10^{-3}	70.7	2.0	1000*	2.4×10^{-5}	2.4	2.3
9	0.025*	1.7×10^{-3}	70.8	2.1	1000*	2.4×10^{-5}	2.4	2.5
10	0.025*	1.7×10^{-3}	70.8	2.1	1000*	2.4×10^{-5}	2.4	2.5

Table A.8 Batch fitting parameters of the 1D I vs Q plots taken from position 1 of the Carb-Val hydrogel during the attempted electropolymerisation experiment. Values annotated with an asterisk (*) were fixed and not allowed to refine during the fitting process.